Characterizing the distribution of relative humidity in ice-clouds depending on location, evolution and meteorological conditions

Georgios Dekoutsidis

München 2024

Characterizing the distribution of relative humidity in ice-clouds depending on location, evolution and meteorological conditions

Georgios Dekoutsidis

Dissertation

an der Fakultät für Physik

der Ludwig–Maximilians–Universität
München

vorgelegt von

Georgios Dekoutsidis

aus Thessaloniki, Griechenland

München, den 04/11/2024

Erstgutachter: Prof. Dr. Markus Rapp
Zweitgutachterin: PD. Dr. Silke Groß
Tag der mündlichen Prüfung: 19/12/2024

Zusammenfassung

Eiswolken, befinden sich in der oberen Troposphäre, sind kalt und vergleichsweise dünn und bestehen aus Eiskristallen. Sie spielen eine wichtige Rolle in der Erdatmosphäre, vor allem indem sie den Strahlungshaushalt beeinflussen. Aufgrund ihrer einzigartigen Eigenschaften unter den Wolken, verursachen sie weltweit eine jährliche Nettoerwärmung und tragen so zu Phänomenen wie der globalen Erwärmung und der arktischen Verstärkung, d. h. der beschleunigten Erwärmung der Arktis, bei.

Ihre makrophysikalischen und optischen Eigenschaften sowie ihre Strahlungseffekte sind stark von ihren mikrophysikalischen Eigenschaften abhängig. Diese wiederum, werden größtenteils bereits während ihrer Entstehung festgelegt, können sich aber im Laufe der Entwicklung der Wolke ändern. Der Prozess, der bei der Bildung von Eiswolken stattfindet, wird seinerseits durch die Lage der Wolken und die meteorologischen Umgebungsbedingungen beeinflusst.

Die relative Luftfeuchtigkeit über Eis (RHi) ist ein Parameter, der die makrophysikalischen mit den mikrophysikalischen Eigenschaften verbindet. Je nach Umgebungsfeuchte bildet sich ein Eiskristall auf verschiedenen Wegen, was zu Wolken mit unterschiedlichen mikrophysikalischen Eigenschaften führt. Die vertikale Struktur und Verteilung von RHi innerhalb einer Eiswolke ändert sich mit der Entwicklung der Wolke und kann als Indikator für ihr Alter verwendet werden.

Die Auswirkungen unterschiedlicher Umgebungsbedingungen auf die Bildung und Entwicklung von Eiswolken und die kleinräumigen mikrophysikalischen Prozesse, die während ihrer Bildung ablaufen, sind noch nicht vollständig verstanden, was auch zu Problemen bei ihrer Modellierung führt. Darüber hinaus sind auch ihre Strahlungseffekte noch nicht genau quantifiziert, obwohl anerkannt ist, dass sie eine Erwärmung verursachen. Eiswolken sind auch in vielen globalen Vorhersagemodellen häufig unterrepräsentiert, da diese einfache Parametrisierungen verwenden, die häufig keine hohen RHi-Werte zulassen, die für ihre Bildung erforderlich sind.

In dieser Arbeit wird der RHi-Wert innerhalb und in der Nähe von Eiswolken analysiert, der mit Hilfe von luftgestützten Lidar-Messungen über den mittleren und hohen Breiten gemessen wurde. Untersucht wird seine Abhängigkeit von Standort, Umgebungsbedingungen und Wolkenalter. Es zeigt sich, dass Eiswolken, die sich über der Arktis gebildet haben, häufiger hohe RHi-Werte aufweisen, was auf einen Unterschied in ihrem Entstehungsprozess hinweist. Nach der Untersuchung von Fällen über den mittleren Breiten wird festgestellt, dass Wolken in verschiedenen Entwicklungsstadien eine deutliche RHi-Signatur aufweisen.

In Bezug auf den Entstehungsprozess wird festgestellt, dass Wolken, die sich in-situ über den mittleren Breiten gebildet haben, im Allgemeinen kälter und häufiger untersättigt sind als Eiswolken die aus einer Flüssigen Wolke stammen. Eiswolken über der Arktis werden in Abhängigkeit von den Umgebungsbedingungen untersucht. Wolken, die während des Eindringens von Warmluft aus den mittleren Breiten in die Arktis gemessen wurden, waren im Vergleich zu Wolken, die unter ungestörten arktischen Bedingungen gemessen wurden, geometrisch und optisch dicker und häufiger übersättigt. Eine Untersuchung der mikrophysikalischen Eigenschaften ergab ebenfalls Unterschiede zwischen den beiden Wolkentypen.

Περίληψη

Τα νέφη πάγου, βρίσκονται στην ανώτερη τροπόσφαιρα, είναι ψυχρά, λεπτά και αποτελούνται από παγοκρυστάλλους. Παίζουν σημαντικό ρόλο στο σύστημα της γήινης ατμόσφαιρας, επηρεάζοντας κυρίως το ισοζύγιο της ακτινοβολίας. Λόγω των μοναδικών χαρακτηριστικών τους μεταξύ των νεφών, προκαλούν θέρμανση σε παγκόσμιο επίπεδο, συμβάλλοντας έτσι σε φαινόμενα όπως η υπερθέρμανση του πλανήτη και η αρκτική ενίσχυση, δηλαδή η επιταχυνόμενη θέρμανση της Αρκτικής.

Τα μακροφυσικά και οπτικά χαρακτηριστικά τους, καθώς και οι επιδράσεις τους στην ακτινοβολία εξαρτώνται σε μεγάλο βαθμό από τις μικροφυσικές τους ιδιότητες. Αυτές με τη σειρά τους καθορίζονται σε μεγάλο βαθμό ήδη κατά τον σχηματισμό τους, αλλά ενδέχεται να αλλάξουν καθώς το νέφος εξελίσσεται. Η διαδικασία που λαμβάνει χώρα κατά το σχηματισμό των νεφών πάγου, επηρεάζεται από τη θέση τους και τις μετεωρολογικές συνθήκες.

Η σχετική υγρασία ως προς τον πάγο (RHi) είναι μια παράμετρος που συνδέει τις μακροφυσικές με τις μικροφυσικές ιδιότητες. Ανάλογα με την RHi του περιβάλλοντος, ένας παγοκρύσταλλος σχηματίζεται ακολουθώντας διαφορετικές διαδικασίες που οδηγούν σε νέφη με διαφορετικές μικροφυσικές ιδιότητες. Η κατακόρυφη δομή και η κατανομή της RHi μέσα σε ένα νέφος πάγου αλλάζει με την εξέλιξη του νέφους και μπορεί να χρησιμοποιηθεί ως δείκτης της ηλικίας του.

Παρά τα προαναφερθέντα, η κατανόηση του τρόπου με τον οποίο οι διαφορετικές περιβαλλοντικές συνθήκες επηρεάζουν το σχηματισμό και την εξέλιξη των νεφών πάγου και οι μικροφυσικές διεργασίες μικρής κλίμακας που λαμβάνουν χώρα κατά το σχηματισμό τους, δεν είναι ακόμη πλήρως κατανοητές, γεγονός που οδηγεί επίσης σε προκλήσεις στη μοντελοποίησή τους. Επιπλέον, η ακριβής επίδρασή τους στο ισοζύγιο ακτινοβολίας δεν είναι απόλυτα ποσοτικοποιημένη, αν και είναι αποδεκτό ότι προκαλούν αύξηση της θερμοκρασίας. Τα νέφη πάγου υποεκπροσωπούνται επίσης συχνά σε πολλά παγκόσμια προγνωστικά μοντέλα, τα οποία χρησιμοποιούν απλές παραμετροποιήσεις που συνήθως δεν επιτρέπουν υψηλές τιμές RHi, απαραίτητες για το σχηματισμό αυτών των νεφών μέσω όλων των πιθανών οδών.

Σε αυτή την εργασία αναλύεται η RHi εντός και πλησίον των νεφών πάγου που μετρήθηκαν με αερομεταφερόμενο lidar πάνω από τα μεσαία και υψηλά γεωγραφικά πλάτη. Διερευνάται η εξάρτησή της από τη θέση, τις περιβαλλοντικές συνθήκες και την ηλικία του νέφους. Διαπιστώνεται ότι τα νέφη πάγου που σχηματίστηκαν πάνω από την Αρκτική ανιχνεύονται συχνότερα με υψηλές τιμές RHi, γεγονός που υποδηλώνει διαφορά στη διαδικασία σχηματισμού τους. Αφού μελετήθηκαν περιπτώσεις πάνω από τα μεσαία γεωγραφικά πλάτη, διαπιστώθηκε ότι νέφη σε διαφορετικά εξελικτικά στάδια έχουν μια ξεχωριστή, χαρακτηριστική υπογραφή RHi.

Όσον αφορά τη διαδικασία σχηματισμού, διαπιστώνεται ότι τα νέφη που σχηματίστηκαν επί τόπου πάνω από τα μεσαία πλάτη είναι γενικά ψυχρότερα και συχνότερα υποκορεσμένα σε σύγκριση με τα νέφη πάγου που προήλθαν από υγρά νέφη. Τα νέφη πάγου πάνω από την Αρκτική μελετώνται με βάση τις περιβαλλοντικές συνθήκες. Τα σύννεφα που μετρήθηκαν κατά τη διάρκεια εισβολής θερμού αέρα στην Αρκτική από τα μέσα γεωγραφικά πλάτη ήταν γεωμετρικά και οπτικά παχύτερα σε σύγκριση με τα σύννεφα που μετρήθηκαν σε αδιατάρακτες αρκτικές συνθήκες και συχνότερα υπερκορεσμένα. Η μελέτη των μικροφυσικών ιδιοτήτων αποκάλυψε επίσης διαφορές μεταξύ των δύο τύπων νέφους.

Abstract

Ice-clouds, found in the upper troposphere, cold, comparably thin and made up of ice crystals, play a significant role in the earth's atmosphere system, mainly by affecting the radiation budget. Due to their unique characteristics among the clouds, they cause a net annual warming globally, thus contributing to phenomena like global warming and arctic amplification, i.e. the accelerated warming of the arctic.

Their macrophysical and optical characteristics, as well as their radiative effects are strongly dependent on their microphysical properties. These are in turn largely decided already during their formation, but might change as the cloud evolves. The process that takes place during the formation of ice clouds is itself steered by the location of the clouds and the ambient meteorological conditions.

The relative humidity over ice (RHi) is a parameter that connects the macrophysical to the microphysical properties. Depending on the ambient RHi an ice crystal forms following different pathways leading to clouds that have different microphysical properties. The vertical structure and distribution of RHi within an ice cloud changes with the clouds evolution and can be used as an indicator of the clouds age.

Despite the abovementioned, the understanding of how different ambient conditions affect the formation and evolution of ice clouds and the small-scale microphysical processes that take place during their formation are not yet completely understood, which also leads to challenges in their modelling. Moreover, their exact radiative effects are also not perfectly quantified, although it is accepted that they cause warming. Ice-clouds are also frequently underrepresented in many global forecasting models, which use simple parametrizations, frequently not allowing high RHi values necessary for ice-cloud formation via all possible pathways.

In this work the RHi within and in the vicinity of ice-clouds measured by means of airborne lidar over the mid- and high latitudes is analyzed. Its dependence on location, ambient conditions and cloud age is investigated. It is found that ice-clouds that formed over the arctic are more frequently detected with high RHi values, indicating a difference in their formation process. After studying two cases over the midlatitudes, it is found that clouds at different evolutionary stages have a distinct RHi signature.

Regarding the formation process, it is found that clouds that formed in-situ over the midlatitudes are generally colder and more frequently subsaturated compared to ice-clouds with a liquid predecessor cloud. Ice-clouds over the arctic are studied depending on the ambient conditions. Clouds that were measured during intrusions of warm air into the arctic from the midlatitudes were geometrically and optically thicker compared to clouds measured in undisturbed arctic conditions and more frequently supersaturated. A study of the microphysical properties also revealed differences for the two cloud types.

List of Publications

Parts of the work presented in this thesis have been published in the following peer-reviewed articles:

- Dekoutsidis, G., Wirth, M., and Groß, S.: The effects of warm-air intrusions in the high Arctic on cirrus clouds, Atmospheric Chemistry and Physics, 24, 5971–5987, https://doi.org/10.5194/acp-24-5971-2024, 2024.

- Dekoutsidis, G., Groß, S., Wirth, M., Krämer, M., and Rolf, C.: Characteristics of supersaturation in midlatitude cirrus clouds and their adjacent cloud-free air, Atmospheric Chemistry and Physics, 23, 3103–3117, https://doi.org/10.5194/acp-23-3103-2023, 2023.

- Li, Y., Mahnke, C., Rohs, S., Bundke, U., Spelten, N., Dekoutsidis, G., Groß, S., Voigt, C., Schumann, U., Petzold, A., and Krämer, M.: Upper-tropospheric slightly ice-subsaturated regions: frequency of occurrence and statistical evidence for the appearance of contrail cirrus, Atmospheric Chemistry and Physics, 23, 2251–2271, https://doi.org/10.5194/acp-23-2251-2023, 2023.

- Wang, Z., Bugliaro, L., Jurkat-Witschas, T., Heller, R., Burkhardt, U., Ziereis, H., Dekoutsidis, G., Wirth, M., Groß, S., Kirschler, S., Kaufmann, S., and Voigt, C.: Observations of microphysical properties and radiative effects of a contrail cirrus outbreak over the North Atlantic, Atmospheric Chemistry and Physics, 23, 1941–1961, https://doi.org/10.5194/acp-23-1941-2023, 2023.

Table of contents

Zusammenfassung v
Περίληψη vii
Abstract ix
List of Publications xi
Table of contents xiii
Introduction 1
1.1 Ice clouds 1
1.2 The importance of cirrus 9
1.2.1 Over the midlatitudes 9
1.2.2 Over the high latitudes 10
1.3 Challenges 11
1.4 Why relative humidity and supersaturation? 12
1.5 Objectives and structure of this thesis 13
1.6 Data sources 14
Theoretical background 15
2.1 Atmospheric Lidar 15
2.1.1 Basic setup and the lidar equation 16
2.1.2 High Spectral Resolution Lidar (HSRL) 19
2.1.3 Differential Absorption Lidar (DIAL) 21
2.1.4 Depolarization lidar 24
2.2 Ice nucleation 27
Methods and data 29
3.1 WALES lidar system 29
3.1.1 The Transmitter 31
3.1.2 The Receiver 32
3.1.3 Measurement attributes and error estimates 33
3.2 HALO research aircraft 37
3.3 The ML-CIRRUS campaign 39
3.4 The HALO-(AC)^3 Campaign 42
3.5 Calculation of products 45
3.6 Uncertainty in the calculation of RHi 47

3.7 Masking 48
Midlatitudes 48
High latitudes 49
3.8 Cirrus classifications 53
3.8.1 Based on formation: In-situ formed vs Liquid origin 53
3.8.2 Based on ambient conditions: Arctic vs WAI conditions 54
Results 57
4.1 Characterization of midlatitude cirrus clouds based on their RHi 57
4.1.1 Distribution of RHi in midlatitude cirrus 58
4.1.2 The vertical structure of RHi in midlatitude cirrus 60
4.1.3 In-situ and liquid origin cirrus over the midlatitudes 62
Distribution of RHi 62
Comparison of the vertical structure of RHi in in-situ and liquid origin cirrus 64
4.1.4 Relative humidity in different cloud evolution stages 65
Case 1: Mesoscale Convective System 65
Case 2: Warm Conveyor Belt 67
4.2 Characteristics of supersaturation of cirrus clouds over the arctic 69
4.2.1 Distribution of RHi in and around cirrus over the arctic 69
4.2.2 Vertical structure of supersaturation in arctic cirrus clouds 72
4.2.3 Cirrus clouds in the arctic under AC and WAI conditions 73
The high arctic under AC and WAI conditions 73
Geometrical and optical characteristics 75
Distribution of RHi 76
Vertical structure of RHi inside AC and WAI cirrus 79
Discussion 83
5.1 Cirrus cloud characteristics over the midlatitudes 84
5.1.1 Relative humidity in midlatitude cirrus clouds 84
Properties of RHi 84
Distribution of RHi through the cloud layers 86
5.1.2 Differences between liquid origin and in-situ formed cirrus 86
Characteristics of RHi with respect to temperature 86
Vertical structure of RHi 87
The role of the ambient updraft 87
5.1.3 Temporal evolution of RHi distribution with cloud age 88

5.2 Cirrus cloud characteristics over the arctic 89
5.2.1 RHi of cirrus clouds in the arctic 90
RHi distribution with respect to temperature 90
In-cloud RHi layers 90
5.2.2 Warm air intrusions into the arctic 91
5.2.3 Cirrus clouds under AC and WAI conditions 92
Geometrical and optical properties 92
Differences in RHi distribution 93
In-cloud vertical RHi layers 94
Nucleation processes and microphysics 94
5.3 Differences between the mid- and high latitudes 96
5.3.1 Overview 97
RHi distribution with respect to temperature 97
In-cloud RHi layers 97
5.3.2 Cirrus types with different location, formation and airmass 98
Distribution and vertical structure of RHi from mid- to high latitudes 99
5.4 Assessment of the uncertainties of RHi 103
Conclusion and outlook 105
6.1 Summary 105
6.2 Open questions 108
Abbreviations and Symbols 110
List of Abbreviations 110
List of Symbols 112
List of Figures 114
List of Tables 116
References 117
Acknowledgements 139

Chapter 1

Introduction

1.1 Ice clouds

cirrus noun (2)

/ˈsɪrəs/

1. *literal*: A curl-like tuft, fringe, or filament.
2. *meteorology*: A form of cloud, generally at a high elevation, presenting the appearance of diverging filaments or wisps, often resembling a curl or lock of hair or wool. Particular varieties are known as cat's or mare's tails.

(Oxford English Dictionary, 2023)

Figure 1.1: Cirrus clouds with their characteristic bright white color and wispy features captured over Mount Pangaion, Central Macedonia, Greece. Photo: Georgios Dekoutsidis, 20/12/2023.

Ice clouds, despite being arguably one of the most intriguing, unique and beautiful cloud types, were considered omens of bad weather in ancient Greece. Aristotle was the first to grasp the process of cloud formation as the transformation of water vapor at colder temperatures and higher altitudes:

"μενούσης δὲ τῆς γῆς, τὸ περὶ αὐτὴν ὑγρὸν ὑπὸ τῶν ἀκτίνων καὶ ὑπὸ τῆς ἄλλης τῆς ἄνωθεν θερμότητος ἀτμιδούμενον φέρεται ἄνω· τῆς δὲ θερμότητος ἀπολιπούσης τῆς ἀναγούσης αὐτό, καὶ τῆς μὲν διασκεδαννυμένης πρὸς τὸν ἄνω τόπον, τῆς δὲ καὶ σβεννυμένης διὰ τὸ μετεωρίζεσθαι πορρώτερον εἰς τὸν ὑπὲρ τῆς γῆς ἀέρα, συνίσταται πάλιν ἡ ἀτμὶς ψυχομένη διά τε τὴν ἀπόλειψιν τοῦ θερμοῦ καὶ τὸν τόπον, καὶ γίγνεται ὕδωρ ἐξ ἀέρος· [ ] ἔστι δ' ἡ μὲν ἐξ ὕδατος ἀναθυμίασις ἀτμίς, ἡ δ' ἐξ ἀέρος εἰς ὕδωρ νέφος·"

346 b 24 – 31 & 32 – 34 (Aristotle, 340BC).

"while the earth remains, the moisture surrounding it is evaporated by the rays and the heat from above and rises. Once the heat that was rising it is diminished, by scattering to the higher realm and by weakening after rising higher over the earth, the vapor is cooled again because of the missing heat and the cold surrounding, and water is formed from air. [ ] then the transformation to gas from water is vapor and the transformation from air to water is cloud." (Unofficial translation by the author).

Aristotle's successor Theophrastus of Eresus as well as Aratus of Soli, already in the 3rd century BC, described clouds appearing like fleece of wool, sometimes plucked and mottled and defined them as a sign of bad weather. (Aratus of Soli, 3rd century BC; Theophrastus of Eresus, 3rd century BC). Without knowing it, what they described were different groups (genera) and species of ice clouds.

Back then clouds were described and defined based solely on their visual properties. Over the millennia this has not changed drastically. In modern times the World Meteorological Organization (WMO) is responsible for the definition of clouds and comprises the international cloud atlas (WMO-No. 407). The clouds are grouped there based on their characteristic forms.

At high levels above the earth's surface, three cloud genera are defined, cirrus, cirrocumulus and cirrostratus, each with its own species and varieties. All three cloud genera are found at high altitudes and are described as being thin, nearly transparent and comprised almost exclusively of ice crystals (WMO International Cloud Atlas, 2017 Edition, 2024).

From a scientific point of view the common properties of the three cloud genera listed in the cloud atlas are more important than their appearance. Especially the fact that they are made up of ice crystals, distinguishes them from all others and implies that they have different characteristics, since ice crystals have different properties and interactions to water droplets. Thus, for academic purposes it is meaningful to group cirrus, cirrocumulus and cirrostratus together and characterize them as ice clouds (Lynch et al., 2002).

Commonly for this whole group of three genera the term cirrus is used as a synonym for ice clouds. Henceforth also in this thesis the term cirrus will be used to described cold, high-altitude, optically thin clouds, comprised of ice crystals, not taking into account their appearance, as is common also in bibliography (Lynch et al., 2002).

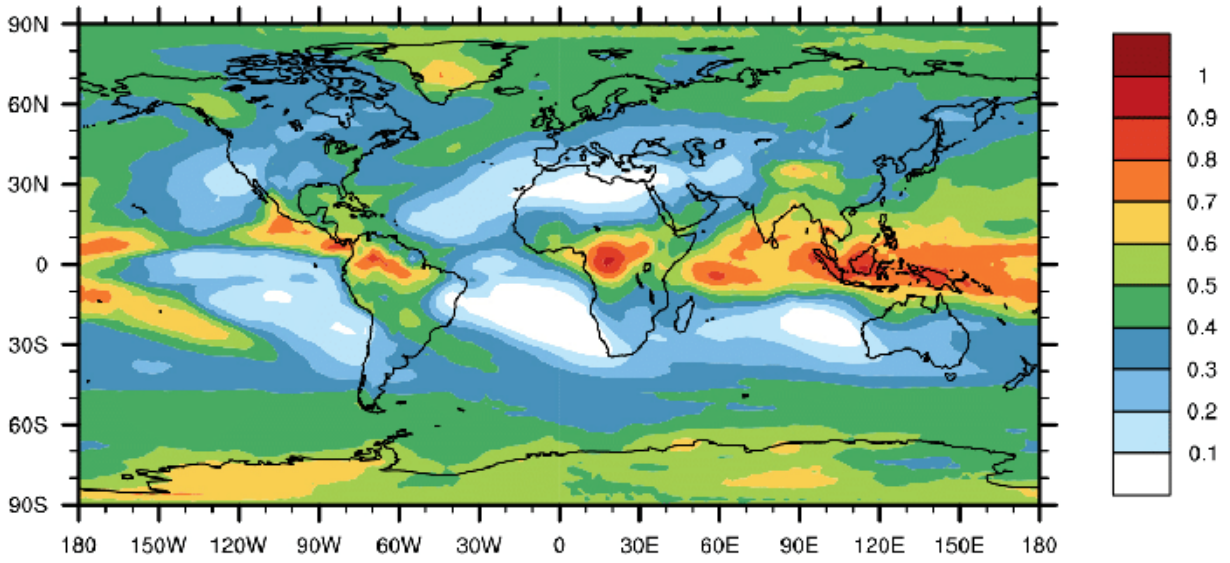

Figure 1.2: Map of the global, annual, mean cirrus cover. Calculated with the global climate model CAM3 (Community Atmosphere Model), including aerosol-cloud interactions and ice supersaturation for cirrus. Values calculated based on (Wang and Penner, 2010). Figure adapted from Schumann et al. (2015), their Figure 11 (a).

Starting from the global scale and Fig. 1.2, which contains the annual mean cirrus cover, it is obvious that cirrus clouds are an important part of the earth's atmosphere. Using model calculations, Schumann et al. (2015) find a mean global cirrus cover of 40 % annually. This value is close to the cirrus cloud cover of 40 % - 50 % reported by Stubenrauch et al. (2013), who used a range of satellite observations. Sassen et al. (2008) on the other hand also performed a study based on satellite measurements and found a mean, global, annual cirrus cloud cover of 16.7%. The difference, according to Stubenrauch et al. (2013), might be explained by the fact that the instrument they used was less sensitive and might not have detect thin subvisible cirrus.

The high frequency with which cirrus are detected globally is a first indication of their importance to the earth's atmosphere and climate system. Due to the large cirrus cloud cover, even if each cirrus has a small contribution to a certain atmospheric process, as a whole this effect might become significant in the larger scale.

Another characteristic of cirrus clouds becoming evident from Fig. 1.2, is that they are not evenly distributed over the globe. The highest frequency of occurrence is found over the tropics and the Intertropical Convergence Zone (ITCZ), with some hot spots also being evident. Additionally, both the Arctic and Antarctic regions also appear with a high annual cirrus cover, while the oceans of the midlatitude southern hemisphere are rather cirrus cloud free.

The non-uniform distribution of cirrus cloud cover over the globe, might stem from differences in meteorological conditions, weather patterns and pollution levels over certain areas. These factors can alter the conditions under which cirrus clouds form and affect the processes that take place during their formation, which as a result might lead to cirrus clouds having different characteristics over different regions.

It has been established, that cirrus clouds are an important part of the earth's atmosphere and climate system, but how do they affect it? Part of the answer is given by Gasparini and Lohmann, (2016), and is shown in Fig. 1.3. In this figure the cirrus Cloud Radiative Effect (CRE) at the Top of the Atmosphere (TOA) is presented. The CRE is a parameter showing how the radiation balance of the atmosphere changes when clouds are introduced in the system compared to clear-sky conditions. The net CRE at TOA due to ice clouds is split up into the effects of cirrus on the longwave (LW) radiation emitted from the earth and the shortwave (SW) radiation reaching the earth from the sun.

Cirrus clouds cause an all-year net warming globally, although their exact radiative effects are still not well quantified (Hong and Liu, 2015; Gasparini and Lohmann, 2016; Hong et al., 2016). More precisely, Gasparini and Lohmann, (2016) performed a modeling study and detected a positive net global mean ice cloud CRE of 5.7 W/m^2. Hartmann et al. (1992) used satellite data and found a mean global CRE of 2.4 W/m^2 and 2.3 W/m^2 induced by high thin clouds for summer

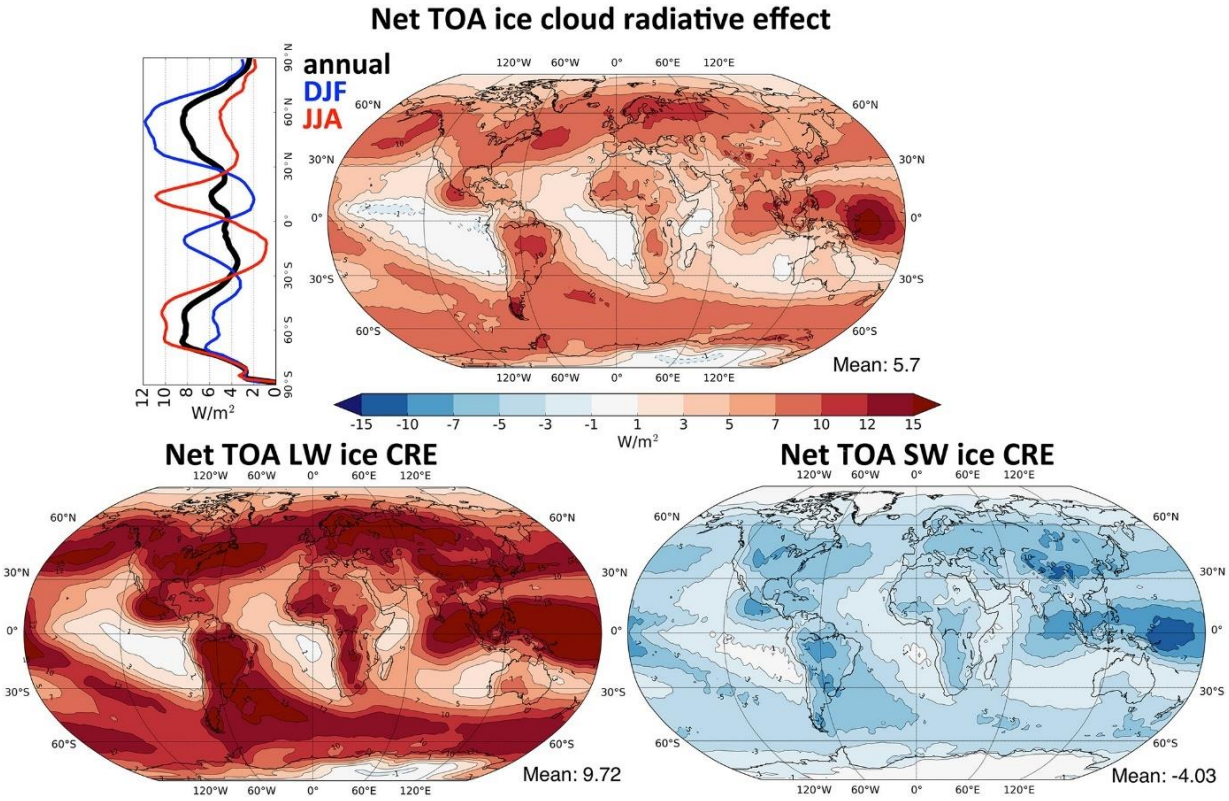

Figure 1.3: (Top Right) Map of the global distribution of annual average cirrus Cloud Radiative Effect (CRE) at the Top of the Atmosphere (TOA) for clouds at temperatures lower than -35°C. (Top Left) Zonally averaged values for annual (black), June July August (JJA) (red), and December January February (DJF) (blue) means. (Bottom Left) CRE due to interaction of cirrus with the outgoing thermal longwave (LW) radiation. (Bottom Right) solar shortwave (SW) radiation component of ice CRE. Calculated using the general circulation model ECHAM6 (Stevens et al., 2013) coupled with the two-moment microphysical and aerosol Hamburg Aerosol Module (HAM2) (Zhang et al., 2012). Reprinted from Gasparini and Lohmann, (2016), their Figure 2.

and winter respectively. Chen et al. (2000) also used satellite data and found a mean global annual CRE of 5.4 W/m^2 caused by cirrus at TOA. For cirrostratus, which are generally optically thicker, they found a negative CRE at TOA but still a positive one for the whole atmosphere. A more recent satellite study by Hong et al. (2016) yielded a net cirrus CRE of 5.1 W/m^2. Shi et al. (2024) performed a modeling study and found a positive ice cloud net CRE of 6.53 W/m^2. Gasparini et al. (2020) used two different models and found a net cirrus CRE of 6.8 W/m^2 and 4.8 W/m^2 from each.

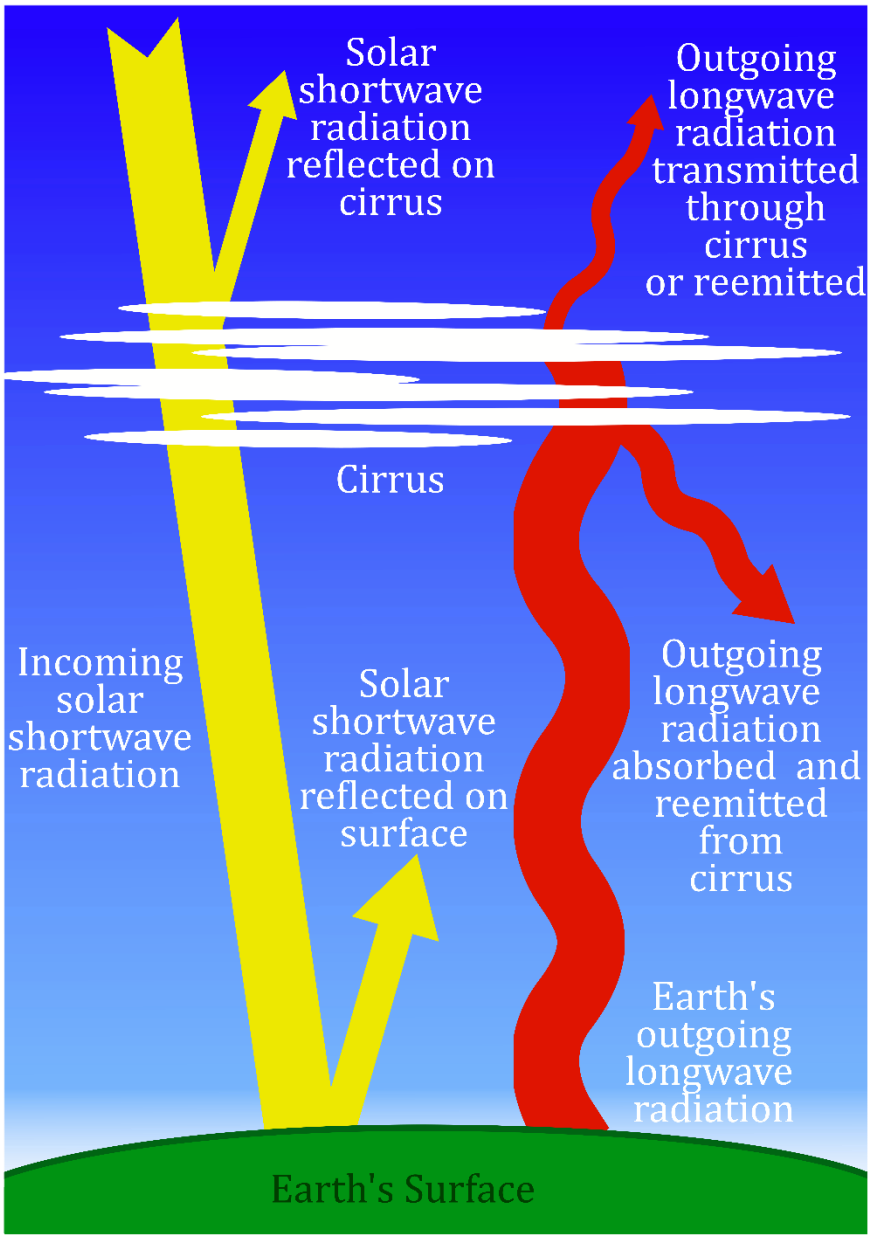

Figure 1.4: Schematic representation of the interaction of cirrus clouds with the incoming shortwave radiation from the sun and the outgoing longwave thermal radiation from the earth.

Regarding the geographical distribution of cirrus CRE at TOA, and comparing Fig. 1.2 and Fig. 1.3 it is evident that regions with a higher cirrus occurrence frequency also have a stronger cirrus CRE. Nevertheless, this is not the case on all occasions as for example in the polar regions. Thus, cirrus that form over different regions like the mid- and high latitudes, might have different effects on the radiation budget, which could stem from their different properties.

Despite there still being uncertainties on the exact CRE of cirrus, it is generally accepted that they cause a warming of the atmosphere (Hartmann et al., 1992; Chen et al., 2000; Boucher et al., 2013; Gasparini and Lohmann, 2016; Hong et al., 2016; Gasparini et al., 2020; Shi et al., 2024). Fig. 1.3 also hints to the reasons behind this observation. Ice clouds appear to have a cooling effect with respect to the incoming shortwave radiation from the sun, but a much stronger warming effect with respect to the outgoing thermal radiation from the earth (Gasparini and Lohmann, 2016; Shi et al., 2024). The next question to be asked is why does this happen and how do individual clouds interact with the LW and SW radiations?

In Fig. 1.4 the answer to this question is presented. It has already been established that cirrus clouds are found at higher altitudes, higher than the other cloud types, and are most commonly optically thin and made up off ice crystals. Due to these properties, they only reflect a small part of the incoming SW radiation from the sun, and let a big part of this incoming energy through. Thus, they contribute only a little to the solar albedo effect, contrary to lower level water clouds. On the other hand, they are very efficient in absorbing and reemitting the LW thermal radiation emitted from the earth. A part of this radiation is reemitted downwards in the atmosphere back towards the earth's surface, thus it is like this, otherwise outgoing, energy is trapped in the system due to the cirrus clouds (Manabe and Strickler, 1964; Cox, 1971; Ramanathan et al., 1983; Liou, 1986; Stephens et al., 1990; Chen et al., 2000; Lynch et al., 2002; Hong and Liu, 2015; Gasparini and Lohmann, 2016; Hong et al., 2016; Gasparini et al., 2018; Campbell et al., 2021; Marsing et al., 2023).

While the processes described above generally hold true for ice clouds viewed as a group, the effects may vary from cloud to cloud or clouds over different regions, potentially also resulting in the geographical distribution of ice cloud CRE shown in Fig. 1.3.

The macrophysical and optical properties of individual clouds might differ drastically depending, among others also on their location and formation process. For example, convective outflow cirrus commonly found over the tropics and subtropics are usually thicker. Thus, they can contribute more to the solar albedo effect and have a similar SW cooling and LW warming leading to a net zero CRE (Boucher et al., 2013; Gasparini and Lohmann, 2016). On the other hand, as seen also in Fig. 1.3, the ice cloud CRE is very high over the maritime continent and other tropical regions where optically thin and subvisible cirrus, i.e. thin clouds hardly detectable with the naked eye, commonly with an optical depth below 0.03, are frequently detected. These clouds allow a big part of the incoming SW radiation to penetrate through them, only minimally contributing to SW cooling, but still have a significant LW warming effect leading to a strong overall warming at TOA (McFarquhar et al., 2000; Haladay and Stephens, 2009; Martins et al., 2011; Henderson et al., 2013; Hong and Liu, 2015).

The smallest scale in the study of ice clouds are the microphysics, looking at the individual ice crystals from which the cirrus clouds are formed. Fig. 1.5 showcases the great variability of ice crystal shapes and sizes found in cirrus clouds. The different ice crystals also have different

interactions with the LW and SW radiation. Thus, it is the microphysical properties that define the radiative effects of the clouds. Also evident from Fig. 1.5, is the importance of the ambient conditions on the resulting ice crystals. Depending on the ambient conditions, such as temperature, ice supersaturation and available INP, a different formation process takes place resulting in different ice crystal number, shape and size (Stephens et al., 1990; Lynch et al., 2002). This in turn highlights the importance of this thesis. The microphysical properties are the defining parameter for the effects of cirrus clouds on the climate system, but they are themselves dependent on the ambient conditions, such as the relative humidity and can change as the cloud ages. Hence, understanding the characteristics of relative humidity in ice clouds and the dependence on cloud type, age and location, is a prerequisite to better understand, model and predict cirrus clouds and their effects.

In conclusion, the radiative effects of cirrus clouds strongly depend on their microphysical properties, such as ice crystal shape, size and concentration (Stephens et al., 1990; Haag and Kärcher, 2004; Fusina et al., 2007). These are in turn altered as the cloud ages and are largely determined by the initial ice nucleation process, which can for example affect ice crystal size and number concentration. Ice nucleation itself strongly depends on the ambient conditions and location of the clouds (e.g., temperature, available aerosol, turbulence) (Heymsfield, 1977; Khvorostyanov and Sassen, 1998; Kärcher and Lohmann, 2003; Seifert et al., 2004; Gensch et al., 2008; Krämer et al., 2016; Luebke et al., 2016). Thus, it has been highlighted that location, ambient conditions and evolutionary stage of a cirrus have a strong correlation to the cloud's macro- and microphysical, as well as radiative properties.

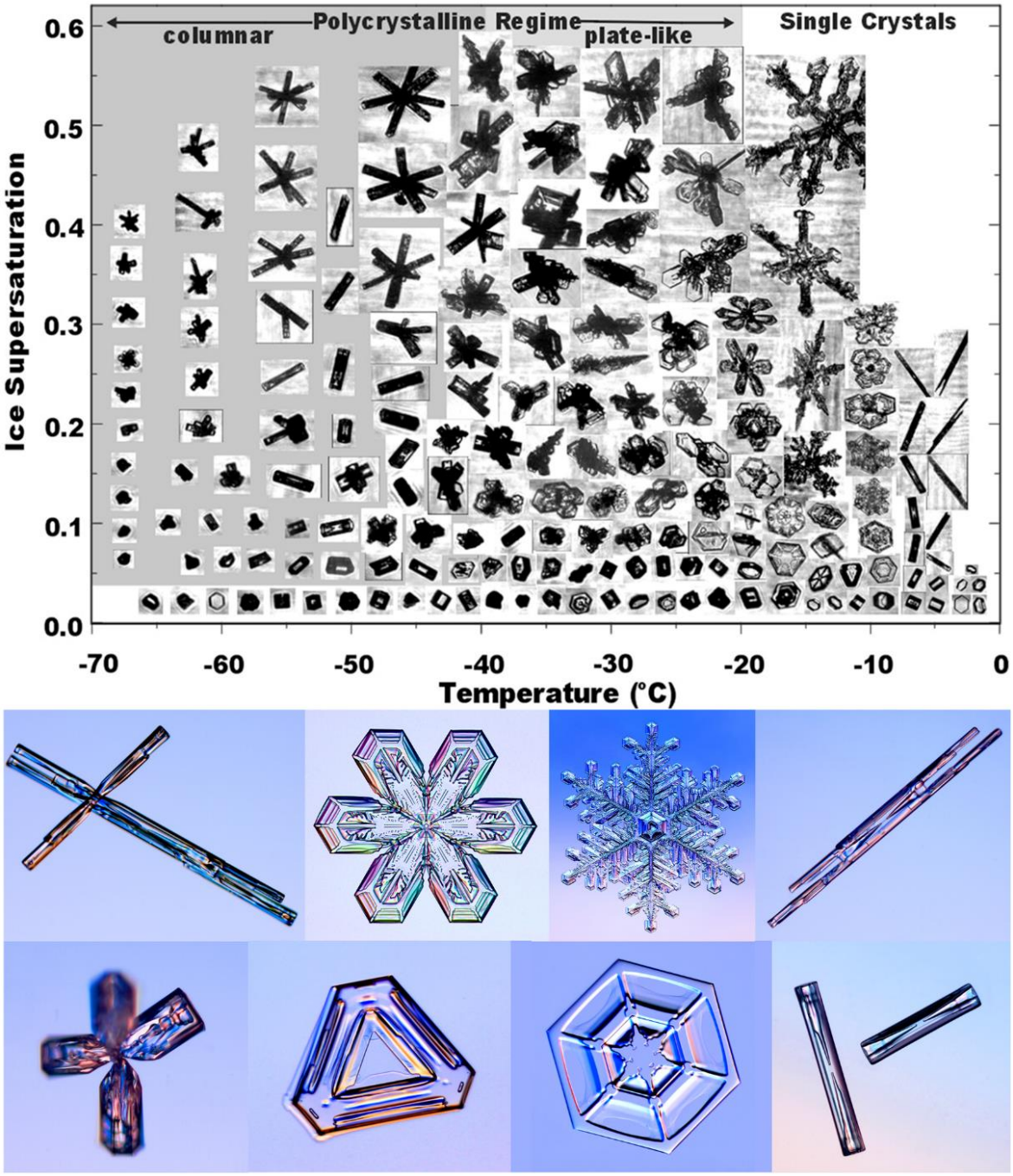

Figure 1.5: Top: Diagram showcasing the different ice habits that form for different temperature and ice supersaturation. Results from laboratory studies (Bailey and Hallett, 2004) and pictures from the Cloud Particle Imager (CPI), gathered during various field campaigns, predominantly the Second Alliance Icing Research Study (AIRS II). Adapted from Bailey and Hallett, (2009), their Figure 5. Bottom: Photographs of various snow crystal habits as captured by Prof. Kenneth G. Libbrecht at the California Institute of Technology (Caltech). Permission to use after personal communication with Prof. Libbrecht, who holds all rights to the images (SnowCrystals.com, 2024).

1.2 The importance of cirrus

It has been established, that cirrus clouds alter the radiation budget at TOA causing a net warming. They can be characterized as the thermal blanket of the atmosphere (Lynch et al., 2002). Their importance is enhanced by the fact that they are responsible for a big part of the earth's total cloud cover. As shown in Fig. 1.6, the temperature of the earth's surface is steadily rising. Global warming, as this phenomenon is labelled, is a well-studied and generally accepted fact and cirrus clouds with their warming effect play a significant role in it (e.g. Hansen et al., 2010; IPCC, 2021).

As shown in Fig. 1.3 there is a strong seasonal and geographical variation in the radiative effects of cirrus clouds, altering their importance in space and time. Depending on the region and season in which they form, cirrus clouds interact with different conditions and systems, which can result in them having a stronger or weaker effect.

1.2.1 Over the midlatitudes

The midlatitudes are a very active, ever-changing region. Many different weather systems (e.g. frontal systems, Warm Conveyor Belts (WCB), ridges, jet streams, convection and others), strong and frequent meridional transports, land-ocean contrasts, elevated natural, as well as strong anthropogenic aerosol emissions, due to the industrialization and dense air traffic are characteristics of the midlatitudes.

Cirrus clouds cover about 30 % of the midlatitudes (Wylie and Menzel, 1999). They form in this very variable environment, are affected by the abovementioned and might also be part of feedback mechanisms. The high level of complexity present over the midlatitudes, due to the great amount of dynamic mechanisms that interact and affect the formation and properties of cirrus clouds, as well as the general difficulty to measure these clouds due to their high altitude, results in a suboptimal representation of cirrus in weather prediction models and an introduction of uncertainties regarding climate sensitivity (Stevens and Bony, 2013; Bauer et al., 2015; Voigt et al., 2017).

As mentioned above, the very high density of air traffic, is a characteristic of the midlatitudes. Over Europe for example around 30000 flights are conducted daily. Under favorable conditions, cruising airplanes might induce the formation of condensation trails (contrails). Contrails are anthropogenic ice clouds with a linear shape that form behind airplanes. They are considered to be a major contributor to the climate impact of aviation. Despite this, still many uncertainties remain regarding their microphysical and radiative properties and their effects on the climate (Heymsfield et al., 2010; IPCC, 2021; Dekoutsidis et al., 2023b).

Under certain ambient conditions contrails can survive over longer periods of time and evolve into so-called contrail cirrus. These anthropogenic cirrus clouds are indistinguishable from natural ones on many aspects, but they form in regions and times where no ice clouds would form naturally. Thus, they artificially increase the cirrus cloud cover over the midlatitudes and might induce a warming due to the cirrus CRE. They are expected to have different properties and effects but their distinction and thus study are challenging, leaving many open questions.

1.2.2 Over the high latitudes

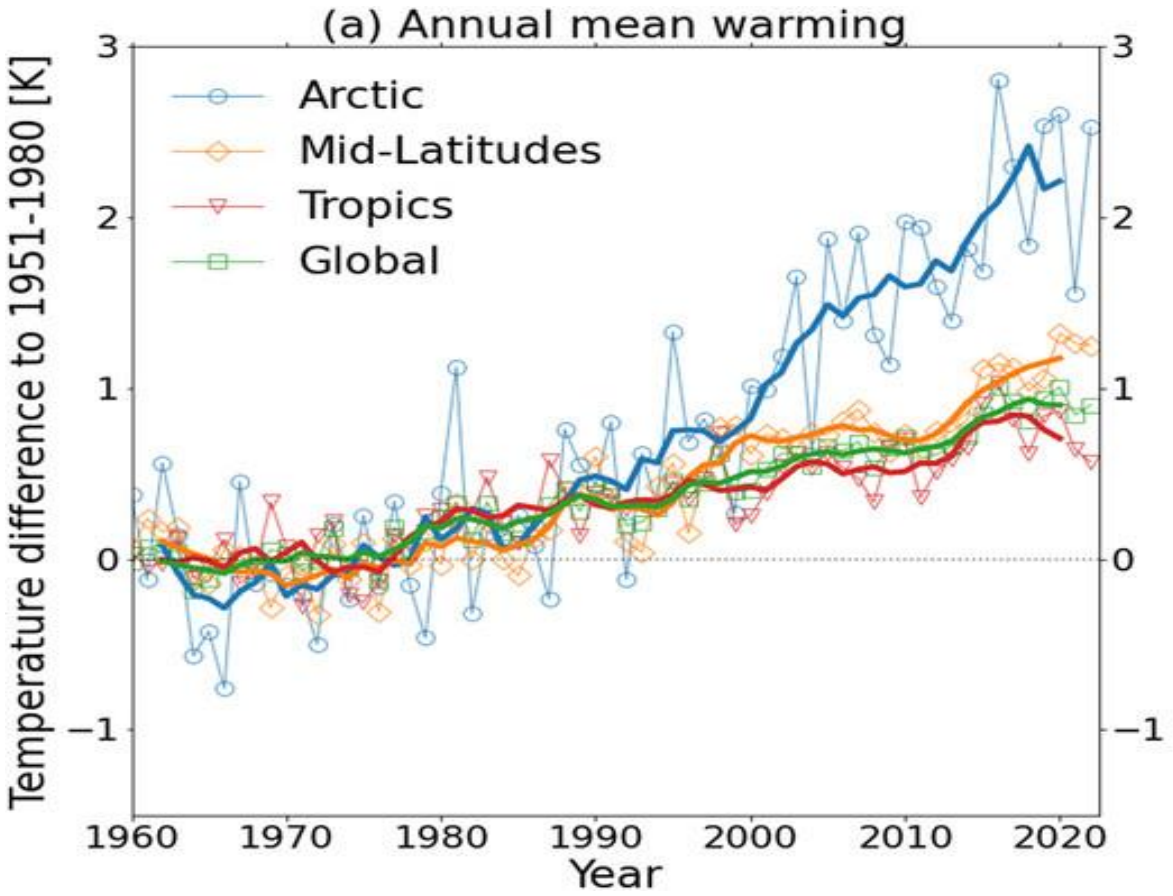

Figure 1.6: Time series of annually averaged near-surface air temperature anomalies relative to the 1951-1980 average. Four time series presented for the Arctic (60°–90°N), midlatitudes (30°–60°N), tropics (20°S–20°N), and global. Solid lines represent a 5-year running average. From Wendisch et al. (2023), their Fig. SB1.

In the past couple of decades an extraordinary change has been observed in the arctic climate, as is evident also in Fig. 1.6. Notably, the average near-surface temperature of the arctic has been increasing at a rapid rate, much faster than the global average. The term Arctic Amplification has been coined to this phenomenon (Serreze and Francis, 2006; Graversen and Wang, 2009; Hansen et al., 2010; Wendisch et al., 2023). The exact mechanisms and feedback processes of arctic amplification are a matter of ongoing research (e.g. Graversen and Wang, 2009; Pithan et al., 2018; Stuecker et al., 2018; Wendisch et al., 2019, 2023; Winton, 2006).

Given the role of cirrus clouds in the Earth's energy budget and their considerably large occurrence in the Arctic, it is also likely that they play a role in the feedback processes involved in arctic amplification, which also remains to be identified (Winton, 2006; Graversen and Wang, 2009; Pithan et al., 2018; Stuecker et al., 2018; Wendisch et al., 2019, 2023; Dekoutsidis et al., 2024).

Except for their effect on the radiation budget at TOA, cirrus clouds are one of the important factors in the regulation of water vapor uptake and distribution in the upper troposphere. This is important since water vapor is on its own a strong greenhouse gas. Ice nucleation removes water vapor from the system and binds it into ice crystals while also releasing latent heat in the process. Due to their weight and under weak updrafts the formed ice crystals will eventually start falling which will also result in less water vapor being available in the system for new ice formation (Kärcher, 2012; Zhao and Shi, 2023).

1.3 Challenges

Interestingly, the unique characteristics of cirrus clouds, such as their high altitude and small optical thickness, are the ones creating the challenges in their study. Satellite remote sensing of cirrus clouds commonly suffers from deficits in the detection and recognition especially of thin, subvisible cirrus, particularly when they are accompanied by lower level clouds below them (Lynch et al., 2002). Unfortunately, it is these thin cirrus that cause the largest amount of warming and are thus useful to be studied. On the other hand, cold clouds that are not necessarily ice clouds, such as supercooled liquid phase clouds, are also frequently misinterpreted due to the lack of information regarding the microphysical properties of the measured clouds.

Ground-based remote sensing measurements via lidar and radar are an improvement on the aspect of detection and recognition of cirrus but have the drawback of lacking versatility and targeted measurements. As technology has improved, new, light and easily transportable ground-based lidar instruments have become available so that clouds can be measured at different location but the limitations are still present.

Airborne measurements seem to be the best option, although they also face challenges. First and foremost, in order to take full advantage of an airborne platform a good prediction of cirrus formation location and altitude is necessary. This is hindered by the fact that many models still commonly use simple parametrizations and many still do not allow high supersaturations, which are necessary for cirrus formation (Kärcher and Lohmann, 2002, 2003; Haag et al., 2003; Lohmann et al., 2004; Liu et al., 2007; Comstock et al., 2008). Additionally, the high altitudes and cold temperatures at which cirrus are found, present a challenge, as only few research aircraft are capable of reaching these regions safely, in order to perform airborne measurements (Groß et al., 2014).

Airborne measurements can be either in-situ or remote sensing. In-situ measurements are very useful for measuring parameters such as ice crystal and aerosol shapes, but they have the drawback of providing information only on a single level through the cloud at a time. This leaves airborne remote sensing measurements via lidar and/or radar. These might frequently be not as accurate as in-situ but they have the advantage of providing information on a second dimension, most frequently in the form of a vertical curtain.

It is not only the measuring but also the modelling of cirrus clouds that is challenging. As has been mentioned previously, the macrophysical and radiative effects of cirrus are strongly dependent on the microphysical properties and processes. Modeling these is not always easy (Burkhardt, 2012; Kärcher, 2017). The simple parametrizations and approximations commonly

used, can lead to inaccuracies in the prediction of cirrus formation, evolution and effects (Liu and Penner, 2005; Kärcher et al., 2006; Phillips et al., 2008; Wang and Penner, 2010).

In order to accurately and reliably model cirrus clouds and their exact effects and interactions and be able to also predict all the above, a better understanding of the micro- and macrophysical properties of cirrus clouds is a prerequisite (Haag et al., 2003; Di Girolamo et al., 2009; Groß et al., 2014).

1.4 Why relative humidity and supersaturation?

Relative humidity and more specifically Relative Humidity over ice (RHi) is the main parameter used in this thesis. The RHi essentially describes the rates at which water transitions from its gaseous state, water vapor, to its solid state, ice and vice versa. An RHi of 1 or 100 % indicates that deposition, the transition from water vapor to ice, occurs at the same rate as sublimation, the transition from ice to water vapor. An airmass with RHi = 100 % is described as being in ice saturation.

Ice supersaturation, RHi>100%, is a common occurrence inside cirrus clouds but also in cloud-free areas of the upper troposphere (Ovarlez et al., 2002; Spichtinger and Gierens, 2009; Krämer et al., 2016; Gierens et al., 2020; Dekoutsidis et al., 2023a, 2024). Ice supersaturation is a prerequisite for ice nucleation and cirrus formation for both nucleation paths, HOM and HET.

As already shown in Fig. 1.5 and briefly discussed in Sect. 1.1, the RHi is closely related to the nucleation process that will take place and thus the resulting ice crystal properties. For example, at very high supersaturations, HOM nucleation can take place, which leads to clouds with a large number of small ice crystals.

On the other hand, HET nucleation commonly produces cirrus with fewer, but bigger ice crystals. This in turn can alter the radiative properties of the resulting cloud (Heymsfield and Miloshevich, 1995; Koop et al., 2000; Comstock et al., 2002; Kärcher and Lohmann, 2002, 2003; Haag et al., 2003; Ström et al., 2003; Krämer et al., 2009; Spichtinger and Gierens, 2009; Sakai et al., 2014; Urbanek et al., 2017; Dekoutsidis et al., 2023a, 2024).

It is now clear that the RHi is the deciding factor regarding the nucleation process that takes place during the formation of a cirrus cloud, which then also defines the microphysical properties of the cloud, which are further responsible for the radiative effects. Moreover, RHi is also an important parameter on the evolution and life cycle of cirrus. As the clouds age and evolve, their internal structure and distribution of supersaturation are changing. Thus, the RHi can be used as a signature of the clouds age.

In summary, the Relative Humidity over ice (RHi) is a parameter that can describe the connection between the macro- and microphysical realms, and holds information on the processes taking place in the formation and evolution of cirrus.

1.5 Objectives and structure of this thesis

In this thesis the properties and distribution of relative humidity within and around ice clouds over the mid- and high latitudes are studied. More specifically, the effects of the ambient conditions, formation process and the evolutionary stage are investigated. The main objective is to characterize ice clouds based on the relative humidity over ice (RHi) inside them and in their vicinity. An additional objective is to use this versatile parameter to extract information on the nucleation processes that took place during their formation, thus connecting their macrophysical and optical with their microphysical properties.

To achieve these objectives, airborne lidar measurements of water vapor concentration from two field campaigns are used. More specifically measurements performed by the combined water vapor differential absorption lidar (DIAL) and high spectral resolution lidar (HSRL) system WALES (from Water vapour Lidar Experiment in Space (Wirth et al., 2009)) during the ML-CIRRUS (Voigt et al., 2017) and the HALO-(AC)^3 (Ehrlich et al., 2023; HALO AC3, 2023) campaigns are analyzed. ML-CIRRUS was conducted over the midlatitudes and HALO-(AC)^3 over the arctic, thus being suitable for the purposes of this thesis. For both campaigns the German High Altitude and Long-range research aircraft (HALO) was used as the platform (Krautstrunk and Giez, 2012). WALES is capable of providing measurements of water vapor concentration and aerosol and cloud particle properties, on a 2D grid including information also on the vertical structure of the clouds and the atmosphere. These measurements are analyzed with the aim of answering the following scientific questions (SQ):

S.Q. 1: What are the characteristics of ice supersaturation in cirrus clouds at mid- and high latitudes depending on the meteorological conditions, their formation process and their evolutionary stage?

S.Q. 2: What are the differences of cirrus clouds between the mid- and high latitudes?

To approach these questions, first the cirrus clouds are identified in the datasets of the two campaigns, by applying a cirrus cloud mask based on various parameters. Then, the RHi is calculated from the measured water vapor mixing ratios, combined with model temperatures. Cirrus clouds over the midlatitudes are further split into two groups in order to study the effects of the formation process on their characteristics. Similarly, the arctic cirrus are split into two groups based on the ambient meteorological conditions. To study the effects of cloud evolution on the properties of the ice clouds, two cases are selected over the midlatitudes and analyzed.

In Chapter 2 the theoretical background necessary for this study is presented. The basic working principles and main techniques of lidar for atmospheric measurements are described in Sect. 2.1. Sect. 2.2 contains a description of the ice nucleation pathways that are possible during the formation of a cirrus cloud. In Chapter 3 the instruments, methods and data used in this study are presented. The WALES instrument, its components, capabilities and products are presented in Sect. 3.1, followed in Sect. 3.2 by a brief presentation of the characteristics and capabilities of the HALO research aircraft. Sect. 3.3 contains a description of the scopes, flight strategies and

Missions of the ML-CIRRUS campaign. Sect. 3.4 is the respective description of the HALO-(AC)^3 campaign. In Sect. 3.5, 3.6, 3.7 and 3.8 the focus is on the methodology and more precisely, calculation of products and their respective uncertainties, setting of the RHi regimes used throughout the thesis, cirrus cloud masking strategies and cirrus cloud classifications depending on their formation process (Sect. 3.8.1) and ambient meteorological conditions (Sect. 3.8.2).

The results of the analysis are presented in Sect. 4.1 and 4.2 for the midlatitude and high latitude cirrus respectively. In Sect. 4.1 first the general characteristics of RHi within and around the measured midlatitude cirrus clouds are presented, followed by an analysis of the two groups with different formation processes in Sect 4.1.3. The results regarding the changes in the distribution of RHi during the evolution of the clouds are shown in Sect. 4.1.4. Sect. 4.2 contains a similar analysis for the cirrus clouds measured in the arctic. The findings on the comparison of clouds measured under different meteorological conditions are presented in Sect 4.2.3. In Chapter 5 the results are discussed, and compared to other studies. Conclusions are drawn and implications are discussed. The thesis concludes with a summary of all presented findings and a discussion of open research questions that could be addressed in future studies, in Chapter 6.

1.6 Data sources

At the core of this thesis are airborne measurements performed by the WALES lidar system during the ML-CIRRUS and HALO-(AC)^3 campaigns (Wirth et al., 2009; HALO database, 2023). WALES data are used for the calculation of cirrus RHi and the construction of cirrus clouds masks. For the ML-CIRRUS missions, WALES was operated by Martin Wirth, Silke Groß and Andreas Fix. The initial processing and quality analysis of the raw data as well as the preparation of products, was carried out by Martin Wirth. For the HALO-(AC)^3 campaign, WALES was operated by Martin Wirth, Silke Groß, Manuel Gutleben and Georgios Dekoutsidis. Initial analysis, quality assessment and product calculation were once again performed by Martin Wirth.

For both campaigns, backwards trajectories were calculated based on the respective measurements. They were used in order to define the origin and properties of the airmasses in which cirrus clouds formed and classify them accordingly. Calculation of the trajectories was performed by Christian Rolf and Martina Krämer using the CLaMS-Ice model (McKenna et al., 2002). For the HALO-(AC)^3 campaign additional backwards trajectories were calculated by Andreas Schäfler, using the Lagrangian model LAGRANTO (Sprenger and Wernli, 2015).

Data retrieved during the HALO-(AC)^3 campaign by the optimal estimate retrieval VarCloud, which combines radar and lidar measurements to calculate microphysical properties of ice clouds are also used in this thesis in the discussion of the microphysical properties of cirrus over the arctic (Delanoë and Hogan, 2008; Ewald et al., 2021; Aubry et al., 2024). Application of the retrieval, calculation of products and quality analysis were performed by Florian Ewald and Clemantyne Aubry.

Finally, throughout this thesis data fields from the ERA-5 reanalysis dataset are also used in various applications, such as characterization and classification of ambient conditions (Hersbach et al., 2018).

Chapter 2

Theoretical background

In this chapter, theoretical principles that will aid to the understanding of the methods and results are presented. First a brief introduction on the general characteristics and basic principles of atmospheric lidar is provided (Sect. 2.1.1). It is followed by a more in-depth description of lidar techniques and measuring methods, namely the High Spectral Resolution Lidar (HSRL) in Section 2.1.2, the Differential Absorption Lidar (DIAL) in Section 2.1.3 and the depolarization lidar in Section 2.1.4. The chapter closes with a detailed description of the theories surrounding the ice nucleation processes in Section 2.2.

2.1 Atmospheric Lidar

Lidar instruments today emit pulsed laser light of various frequencies into the atmosphere and measure the properties of the backscattered light after its interaction with the particles and molecules found along its path. The use of light as a means to perform measurements of the atmosphere was already introduced in the early 1930s. Scientists back then used searchlight beams and distant telescopes to determine air density profiles of the upper troposphere and cloud-base altitudes (Synge, 1930; Tuve et al., 1935; Hulburt, 1937; Johnson et al., 1939; Elterman, 1951). Soon after, the continuous light of the searchlight beams was replaced by light pulses (Bureau, 1946; Friedland et al., 1956; Curcio and Knestrick, 1958; Horman, 1961). This allowed for the cloud-base height to be determined, by the time between emitting and receiving pulses. Since this technique was similar in nature to the, then already known, principles of the radar (radio-wave detection and ranging) the term lidar was coined for this type of measurement by Middleton and Spilhaus in 1953. In that and future studies the term was used either as a combination of the words light and radar or as an acronym from light detection and ranging.

Lidar instruments kept steadily improving and a big leap forward in their development came in the early 60's with the invention of the laser, the world's first coherent light source (Maiman, 1960) and especially the giant-pulse or Q-switched laser (McClung and Hellwarth, 1962). Scientist immediately recognized the importance of this invention and started to conceptualize and propose its use for atmospheric measurements (Goyer and Watson, 1963; Clemesha et al., 1965; Collis, 1966). The rapid evolution of the laser technology immediately impacted lidar instruments as well. They became smaller enabling for airborne and spaceborne instruments, more efficient and more accurate. Soon cirrus clouds were also measured (Collis, 1966; Evans, 1968). Advanced techniques such as the high spectral resolution lidar (HSRL) (Fiocco and Dewolf, 1968) and the differential absorption lidar (DIAL) for water vapor (Browell et al., 1979) were important milestones allowing scientists to characterize and quantify the optical and macrophysical properties of aerosols and clouds and measure the concentrations of atmospheric gases.

2.1.1 Basic setup and the lidar equation

Lidar has come a long way since the invention of the laser and the construction of the first instruments. Nowadays lidar instruments are found ground-based, aboard ships, airborne and spaceborne and are used in almost every branch of atmospheric physics. They employ many different techniques (elastic-backscatter lidar, differential-absorption lidar, Raman lidar, fluorescence lidar, Doppler lidar) targeted to measuring a rich number of parameters in the atmosphere. Despite that, they all share a common basic structure and operating principle shown in Fig. 2.1 and described in the following based mainly on Weitkamp, 2005 and Gimmestad and Roberts, 2023.

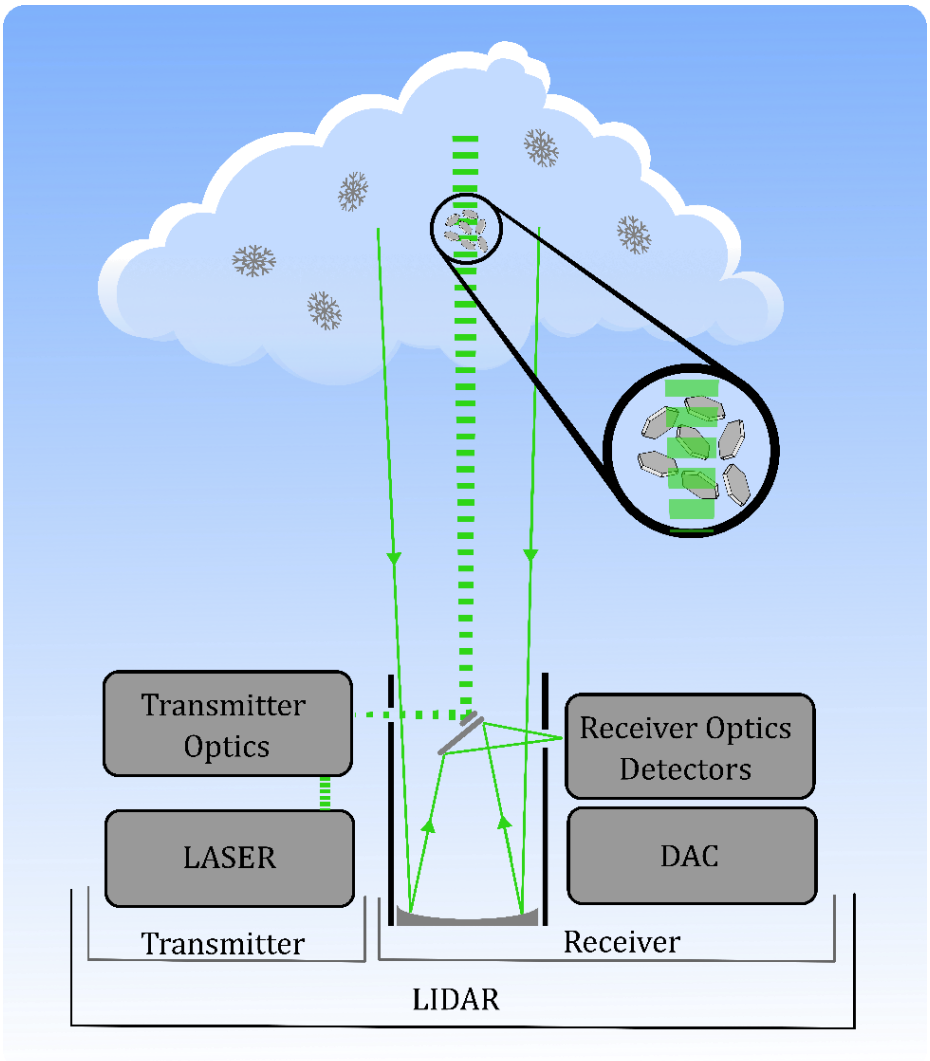

Figure 2.1: Schematic representation of a basic lidar setup and its working principle. Short light pulses are generated by a laser, get modified to fit particular applications and are emitted into the atmosphere. There, they react with the atmospheric constituents, aerosols, cloud particles and gas molecules. A part of the emitted light gets scattered back to the lidar where it gets collected by the telescope, fed through filters and detectors and finally the generated electrical signal is stored in a data acquisition (DAC).

Lidar systems are active remote sensing instruments, meaning they both emit and receive signals. Thus, every lidar consists of two main parts, a transmitter and a receiver. In the transmitter the heart of the instrument is found, the laser. It produces short light pulses of a certain frequency depending on its type. For example, the very commonly used Nd:YAG (Neodymium-doped Yttrium Aluminum Garnet) lasers produce light with a wavelength of 1064 nm. In many cases, depending on the intended use of the lidar the characteristics of the initially created light pulses might need to be altered. For this, in most modern lidar systems, the light from the laser passes through the transmitter optics where, for example, its frequency can be converted and the polarization set. In some instruments a beam expander is also applied. The light pulses are then released into the atmosphere, they interact with the particles and molecules, a part of the light gets backscatter and is collected by the receiver.

The receiver of a lidar consists of a telescope, the receiver optics and the data acquisition computer (DAC). The telescope collects the photons that were backscattered from the atmosphere. These photons are then fed through the receiver optics, where specific wavelengths and/or polarizations are filtered out depending on the applications of the instrument. The filtered photons are then captured by detectors such as photomultipliers and avalanche photo diodes. These detectors convert the optical signal into an electrical signal i.e. the photons to electrons, which then gets stored in the DAC.

The backscattered signal detected from the lidar is described by the lidar equation. In its simplest form the lidar equation can be written as:

$$P\ R\ = K\ G\ R\ \beta\ R\ T\ R \tag{2.1}$$

The power P of a signal received from a distance R, $P(R)$, depends on four factors. The first two, K and G, are determined solely by the set-up of the lidar instrument and can thus be calculated and even set by the ones building and using the instrument.

In more detail K is the system factor and can be written as:

$$K = P_0 \frac{c\tau}{2} A\eta \tag{2.2}$$

where P_0 is the average power of an emitted pulse, τ its duration and c the speed of light. The parameter: A, corresponds to the surface area of the telescope receiving the backscattered light and η is the overall efficiency of the instrument. Finally, the factor ½ is necessary since the light covers the same distance twice, from the lidar to the target and back.

The second factor $G(R)$ is the so-called geometric factor and can be written as:

$$G\ R\ = \frac{O\ R}{R^2} \tag{2.3}$$

$O(R)$ is the laser-beam receiver-field-of-view overlap function. It defines how much of the laser beam is within the field of view of the receiver at a certain distance. There are two possible lidar designs on that matter. In coaxial systems, the laser beam is emitted along the field of the receiver. In biaxial systems the laser beam is emitted from a distance of at least one receiver radius, next to the receiver. In both cases, close to the instrument the laser beam cannot be completely imaged on the receiver. The overlap increases with distance and is described by $O(R)$. The term R^{-2} denotes the quadratic decrease of the signal intensity with distance. When the laser pulses reach

a scattering volume, they are scattered in all directions. The relative intensities for each direction are given by the phase function and are strongly peaked in forward and backward directions for lager particles. The area of the receiver telescope is a part of this sphere. The greater the distance, the bigger the sphere, the smaller part of its surface is covered by the telescope, the less intensity is received.

The last two factors β and T are the atmospheric parameters of the lidar equation. $\beta(R,\lambda)$ is the backscatter coefficient. It describes the amount of light from the emitted laser pulses that gets scattered into the backwards direction i.e. towards the receiver. In the atmosphere the laser light can be scattered by molecules of various gases as well as aerosol and cloud particles. Thus, the backscatter coefficient has two components:

$$\beta\ R,\lambda\ =\ \beta_{mol}\ R,\lambda\ +\beta_{par}\ R,\lambda \tag{2.4}$$

The final factor of the lidar equation is the transmission term $T\ (R,\ \lambda)$. It describes the amount of light that was extinct while being transmitted through the atmosphere. In more detail it is given by:

$$T\ R,\lambda\ = exp\left[-2\int_0^R a\ R,\lambda\ dr\right] \tag{2.5}$$

The factor 2 denotes the two-way transmission path from the lidar to the backscattering volume and back. The sum of all losses along the transmission path of the light pulses is described by the term: light extinction, and $\alpha\ (R,\ \lambda)$ is the extinction coefficient. Extinction of the emitted light occurs because of absorption and scattering. Both phenomena can once again happen by molecules and particles. Thus, the extinction coefficient is written as:

$$a\ R,\lambda\ = a_{mol,sca}\ R,\lambda\ + a_{mol,abs}\ R,\lambda\ + a_{par,sca}\ R,\lambda\ + a_{par,abs}\ R,\lambda \tag{2.6}$$

The extinction coefficient is dependent on the wavelength. For most applications where particle properties are measured, such as the HSRL technique described in the following section, the wavelength of the emitted light is carefully chosen so that the absorption by atmospheric molecules $\alpha_{mol,abs}$ can be assumed to be zero. Absorption and scattering by particles both lead to extinction, thus the two can be combined into one term of particle extinction including both processes:

$$a_{par}\ R,\lambda\ = a_{par,sca}\ R,\lambda\ + a_{par,abs}\ R,\lambda \tag{2.7}$$

Finally, by combining the terms from Equations 2.2 – 2.7 into Equation 2.1, a more common form of the lidar equation is produced:

$$P\ R,\lambda\ = P_0\frac{c\tau}{2}A\eta\frac{O\ R}{R^2}[\beta_{mol}\ R,\lambda\ +\beta_{par}\ R,\lambda\ ]exp\left[-2\int_0^R[\alpha_{mol}\ R,\lambda\ +\alpha_{par}\ R,\lambda\ ]dr\right] \tag{2.8}$$

In Equation 2.8 we find four unknown atmospheric parameters. The backscatter coefficients and the extinction coefficients from molecules and particles respectively, β_{mol}, α_{mol}, β_{par} *and* α_{par}. This makes the lidar equation in this form impossible to solve.

The molecular backscatter coefficient, $\beta_{mol,}$ however, depends on ambient conditions, as it is proportional to atmospheric density, and the wavelength and can be determined by Rayleigh scattering (McCartney, 1976; Young, 1982; Bucholtz, 1995; Bohren and Huffman, 2008; Seinfeld and Pandis, 2016; Gimmestad and Roberts, 2023). At standard temperature and pressure (STP),

which is usually determined as a temperature T_s=*273,15 K* or T_s=*288,15 K* and pressure P_s=*101,325 kPa*, and a wavelength of 0,55 µm, Collis and Russell, 1976, for example, calculate:

$$\beta_{mol_s} = 1.39 \times 10^{-6} \times \left(\frac{550\ nm}{\lambda}\right)^4 m^{-1} sr^{-1} \tag{2.9}$$

If ambient temperature and pressure are known i.e. from measurements or models, the molecular backscatter coefficient $\beta_{mol}(h)$ at any altitude can also be calculated from the STP value with the following equation, based on the ideal gas law:

$$\beta_{mol}\ h\ = \beta_s \frac{P\ h\ T_s}{P_s T\ h} \tag{2.10}$$

Molecular scattering in the atmosphere also results in extinction of the emitted laser light. The molecular extinction coefficient, α_{mol} is thus related to the backscatter coefficient and can also be calculated. The two coefficients are linked by the so-called molecular lidar ratio:

$$S_{mol} = \frac{\alpha_{mol}\ R}{\beta_{mol}\ R} = \frac{8\pi}{3}\ sr \tag{2.11}$$

Despite providing a way to calculate the molecular backscatter and extinction coefficients, Equation 2.8 is still underdetermined, since the particle backscatter and extinction coefficients remain unknown. One way of overcoming this problem is to define a correlation between the two unknowns. Similar to the molecular, a fixed lidar ratio can be defined also for particles:

$$S_{par} = \frac{\alpha_{par}\ R}{\beta_{par}\ R} \tag{2.12}$$

Thus, the number of unknowns in the lidar equation (Eq. 2.8) is reduced to one and the equation can be solved (Klett, 1981). Nevertheless, there is a downside. Contrary to the molecular, the particle lidar ratio is in most cases not a constant. It is dependent on the microphysical, chemical and morphological properties of the particles. Despite lidar ratios being well studied and defined for most aerosol and cloud types this can still introduce errors and uncertainties in the measurements (e.g. Groß et al., 2011).

Another way of overcoming the problem of having two unknowns in the lidar equation would be to have two independent atmospheric signals. This method is applied among others in the High Spectral Resolution Lidar (HSRL) and Raman Lidar techniques

2.1.2 High Spectral Resolution Lidar (HSRL)

The High Spectral Resolution Lidar (HSRL) technique provides direct measurements of aerosol and cloud particle transmission and backscatter without the need of a lidar ratio. It takes advantage of the different spectral broadening of the signal backscattered by particles and molecules. Due to their much smaller mass, molecules have a much higher thermal velocity. This leads to a spectral broadening of the backscattered laser light, of ~1 GHz, due to the Doppler effect. The movements of aerosol and cloud particles, on the other hand, are determined predominantly by the wind and turbulence and produce much smaller doppler shifts of ~30 MHz and ~3 MHz respectively, while the spectral broadening due to their thermal velocity is much lower due to their bigger mass. Thus, when the frequency distribution of the backscattered light is plotted, it consists of a narrow spike centered around the frequency of the emitted laser light,

which is caused by particle scattering, combined with a much wider near-Gaussian distribution caused by molecular scattering (Fig. 2.2).

As discussed in Sect. 2.1.1, in order to calculate the particle extinction and backscatter coefficients using the lidar equation, two independent atmospheric signals are necessary. For the HSRL technique, the backscattered signal is split into two channels. In one channel a narrow bandpass optical filter is used in order to cut the central peak out of the backscattered signal, allowing only photons from molecular scattering to pass through. In the other channel, the total signal is detected. For each channel a separate lidar equation can be written:

$$P_{tot}\ R,\lambda\ = C_{tot}\frac{\beta_{mol}\ R,\lambda\ +\beta_{par}\ R,\lambda}{r^2}exp\left[-2\int_0^R[\alpha_{mol}\ R,\lambda\ +\alpha_{par}\ R,\lambda\ ]dr\right] \tag{2.13}$$

for the channel with the total backscatter. And:

$$P_{mol}\ R,\lambda\ = C_{mol}\frac{\beta_{mol}\ R,\lambda}{r^2}exp\left[-2\int_0^R[\alpha_{mol}\ R,\lambda\ +\alpha_{par}\ R,\lambda\ ]dr\right] \tag{2.14}$$

for the channel including only the molecular backscatter. C_{tot} and C_{mol} are the instrument parameters. C_{mol} also accounts for the fact that part of the molecular backscatter signal is rejected by the filter. Since β_{mol} *and* α_{mol} can be calculated with good accuracy from, usually, readily available data (see Sect. 2.1.1), the only unknown in Eq. 2.14 is the particle extinction coefficient α_{par} which can thus be calculated. Introducing the calculated α_{par} to the lidar equation of the total signal (Eq. 2.13) the particle backscatter coefficient, β_{par}, can then also be calculated.

Apart from the backscatter coefficient, the backscatter ratio, BSR, is another useful parameter that can be calculated via the HSRL method. It is defined as the ratio of the total backscatter over the molecular backscatter:

$$BSR = \frac{\beta_{tot}}{\beta_{mol}} = \frac{\beta_{par}+\beta_{mol}}{\beta_{mol}} \tag{2.15}$$

On the challenges of this method, in order to separate the particle from the molecular signal, a very narrow filter is required which must also be perfectly centered to the emitted laser light, which in turn also needs to have a high spectral purity. HSRL lidars are therefore technically very demanding to construct. On the other hand, they provide a very strong signal, compared to Raman lidars, making them suitable also for measurements during the daytime when the background light is strong. This, in combination with a very small integration time of only a few seconds required, makes HSRL suitable also for airborne measurements (Groß et al., 2012).

As briefly mentioned at the end of the previous section, the Raman lidar technique is another way of determining the lidar equation for measurements of particle extinction and subsequently backscatter coefficients. Similar to the HSRL technique, Raman measures two signals in order to distinguish between molecular and particle contribution. One is the elastic backscatter by molecules and particles and the other the inelastic or Raman backscatter by an atmospheric gas, commonly nitrogen and/or oxygen.

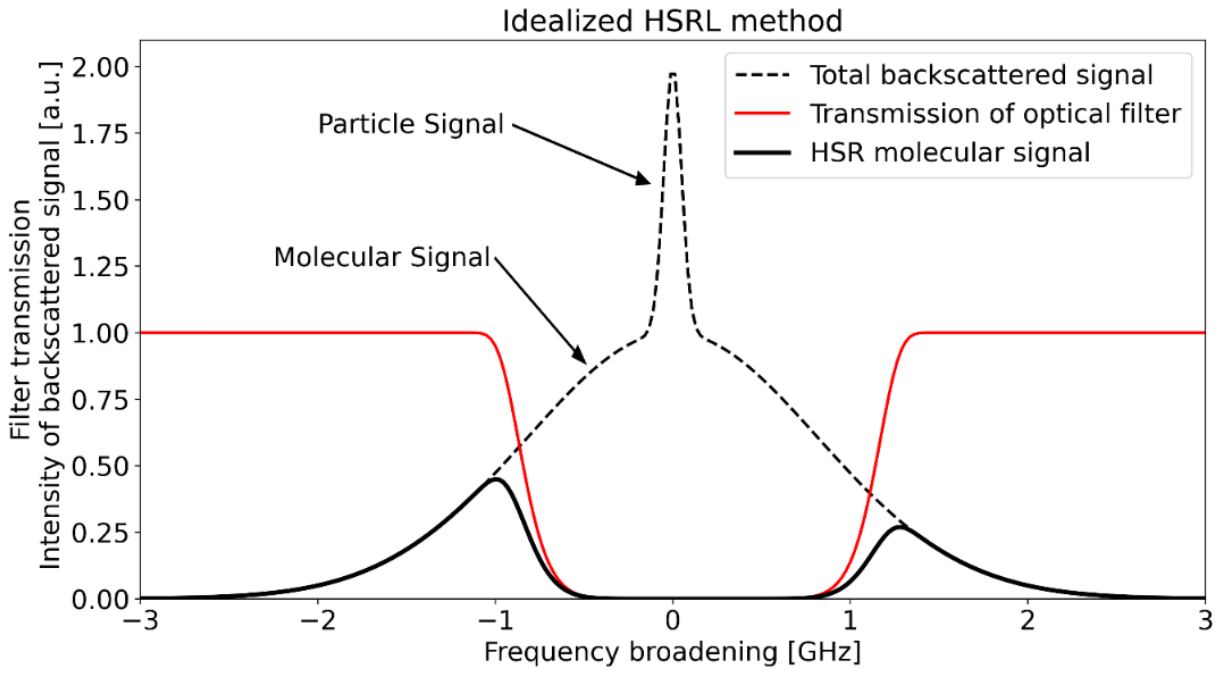

Figure 2.2: Idealized representation of the frequency broadening of a backscattered signal that interacted with particles and molecules *(dashed line)*. For the HSRL method, the backscattered signal is fed through a narrow-bandwidth optical filter *(red line)* allowing only the frequency-broadened molecular part of the signal to pass through *(solid black line)*.

2.1.3 Differential Absorption Lidar (DIAL)

The Differential Absorption Lidar (DIAL) method, also uses two signals, but instead of aerosol and cloud particle extinction it is used to detect atmospheric trace gases such as O_3, NO_2, NO, CH_4 and others. While for the HSRL method wavelengths are chosen so that molecular absorption can be considered zero, DIAL uses specific wavelengths aimed at determining the molecular absorption of an atmospheric gas by disregarding the contributions by particles. Importantly for this thesis, DIAL is also commonly used to measure water vapor in the atmosphere.

The central idea behind the DIAL technique, is that atmospheric gases have certain absorption lines, i.e. wavelengths at which they absorb light. DIAL instruments emit at least two laser pulses with two different but neighboring wavelengths, one of which coincides with an absorption line. The difference in the molecular absorption coefficients of the backscattered signals from the two wavelengths can be measured and from it the number concentration of the selected gas can be determined (Fig. 2.3)(Schotland, 1965, 1966; Browell et al., 1979; Ehret et al., 1993; Bösenberg, 1998).

In more detail, let's consider an atmospheric trace gas of interest and a lidar system emitting laser pulses in two neighboring wavelengths λ_{on} and λ_{off}. The first wavelength is on an absorption line of this gas i.e. it has a greater molecular absorption cross section $\sigma_{abs}(\lambda_{on})$ compared to the off-line

wavelength, $\sigma_{abs}(\lambda_{off})$. In that case the signals from the two wavelengths measured by the lidar would be:

$$P_{on}\ R,\lambda_{on}\ = P_{0[on]}\frac{c\tau}{2}A\eta\frac{O\ R}{R^2}\beta_{on}\ R,\lambda_{on}\ exp\left[-2\int_0^R[\alpha_{on}\ R,\lambda_{on}\ ]dr\right]$$
$$P_{off}(R,\lambda_{off}) = P_{0[off]}\frac{c\tau}{2}A\eta\frac{O\ R}{R^2}\beta_{off}(R,\lambda_{off})exp\left[-2\int_0^R[\alpha_{off}(R,\lambda_{off})]dr\right] \quad 2.16$$

In an idealized scenario, we can assume that the atmospheric backscatter coefficients $\beta(R,\lambda)$ are identical for the two wavelengths, because they are selected close to each other, as are the instruments parameters. Thus, combining the two equations results in:

$$\frac{P_{on}\ R,\lambda_{on}}{P_{off}(R,\lambda_{off})} = \frac{P_{0[on]}}{P_{0[off]}}exp\left[-2\int_0^R[\alpha_{on}\ R,\lambda_{on}\ -\alpha_{off}(R,\lambda_{off})]dr\right] \quad 2.17$$

From Eq. 2.6, for the same reason, it can also be extracted that the difference in atmospheric extinction coefficients α_{on}-α_{off} for the two wavelengths, is a result only of the molecular absorption $\alpha_{mol,abs}(R,\lambda)$ of the selected trace gas. That is:

$$\Delta\alpha = N\Delta\sigma \quad 2.18$$

where N is the molecule number density of the trace gas and $\Delta\sigma$ the difference between the absorption cross sections of the selected gas at the two emitted wavelengths. Introducing this into Eq. 2.17 and performing some algebraic transformations, the so-called DIAL equation is produced:

$$N = \frac{1}{2\Delta\sigma}\left[\frac{d}{dR}ln\left(\frac{P_{off}(R,\lambda_{off})}{P_{on}\ R,\lambda_{on}}\right)\right] \quad 2.19$$

The molecular absorption cross sections σ_{abs} for various gases and wavelengths, are well studied and documented by laboratory measurements. Thus, by inputting the power of the backscattered signals from both wavelengths in the DIAL equation (Eq. 2.19), the number concentration N of a trace gas can be determined.

Interestingly the DIAL equation (Eq. 2.19) doesn't contain any instrument parameters making DIAL a self-calibrating measurement technique. A source of uncertainties lies in the fact that the atmospheric backscatter coefficient $\beta(R,\lambda)$ and the atmospheric extinction coefficient due to scattering $\alpha_{sca}(R,\lambda)$ are generally not exactly the same for the on-line and off-line signals, as previously assumed. This uncertainty can become bigger if the on-line and off-line wavelengths are separated by more than a few nanometers, or a line is too close to an absorption line of another gas. Thus, while for an H_2O DIAL in the near infrared, for example, this error is negligible, it is different for an O_3 DIAL where the on-line and off-line wavelength cannot be chosen close together. Another potential source of uncertainty stems from the Rayleigh-Doppler broadening. The light scattered back by air molecules is Doppler broadened, as described above for the HSRL. After being scattered back, the spectrum of the light is changed at least for the part scattered by molecules. For an accurate determination of H_2O for example, as is the case herein, this has to be taken into account, as the absorption line has a width comparable to the broadened spectrum. If not considered, this can lead to errors of 10%-20%.

This being said, the biggest challenge when constructing DIAL instruments, especially for the measurement of water vapor, whose absorption lines are very narrow, is the very high stability and spectral purity required. The most important systematic error sources are: uncertainties in the absorption cross sections of gases from lab measurements (2%-3% or even 5% for small lines), uncertainty of the laser wavelength (should be better than 0.2 pm to cause less than 1% error), uncertainty of the laser spectral shape and especially the intensity of side modes.

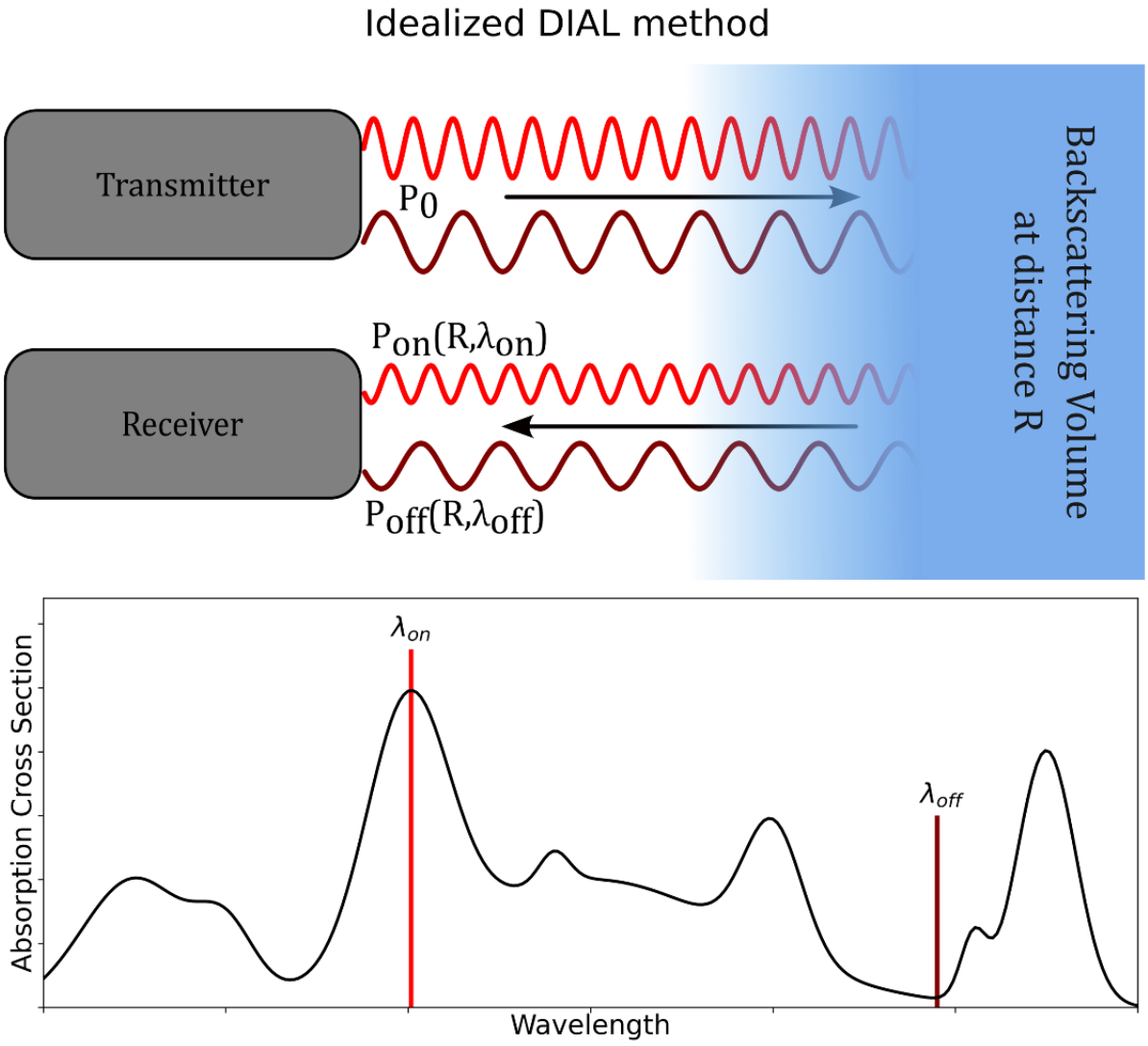

Figure 2.3: Idealized representation of the DIAL method. Lidar pulses with two different wavelengths are emitted into the atmosphere from the transmitter with the same power P_0. One wavelength is selected at a strong absorption line of a desired gas λ_{on} and the second one at a neighboring wavelength at which the gas has a smaller absorption cross section, λ_{off}. Light of both wavelengths gets backscattered and collected by the receiver. The difference in the power of the backscattered signals for the two wavelengths can be used to determine the number concentration of the selected gas.

2.1.4 Depolarization lidar

Light is an electromagnetic wave consisting of an electric and a magnetic field, which oscillate perpendicular to each other and to the direction in which the wave propagates. At any time, the oscillation of these fields has a specific orientation or polarization. If the orientation does not change with time, the light is considered to be polarized and more specifically have a linear polarization at a specific plane. The lasers used in lidar applications most commonly produce linearly polarized light (Weitkamp, 2005).

When this linearly polarized laser light is scattered by homogeneous spherical particles, such as water droplets, the backscattered light remains linearly polarized and maintains the orientation of its polarization according to the Lorenz-Mie theory. Scattering on non-spherical particles, however, such as ice crystals in cirrus clouds, can result in different polarization states being present in the backscattered light. This phenomenon is called depolarization.

The depolarization lidar technique involves first the transmission of linearly polarized laser pulses on a specific plane into the atmosphere. The polarization state of the backscattered light is then detected and the level of depolarization determined. This way the atmospheric particles that reacted with the laser pulses can be characterized.

More specifically, polarization optics, commonly polarizing beam-splitter (PBS) cubes, are employed at the receiver of the lidar and the incident backscattered light is split into its co and cross polarized components with respect to the plane of polarization of the emitted linearly polarized light. The powers $P_{\parallel}$ and $P_{\perp}$ of the co- and cross-polarized components of the backscattered light respectively are expressed by the lidar equations:

$$P_{\parallel} = \frac{C_{\parallel}}{r^2}\beta_{\parallel}T^2 \tag{2.20}$$

and

$$P_{\perp} = \frac{C_{\perp}}{r^2}\beta_{\perp}T^2 \tag{2.21}$$

where $\beta_{\parallel}$ and $\beta_{\perp}$are the co- and cross-polarized components of the total backscatter coefficient respectively, $C_{\parallel}$ and $C_{\perp}$are the system constants and T^2 the atmospheric transmittance. It is technically possible for the transmittance to also be different for the two polarization components, however these instances are rare in the real atmosphere (Weitkamp, 2005).

In some cases, the plane at which the PBS splits the signal, might not be exactly aligned to the planes of polarization of the emitted laser light (see Fig. 2.4). In that case after the PBS, the power of the parallel P_P and perpendicular P_S signal contains parts of both the co- and cross-polarized light. Depending on the angle φ, they can be written as:

$$P_P = P_{\parallel}cos^2\ \varphi\ + P_{\perp}sin^2\ \varphi \tag{2.22}$$

and

$$P_S = P_{\parallel}sin^2\ \varphi\ + P_{\perp}cos^2\ \varphi \tag{2.23}$$

These two components are transmitted and reflected by the PBS according to its transmittances ($T_P,\ T_S$) and reflectances ($R_P,\ R_S$) (see Fig. 2.4). Subsequently they are amplified based on the

amplification factors (V_R, V_T) into two channels, one reflected with power P_R and one transmitted with power P_T, given by:

$$P_R = [P_P \ \varphi \ R_P + P_S \ \varphi \ R_S]V_R$$
$$P_T = [P_P \ \varphi \ T_P + P_S \ \varphi \ T_S]V_T \qquad 2.24$$

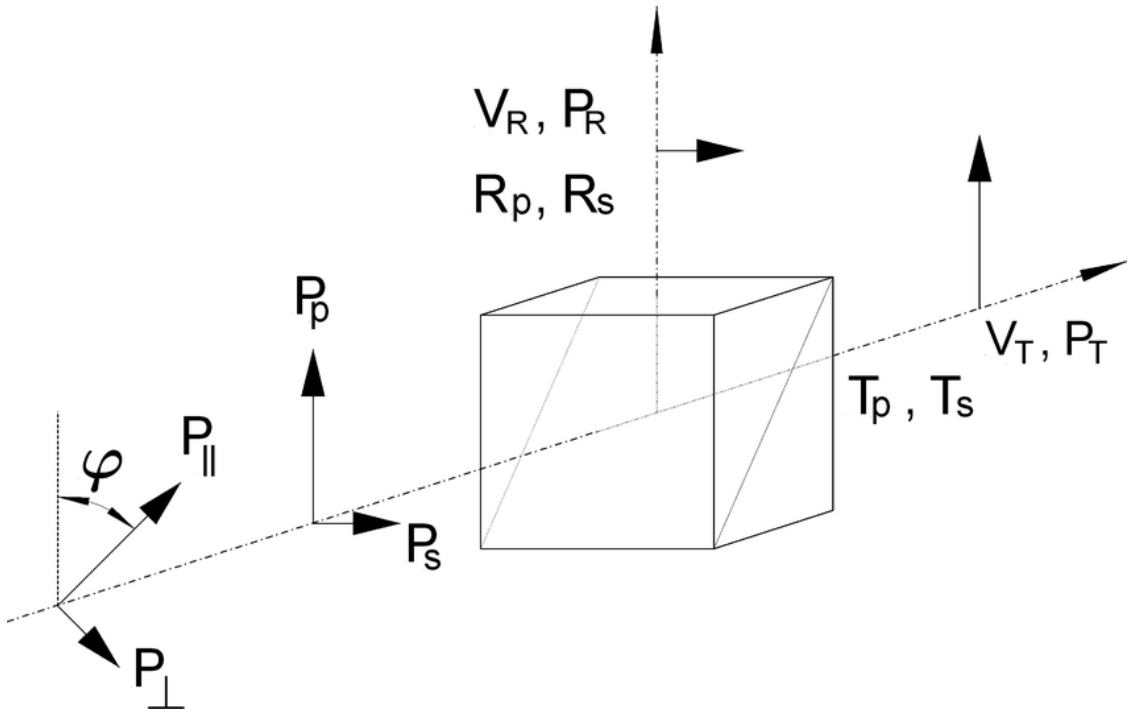

Figure 2.4: Schematic representation of the measurement process in a depolarization lidar with a PBS cube. The incident light with a co- and a cross-polarized power component ($P_\parallel$, $P_\perp$) with respect to the polarization plane of the emitted laser light reaches the receiver. P_P and P_S are the power components oriented parallel and perpendicular to the plane of the PBS, each containing part of the co and cross polarized components. According to the transmittances (T_P, T_S) and reflectances (R_P, R_S) of the PBS part of the incident light is transmitted and part reflected. After the corresponding amplifications (V_R, V_T) the power of the reflected and transmitted signals (P_R, P_T) are split into two channels and measured. Picture from, Freudenthaler et al. (2009), their Figure 1.

From these measured components, first the volume depolarization ratio δ_v, can be determined. It describes the depolarization of the total light backscattered from molecules and particles. For an alignment of φ=0^o, it is given by:

$$\delta_v = \frac{P_\perp}{P_\parallel} = \frac{P_S}{P_P}, \varphi = 0^o \tag{2.25}$$

However, for common commercial PBS, R_S is typically much closer to 1 compared to the T_P. Thus, in order to reduce cross-talk of the strong parallel-polarized signal onto the weaker cross-polarized signal, an alignment of φ=90^o is commonly used and the δ_v is calculated by:

$$\delta_v = \frac{P_\perp}{P_\parallel} = \frac{P_P}{P_S}, \varphi = 90^o \tag{2.26}$$

Introducing for convenience the signal ratio δ^* and the relative amplification factor V^*, calculated as:

$$\delta^* = \frac{P_R\ \varphi}{P_T\ \varphi}, \qquad V^* = \frac{V_R}{V_T} \tag{2.27}$$

The volume depolarization ratio can be calculated as:

$$\delta_v = \frac{P_P}{P_S} = \frac{R_S - \frac{\delta^*}{V^*} T_S}{\frac{\delta^*}{V^*} T_P - R_P} \tag{2.28}$$

Using the volume depolarization ratio δ_v and the backscatter ratio R (see Eq. 2.15) the particle linear depolarization ratio δ_p can then be calculated. It is a useful parameter as it provides information about the shape and thus potentially also the nature, of aerosols or aerosol mixtures. It can be calculated according to (Biele et al., 2000):

$$\delta_p = \frac{1+\delta_m\ R\delta_v - \ 1+\delta_v\ \delta_m}{1+\delta_m\ R - \ 1+\delta_v} \tag{2.29}$$

Where δ_m is the is the linear depolarization ratio resulting from molecules. It is dependent on the ambient temperature of the atmosphere and can be determined with high accuracy (Behrendt and Nakamura, 2002).

For the calibration of a depolarization lidar as described above, the V^* needs to be defined. Different methods are available. Freudenthaler et al. (2009), propose performing subsequent measurements at φ= +45 ° and φ=-45°, by rotating the receiver unit, e.g. via mechanical stops. Then V^* can be calculated by:

$$V^* = \frac{T_P + T_S}{R_P + R_S} \sqrt{\delta^*\ +45^o\ \cdot \delta^*\ -45^o} \tag{2.30}$$

This way the calibration is independent of δ_v and the calibration errors due to a potential misalignment of the PBS with respect to the laser polarization plane are compensated very well according to Freudenthaler et al. (2009).

2.2 Ice nucleation

Cirrus clouds are made up of ice crystals. The formation of ice crystals is called ice nucleation. Ice nucleation can occur via two possible phase transitions. Either freezing of a liquid droplet or deposition of water vapor (Yau and Rogers, 1996). The nucleation process is largely dependent on the ambient conditions and RHi and can affect the macro- and microphysical characteristics of the resulting cirrus. In order to better understand these mechanisms, let us first consider an air parcel at surface temperature and pressure of the standard atmosphere (see Sect. 2.1.1). This parcel has a certain water content resulting in a certain water vapor pressure e. At a given temperature if this vapor pressure is low enough, freezing/deposition of water droplets/vapor is suppressed whereas melting/sublimation can occur at a higher rate. If this air parcel rises, it expands and cools adiabatically. This leads to an increase in the probability of freezing/deposition occurring, while the rate of melting/sublimation reduces. At any given temperature there is a so-called saturation vapor pressure e_{si} at which the rates of freezing/deposition and melting/sublimation are equal. Just over this saturation vapor pressure, supersaturation occurs. The freezing/deposition processes happen at a faster rate than melting/sublimation. Thus, new, stable ice crystals can form, persist and grow.

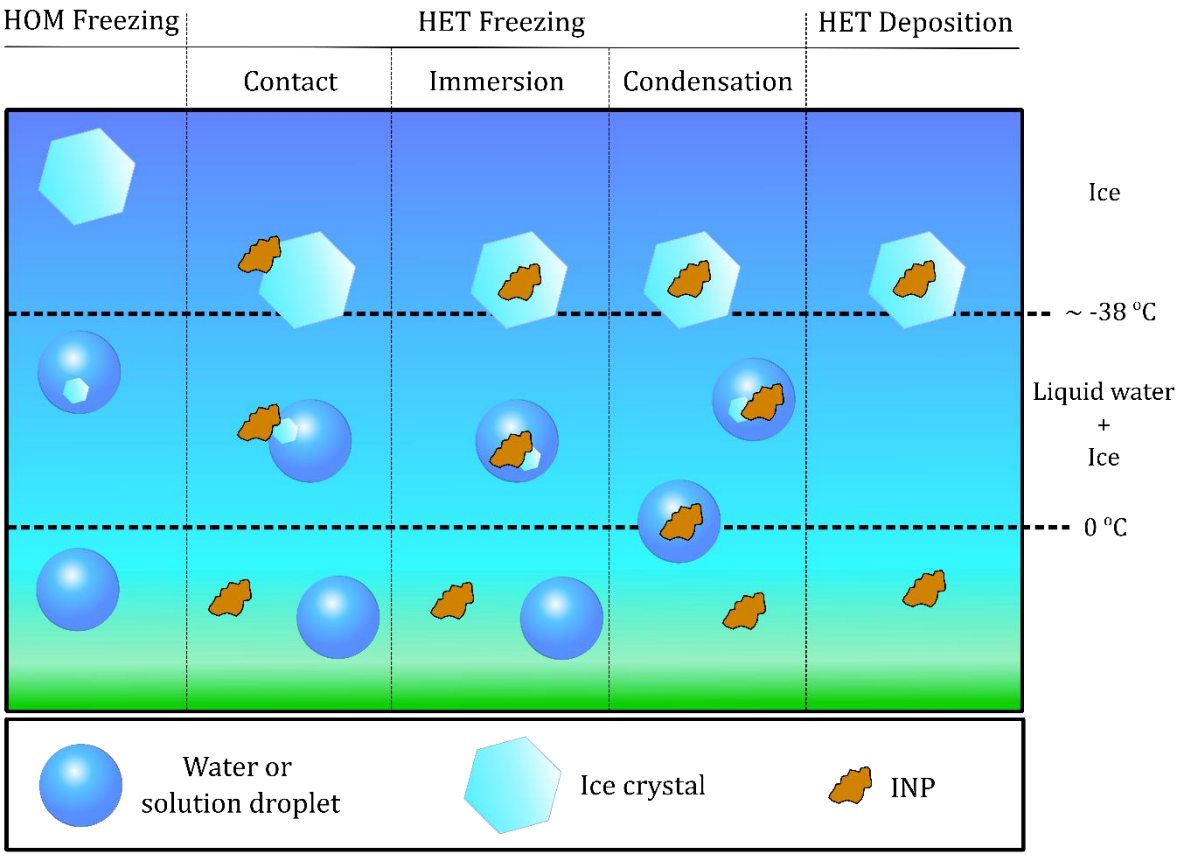

Figure 2.5: Possible pathways for ice nucleation, based on Hoose and Möhler, 2012.

The relative humidity over ice (RHi) of this air parcel is defined as the ratio between the parcel's vapor pressure and saturation vapor pressure:

$$\% \ RH_i = \frac{e}{e_{s_i}} * 100 \tag{2.31}$$

At saturation RHi is 100 % and any value larger than this is considered supersaturation.

Both phase transitions: freezing of water droplets or deposition of water vapor, can occur either homogeneously (HOM) or heterogeneously (HET) (Fig. 2.5). In the following a detailed description of these processes is provided.

HOM: During HOM nucleation, new ice crystals form from pure water droplets, aqueous solutions or water vapor.
Homogeneous freezing of pure water droplets or more commonly aqueous solution droplets occurs when stochastic fluctuations of their molecules, happen to locally arrange into an ice-like structure which then serves as an ice nucleus allowing the rest of the droplet to freeze (Yau and Rogers, 1996). High supersaturations and low temperatures are necessary for this process to take place, but it is commonly observed. It is generally accepted that HOM freezing occurs at temperatures < 235 K and RHi > 140 % (Kärcher and Lohmann, 2002; Lynch et al., 2002; Ström et al., 2003; Kärcher and Seifert, 2016).
Homogeneous deposition on the other hand occurs when water vapor molecules randomly collide with each other to form a stable ice nucleus. This process, while theoretically possible for extremely high supersaturations, is difficult to be experimentally tested and is not expected to take place for the conditions and clouds studied herein. Henceforth the term HOM nucleation shall refer to homogeneous nucleation by freezing of water droplets or aqueous solution droplets (Yau and Rogers, 1996; Koop et al., 2000).

HET: HET nucleation requires the presence of a solid foreign material, called an Ice Nucleating Particle (INP). The morphology of an INP needs to resemble the structure of ice. Similar to HOM nucleation, it serves as an ice nucleus but without depending on rare chance collisions. Thus, the high supersaturations of the HOM process are also not necessary allowing for formation of ice crystals at temperatures warmer than 235 K. The more an INPs structure resembles an ice crystal plane, the easier it will become activated, i.e. be used in the formation of an ice crystal. Larger INPs are also more likely to lead to stable crystals. HET nucleation is possible for temperatures up to 273 K and RHi reaching down to 100 % (Yau and Rogers, 1996; Kärcher and Lohmann, 2003).
Heterogeneous freezing of water droplets can occur in three different ways. During *contact freezing* an ice crystal forms directly after the INP comes into contact with the surface of a water droplet. *Immersion freezing* happens by INP which first become immersed in a water or solution droplet and then lead to the initiation of freezing. *Condensation freezing* INP first promote condensation to a water droplet and then its freezing.
Heterogeneous deposition from water vapor is readily possible if suitable deposition INP are available. Henceforth, HET nucleation shall refer to all abovementioned processes (Yau and Rogers, 1996). A visual representation of the potential ice nucleation pathways is presented in Fig. 2.5.

Chapter 3

Methods and data

The HSRL, DIAL and depolarization lidar techniques described above, are all employed by the WALES lidar system. WALES is a central part of this thesis, since the scientific findings presented here are predominantly extracted from data collected by WALES during the ML-CIRRUS and HALO-(AC)^3 campaigns. The WALES lidar system is presented in Section 3.1. In Section 3.2 the HALO research aircraft is presented. The goals, flight planning and instrumentation for the ML-CIRRUS and HALO-(AC)^3 campaigns are presented in Sections 3.3 and 3.4 respectively. In Section 3.5 I describe the calculations I perform on the collected data and introduce schemes used throughout this thesis. In Section 3.6 I present the uncertainties in the calculated RHi, which is the main parameter. Section 3.7 contains all the parameters and description of the applied cirrus cloud masks. Finally, in Section 3.8 cirrus classifications based on their formation process and ambient conditions, which I use for the analysis over the mid- and high latitudes are introduced.

3.1 WALES lidar system

WALES (WAter vapor Lidar Experiment in Space) is a lidar system developed at the German Aerospace Center (DLR). It is a combined water vapor differential absorption lidar (DIAL) and high spectral resolution lidar (HSRL) system (see Sect. 2.1.2 and 2.1.3). As such, it is capable of providing synchronous measurements of water vapor concentration, and particle extinction. WALES is also capable of measuring the depolarization ratio between emitted and received signals. This, in combination with the HSRL technique allows for improved definition of aerosol and cloud optical properties as well as characterization of atmospheric aerosols. It was conceptualized as an airborne instrument and still operates as such (Fig. 3.1 & 3.4).

For the water vapor measurements with the DIAL technique a four-wavelength/three-absorption line scheme was selected, with online frequencies in the water vapor absorption band found around 935 nm. This scheme allows for airborne measurements that can cover the whole troposphere and lower stratosphere. The three on-line frequencies have different absorption cross sections, from stronger to weaker, and can thus be used for measurements at different altitudes. More specifically, an emitted laser pulse at a frequency coinciding with a strong absorption line can provide more precise measurements, especially in dry conditions, due to the larger $\Delta\sigma$ (see Eq. 2.19), but will also be completely extinct at a distance closer to the instrument. The other two on-line frequencies coincide with progressively less strong water vapor absorption lines; thus, they travel deeper into the atmosphere before becoming completely extinct and provide measurements at further distances to the instrument.

Depending on the ambient conditions, the online wavelengths can be adjusted. While remaining in the 935 nm absorption band of water vapor, the online wavelengths are selected in such a way that they provide measurements with the best possible precision and coverage. For example,

wavelengths at stronger absorption lines can be selected at the relatively drier high latitudes, compared to the moister tropics where the same wavelengths would become extinct already at high altitudes due to the larger amount of water vapor.

For the measurement of aerosol extinction and backscatter coefficients via the HSRL technique, laser light with a frequency of 532 nm is used. The required suppression of the backscattered signal due to particles (see Sect. 2.1.2), occurs via an iodine, I_2, vapor cell.

WALES is a central element of this thesis as the data analyzed herein stem predominantly from this instrument. In the following the systems design and set-up are described in more detail, focusing on the two basic parts, the transmitter and the receiver (see Sect 2.1.1). Finally, its capabilities, performance parameters and measurement errors are presented. For an in depth description of the system, see Esselborn et al. 2008, Wirth et al. 2009 and Fix et al., 2019.

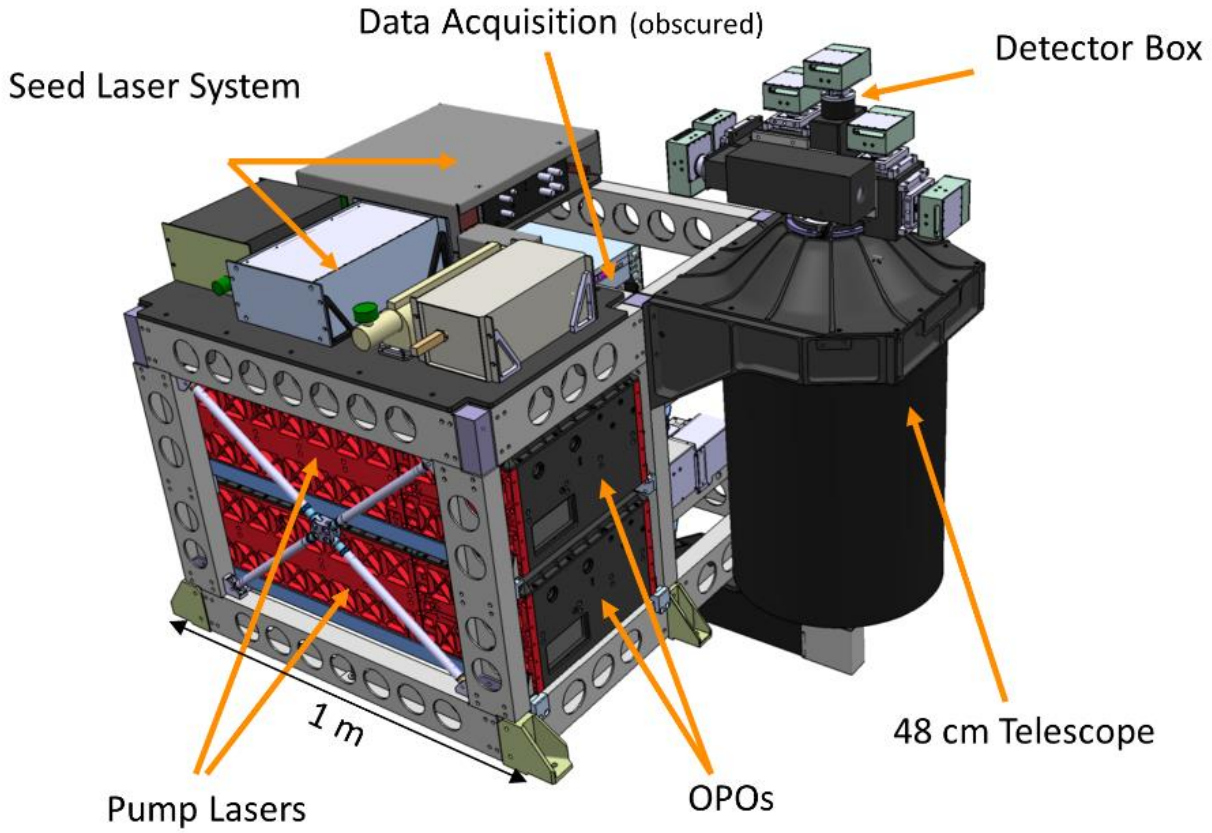

Figure 3.1: Graphic of the WALES instrument rack conceived for integration of the instrument inside DLR's Falcon F20 and HALO research aircraft. Graphic from Wirth et al., 2009.

3.1.1 The Transmitter

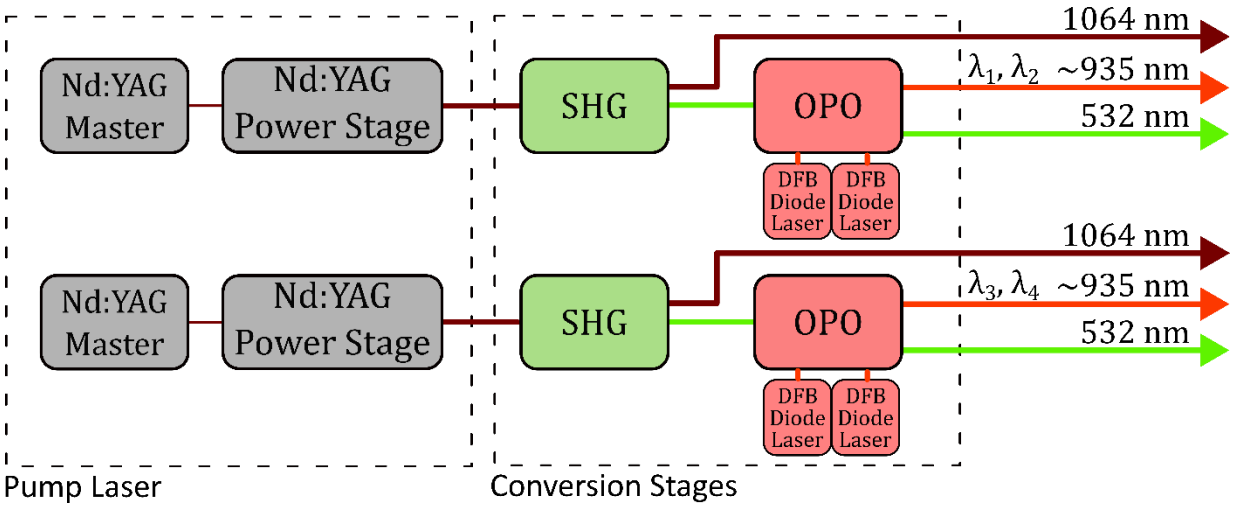

Figure 3.2: Schematic of the WALES transmitter. Two identical laser chains are in place, each with a pump laser and two non-linear conversion stages. Light pulses with four wavelengths around 935 nm are created for the measurement of water vapor via the DIAL method. Each chain alternates between generating two wavelengths. The pump laser radiation at 1064 nm and the frequency-doubled at 532 nm are also emitted to the atmosphere for aerosol measurements and the HSRL method respectively.

The pump laser: The transmitter of WALES consists of two identical pump laser systems, shown in Fig. 3.2. The beating heart of the instrument, are the two Q-switched monolithic Nd:YAG ring lasers found in each of the systems. These master oscillator lasers produce light pulses at 1064 nm with a repetition rate of 4 kHz. Each pulse has a length of 7.7 ns full width at half maximum (FWHM) and an energy of 40 µJ.

The exact frequency of the laser is temperature- and stress-tunable. The tuning schemes are used to stabilize the lasers to the iodine (I_2) absorption line used for the suppression of the particle signal for the HSRL technique (see Sec. 2.1.2 & 2.2).

The master oscillator laser in each system is followed by a three-stage amplifier chain, side-pumped by diodes to increase the pulse energies. The amplifiers are pumped at a repetition rate of 100 Hz. The timing of the pulses of the master laser is synchronized to the power amplifying stages via a phase-locked loop, so that every 40^{th} pulse is amplified. The signal of the master laser is amplified by a factor of 10^4 resulting in an energy output of more than 400 mJ, per pulse.

The non-linear conversions: The pulses generated by the pump lasers are fed through two nonlinear conversion stages, both using potassium titanyl phosphate ($KTiOPO_4$ or short KTP) as the nonlinear material. First the frequency of each pump laser is doubled by a second-harmonic generator (SHG) from 1064 nm to 532 nm. The conversion has an efficiency of up to 55% at full laser power resulting in an output energy from the SHG of up to 220 mJ. Subsequently, the laser light is converted by an optical parametric oscillator (OPO) to wavelengths close to 935 nm. As

described in Sect 3.1, WALES uses four wavelengths in the 935 nm absorption band of water vapor for the DIAL method (see Sect. 2.1.3).

The OPO has a four-mirror ring-oscillator configuration. Two KTP-crystals mounted on a common rotation stage are responsible for a coarse setting of the wavelengths (±10 nm). Each crystal is also mounted on a piezo-transducer-driven flexure stage. This set-up allows on the one hand for fine tuning of the wavelengths with a tuning range of ± 0.5 nm and on the other hand for rapid switching of the phase matching angle allowing the wavelength to be set on a shot-by-shot basis.

Both OPOs achieve their narrow-band operations using injection seeding. To seed the OPOs, four independent distributed feedback (DFB) diode lasers are used. Each DFB laser is tuned to exactly one of the four frequencies used in the water vapor DIAL technique. To assure high accuracy of the measurements, one of the DFB lasers is absolutely stabilized to a strong water vapor absorption line within the 935 nm band. The other DFB lasers are then stabilized using a wave-meter which is continuously re-calibrated relative to the first one. This way a frequency stability of 20 MHz can be achieved for all seed lasers.

Each OPO generates two DIAL frequencies. The output is switched between the two with a rate of 50 Hz. By having two identical systems, pulses with four different wavelengths are emitted with a total pulse rate of 200 Hz and a repetition rate of 50 Hz for each wavelength. The 1064 nm radiation from the pump laser and the 532 nm radiation from the SHG are fed through high-power polarizers allowing for measurements of depolarization. Finally, all beams: 1064 nm from Nd:YAG laser , 935 nm from OPOs and 532 nm from SHG, are combined onto the same optical axis and released into the atmosphere (Fig. 3.2).

3.1.2 The Receiver

The receiver of WALES features a 48 cm Cassegrain telescope and a detector box in a monostatic set-up, as well as a data acquisition computer. The telescope collects and guides the incoming radiation towards the detector box. There, dielectric beam splitters separate the different wavelengths and create three channels at 1064 nm, 935 nm and 532 nm. 1nm band width interference filters are used to suppress the solar background radiation (Fig. 3.3).

All four wavelengths for the water vapor DIAL method at 935 nm are fed to one detector. The aerosol channels at 1064 nm and 532 nm are guided through double polarizing beam splitters which separate the cross-polarized light from the parallel-polarized light allowing for the measurement of the depolarization ratio. For the calibration of the depolarization measurement the whole detector box can be rotated $\pm 45^{o}$ around the axis of the telescope (Freudenthaler et al., 2009). Finally, for the HSRL method, part of the 532 nm channel is fed through an iodine (I_2) vapor cell. The strong I_2 absorption line close to 532 nm, results in the suppression of the particle backscatter signal to more than 10^{-4}, allowing for the retrieval of the aerosol extinction coefficient.

The received light signals in every channel are translated to electrical currents in order for the information to be saved in the data acquisition unit. For the infrared signals at 1064 nm and 935 nm avalanche photo diodes (APD) are used, whereas for the 532 nm channels photo-multipliers (PM). In 2020 this original design was modified. The depolarization channel at 1064 nm was replace by a low sensitivity channel at 532 nm.

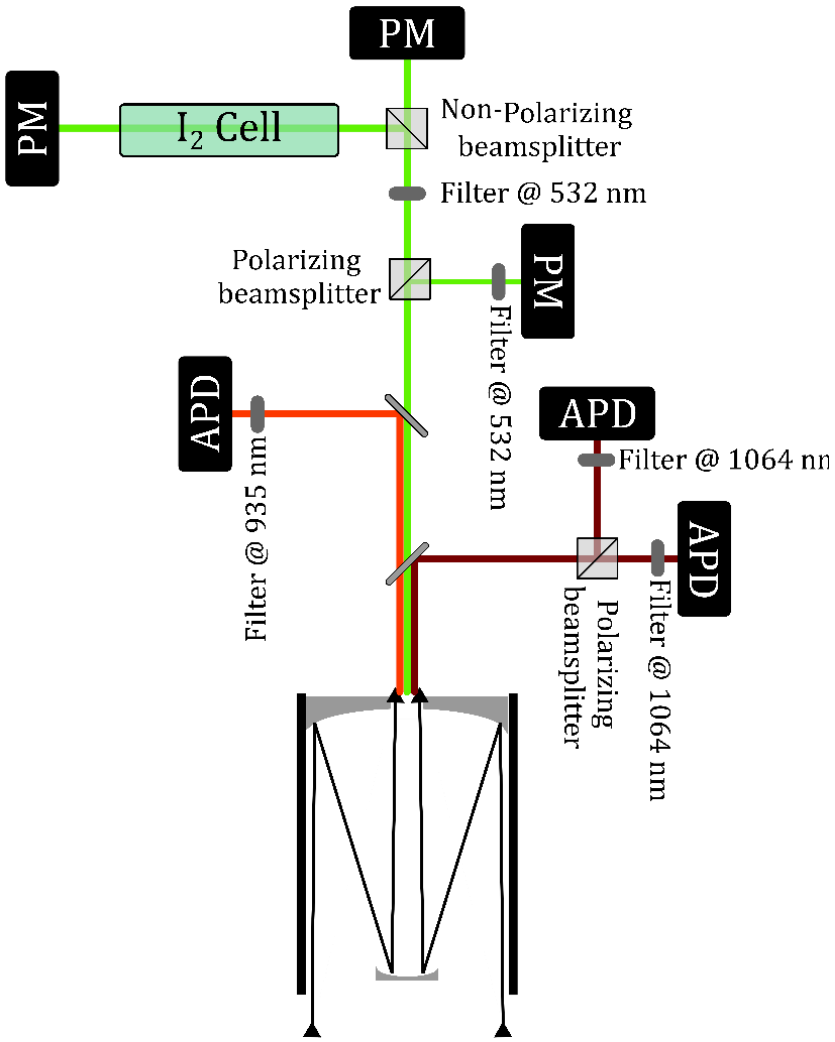

Figure 3.3: WALES receiver layout. Light is collected by a Cassegrain telescope. The different wavelengths are separated into three channels by polarizing dielectric beam splitters. Interference filters are used to suppress the solar background radiation. For the HSRL method part of the 532 nm channel is fed through a 40 cm I_2 cell. For the calibration of the depolarization measurements the whole detector unit can be rotated $\pm 45^{o}$ about the axis of the telescope.

3.1.3 Measurement attributes and error estimates

WALES is an airborne lidar system capable of providing 2D measurements from the aircraft to the ground along the flight path with high accuracy, temporal and spatial resolution. Using the HSRL method at 532 nm, the particle extinction and backscatter coefficients can be measured. Depolarization ratios can be determined at 1064 nm and 532 nm. The DIAL technique at ~935 nm provides measurements of the water vapor mixing ratio. The aerosol and cloud particle measurements have a vertical resolution of 15 m and time resolution of 1s. The water vapor DIAL measurements have a vertical resolution of ~300 m and time resolution of 12s. Details regarding the performance of the transmitter are shown in Table 3.1. An overview of the attributes of the products from WALES is presented in Table 3.2.

For this thesis, several products are used, either directly or for the calculation of secondary products and creation of masks. Specifically, I use the backscatter ratio (BSR), the particle linear depolarization ratio (PLDR), the water vapor volume mixing ratio (WVMR) and the two-way optical transmission. An example of the products provided by WALES and used in this thesis is shown in Figure 3.5.

For the water vapor retrieval, Kiemle et al. (2008) estimated the statistical error of the measurements to be about 5 %, although the exact value is dependent on various parameters that differ for individual measurements. Especially for the study of cirrus clouds, errors that arise due to the high spatial inhomogeneity of the backscatter within these clouds are kept below 5 % by filtering. Additionally, the Rayleigh–Doppler effect is corrected in the retrieval algorithm, leaving an error of less than 2 % (Groß et al., 2014). Groß et al. (2014) compared water vapor DIAL measurements from WALES, taken during a flight of the HALO TECHNO mission with simultaneous in-situ measurements taken from an aircraft flying below HALO (their Fig. 4). They found the measurements to be in a good agreement with a deviation of < 1 % for the time periods where the two aircraft were on close horizontal distances. They also note the capability of the WALES-DIAL measurements to resolve even small-scale features. For the measured backscatter and extinction coefficients via the HSRL method at 532 nm relative uncertainties of less than 5 % and 10 % to 20 % must be considered, respectively (Esselborn et al., 2008).

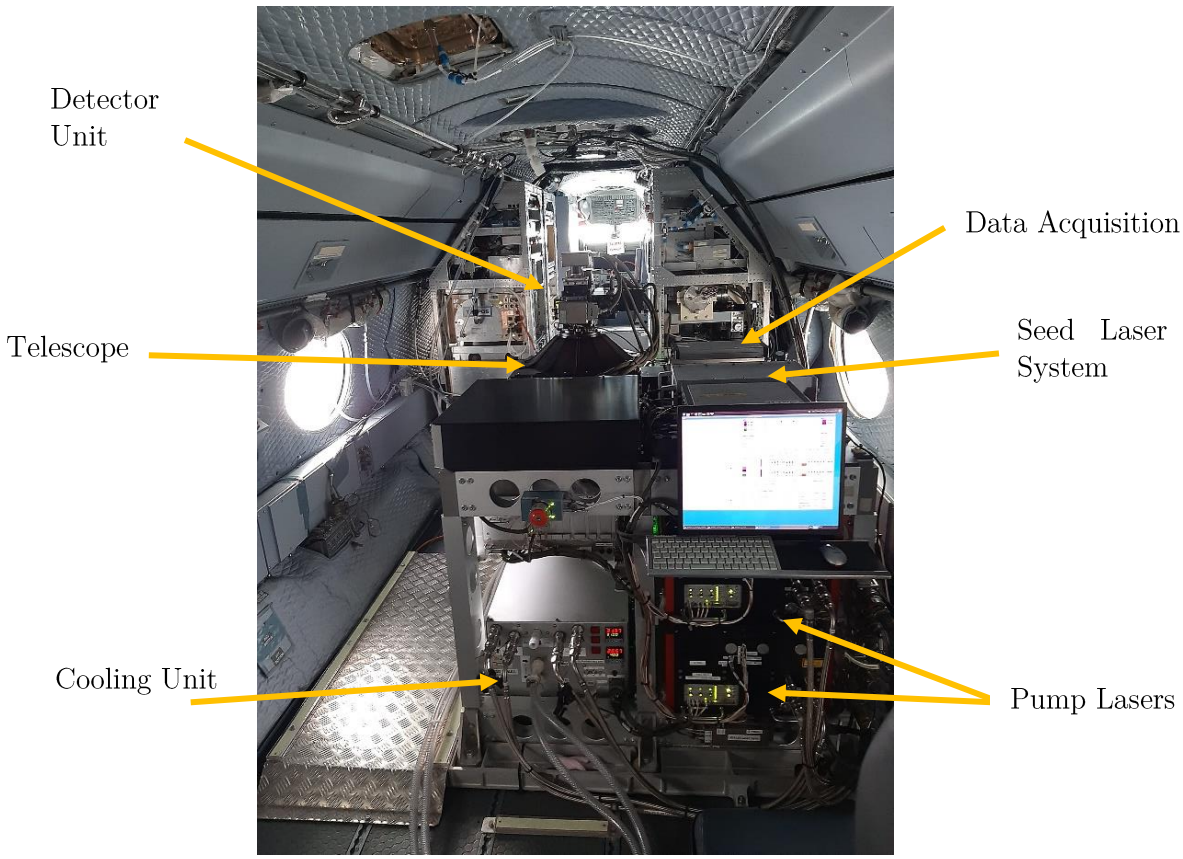

Figure 3.4: Picture of WALES integrated inside the German research aircraft HALO.

As described in Sect. 2.1.1, the intensity of the backscattered signal reaching a lidar is strongly dependent on the distance. Clouds in the near field of the lidar can lead to an overload of the detectors (APDs and PMs) as well as the data acquisition resulting in the cloud not being properly measured. For cirrus clouds a minimum distance of around 2 km above the cloud top is required to avoid this problem. On the other hand, the emitted light pulses from the lidar might also become completely attenuated before reaching the base of a cloud, resulting once again in an incomplete measurement of the vertical extent of a cloud. Maintaining sufficient sensitivity during measurements without overloading the detectors is a delicate balance which can be achieved by adjusting the voltage of the detectors.

Table 3.1: WALES transmitter performance parameters.

Parameter	Value
Repetition rate per laser	100 Hz
Beam Divergence	1 mrad
Pulse length @ 1064 nm	8 ns (FWHM)
Pulse length @ 935 nm	5.5 ns (FWHM)
Pulse length @ 532 nm	7.5 ns (FWHM)
Frequency stability @ 1064 nm	≤1 MHz
Frequency stability @ 935 nm	≤30 MHz
Spectral purity @ 935 nm	≥99.9%
Spectral purity @ 532 nm	≥99.995%

Table 3.2: Characteristics of WALES DIAL and HSRL measurements.

DIAL		HSRL	
		Raw vertical resolution	7.5 m
Effective vertical resolution	286 m	Averaged vertical resolution	15 m
		Raw time resolution	0.2 s
Averaged time resolution	12 s	Averaged time resolution	1 s
Retrieval error	~5 %	Retrieval error	$< 5\%$ for β 10 % -20 % for α

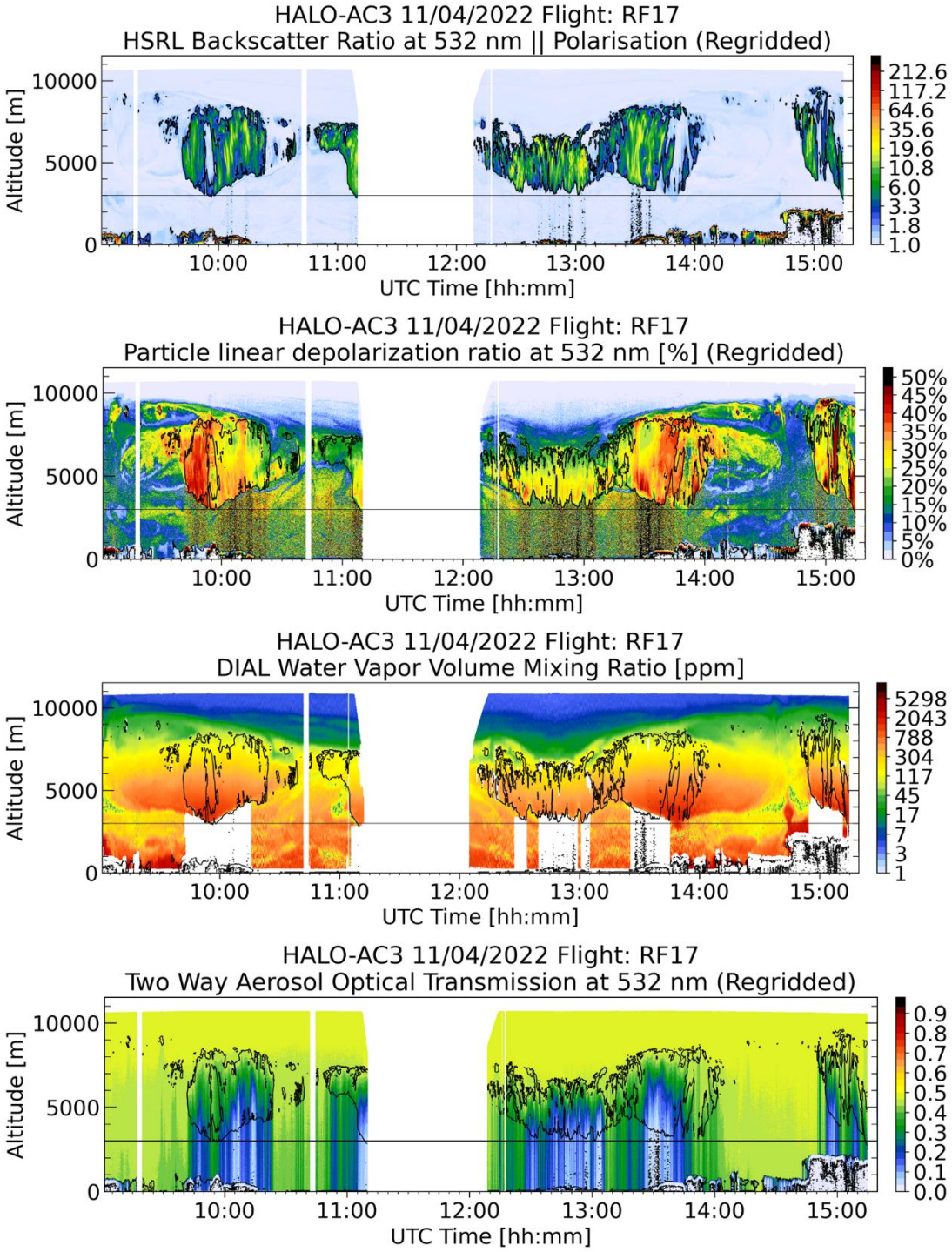

Figure 3.5: Example of WALES products used in this thesis from Research Flight (RF) 17 of the HALO-(AC)^3 campaign. **a)** The backscatter ratio (BSR) from the HSRL technique at 532 nm. **b)** The particle linear depolarization ratio (PLDR) at 532 nm. **c)** The water vapor mixing ratio (WVMR) from the DIAL technique using four wavelengths ~935 nm. **d)** The two-way aerosol optical transmission at 532 nm. Also included on each panel are the parameters of a cloud-mask used for the identification of cirrus clouds in the HALO-(AC)^3 dataset.

3.2 HALO research aircraft

Figure 3.6: The German research aircraft HALO on the apron of the Kiruna airport during the HALO-(AC)^3 campaign. Research Flight 04, 14/03/2022.

In the beginning of the 21st century the need for a research aircraft capable of carrying heavier payloads and having a greater flight ceiling and range became evident among the German and international atmospheric research community. The High Altitude and LOng-range research aircraft (HALO) project was conceptualized and initiated due to this need. Soon after the German Aerospace Center (DLR) proceeded to purchase a Gulfstream G550 business jet, which was then modified and adapted to function as a platform for airborne measurements of the atmosphere (Fig. 3.6). Among the modifications were the creation of apertures in the fuselage (Fig. 3.7), reinforcements, a belly pod to house instruments (Fig. 3.6), a noseboom with sensors, cooling systems and others (Krautstrunk and Giez, 2012).

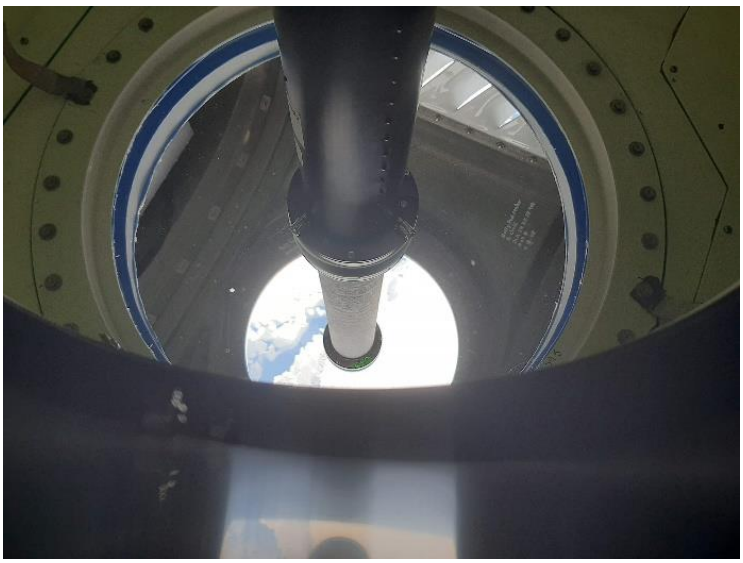

Figure 3.7: Aperture and window in the fuselage of HALO allowing for measurements with the WALES lidar system. HALO-(AC)^3 campaign, Research Flight 12, 01/04/2022.

After a lengthy process of construction, certification and testing, the German research aircraft HALO came to be. With a maximum range of 12500 km, a flight ceiling of 15540 m, a cabin volume of 47.3 m^3 and a maximum payload of 3 tons it is capable of housing a great number of instruments and personnel and transporting them to remote regions e.g. the arctic and oceans, while also reaching high altitudes (Krautstrunk and Giez, 2012). The WALES lidar system (Sect. 3.1) can also be integrated into HALO via a special flight module (Fig. 3.1, 3.4 & 3.7). This makes it overall an ideal platform for the study of cirrus clouds over the mid- and high latitudes (Groß et al., 2014). A list of some characteristics of HALO is presented in Table 3.3.

Table 3.3: Characteristics of the research aircraft HALO.

Parameter	Value
Exterior	
Length	29.4 m
Height	7.9 m
Wingspan	28.5 m
Interior	
Cabin length	15.3 m
Cabin Height	1.88 m
Cabin Width	2.24 m
Cabin Volume	47.3 m^3
Performance	
Max. range	12500 km
Max. cruise altitude	15540 m
Max. payload	3 t

The HALO research aircraft was used as the platform for to perform airborne measurements, among others, also during the ML-CIRRUS and HALO-$(AC)^3$ campaigns. On both occasions the WALES lidar system was aboard HALO performing measurements. Among the goals of both campaigns was the study and characterization of ice clouds over the mid- and high latitudes respectively. The details about the aims, instrumentation and flight strategies of the two campaigns are presented in the following.

3.3 The ML-CIRRUS campaign

The ML-CIRRUS campaign was conducted during March and April of 2014. The primary goal of this campaign was to study the properties of cirrus clouds under meteorological conditions typically occurring at the midlatitudes. More specifically, the macro- and microphysical, optical and radiative properties of cirrus clouds -both natural and anthropogenic (contrails)- were investigated.

As already mentioned, the midlatitudes showcase a variety of different dynamical weather systems (frontal systems, Warm Conveyor Belts (WCB), jet stream etc.) especially during spring. Strong aerosol emissions as well as dense air traffic, are also affecting the atmosphere over the midlatitudes, leading to increased formation of contrails and contrail cirrus. The many open questions and uncertainties resulting from this multitude of conditions detected over the midlatitudes highlight the importance of the ML-CIRRUS campaign.

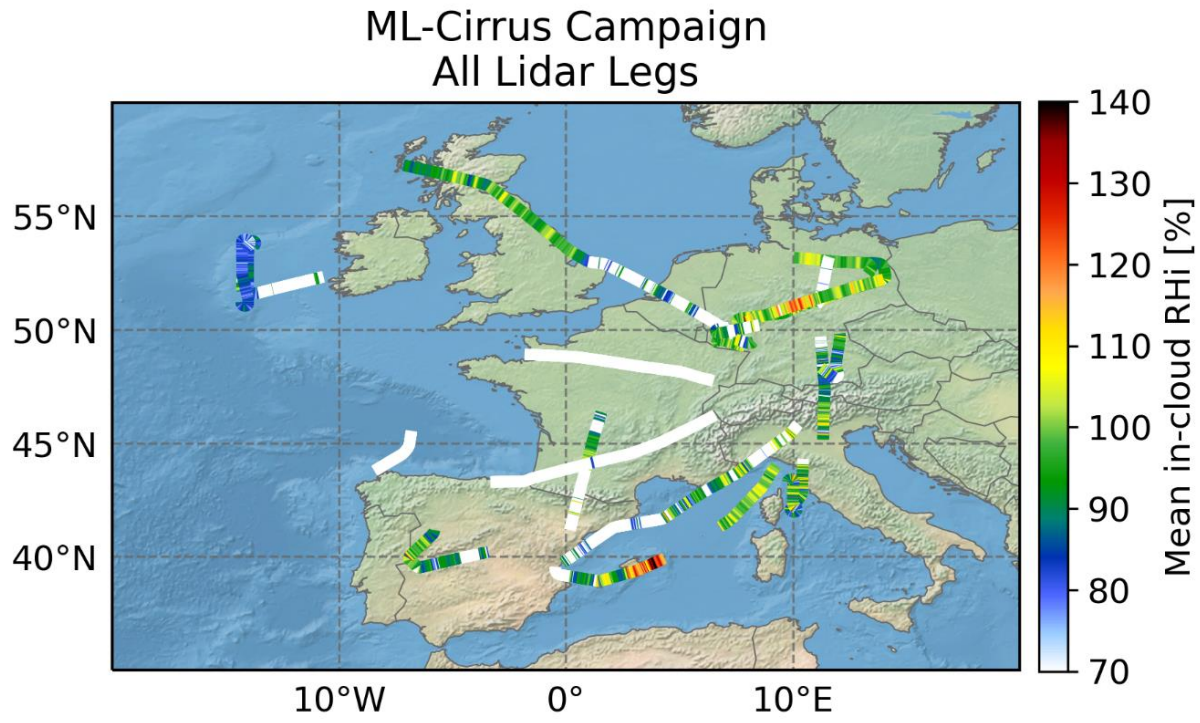

Figure 3.8: Map containing the flight tracks of the lidar measurement segments (legs) conducted during the missions of the ML-CIRRUS campaign. The color scale represents the average Relative Humidity over ice (RHi) from cloud base to cloud top on each time step. The white color signifies a mean RHi below 70 % or absence of cirrus clouds. Background map tiles, borders and coastlines from Natural Earth. License: Public domain.

To conduct this research campaign, the German Research aircraft HALO was employed (see Sect. 3.2). It was equipped with a unique suite of remote sensing as well as in-situ instruments, including WALES, which provided measurements of many different parameters, allowing for an all-round characterization of the targeted clouds and their environment. The aircraft measurements were also complimented by satellite data from various instruments and platforms.

A total of 16 flight missions were performed covering an area over central Europe and the NE Atlantic (Fig. 3.8). Each flight was meticulously planned, normally two days in advance. The flight planning was largely guided by operational forecasts of the European Centre for Medium-Range Weather Forecasts (ECMWF). From these forecasts cirrus formation could be predicted (Schumann, 2012; Schumann and Graf, 2013) and cirrus cloud systems of interest could be selected to be probed. Overpasses of satellites and overflights over ground-based stations were also considered and favored during flight planning. After a clear target was selected for a certain date, the mission would be planned and a flight plan submitted. Furthermore, each research flight was separated into different legs. During remote sensing or lidar legs, HALO was flying over the selected cirrus clouds. One of HALO's notable features is its high flight ceiling, which ensured that a minimum distance of around 2 km above the cloud tops could be maintained, aiding to accurate lidar measurements by WALES (see Sect. 3.1). The in-situ legs, were conducted at lower altitudes at cloud level. The data collected during the lidar legs were frequently used during the flights in order to verify and better define the predicted cirrus cloud locations and cloud top and base altitudes for the in-situ measurements.

In order to study contrails and especially newly formed ones, HALO was frequently given clearance by air traffic control to enter air traffic corridors with high airplane densities, as well as restricted airspaces. A highlight mission was conducted on 11/04, during which a quasi-Lagrangian flight path following the outflow of a warm conveyor belt (WCB) system was flown. This mission is also used in this work, to study the evolution of cirrus cloud life cycles. A description of the 16 missions with additional details is presented in Table 3.4. An in-depth presentation of the ML-CIRRUS campaign can be found in Voigt et al. (2017).

Table 3.4: Overview off the ML-CIRRUS missions. Table adapted and enriched from Voigt et al., 2017.

Flight Date(s)	**Mission(s)**	**Total flight time**	**Lidar Legs**	**DIAL data points in-cloud**	**Mission goals**
21 & 22.03.2014	M1-M3	6 h	-	-	Instrument test flights
26.03.2014	M4	8 h 30 min	3	43390	Contrails and contrail cirrus
27.03.2014	M5	4 h 45 min	2	44534	Frontal cirrus, WCB in- and outflow
29.03.2014	M6	7 h 30 min	3	30791	Lee-wave cirrus, WCB, jet stream divergence, convective cirrus, ***Saharan dust layer***
01.04.2014	M7	6 h 35 min	2	33915	Cirrus, contrail cirrus
03.04.2014	M8	5 h 15 min	3	2466	Frontal cirrus, WCB outflow
04.04.2014	M9 & M10	9 h 55 min	2	16582	Clean jet stream cirrus (M9), polluted WCB (M10), ***CALIPSO overpass***
07.04.2014	M11	5 h 35 min	2	22917	Contrail cirrus, cirrus sublimation, Halo
10.04.2014	M12	3 h 15 min	1	1864	Contrails and contrail cirrus
11.04.2014	M13 & M14	10 h	2	30959	Frontal cirrus, large WCB, ridge cirrus, ***Lagrangian approach along WCB outflow***
13.04.2014	M15	7 h 15 min	3	24	High pressure system, jet stream cirrus
15.04.2014	M16	3 h	-	-	Foehn, divergence, gravity wave cirrus, Instrument testing
Total	**16**	**77 h 35 min**	**23**	**227442**	

3.4 The HALO-(AC)³ Campaign

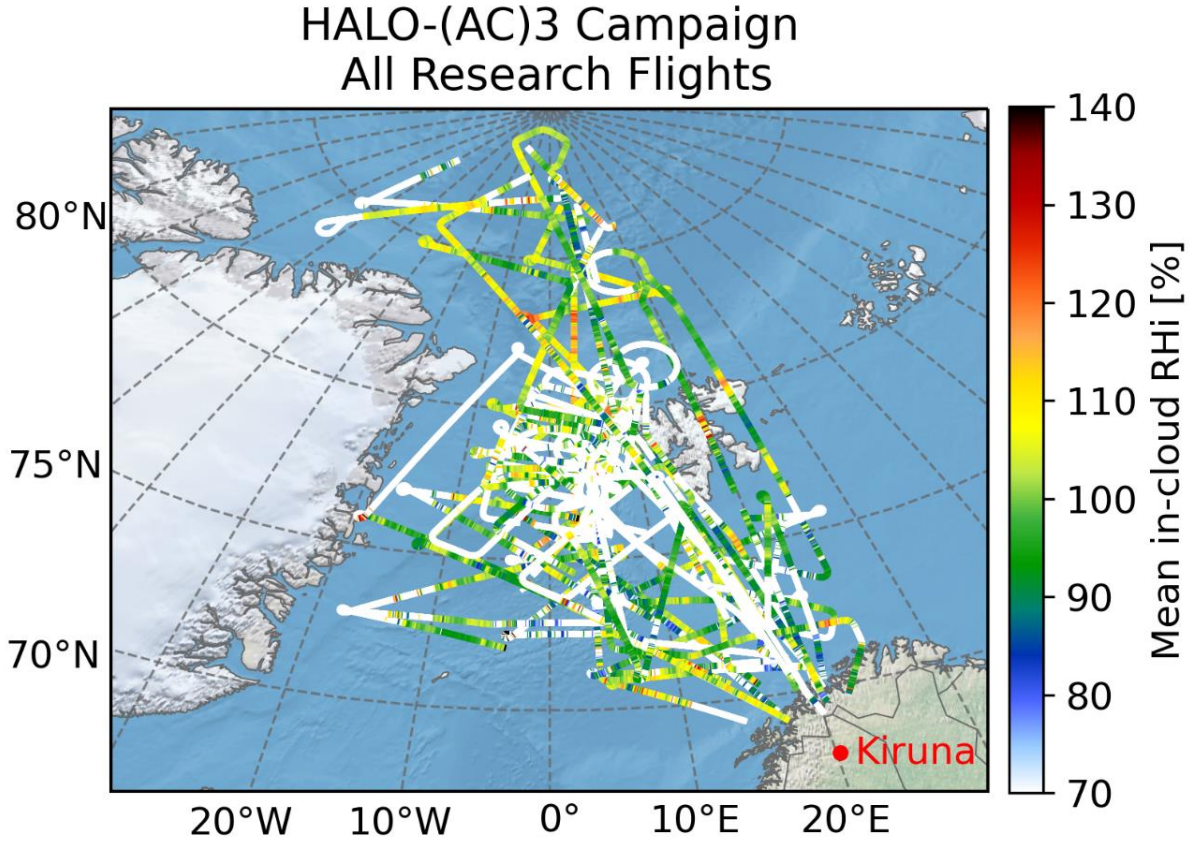

Figure 3.9: Map containing the flight tracks of the research flights (RFs) from the HALO-(AC)³ campaign. The color scale represents the average relative humidity over ice (RHi) from cloud base to cloud top. White color is representative of a mean RHi value below 70 % or parts where no cirrus clouds were detected. Background map tiles, borders and coastlines from Natural Earth. License: Public domain.

The arctic region of the earth is warming at a much faster rate in the past few decades, compared to other regions or the global average. This phenomenon has been named arctic amplification (Serreze and Francis, 2006; Graversen and Wang, 2009; Hansen et al., 2010; Wendisch et al., 2023) (Sect. 1.2.2). Arctic cirrus clouds are speculated to play a significant role also in the arctic-specific feedback processes involved in arctic amplification, especially during polar day and night (Winton, 2006; Graversen and Wang, 2009; Pithan et al., 2018; Stuecker et al., 2018; Wendisch et al., 2019, 2023; Dekoutsidis et al., 2024).

Meridional transport of airmasses into the arctic has also been speculated as one of the culprits of arctic amplification (Park et al., 2015; Binder et al., 2017; Dahlke and Maturilli, 2017). During Warm Air Intrusion (WAI) events, as they are called, warm, water-vapor- and aerosol-rich airmasses from the midlatitudes are transported into the arctic (Doyle et al., 2011; Stramler et al., 2011; Woods and Caballero, 2016; Liu et al., 2018; Pithan et al., 2018; Hartmann et al., 2019,

2021; Beer et al., 2022; Dada et al., 2022). These WAI events transfer sensible heat and great amounts of water vapor -a strong greenhouse gas- into the arctic and thus can lead to an increased cloudiness and alter the characteristics of the cirrus clouds that form in the arctic. Studies have also shown that WAI events are becoming more frequent and long-lasting, making the study of their effects more important (Woods and Caballero, 2016; Graham et al., 2017; Henderson et al., 2021). Despite the abovementioned, the arctic remains a region where atmospheric measurements are sparser than at lower latitudes especially in the upper troposphere and lower stratosphere (UTLS). Direct measurements of WAI events in the arctic and especially of cirrus during these events are also lacking (Wendisch et al., 2019).

The HALO-$(AC)^3$ campaign was conducted during March and April of 2022 aiming to fill part of this observational gap and provide insights regarding the role of clouds and airmass transportations into the arctic on arctic amplification (Wendisch et al., 2024; HALO AC3, 2023). Early on in the planning of the campaign it became clear that the best way of studying airmass transformations into the arctic, including WAI, would be in a quasi-Lagrangian approach i.e. following the evolution of an airmass over long periods of time as it was unfolding. The research aircraft HALO, with its high flight ceiling, long range and heavy payload was perfectly suited as a platform (see Sect. 3.2).

HALO was equipped with state-of-the-art, active and passive remote sensing instrumentation as well as dropsondes and was stationed in Kiruna, Sweden (Ehrlich et al., 2023; Wendisch et al., 2024). Part of the instrumentation for this campaign was also the WALES lidar system (see Sect. 3.1). HALO performed a total of 17 research flights (RFs) and launched over 300 dropsondes, collecting data over a vast area in the arctic (Fig. 3.9). Flights were performed at high altitudes allowing for measurements of cirrus clouds and also providing 2D data covering the whole atmospheric column along the flight track under favorable conditions.

In order to provide the most comprehensive measurements possible, HALO was accompanied by two more research airplanes by the Alfred Wegener Institute (AWI), POLAR 5 and POLAR 6 (Herber et al., 2008). Due to their shorter range they were stationed further north at Longyearbyen, Svalbard and performed remote sensing (Polar 5) and in-situ (Polar 6) measurements in the lower troposphere over the Fram Strait. The tethered balloon BELUGA (Balloon-bornE moduLar Utility for profilinG the lower Atmosphere) was also stationed at Ny-Ålesund, Svalbard and provided vertical profiles of the atmospheric boundary layer (Egerer et al., 2019). Two more research aircraft with in-situ instrumentation, the FAAM (Facility for Airborne Atmospheric Measurements) a modified BAE-146-301 (www.faam.ac.uk), and the ATR42 of the SAFIRE (Service des Avions Français Instrumentés pour la Recherche en Environnement) (www.safire.fr) were performing measurements out of Kiruna the same period.

Products from ECMWF and ICON (Icosahedral Nonhydrostatic) Model, specially calculated atmospheric indexes, such as the Marine Cold Air Outbreak (MCAO) index (Paprtiz and Spenzler, 2017), along with surface analysis products by DWD (German weather service) were used for the flight planning. Forecasts were carried out at least two days in advance, areas of interest were noted and potential flight plans were discussed. Central goal in the planning was to identify and measure airmass transformation over a period of 2-3 days. Circular flight patterns were also introduced in several flights in order to obtain measurements of large-scale vertical motion via dropsondes.

Table 3.5: Overview of the research flights performed during the HALO-(AC)^3 campaign.

Flight Date	**Research Flight #**	**Flight duration**	**DIAL data points in-cloud**	**Description / Objective**
25.02.2022	RF00	04 h 40 min	-	HALO Scientific test flight
11.03.2022	RF01	03 h	-	HALO Transfer flight from Oberpfaffenhofen to Kiruna
12.03.2022	RF02	08 h 20 min	88109	Warm Air Intrusion (WAI) day #1
13.03.2022	RF03	08 h 50 min	364889	WAI day #2
14.03.2022	RF04	08 h 35 min	80259	WAI day #3
15.03.2022	RF05	08 h 40 min	148955	Atmospheric river (AR) day #1
16.03.2022	RF06	09 h 30 min	129346	AR day #2, ***collocated leg with FAAM*** (BAe-146), ***overpass of NyRAD-35***
20.03.2022	RF07	09 h 10 min	246106	Day before a Cold Air Outbreak (CAO), ***collocated segments with P5 and P6*** over sea-ice and open ocean
21.03.2022	RF08	07 h 45 min	124124	1st CAO, ***coordinated leg with the FAAM***
28.03.2022	RF09	07 h 25 min	2199	2nd CAO, convergence along sea ice border, ***BELUGA profiles***
29.03.2022	RF10	08 h 25 min	158103	2nd CAO, circles for ***dropsondes, FAAM and SAFIRE*** (ATR42) coordination
30.03.2022	RF11	08 h 25 min	89649	2nd CAO, ***Lagrangian mesoscale divergence circles***, collocated measurements with the ***FAAM and SAFIRE***
01.04.2022	RF12	08 h 10 min	65323	2nd CAO, rectangular divergence pattern sea ice edge, collocated segment with ***P5 and P6, BELUGA*** profiles
04.04.2022	RF13	08 h 50 min	38859	3 objectives flight (ice edge, cirrus, water vapour), ***BELUGA*** profiles
07.04.2022	RF14	07 h 45 min	40822	Arctic Cirrus #1, ***collocated with P5***, ***BELUGA*** profiles
08.04.2022	RF15	07 h 20 min	19368	Polar Low
10.04.2022	RF16	06 h 30 min	130553	Moist air advection, Arctic Cirrus #2 Day 1
11.04.2022	RF17	07 h 55 min	158796	Arctic Cirrus #2 Day 2
12.04.2022	RF18	08 h 05 min	114362	Arctic Cirrus #2 Day 3
Total	**19**	**147 h 20 min**	**1999822**	

Collocated flights between the available aircraft were preferential with HALO providing a large-scale overview of the atmosphere along the transported airmasses from the upper troposphere, POLAR 5 focusing on clouds and precipitation in the lower troposphere and Polar 6 providing in-situ measurements at even lower altitudes in the boundary layer. Coordinated flights with the FAAM and the SAFIRE ATR42 were also planned and performed. The big number of airborne means, the various instruments aboard each and a careful, coordinated flight planning resulted in achieving the goals of the campaign and creating a detailed all-around database of remote sensing and in-situ measurements of numerous parameters of CAO (Cold Air Outbreaks) and WAI events, arctic cirrus clouds and others. A detailed description of the RFs performed during HALO-(AC)^3 is presented in Table 3.5.

3.5 Calculation of products

In this thesis, predominantly data collected by the WALES lidar system are used. Different products are used for different aspects of the analysis, such as the backscatter ratio (BSR), the particle linear depolarization ratio (PLDR), the two-way optical transmission (α), and the water vapor mixing ratio (WVMR).

As described in Sect 1.4, the relative humidity over ice (RHi) is a parameter controlling ice formation as well as growth and melting/sublimation within cirrus clouds, and thus can be used to characterize them. The RHi can be calculated if ambient temperature and water vapor concentration are known.

In this thesis the RHi for each ML-CIRRUS mission and HALO-(AC)^3 research flight is calculated from the retrieved water vapor mixing ratio by WALES and model temperature from the 6-hourly analysis data by the Integrated Forecasting System (IFS) of the European Centre for Medium Range Weather Forecasts (ECMWF) (Esselborn et al., 2008). More precisely, operational analysis and short-term forecast fields from the atmospheric high-resolution model (HRES, 0.125x0.125 grid, 137 model levels) are interpolated in space and time in order to match the locations of the measurements. More details regarding the used data and the interpolation process can be found in Schäfler et al. (2020).

The first step to retrieve the RHi, is to calculate the saturation vapor pressure of water vapor over ice for the whole temperature range. Here a formula by Huang (2018) is used:

$$e_{s_i} = \frac{exp\left(43.494 - \frac{6545.8}{\theta + 278}\right)}{\theta + 868\ ^2} \quad \theta \leq 0°C \tag{3.1}$$

with a mean relative error (MRE) of 0.006 % compared to a reference dataset from experimental data of the International Association for the Properties of Water and Steam (IAPWS). θ denotes the temperature in °C.

Then, the RHi is calculated by:

$$RH_i = \frac{r_{wv} \rho k_B T}{e_{s_i}} \tag{3.2}$$

where r_{wv} is the water vapor mixing ratio, ρ is the volume number density of air, k_B the Boltzmann constant, e_{si} the saturation vapor pressure for water over ice and T the temperature.

Knowing the RHi supersaturation within and around a cloud allows to estimate not only how the already existing ice crystals formed, but also how new ice crystals might form, and which parts of a cloud are more likely to facilitate new ice formation or rather sublimation. In this work, in an effort to provide a detailed characterization of the studied cirrus clouds, three temperature-dependent thresholds are calculated, two for heterogeneous nucleation (HET) and one for homogeneous nucleation (HOM). They are used along with the ice and water saturation thresholds and are shown in Fig. 3.10.

The ice saturation threshold RHi = 100 % denotes the point over which ice crystal formation is possible and under which ice crystals melt or sublimate. The water saturation threshold is the limit above which water droplet formation is favored instead of ice crystal formation. It is calculated using a formula by Huang (2018). For RHi between the ice and water saturation threshold, ice nucleation is possible via the abovementioned pathways of HET and HOM nucleation (Fig. 2.5).

The *HOM nucleation threshold*, signifies the limit over which HOM nucleation is possible. It is calculated based on the findings and formula presented by Koop et al. (2000), and also described by Urbanek et al. (2017). Between the HOM nucleation threshold and the water saturation threshold, the *HOM regime* is defined (red color in Fig. 3.10). It contains RHi values, which would allow HOM nucleation to take place under favorable conditions. Between the HOM nucleation threshold and ice saturation threshold the *HET regime* is defined (yellow and green color in Fig. 3.10). RHi values in this regime would suffice for HET nucleation to take place on different INP. As is shown in Fig. 3.10 the HET regime covers a rather wide range of RHi supersaturation. Within this regime a wide variety of different INP can become activated with different activation thresholds. For a more detailed analysis, a *high HET* threshold and a *low HET* threshold are defined representing inefficient and efficient INPs requiring higher and lower supersaturations for activation respectively. For the high threshold, coated soot (CS) is selected as an inefficient INP, and for the low threshold mineral dust (MD), which is more efficient as an INP and more abundant (Kärcher and Lohmann, 2003; Gensch et al., 2008; Pruppacher and Klett, 2010; Hoose and Möhler, 2012; Cziczo et al., 2013; Krämer et al., 2016; Ansmann et al., 2019; Beer et al., 2022). The HOM nucleation, CS activation and MD activation thresholds are calculated by the following equations:

$$\begin{aligned} RHi_{HOM} &= 242.3 - \ 0.41T \\ RHi_{HET}^{CS} &= 230. - (0.4\overline{33}T) \\ RHi_{HET}^{MD} &= 134. - \ 0.1T \end{aligned} \tag{3.3}$$

(Urbanek et al., 2017, their Table 1, and original formulations from Koop et al. (2000) (HOM) and Krämer et al. (2016) (HET)).

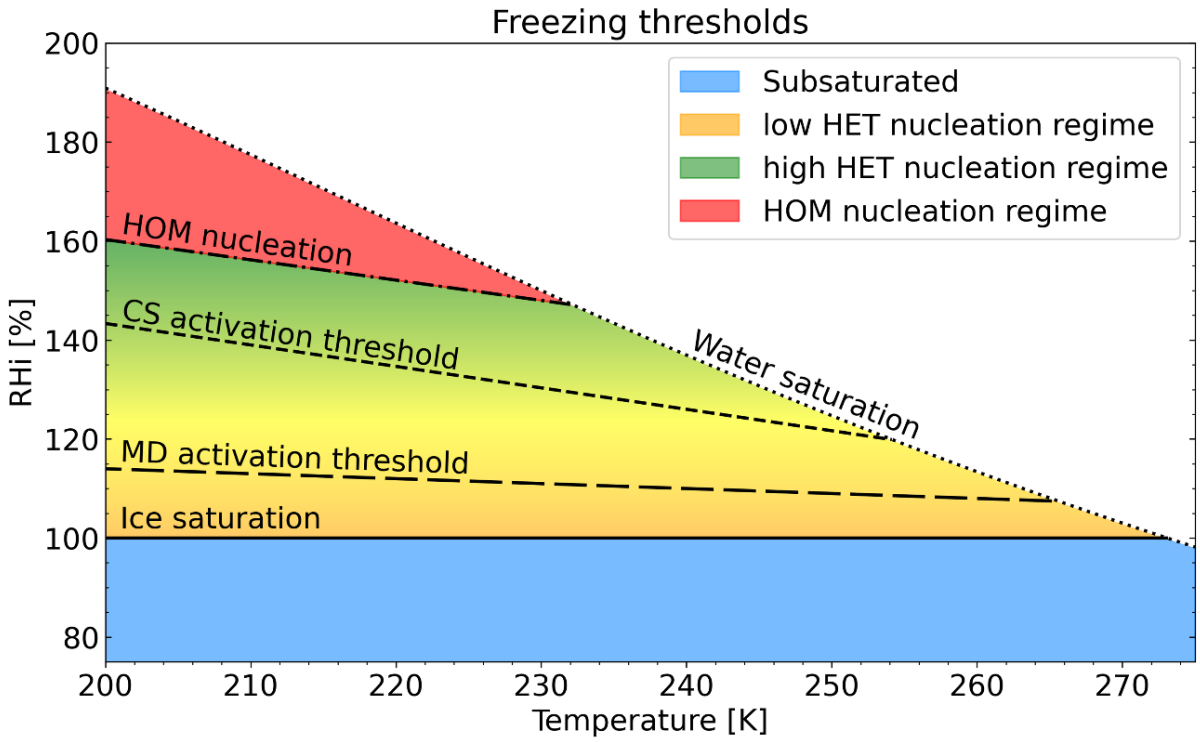

Figure 3.10: Temperature dependent RHi thresholds for different ice nucleation pathways. Ice saturation is possible above the ice saturation threshold and below the water saturation threshold. The heterogeneous nucleation (HET) regime (yellow and green colors) contains two additional thresholds. One for mineral dust (MD) as an INP, which is easily activated and requires lower RHi and one for coated soot (CS) which is less easily activated. The HOM nucleation threshold signifies the limit over which homogeneous nucleation is possible.

In addition to the abovementioned, for the analysis of the high latitude cirrus clouds measured during the HALO-(AC)^3 campaign the optical depth τ was calculated from the two-way optical transmission α measured by WALES:

$$\tau\ r\ = -\frac{1}{2}\ln(\alpha) \tag{3.4}$$

3.6 Uncertainty in the calculation of RHi

The accuracy of the RHi calculated via the abovementioned method depends primarily on the accuracies of the inputted humidity and temperature. As has been mentioned in Sect 3.1.3 the water vapor retrieval by WALES has a mean statistical inaccuracy of 5 %. This stems predominantly from uncertainties in the definition of water vapor absorption cross sections, the air density profiles and the spectral purity and shape of the laser light, as discussed in Sect. 3.1.3. Groß et al. (2014) and Urbanek et al. (2018) use similar methods applied on WALES data with

the later also using the ML-CIRRUS campaign measurements. Regarding the second source of uncertainty, Groß et al. (2014) additionally preformed an investigation of the applicability of the ECMWF temperature field for the calculation of RHi. They compared the ambient temperatures measured by in-situ instruments aboard the HALO research aircraft during descends into and ascents from airports, to ECMWF temperatures. They found a difference of 0.8 K (T_{HALO} - T_{ECMWF}) for the typical height and temperature range of cirrus clouds. From this they estimated a maximum error of about 10 % to 15 % in the calculated RHi for cirrus clouds, ΔRHi: 10-15 %.

The big number of dropsondes launched during the HALO-(AC)^3 campaign allowed for a more detailed study of the temperature induced error on the RHi calculation (Wirth and Groß, 2023). A comparison of the measurements from 339 dropsondes to the ECMWF IFS temperature field yielded an average temperature bias of around 0.2 K with a precision of 0.4 K. After the calculations this translates to an error of 2 % bias and 4 % precision induced on the RHi due to the model temperatures. Importantly no bias was detected regarding the atmospheric pressure, which is necessary for the correct assignment of the geometrical altitude in the interpolation of the temperatures on the lidar grid.

3.7 Masking

One of the advantages of using airborne lidar instruments, is that the whole atmospheric column from the airplane to the ground can be measured at every timestep if conditions are favorable, producing a two-dimensional curtain of data along the flight track. This curtain contains various cloud types at different altitudes, aerosol layers, cloud-free air etc. For this thesis the cirrus clouds have to be isolated from the curtain of each lidar measurement.

The backscatter ratio (BSR), particle linear depolarization ratio (PLDR), temperature (T) and altitude (H) are used as parameters to construct cirrus cloud masks. The exact thresholds are adapted to the mid- and high latitudes for the clouds measured during the two campaigns. For the ML-CIRRUS campaign I define the in-cloud and cloud-free areas. For the high latitude cirrus measured during the HALO-(AC)^3 campaign also a near-cloud region is introduced.

Midlatitudes

The BSR is the strongest indicator for the existence of a cloud. For the lidar measurements performed during the ML-CIRRUS campaign over the midlatitudes, a threshold value of BSR = 3 was selected, after a careful analysis. Groß et al. (2014) and Urbanek et al. (2017 & 2018) have used similar cloud masks. They tested a variety of different thresholds and found that a wide range of BSR values from 2 up to 25 can be used without significantly affecting the further analysis and results. The PLDR is used in the mask as a way of identifying ice crystals and thus filtering out non-cirrus clouds. For this study the threshold was set at PLDR = 20 %, as this is indicative of ice crystals (Gobbi, 1998; Chen et al., 2002; Comstock et al., 2004). For a similar reasoning a temperature threshold is set at T = 235 K as this is the temperature below which cirrus clouds commonly form and the ice phase is dominant (Ström et al., 2003; Krämer et al., 2016; Kärcher and Seifert, 2016; Gasparini et al., 2018; Urbanek et al., 2018).

These thresholds are checked against every data point of each curtain. If BSR ≥ 3 and PLDR ≥ 20 % and T < 235 K the data point is considered as being in-cloud. For the thresholds of the

cloud-free area, the altitude is chosen rather than the temperature. For this thesis, only the cloud-free air in the vicinity of cirrus clouds is of interest, thus only areas where ice crystals could form are kept. The threshold is set at H = 7 km, since over this altitude ice crystals would most probably be able to form (Ström et al., 2003; Comstock et al., 2004; Kärcher, 2017; Gasparini et al., 2018). Under vicinity around cirrus clouds a maximum horizontal distance of 250 km from the cloud edges and a zone with altitudes from 7 to 12 km is considered. The thresholds for the cloud mask are shown in Table 3.6. In Fig. 3.11, an example of the application of the cirrus mask on a lidar leg from Mission 5 is presented.

High latitudes

For the cirrus clouds measured during the HALO-(AC)^3 campaign over the high latitudes, three regions are defined on each measurement curtain: In-cloud, near-cloud and cloud-free. The BSR threshold here is set at BSR = 2. The threshold for the PLDR remains the same as for the midlatitude study, at 20 %, which is a representative threshold for ice crystals. Finally, in order to remove all the low-level clouds from the dataset, an altitude threshold is selected at 3000 m. In summary, a data point is considered as being in-cloud for a BSR $\geq$ 2, a PLDR $\geq$ 20 % and an H $\geq$ 3000 m.

The area immediately bordering the clouds edges is of special interest, as important processes such as entrainment, ice nucleation, sedimentation and sublimation, and exchange of water vapor and heat, take place there. Thus, it was concluded that it should be separated from the cloud-free air. The near-cloud area was introduced and defined as a stripe 10 % outside of the cloud edges. For most cases this translates into a band reaching 80 km before and after the cloud edges and 500 m above/below the cloud top/base. Finally, the cloud-free area consists of all the data beyond the near-cloud area. The exact thresholds of the cloud mask are presented in Table 3.7. An example of the masking and the resulting areas is shown in Fig 3.12.

Table 3.6: Parameters and thresholds of the cirrus cloud mask for the definition of the in-cloud and cloud-free areas at midlatitudes.

	In-Cloud	Cloud-free
BSR	≥ 3	< 3
PLDR	≥ 20 %	< 20 %
Temperature	< 235 K	-
Altitude	-	> 7 km

Table 3.7: Parameters and thresholds for the cirrus cloud mask defining the in-cloud, near-cloud and cloud-free regions at high latitudes.

In-cloud	BSR ≥ 2
	PLDR ≥ 20 %
	H ≥ 3000 m
Near-cloud	80 km before and after cloud edges
	500 m over/under cloud top/bottom
	H ≥ 3000 m
Cloud-free	remaining data points
	H ≥ 3000 m

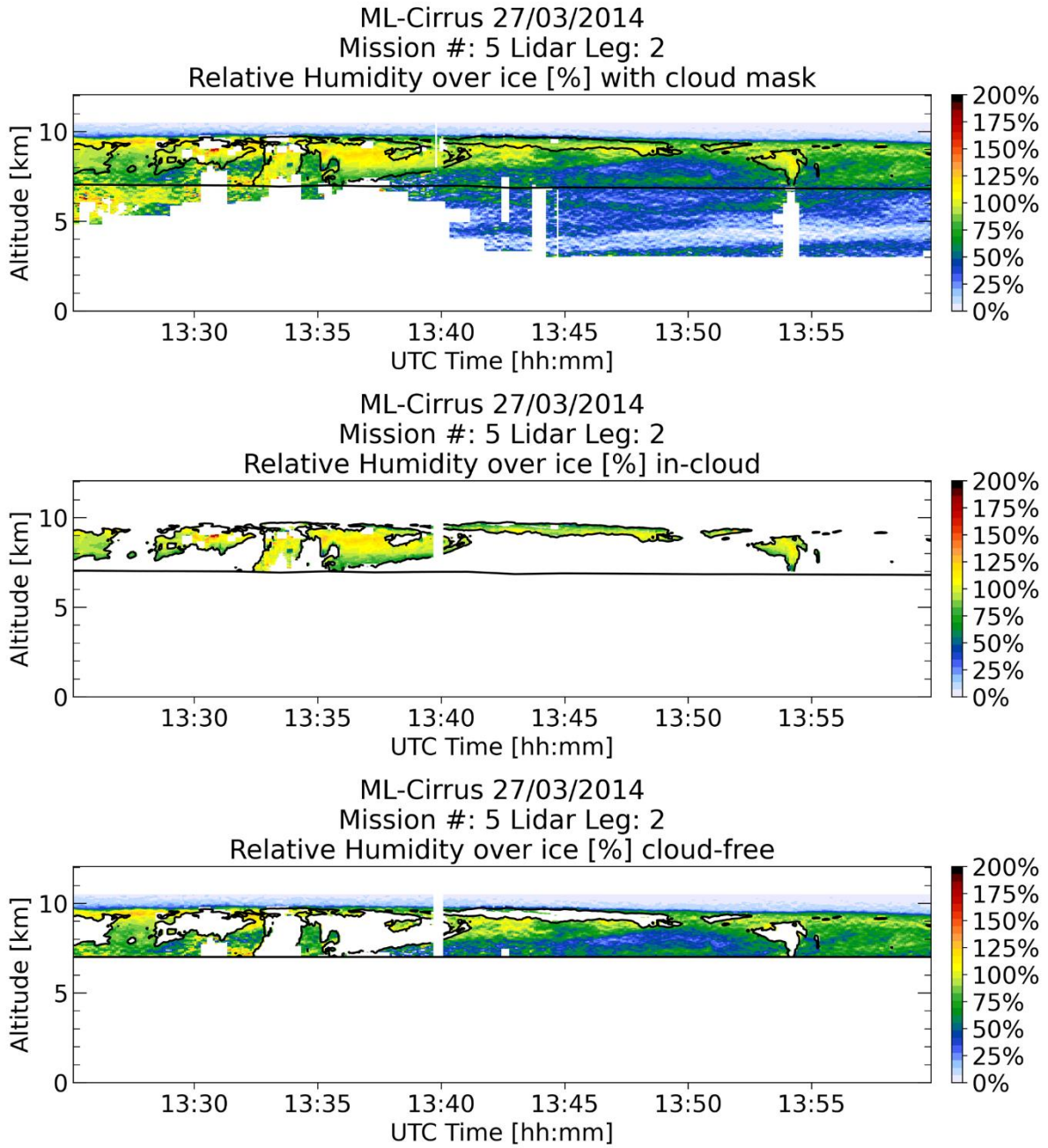

Figure 3.11: Example of the application of the cirrus cloud mask on RHi data from lidar leg 2 of Mission 5 on 27/03/2014. **Top**: the parameters of the cloud mask (black lines) plotted against the RHi curtain. **Middle**: the in-cloud data along with the cloud mask. **Bottom**: the cloud-free data with the cloud mask.

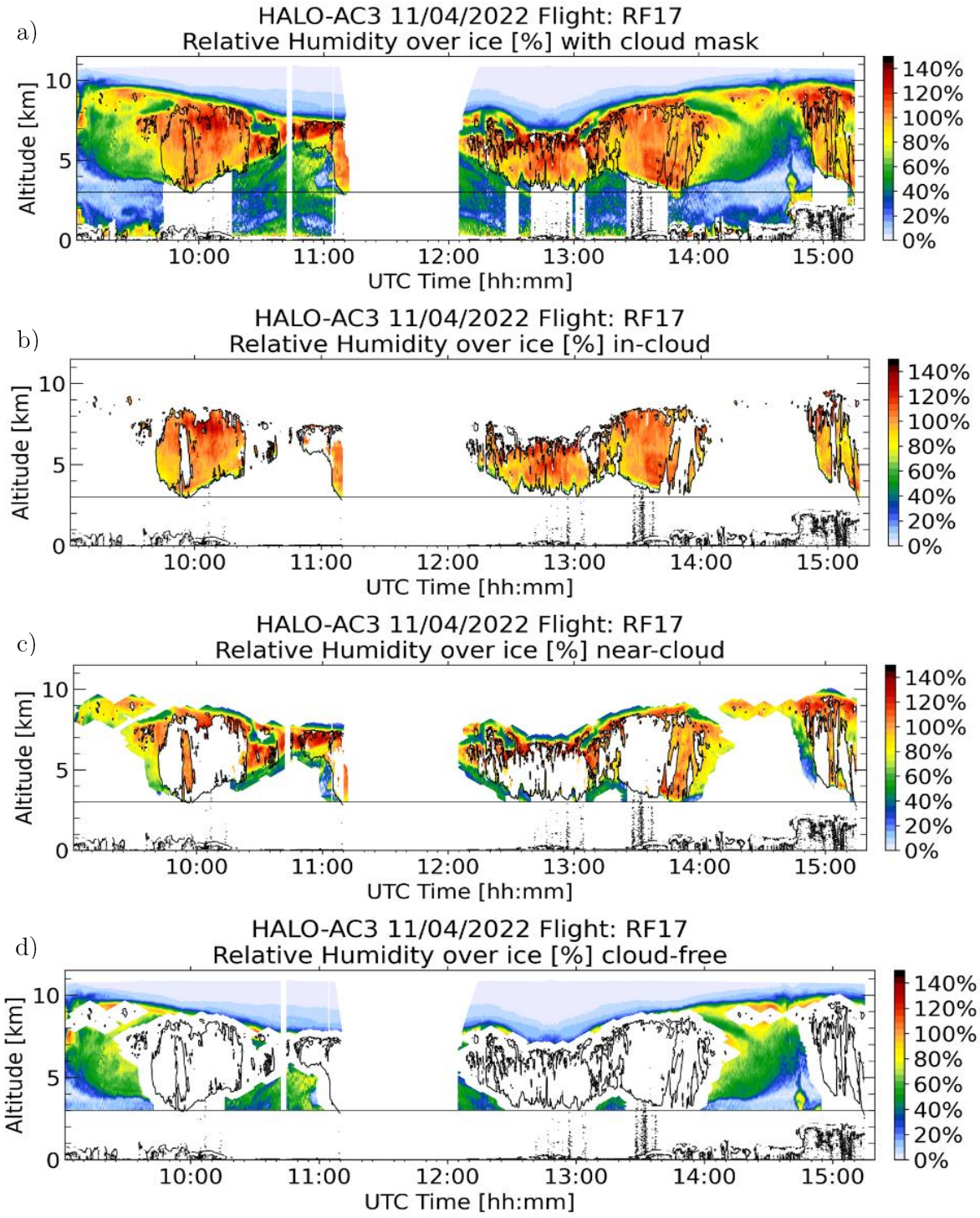

Figure 3.12: Example of the cirrus clouds mask being applied on the RHi curtain from Research Flight 17 of the HALO-(AC)^3 campaign on 11/04/2022. **a)** The whole RHi curtain with the contours of the in-cloud mask. **b)** The in-cloud area with the contours of the cloud-mask. **c)** The near cloud area around the edge of the cirrus with the contours of the cloud mask. **d)** The cloud-free region with the contours of the cloud-mask.

3.8 Cirrus classifications

3.8.1 Based on formation: In-situ formed vs Liquid origin

A primary scientific question of this thesis is: how does the formation process of cirrus clouds affect the characteristics of supersaturation within them. In order to answer this question, the cirrus clouds measured during the ML-CIRRUS campaign needed to be classified based on their formation process. One such classification has been introduced by Krämer et al. (2016) and Luebke et al. (2016) and is described here and shown in Fig. 3.13.

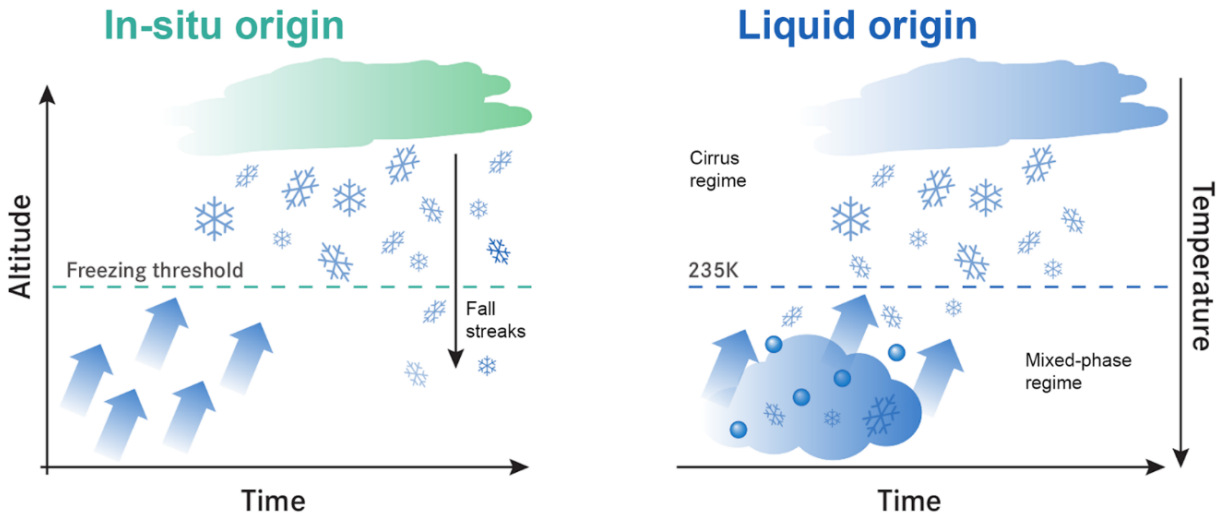

Figure 3.13: Schematic representation of in-situ formed cirrus (Left), forming directly as ice clouds at high altitudes and low temperatures and liquid origin cirrus (Right), resulting from complete glaciation of a mixed-phase predecessor cloud. Graph from Luebke et al. (2016). Their Figure 1.

Krämer et al. (2016) compiled cirrus measurements from 17 field campaigns covering 15 years and vast geographical regions and performed numerous model simulations. From their study, they defined two cirrus types based on the formation mechanism: In-situ formed clouds and liquid-origin clouds. In-situ formed cirrus are clouds that form directly into ice clouds at the high altitude and location they are detected. Liquid-origin cirrus on the other hand, have a liquid or mixed phase predecessor. First the predecessor cloud is formed, then while its liquid droplets are lifted to colder temperatures they freeze until complete glaciation at the latest when the cirrus formation threshold is reached around 235 K (Fig. 3.13).

In the analysis presented herein, the classification from Krämer et al. (2016) and Luebke et al. (2016) is used and the studied cirrus clouds are grouped into in-situ formed and liquid-origin. In order to allocate the clouds to the one or the other group, first their formation process must be detected. To do this, 24 h backward trajectories for each cloud are produced and examined. The trajectories are initiated on a grid with a temporal resolution of 12 s and a vertical resolution of 150 m covering the whole lidar curtain for each mission of the campaign. The calculations are

then performed using horizontal wind data from the ECMWF reanalysis dataset ERA-Interim (ECMWF, 2011). Then, along the calculated backwards trajectories, diabatic heating rates are used with the trajectory module of the Chemical Lagrangian Model of the Stratosphere (CLaMS) for vertical transport (McKenna et al., 2002). Finally, the clouds are characterized as in-situ formed or liquid-origin cirrus depending on the simulated ice water content (IWC), the location of the maximum IWC value and the ambient temperature at their first detection along the backwards trajectory. During the classification process it was seen that some clouds consisted of a liquid-origin layer as well as an in-situ formed layer (most commonly the top layer). In these cases, the detected cloud was split and its parts were grouped accordingly.

3.8.2 Based on ambient conditions: Arctic vs WAI conditions

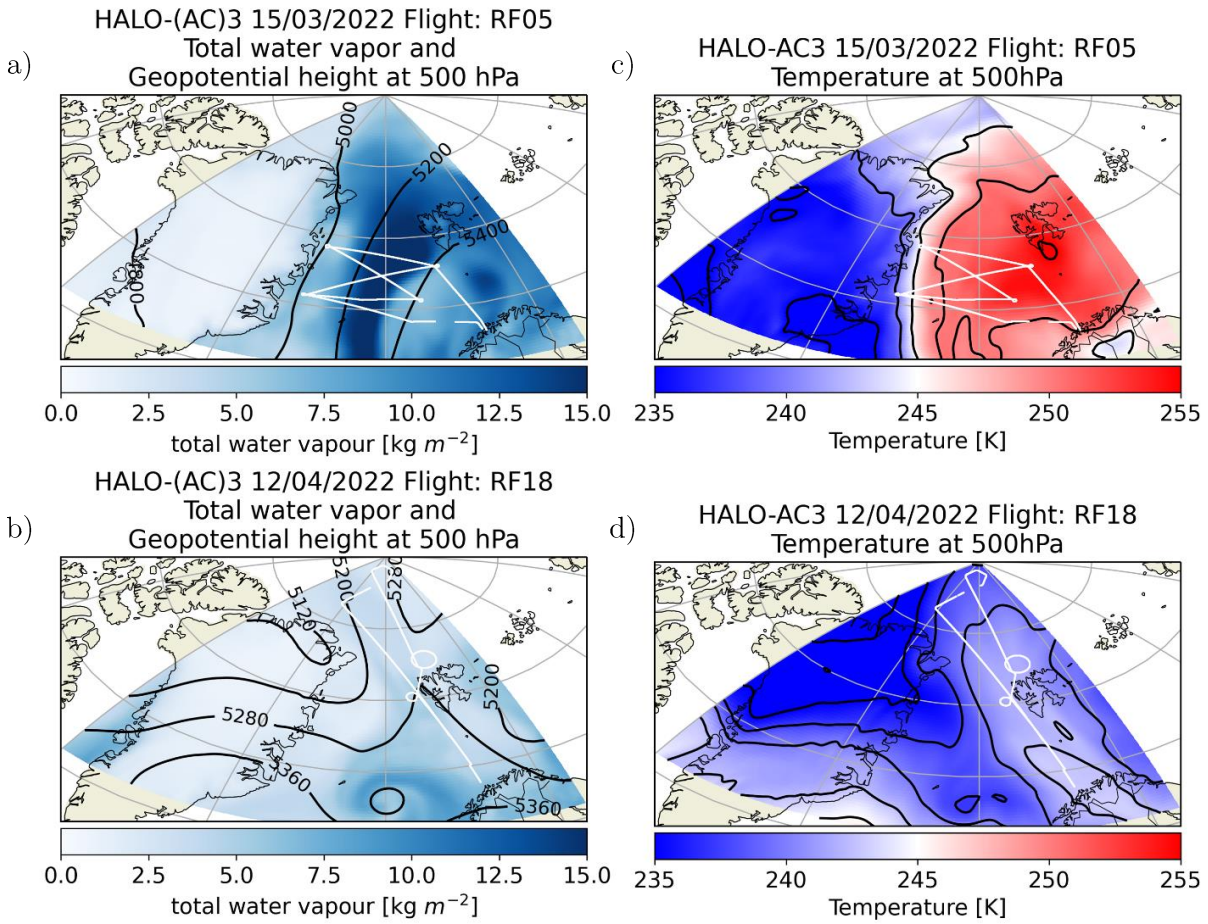

Figure 3.14: Example of a research flight performed under AC and WAI conditions. **Top**: RF05 performed during a warm air intrusion. **a)** The total water vapor and geopotential height at 500 hPa for RF05. **c)** The ambient temperature at 500 hPa for RF05. **Bottom**: RF18 performed during undisturbed arctic conditions. **b)** The total water vapor and geopotential height at 500 hPa for RF18. d) The ambient temperature at 500 hPa for RF18.

A central goal of this thesis is to showcase how the characteristics of water vapor supersaturation and cirrus clouds are affected by different meteorological conditions. When undisturbed, the arctic atmosphere consists of cold airmasses with a lower water vapor content compared to the mid-latitudes. During a Warm Air Intrusion (WAI) event large amounts of warm and moist airmasses are transported into the arctic dramatically changing the ambient conditions. Based on this, two different cirrus types are introduced: **AC cirrus**, which form during undisturbed arctic conditions, and **WAI cirrus,** which form during a WAI event in airmasses transported into the arctic from the midlatitudes.

The first step in studying the differences between AC and WAI cirrus was to group the measured cirrus according to the ambient conditions present during their formation and detection. In order to accurately identify the ambient conditions as AC and WAI and group each flight into one of the two categories, various sources and parameters were used. The first step was already taken during the campaign. Daily weather briefings were held for the flight planning. Discussed during these briefings were amongst others the surface analysis, the development of circulation patterns, the wind fields and airmass advections as well as more specific forecasting indexes like the vertically integrated water vapor transport (IVT). The IVT is calculated from the surface and up to 300 hPa and is used to define WAIs and atmospheric rivers with a common threshold being 250 $kg \cdot m^{-1} \cdot s^{-1}$. This already allowed an early classification of the flights. Additionally, after the campaign the synoptic situation for each flight was once again studied, using the geopotential height, temperature and total column water vapor fields from the ERA-5 reanalysis dataset (Hersbach et al., 2018), as well as the water vapor measurements from WALES. Finally, each research flight was classified as either being performed under undisturbed arctic (AC) conditions or under warm air intrusion (WAI) conditions. An example of an AC conditions and a WAI conditions flight is shown in Fig. 3.14.

The origin of the airmass in which each cirrus was detected is equally important, to the ambient conditions during the measurements. In order to determine the origin of the airmass of each cloud, 24-hour backwards trajectories were calculated. For the calculation, data from the ERA5 reanalysis dataset from ECMWF were used with a horizontal resolution of 1^{o} by 1^{o} and 37 pressure levels vertically. The CLaMS model was used for the diabatic processes regulating the vertical transport of the airmasses. The backwards trajectories for each flight of the two groups, were thus calculated. The trajectories confirmed the initial grouping, based on the ambient conditions and highlighted the fact that the airmasses in which WAI cirrus were detected did in fact originate from the midlatitudes. The combined trajectories for the flights of each group are shown in Fig. 3.15.

The ice nucleation processes with which the cirrus clouds formed in the arctic, remain equally important in defining their microphysical, radiative and also macrophysical characteristics as it was for the midlatitude cirrus. The ice nucleation processes for cirrus clouds have been described in detail in Sect. 2.2 and remain unchanged between cirrus clouds over the midlatitudes or the arctic. Thus, the same principles, parameters and thresholds are applied in their study over the arctic, as was described in Sect. 3.5.

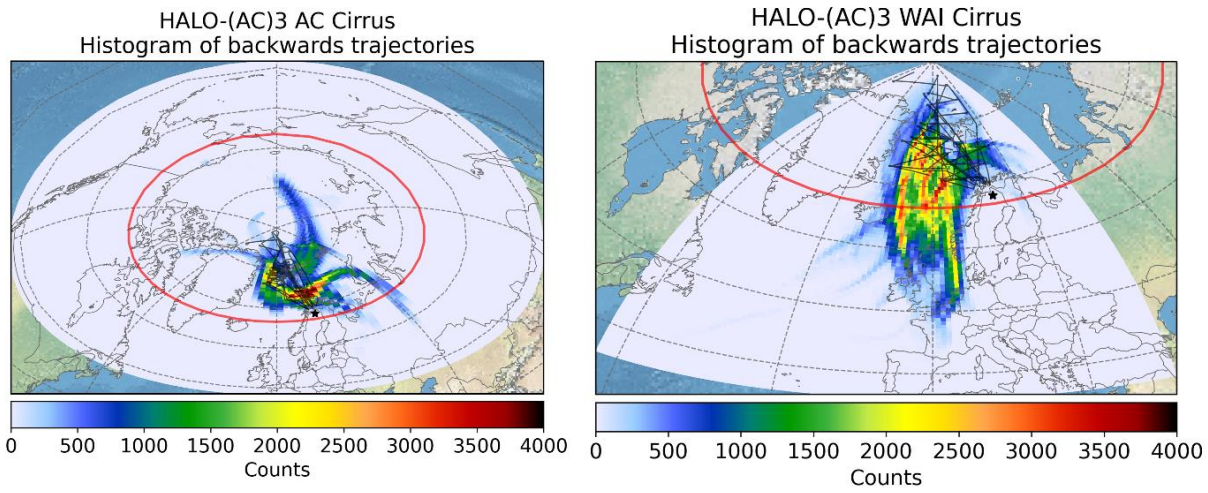

Figure 3.15: Maps containing 2D histograms of the latitude and longitude of the 24-hour backwards trajectories calculated from the cirrus clouds measured during the research flights of the HALO-(AC)^3 campaign. **Left:** backwards trajectories starting from research flights classified as AC conditions. **Right:** backwards trajectories starting from research flights classified as WAI conditions. The red line represents the latitude of 72° N. Background map tiles, borders and coastlines are by Natural Earth (naturalearthdata.com). License: Public domain.

Chapter 4

Results

In this chapter, the findings of my research are presented. In the first part, Sect. 4.1, midlatitude cirrus clouds are characterized with respect to their relative humidity over ice (RHi). The analysis is based on measurements taken by the airborne lidar system WALES during the ML-CIRRUS campaign. First, an overview is presented containing all cirrus clouds measured over the midlatitudes under various ambient conditions. The distribution of RHi as well as the vertical in-cloud structure are studied (Sect 4.1.1 & 4.1.2). Afterwards, a comparison between the in-situ formed and liquid origin cloud groups is performed (Sect 4.1.3). The analysis includes once again the distribution of RHi and the vertical structures of the two cloud types. Finally, insights into the evolution of midlatitude cirrus with time are presented by means of two detailed case studies (Sect 4.1.4).

In the second part of this chapter, Sect 4.2, results regarding cirrus clouds in the arctic are presented. The focus is once again on the RHi and the data stem from WALES during the HALO-(AC)^3 campaign. First a statistical analysis is provided including all cloud data retrieved under different synoptic situations in the arctic. The focus is once again on the distribution of RHi inside and around the clouds, as well as the in-cloud structure (Sect 4.2.1 & 4.2.2). The chapter continues with a comparison between clouds that formed under undisturbed arctic (AC) and warm air intrusion (WAI) conditions (Sect. 4.2.3). The geometrical and optical characteristics of the two cloud types are presented as well as the distribution of RHi and their vertical structure.

Extensive parts of the results presented herein have been published in the peer-reviewed articles Dekoutsidis et al., (2023, 2024).

4.1 Characterization of midlatitude cirrus clouds based on their RHi

The midlatitudes are a region where a great variety of different weather systems and dynamical processes are found, such as frontal systems, warm conveyor belts (WCB), convection and others. It is also a region that is strongly affected by humans, be it by the elevated aerosol emissions or denser air traffic. Cirrus clouds that form over the midlatitudes are influenced by the various processes and conditions, potentially also leading to a big variability in their characteristics and effects. This variability makes the representation of cirrus clouds in forecasting and climate sensitivity models challenging. Cirrus clouds introduce uncertainties in those fields, highlighting the necessity to study and understand them.

A commonly occurring weather pattern over the midlatitudes are WCBs. They are streams of warm and moist air ascending from the lower to the upper troposphere in front of cold fronts of cyclones. During this ascent, the warm, moisture-rich airmasses rapidly cool down leading to the

formation of low level, liquid clouds. As the airmasses then continue their ascent to colder temperatures ice crystals can start forming. Further lifting can result into the formation of a cirrus cloud from the parent liquid cloud. Cirrus clouds that form via this or similar processes and have a liquid predecessor are called liquid origin cirrus.

Alternatively, cirrus clouds can also form over the midlatitudes directly as ice clouds at high altitudes. In that case they are described as in-situ cirrus. The differences in ambient conditions during the formation of liquid origin and in-situ formed cirrus, such as the temperature, cooling rate, updraft, available moisture and others, can affect the properties of the clouds. Therefore, it is important to study those two cloud types, investigate if there are differences between them and try to identify them. With this in mind, I studied the data collected during the ML-CIRRUS campaign and present my findings in the following.

4.1.1 Distribution of RHi in midlatitude cirrus

The measurements performed by the WALES lidar system during the ML-CIRRUS campaign, were processed in two steps, as mentioned above. First, a statistical analysis of the whole data set was performed allowing for a general characterization of RHi within and around cirrus clouds over the midlatitudes. The results from this analysis can be summarized in Fig. 4.1. In this figure, the probability densities of RHi with respect to the ambient temperature for the in-cloud and cloud-free areas are plotted. Each distribution is accompanied by a total of four lines representing the thresholds for ice saturation and homogeneous (HOM) nucleation, as well as heterogeneous (HET) nucleation thresholds on coated soot (CS) and mineral dust (MD), marking the high and low HET regimes respectively. These thresholds have been introduced in detail in Sect 3.5.

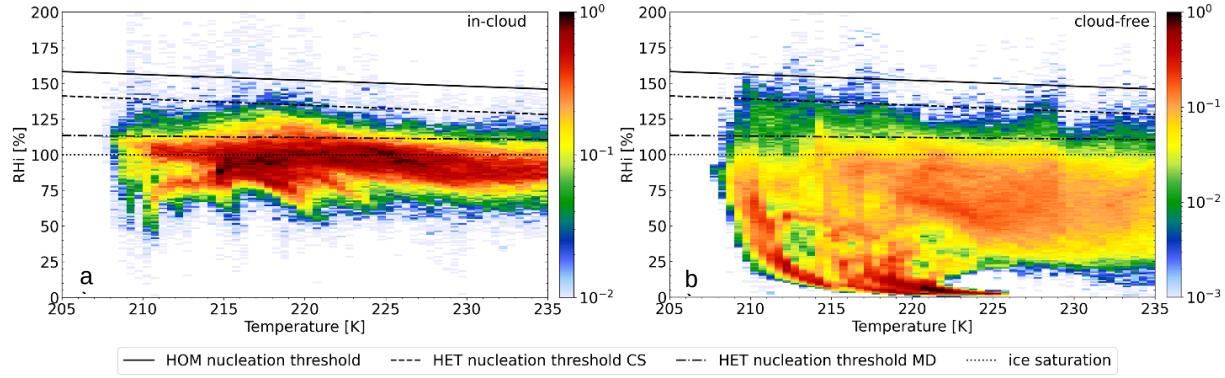

Figure 4.1: Probability density functions (PDF) of the Relative Humidity over ice (RHi) with respect to ambient temperature. **a)** Calculated for the in-cloud data points. **b)** Calculated for the cloud-free data points. The bin sizes are 0.5 K and 1 % RHi. The dotted line depicts the ice saturation threshold at RHi = 100 %. The dash-dotted line is the low threshold for heterogeneous nucleation (HET). The ice nucleating particle (INP) for this threshold corresponds to mineral dust, which is efficient as an initiator of ice formation. The dashed line represents the high threshold for HET nucleation. Here the INP corresponds to coated soot which is not activated as easily as mineral dust. The solid line indicates the threshold at which homogeneous nucleation (HOM) can take place. During HOM nucleation, ice crystals form without the need of INP. The thresholds are also explained in Sect. 3.5.

In Fig 4.1a it is shown, that the studied cirrus clouds over the midlatitudes reach temperatures down to 207 K. The bulk of the in-cloud data points is distributed around the ice saturation threshold (RHi =100 %), throughout the whole temperature range. Interestingly, the distribution appears to be bimodal. One peak is located at a temperature of 225 K and an RHi of 100 % and the other can be seen at a temperature of 218 K and 79 % RHi. Focusing on the supersaturated part and looking into the different ice nucleation regimes, it is evident that most of the supersaturated in-cloud data are found at low supersaturation in the HET regime. For colder temperatures between 218 K and 223 K there is a slight increase in the supersaturated data reaching up to the activation threshold of coated soot. This threshold is rarely exceeded and even less data points are detected with supersaturations that would allow HOM nucleation to take place.

Moving on to Fig. 4.1b and the results of the statistical analysis of RHi for the cloud-free area around cirrus, it is clear that the majority of the data points are detected below the activation threshold for HET nucleation on mineral dust and predominantly also below ice saturation. The MD activation threshold is more frequently reached for temperatures between 230 K and 213 K. The probability densities for supersaturations up to the CS activation threshold are generally low throughout the temperature range, although more data points reach up to higher supersaturations at colder temperatures. The probability of detection for RHi over the high HET and HOM thresholds is very low. A characteristic comma shape at very low supersaturations reaching down to 0% with high probability densities is also seen in Fig 4.1b. This shape was also present in the analysis of the individual clouds and was commonly accompanied by an increase in temperature. Based on this information, it is probably generated by data points measured in the stratosphere around cirrus with a high cloud top. Alternatively, it could be indicative of airmasses in the upper troposphere having a constant water vapor mixing ratio around 1.5 ppmv for a wide temperature range (Krämer et al., 2009).

In the following a more quantitative approach of the RHi distribution is presented in Table 4.1, which includes the RHi mode i.e. the most commonly appearing value, as well as the percentage of detected data points in distinct supersaturation regimes. More specifically, following the same thought process as in Fig. 4.1, three RHi bins are defined: 100 %–120 %, 120 %–140 % and $>$ 140 %. The first two represent HET nucleation by easily and not easily activated INPs and the third one, RHi $>$ 140 % can be considered an approximate threshold over which HOM nucleation is possible (Koop et al., 2000; Haag et al., 2003; Comstock et al., 2004; Khvorostyanov and Curry, 2009; Kärcher, 2012). A detailed description of these regimes is provided in Sect. 3.5. Table 4.1 showcases the results for the analysis of the whole data set including all measured cirrus as well as two groups containing cirrus with different origin, in-situ formed and liquid origin as described in Sect. 3.8.1.

The whole data set, containing all measured midlatitude cirrus clouds, consists of more than 3.2 million RHi data points. The mode value of the RHi distribution in the in-cloud area is 96 %. 34 % of all in-cloud data are supersaturated with respect to ice. Of these, the majority has low supersaturations. 30.3 % are in the RHi regime between 100 % and 120 %. Only 3.3 % of the data present with supersaturation in the high HET regime (RHi 120 % - 140 %) and an even smaller 0.5 % are in the HOM regime (RHi $>$ 140 %). The cloud free area data set consists of almost 3 million data points and has a mode value of the RHi distribution of 68 %. Supersaturation is detected for 6.8 % of the measured data. The majority, 5.7 %, are once again found in the low

HET regime up to 120 % RHi. 1 % of the data has an RHi between 120 % and 140 % and a mere 0.2 % of the data have RHi exceeding 140 %.

It should be kept in mind that for this dataset the calculated individual RHi values have a maximum uncertainty of 10 - 15% as described in Sect. 3.6. This could lead to misclassification of datapoints into the wrong RHi range. However, it can be assumed that the temperature deviations causing this uncertainty are random and there is no temperature range systematically over- or underestimated and thus no RHi range reaches this maximum uncertainty when compared to another.

Table 4.1: Results from the analysis of the probability density functions (PDF) of RHi. RHi mode: most common value of dataset.

	In-cloud			Cloud-free air adjacent to		
	All clouds	In-situ formed	Liquid origin	All clouds	In-situ formed	Liquid origin
# of data points	3,204,381	1,110,675	2,093,857	2,762,080	948,638	1,813,300
RHi mode [%]	96	96	96	68	56	84
RHi PDF [%]						
≥ 100 %	34.1	30.8	36	6.8	5.7	7.5
RHi PDF [%]						
100 % - 120 %	30.3	26.8	32.3	5.7	4.5	6.3
120 % - 140 %	3.3	3.4	3.3	1	1.1	1
≥ 140 %	0.5	0.6	0.5	0.2	0.2	0.2

4.1.2 The vertical structure of RHi in midlatitude cirrus

An important aspect of every cloud is its vertical structure. To study it, I defined the cloud top and cloud base heights for each measured cloud at each timestep. Then I split each cloud into percentiles, each representing a horizontal slice of the cloud. Each data point is grouped into a percentile based on its relative distance to the cloud top. The 10^{th} percentile indicating 10 % of the cloud's total depth, 50^{th} percentile being down to cloud middle and 100^{th} percentile the cloud base. This way the absolute altitudes and individual cloud depths are removed as factors and the vertical structure can be studied universally. Each cloud slice/percentile contains a certain amount of data points with various RHi values. These values are distributed in the bins defined in

Sect. 3.5 and Fig. 3.10, representing the subsaturated (RHi < 100 %), low HET (100 % < RHi < 120 %), high HET (120 % < RHi < 140 %) and HOM (RHi > 140 %) regimes. The results of this analysis are shown in Fig. 4.2.

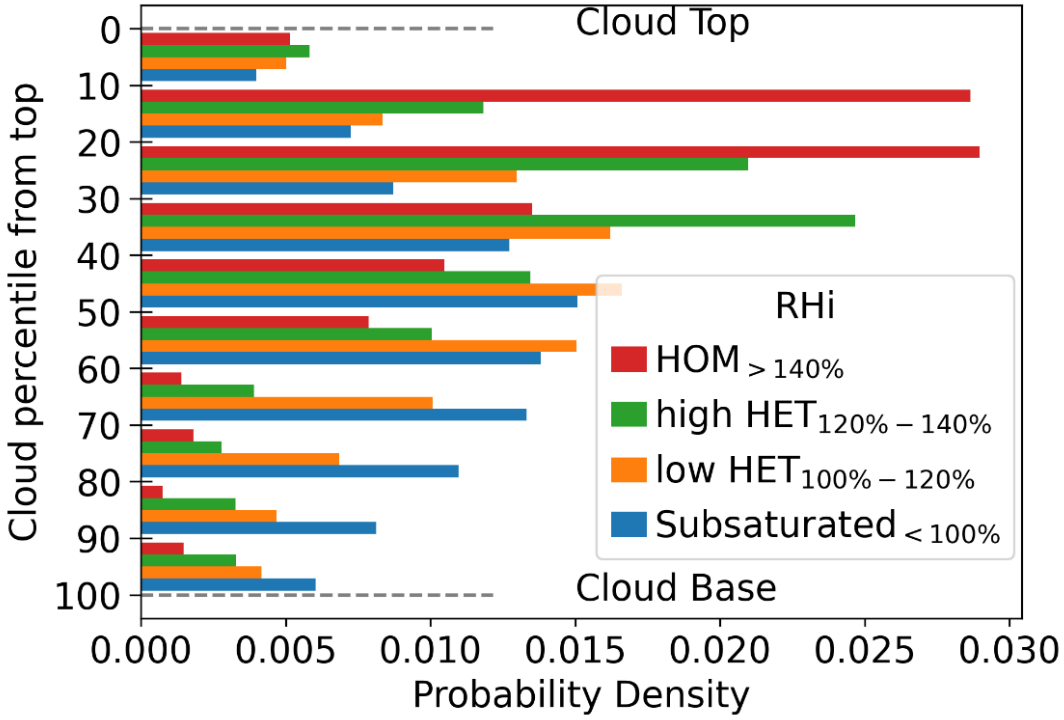

Figure 4.2: Probability densities of RHi as a function of location relative to cloud top. For every cirrus the cloud top and base are defined. From these each cloud is split into percentiles i.e. zones each representing an additional 10 % of total cloud depth starting from the cloud top. The RHi values included in each percentile are grouped into four bins: RHi < 100% or subsaturated data, RHi 100% - 120 % representing the low HET regime with easily activated INP, RHi 120% - 140 % representing the high HET regime with INP needing higher supersaturations to become activated and RHi > 140 % including supersaturations that would allow HOM nucleation. Example: the bin from the 20$^{\text{th}}$ to the 30$^{\text{th}}$ percentile contains the probability of occurrence of RHi in four bins in a slice of the cloud located 20 % to 30 % of the distance between cloud top and cloud base.

The topmost layer of the measured clouds appears to be populated mainly by supersaturated RHi with similar probabilities for the three regimes representing the low and high HET and HOM nucleation. The cloud top area of the clouds from 10 down to 30 % cloud depth consists predominantly of high supersaturations reaching values over 140 %, which would suffice for HOM nucleation to take place. From there the probability density of the HOM regime gradually decreases while subsequent lower RHi regimes become dominant. More specifically, from 30 % to 40 % cloud depth RHi values in the HOM regime remain frequent, but it is the high HET regime that is the most frequent. Around cloud middle, from 40 to 60 % of the total cloud depth, the low HET regime becomes the most dominant. From there and down to cloud base supersaturation

becomes gradually less frequent, especially on the higher end of the RHi range, and the clouds become predominantly subsaturated.

The structure described above indicates that nucleation of new ice crystals likely takes place near the cloud top. The subsaturated cloud base is a sign that ice crystals are capable of surviving over longer periods of time in a subsaturated environment before completely melting or sublimating. The rather distinct layering of RHi in the clouds can be interpreted as a result of weak mixing inside them with a slight updraft supplying moisture to the upper levels for new ice formation and the heavy ice crystals subsequently falling due to gravity.

4.1.3 In-situ and liquid origin cirrus over the midlatitudes

As already discussed in Sect. 3.8.1, midlatitude cirrus clouds can be characterized as in-situ formed or liquid origin, depending on their formation process. In-situ cirrus form directly as ice clouds at high altitudes, whereas liquid origin cirrus stem from a liquid predecessor cloud. Depending on the origin of the clouds, in-situ or liquid, different nucleation processes might have taken place resulting in clouds with different properties and effects. In order to investigate this, the cirrus clouds measured during the ML-CIRRUS campaign were separated into the two groups and a statistical analysis was performed. The results of this analysis are presented hereafter.

Distribution of RHi

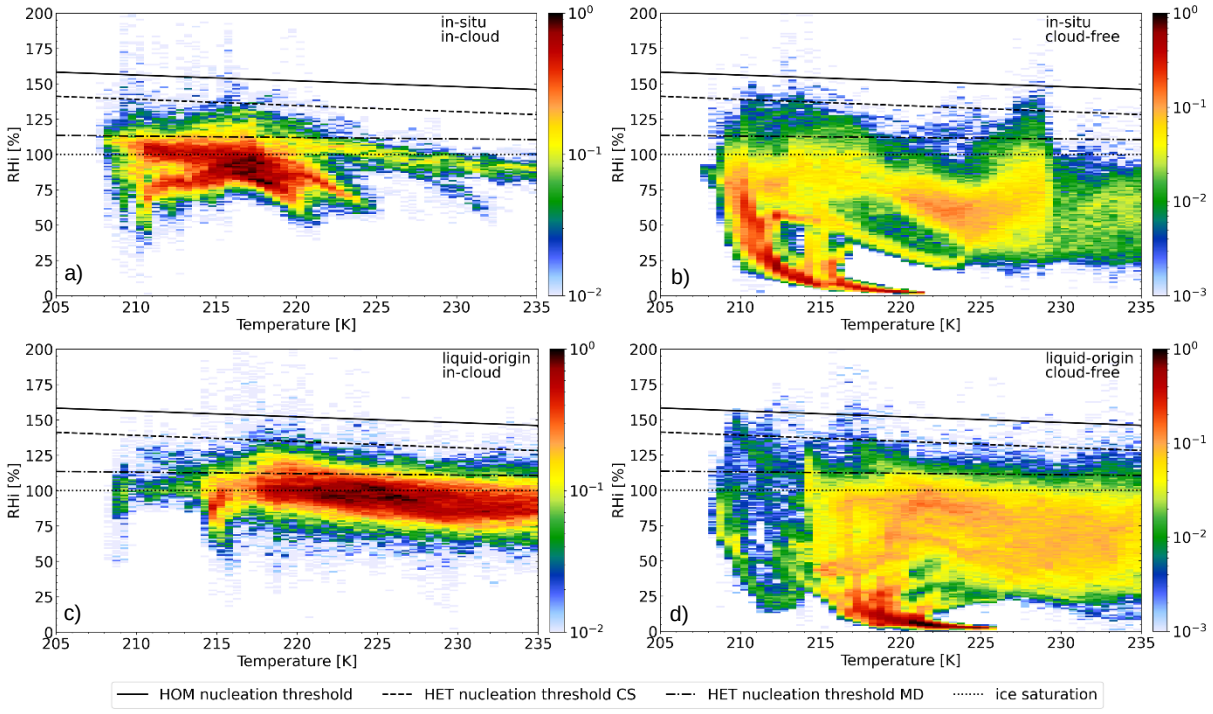

Figure 4.3: PDFs of RHi with respect to ambient temperature. a) in-situ in-cloud data points. b) cloud-free data points around in-situ cirrus. c) liquid-origin in-cloud data points. d) cloud-free data points around liquid-origin cirrus. For a detailed explanation of the plots and thresholds see Fig. 4.1 and Sect. 3.5.

Fig. 4.3 consists of four panels depicting the probability densities of RHi with respect to ambient temperature for the in-cloud and cloud free areas of the in-situ formed and liquid origin clouds respectively. Each panel also includes the ice saturation threshold, as well as two HET and one HOM nucleation thresholds. These have been described in detail in Sect 3.5. Cloud-free air can evidently not be classified as in-situ or liquid origin, despite that the terms in-situ and liquid origin cloud-free are used for simplicity to describe the air adjacent to in-situ and liquid origin clouds respectively.

Starting with the results of the analysis for the in-situ cirrus in-cloud region (Fig. 4.3a), it is evident that they are more frequently measured at temperatures below 225 K. The probability density is the highest for temperatures between 215 K and 218 K and RHi between 70 % and 100 %. The peak of the distribution is at 217 K and an RHi of 90 %. Interestingly, there is a high probability density for RHi below saturation. Supersaturation is mostly found for temperatures below 220 K but RHi values remain predominantly below the low HET threshold. The liquid origin cirrus on the other hand are mostly measured at warmer temperatures above 214 K (Fig. 4.3b). The highest probability densities are detected for temperatures between 221 K and 227 K and RHi between 90 % and 105 %. The peak of the probability density is at 225 K and 100 % RHi. Most of the liquid origin in-cloud data have RHi values around saturation. Supersaturations up to the low HET level are frequent almost throughout the whole temperature range. The high HET threshold is reached more frequently than for the in-situ formed cirrus but probabilities still remain low.

Comparing Fig. 4.3a and c with Fig. 4.1a, it becomes evident that the two peaks noted in the RHi distribution of the whole dataset, closely resemble the in-situ and liquid origin cirrus types. In-situ cirrus being colder than liquid origin but the latter being more frequently supersaturated.

Regarding the cloud-free data points around in-situ cirrus (Fig. 4.3b), they reach temperatures as low as 207 K and are mostly subsaturated. The cloud-free data points in the vicinity of liquid origin cirrus are mostly measured in warmer temperatures, above 215 K (Fig. 4.3d). RHi once again remains mostly below saturation. Contrary to the in-situ cirrus, supersaturations up to the MD activation threshold are somewhat frequently detected. The structure resembling a coma, seen on the cloud-free areas of both the in-situ and liquid origin cirrus most probably stems from data measured in the stratosphere or the tropopause as has already been discussed in Sect. 4.1.1.

The distributions presented in Fig. 4.3 are complimented by the statistics in Table 4.1, providing also a more quantitative perspective. Delving directly into the supersaturation percentages, it is shown that around 31 % of the in-situ and 36 % of the liquid origin in-cloud data points are supersaturated with respect to ice. This difference is localized mostly in the lower supersaturation range for RHi below 120 %, where 32 % of the liquid origin in-cloud data are found compared to almost 27 % of the in-situ. For higher supersaturations in the high HET and HOM regimes the differences between the two cirrus types are minimal. 3.4 % of the in-situ and 3.3 % of the liquid origin cirrus have RHi values between 120 % and 140 % and for RHi over 140 % the probabilities are 0.6 % and 0.5 % respectively.

A similar picture is painted for the cloud-free areas around in-situ and liquid origin cirrus. The cloud-free air around liquid origin cirrus is more frequently supersaturated, 7.5 % compared to in-situ, 5.7 %. The difference is once again greatest in the low HET regime with 6.3 % and 4.5 % for liquid origin and in-situ respectively. 1.1 % of the in-situ cloud-free data and a similar 1 % of the

liquid origin have RHi values from 120 % to 140 %. A mere 0.2 % for both in-situ and liquid origin cloud free data is found in the HOM regime.

For the statistical analysis and the results presented in Fig. 4.3 and Table 4.1, a maximum uncertainty of 10 - 15% for the calculated individual RHi values should be kept in mind, as already described in Sect. 3.6. This uncertainty stems from the used temperature fields in the calculation of the RHi. Assuming, that ECMWF does not systematically over- or underestimate the temperatures for in-situ formed or liquid origin clouds, the statistics for the two cloud types are subject to the same random error making the distributions comparable. Following the same assumption, that the temperature deviations causing the uncertainty occur randomly for various clouds measured during the different research flights, the uncertainty for the distribution is further reduced. Given that 12 lidar legs with in-situ clouds and 13 with liquid-origin clouds are analyzed, the error for the mean value of the distribution for the two cloud types for example reduces to 4.3 % and 4.2 % respectively.

Comparison of the vertical structure of RHi in in-situ and liquid origin cirrus

In Figure 4.4 the vertical distribution of RHi within in-situ formed and liquid origin cirrus is presented in a manner same to what was explained in Sect 4.1.2, Fig. 4.2. At first glance the two distributions look similar to each other and to the one shown in Fig. 4.2. The cloud tops for both cloud types are mostly supersaturated, frequently including RHi values in the HOM regime. These high RHi gradually become less frequent while the high HET, low HET and subsaturated regimes gradually take over moving towards the cloud base.

A more careful analysis however reveals some differences between the two cirrus types. Starting from the cloud tops, the first 10 % for the liquid origin clouds are supersaturated, including an almost equal probability of RHi in all three supersaturated regimes. For the in-situ formed cirrus on the other hand the cloud top is a mixture of sub- and supersaturated RHi, including values over 140 % and under 100 %. From 10 % down to 30 % cloud depth both cirrus types are dominated by very high supersaturations in the HOM regime. While the high HET regime becomes dominant in the next section from 30 % to 40 % cloud depth. Around cloud middle, 40 % to 60 % cloud depth, the characteristics of the two cirrus types differ. While liquid-origin cirrus continue the expected behavior, i.e. the low HET regime taking over as the most dominant, in-situ formed cirrus appear to become mainly subsaturated with a marginally higher frequency compared to the low HET regime. Continuing deeper towards the cloud base, liquid origin cirrus still follow the expected tendency and become subsaturated. In-situ formed cirrus on the other hand remain marginally dominated by the subsaturated regime closely followed by the low HET down to 80 % cloud depth, at which point the low HET regime becomes dominant with the subsaturated having a slightly lower probability density.

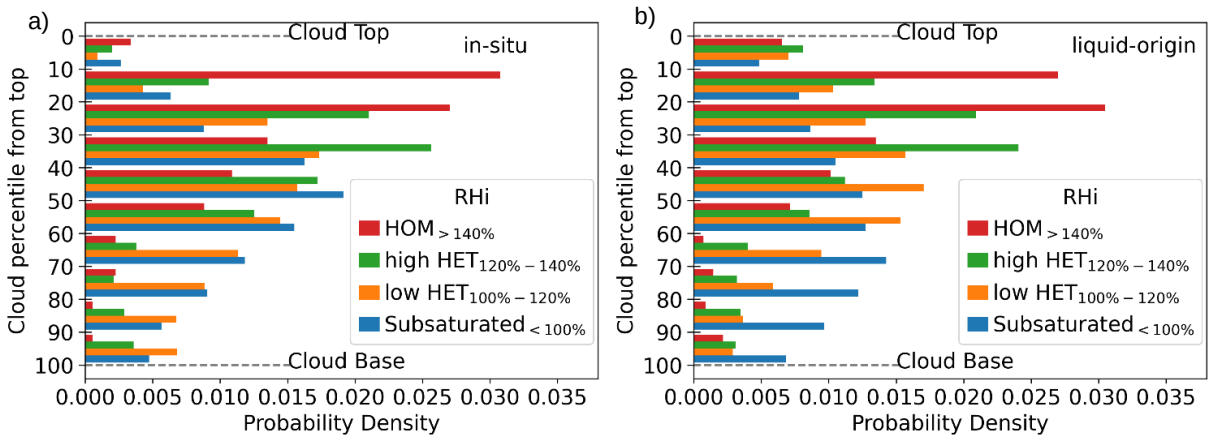

Figure 4.4: Probability densities of RHi in relative location to cloud top. a) in-situ formed clouds. b) Liquid origin clouds. A description of these type of plot is given in Fig. 4.2 and Sect. 4.1.2.

4.1.4 Relative humidity in different cloud evolution stages

During some missions of the ML-CIRRUS campaign, specific cloud systems were targeted and probed over an extensive period of time. This provided an opportunity to study the temporal evolution of cirrus clouds and more specifically the changes in RHi through various stages of the cloud's lifetime. Here I present, two cases where the flight strategy allowed for this type of analysis.

Case 1: Mesoscale Convective System

The first case consists of lidar legs 1 and 2 of Mission 6 of the campaign conducted on 29/03/2014 over the West Mediterranean. Measured during these legs was a multicell thunderstorm evolving into a Mesoscale Convective System (MCS). The flight was conducted in such a way that young, mature and dissipating clouds of the same system were measured. Further details on the mission can be found in Sect 3.3, Table 3.4 and Voigt et al., 2017, their Table 3.

In Fig. 4.5 the BSR curtains captured by WALES during this mission are presented. Leg 1 is further split into two parts representing different cloud evolutionary stages. The first part (p1) contains young newly formed cells and the second part (p2) contains the central mature cell of the system. On leg 2, a third part is identified (p3) which includes the aged dissipating clouds in the outflow of the system. The temporal jump between the two legs is due to in-situ measurements that were performed requiring HALO to fly inside the clouds at lower altitudes where lidar measurements were not possible.

For each one of the three parts of this cloud system, the frequency distribution of RHi was calculated. Additionally, in order to gain insights on the characteristics of the vertical structure inside the clouds during their lifetime, each part was split into slices with a depth of 500 m. The RHi distributions were also calculated for each layer. The total, as well as the vertically layered RHi distributions for each part are presented in Fig. 4.6.

The first part of this multicell thunderstorm (p1), which includes the young newly formed cells, has an overall RHi mode of 95 % and a positive skewness of 1. High supersaturations reaching over the usual threshold for HOM nucleation are measured. With respect to the vertical structure, the very top of the young cells is dominated by very high supersaturations. Deeper into these clouds the mode of the RHi distributions gradually drops to saturation and slightly below at cloud base.

The main cell of the system (p2), has an RHi mode of 118 % and a skewness of 2.7. The majority of the data are supersaturated and reach high RHi values in the HOM regime. Unfortunately, only a few layers of this cell could be measured with the lidar. They all share similar RHi distributions with high supersaturations. Judging from Fig. 4.2 and 4.4, the lower parts of the cloud, which are missing here, would be the ones probably with lower supersaturations or even subsaturation. The absence of measurements in these lower cloud layers might explain the very high RHi values of the main cell.

Finally, the third part (p3) including the aged dissipating clouds of the system has an RHi mode at around saturation and no skewness. High supersaturations allowing for nucleation of new ice crystals are present but a large part of these clouds is subsaturated indicating dissipation, Through the vertical layers the modes of the distributions move gradually from supersaturation to subsaturation, while the shape of the distributions remains similar, near Gaussian.

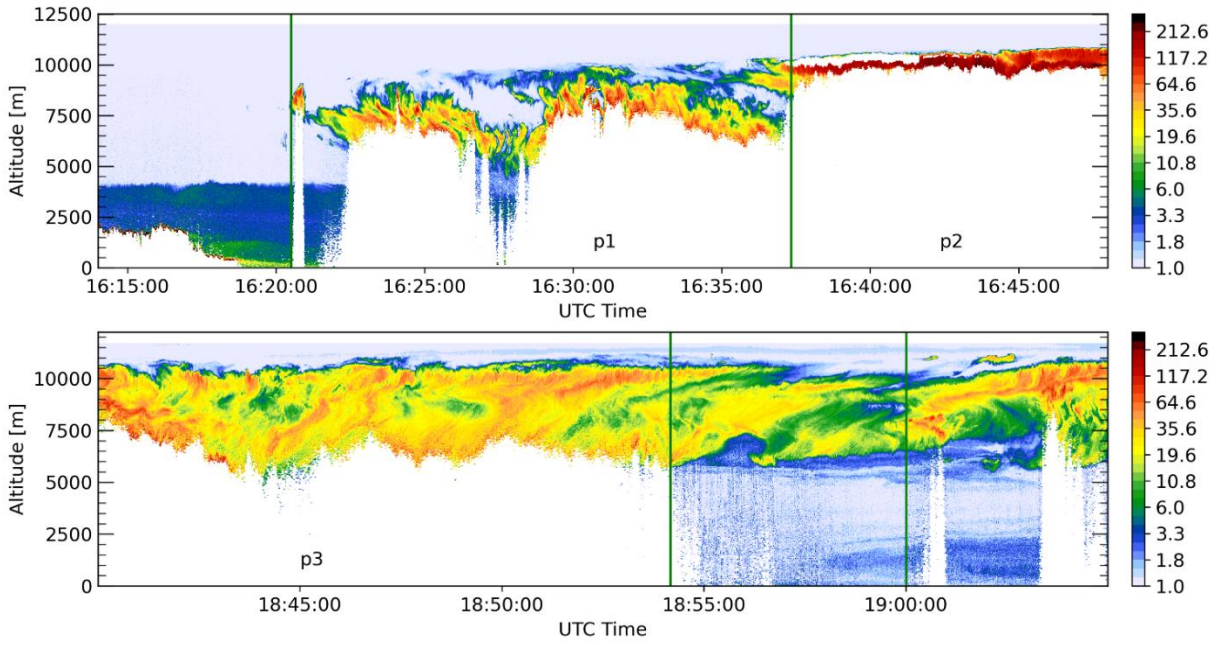

Figure 4.5: Backscatter Ratio (BSR) measured by WALES Lidar at 532nm (color-coded). Two lidar legs performed during Mission 6 of the ML-CIRRUS campaign on 29/03/2014 over the West Mediterranean, depicting a mesoscale convective system. P1 contains two towering convective cells. P2 contains the main convective cell. P3 depicts the outflow of the system. The white regions at cloud top are a result of saturation of the detector. The clouds in p1 and especially p2 are not fully depicted and only the top portions of the cloud could be measured by the lidar system.

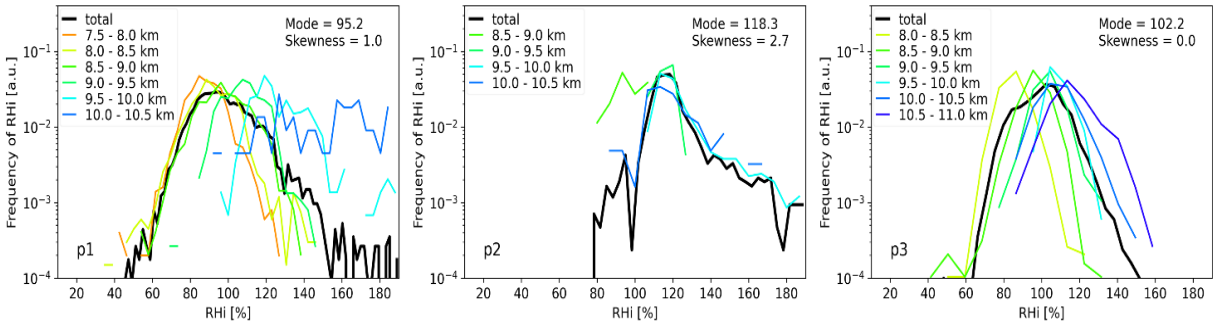

Figure 4.6: PDF of in-cloud RHi in vertical layers with 500m depths from cloud base to cloud top. p1) Young cells, p2) Mature main cell and p3) Aged cell. The cloud parts are in accordance to Fig. 4.5. The number of layers for each part differs depending on the geometrical depth of the measured cloud.

Case 2: Warm Conveyor Belt

The second case chosen to be analyzed was performed following a flight strategy specifically selected to study the evolution of airmasses with time. More precisely, the case is the lidar leg of Mission 14 of the campaign conducted on 11/04/2014 over the United Kingdom and Belgium (Sect 3.4, Table 3.4 and Voigt et al., 2017, their Table 3). The targeted system was the outflow of a warm conveyor belt (WCB). To study the evolution of this system, a quasi-Lagrangian approach was selected. The flight path of the aircraft coincided with the movement and evolution of the cloud system, by following the geopotential lines of the WCB, thus allowing for the measurement of clouds from a single system over time.

The BSR curtain of the WCB as measured by WALES is shown in Fig. 4.7. Once again, the curtain is split into three parts, p1, p2 and p3. Since HALO conducted this flight starting near the center of the WCB where cloud formation is stronger, moving to the edge of the system along the axis of the outflow, p1 is considered to be younger and p3 the oldest, including clouds that have formed many hours earlier. The total and layered RHi distributions are once again calculated for layers with a 500 m depth, between cloud base and cloud top. The results are presented in Fig. 4.8.

P1 of the WCB outflow, has an RHi mode of 95.5 % with a positive skewness of 1.5. High supersaturations are reached especially on the upper layers of the system. The second, slightly older part (p2) has a slightly lower RHi mode around 94 % with no skewness. The vertical structure is rather uniform throughout the cloud with modes around saturation or slightly subsaturated and near zero skewness throughout. Only low supersaturations are detected throughout the cloud. Finally, p3, the furthest from the center of the system and thus oldest, has a subsaturated mode of around 83 % and a slightly negative skewness of -0.3. Vertically the layers are similar to each other as well as the overall RHi distribution.

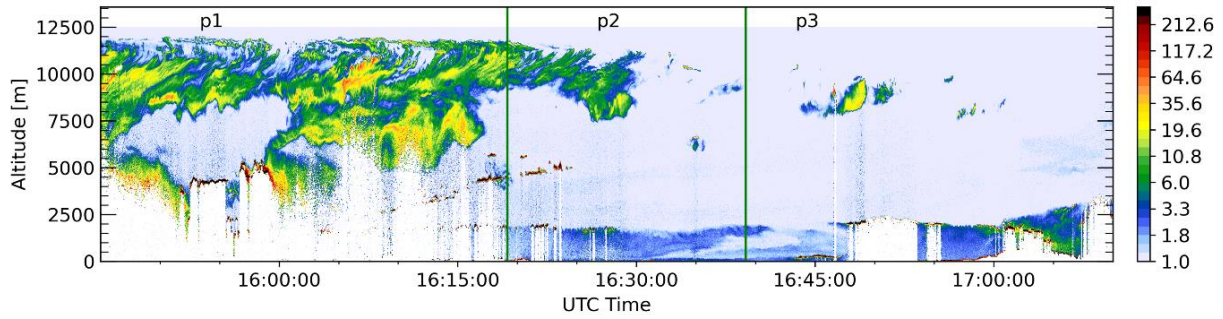

Figure 4.7: Backscatter Ratio (BSR) measured by WALES Lidar at 532nm (color-coded). Measurement performed during Mission 14 of the ML-CIRRUS campaign on 11/04/2014 over the United Kingdom and Belgium, depicting the outflow of a Warm Conveyor Belt (WCB). The flight was conducted in a semi-Lagrangian manner, following the axis of the evolution of the system. P1, P2 and P3 include clouds in different phases of aging from young to old, respectively.

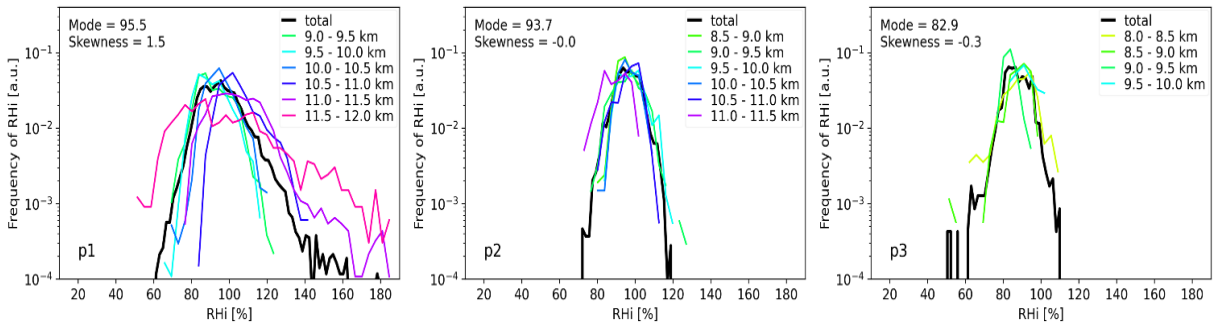

Figure 4.8: PDF of in-cloud RHi in vertical layers with 500m depths from cloud bottom to cloud top. From left to right p1-Young phase, p2-Mature phase and p3-Dissipating phase, in accordance to Figure 4.7. The number of layers differs depending on the depth of the cloud.

4.2 Characteristics of supersaturation of cirrus clouds over the arctic

The arctic is a region significantly different to the midlatitudes. Less dynamical systems, less air traffic density, less aerosol emissions and moisture and colder temperatures are some of the differences. Despite that, cirrus clouds still play an important role over the arctic. It is speculated that they are a contributor to the phenomenon of arctic amplification, i.e. the accelerated warming of the arctic over the past decades. Many questions regarding the formation processes of cirrus in the cold, clean and dry arctic environment, their properties, their effects and feedback processes remain open.

In this rather stable region where, as already mentioned dynamical weather systems are rare, warm air intrusions (WAI) can quickly and dramatically change the ambient conditions. During a WAI event, warm, moist and aerosol rich airmasses are meridionally transported into the arctic from the midlatitudes. The dramatic change in ambient conditions is likely also affecting the cirrus clouds that form there. Unfortunately, the arctic is a region where studies of cirrus clouds are not easily performed and especially the effects of WAI on high latitude cirrus clouds are largely unknown. I used the measurements conducted during the HALO-(AC)^3 campaign in order to study high latitude cirrus clouds under these two different conditions and present my findings in the following.

4.2.1 Distribution of RHi in and around cirrus over the arctic

During the HALO-(AC)^3 campaign the WALES lidar system was used to measure cirrus clouds in the arctic. The collected data were analyzed and the results of this analysis are presented in this and the following subsections. They are presented in a fashion similar to the analysis of midlatitude clouds in Sect 4.1, in order to warrant an easier comparison between the cirrus detected over the two regions. Thus, once again first a statistical analysis of the whole data set, is provided, allowing for a general description of RHi within and around cirrus clouds in the high arctic.

As described in Sect. 3.7, a cirrus cloud mask is applied on each lidar curtain/measurement defining an in-cloud, near-cloud and cloud-free area. Fig. 4.9 contains the probability densities of RHi with respect to the ambient temperature for the three areas. Understanding of the presented results is aided by four thresholds included on each panel. These are the ice saturation threshold at RHi = 100 %, over which ice crystals may form and persist, the activation thresholds for heterogeneous nucleation on mineral dust (MD) and coated soot (CS), as well as the threshold for homogeneous nucleation (HOM). Details on these thresholds are provided in Sect 3.5.

The in-cloud data of the cirrus measured in the arctic, cover a temperature range between 200 K and 265 K (Fig. 4.9a). The distribution resembles a band along almost the whole temperature range. The lower end of this band is at an almost temperature independent RHi of 80 %. The upper limit closely follows the angle of the activation threshold for CS. Higher supersaturations are detected at lower temperatures. The majority of the data is found for temperatures between 218 K and 258 K at around RHi saturation. The maximum of the probability density is at a temperature of 246 K and an RHi of 99%.

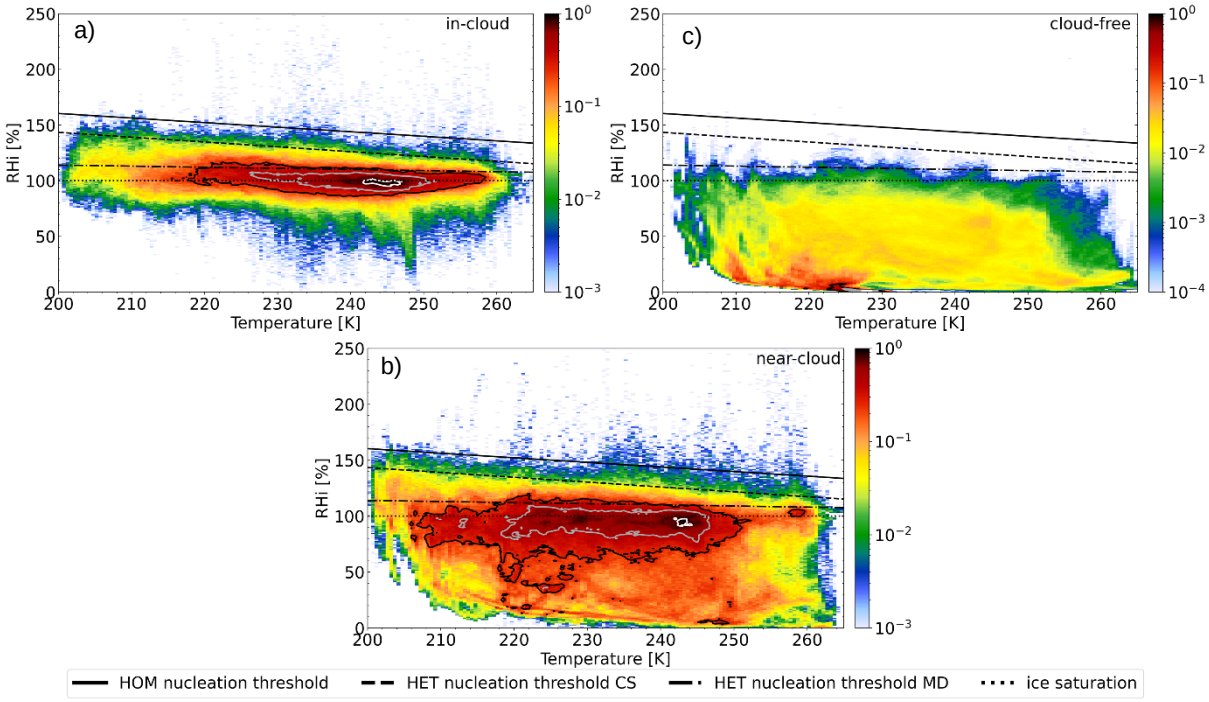

Figure 4.9: Probability densities of the Relative Humidity over ice (RHi) with respect to ambient temperature. Calculated for the data points in the: a) in-cloud area b) near-cloud area c) cloud-free area. The bin sizes are 0.5 K and 1 % RHi. The dotted line depicts the ice saturation threshold at RHi = 100 %. The dash-dotted line is the low threshold for heterogeneous nucleation (HET). The ice nucleating particle (INP) for this threshold corresponds to mineral dust (MD), which is efficient as an initiator of ice formation. The dashed line represents the high threshold for HET nucleation. Here the INP corresponds to coated soot (CS), which is not activated as easily as mineral dust. The solid line indicates the threshold over which homogeneous nucleation (HOM) can take place.

Supersaturation is detected almost throughout the whole temperature range, with higher RHi found at lower temperatures. Most of the supersaturated data are found up to the activation threshold for MD and also with a high probability of detection. RHi values up to the activation threshold of CS are also frequently detected. It is remarkable how well the RHi distribution follows the angle of the CS activation threshold. The probability density drops sharply for RHi values closer to the HOM threshold.

The near-cloud area immediately bordering the cloud edges is an interesting and active region. The probability density of RHi with respect to ambient temperature in this region is plotted in Fig. 4.9b. The temperature range is same to the in-cloud data and so is the shape of the distribution on the supersaturated end. The distribution matches the angle of the higher HET threshold frequently also exceeding it. A striking difference to the in-cloud data is that the majority of the distribution here is subsaturated frequently reaching very low values down to 0 % RHi. The

maximum probability density is found at an RHi of 95 % and a temperature of 243 K, very close to that of the in-cloud data.

Despite the large amount of subsaturation, supersaturation is also frequent and in fact similar to the in-cloud and even more frequent. Supersaturation is found almost throughout the whole temperature range. At lower temperatures higher RHi are detected with the distribution once again being shaped along the angle of the activation threshold for CS. This threshold is also regularly exceeded but with a lower frequency.

The data collected in the cloud-free areas around cirrus clouds are as expected mostly subsaturated (Fig. 4.9c). The maximum of the probability density is found at a mere 1 % RHi and a temperature of 228 K. Supersaturation is very rare and is practically limited to below the activation threshold of MD.

A more quantitative perspective on the distribution of RHi for the in-cloud, near-cloud and cloud-free areas of cirrus measured in the arctic, is included in Table 4.2. There I confirm that more than half of the in-cloud data, and more specifically 55.92 %, are supersaturated. The majority of the supersaturated data are in the regime of HET nucleation and more precisely in the lower bin of this regime. 52.02 % are found with RHi $<$ 123 % and 3.75 % between RHi 123 % and 147 %. The HOM regime is the least populated with a probability of 0.15 %.

The near-cloud data have a supersaturation probability of 23.4 %, but a pattern similar to the in-cloud data is followed. The bulk of the supersaturated data is located in the low HET regime (probability 21.04 %). In the high HET regime, the probability of detection is at 2.17 % and 0.19 % of the data are found in the HOM regime. Finally, the cloud-free data have a very low probability of supersaturation at 0.68 %, which is almost exclusively found in the low HET regime (0.66 %). RHi probability in the high HET regime is just 0.02 % and in the HOM regime it is practically zero.

Table 4.2: Probabilities of RHi for the in-cloud, near-cloud and cloud-free regions of the cirrus clouds measured during the HALO-(AC)^3 campaign.

	In-cloud	Near-cloud	Cloud-free
# of data points	1,629,592	2,829,912	5,996,555
RHi supersaturation probability [%]			
RHi ≥ 100%	55.92	23.4	0.68
RHi probability [%]			
HET (100 % - 147 %)	55.77	23.21	0.68
Low HET (100 % - 123 %)	52.02	21.04	0.66
High HET (123 % - 147 %)	3.75	2.17	0.02
HOM (≥ 147 %)	0.15	0.19	0.00

4.2.2 Vertical structure of supersaturation in arctic cirrus clouds

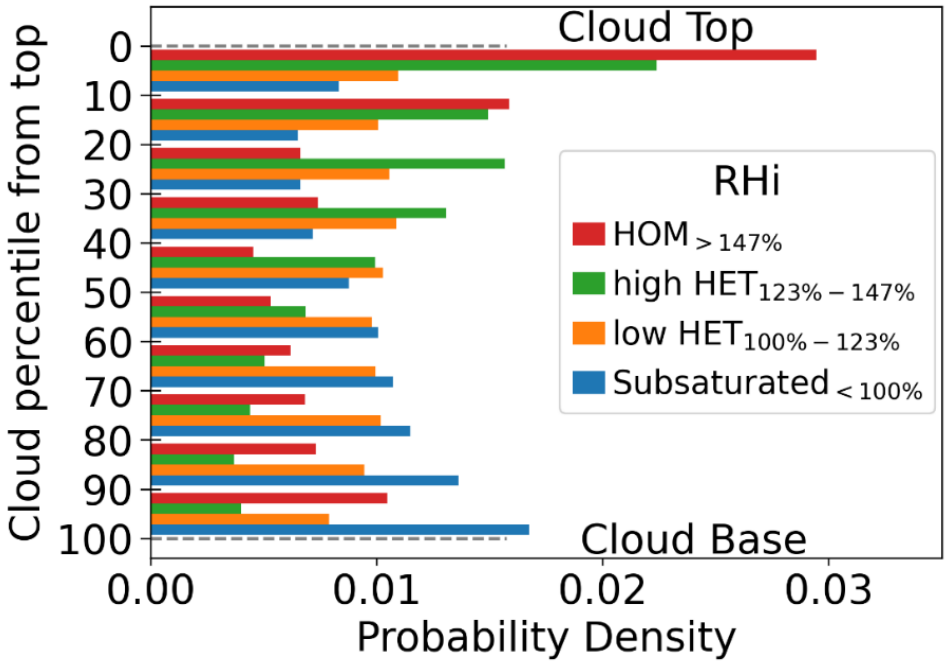

Figure 4.10: Probability densities of in-cloud RHi in a relative location to the cloud top for all cirrus measured in the arctic during the HALO-(AC)^3 campaign. Every cloud is split into ten percentiles from cloud top to cloud base and for each percentile the probability densities of each RHi are calculated in four RHi bins. Details regarding the RHi bins and overall explanation of this type of plot can be found in Sect. 3.5.

Fig. 4.10 showcases the vertical distribution of RHi within the cirrus clouds measured in the arctic. For each timestep of every measurement, the cloud top and base are defined based on the cloud mask. The total dept of each cloud is split into percentiles, leading to horizontal slices of the cloud, each containing 10% of the in-cloud data, at a different cloud depth. The probability densities for the RHi in each slice are calculated in four bins representing the ability of different nucleation processes to take place: subsaturated (RHi $<$ 100 %), low HET (100 % $<$ RHi $<$ 123 %), high HET (123 % $<$ RHi $<$ 147 %) and HOM (RHi $>$ 147 %).

From Fig. 4.10, it is evident that the cloud tops of the cirrus measured in the arctic, down to a cloud depth of 20 %, are mostly populated by data with high supersaturations warranting HOM ice nucleation while the bins with lower RHi have progressively lower probabilities. From there and down to 40 % cloud depth, RHi is mostly detected in the high HET regime. At around cloud middle, 40 to 50 % cloud depth, supersaturation is still the most dominant but RHi in the low HET regime becomes slightly more probable followed by the high HET regime. From cloud middle and down to cloud base subsaturation becomes increasingly more dominant. Interestingly the probability density for RHi in the HOM regime also steadily increases again below cloud middle and even becomes significant at cloud base.

4.2.3 Cirrus clouds in the arctic under AC and WAI conditions

Warm Air Intrusions (WAI), the meridional transport of warm, water-vapor- and aerosol-rich airmasses into the arctic from the midlatitudes, are identified as one of the contributors to arctic amplification, i.e. the accelerated warming of the arctic. They transfer sensible heat and great amounts of water vapor -a strong greenhouse gas- into the arctic and thus can lead to an altering of the characteristics of the arctic troposphere, potentially also affecting the cirrus clouds that form there (Doyle et al., 2011; Stramler et al., 2011; Park et al., 2015; Woods and Caballero, 2016; Binder et al., 2017; Dahlke and Maturilli, 2017; Liu et al., 2018; Pithan et al., 2018; Hartmann et al., 2019, 2021; Beer et al., 2022; Dada et al., 2022). In order to study these effects on the arctic atmosphere and cirrus, I classified each research flight of the HALO-(AC)^3 campaign and the respective cirrus clouds as either being measured under undisturbed arctic (AC) conditions (AC cirrus) or during WAI conditions (WAI cirrus). The flight tracks and measured water vapor for the two groups are shown in Fig. 4.11. Details on the campaign and methodology are provided in Sect 3.4.

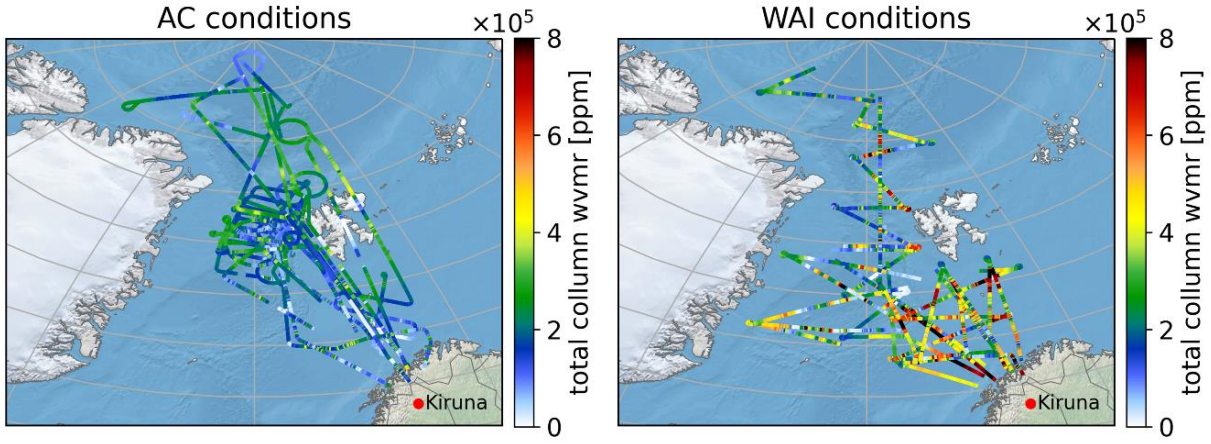

Figure 4.11: Maps containing the total column water vapor mixing ratio measured along the flight tracks of the research flights conducted during the HALO-(AC)^3 campaign. **Left:** Flights conducted under undisturbed arctic conditions (AC). **Right:** Flights conducted during an active Warm Air Intrusion (WAI) event. Background map tiles, borders and coastlines from Natural Earth (naturalearthdata.com). License: Public domain.

The high arctic under AC and WAI conditions

A first step to understanding how the characteristics of cirrus clouds in the arctic are altered during a WAI, is to study how the ambient conditions change during such events. For this, I used the water vapor mixing ratio measurements performed by WALES along the flight tracks, as well as the temperature and water vapor data from the ERA-5 reanalysis dataset. I defined a box with coordinates -30 E to 30 E and 70 N to 85 N in which the HALO-(AC)^3 campaign flights were performed and calculated the means for each of the two groups: AC and WAI. For the temperature data from ERA-5 the pressure levels at 250, 500, 850 and 100 hPa were used. For the vertical

information on the water vapor mixing ratio from WALES, 3-km deep layers from 0 to 12 km altitude were defined. The results from the analysis of the water vapor and temperature data from WALES and ERA-5 are presented in Table 4.3.

Starting with the total column water vapor and temperature data from ERA-5, it is confirmed that, during WAI events the high arctic is on average warmer and contains higher amounts of water vapor. More specifically, the average total column water vapor in the area of interest doubles from 3.4 to 6.9 $kg \cdot m^{-2}$ during AC and WAI conditions respectively. As for the temperature, an average surface warming of 10 K is detected during WAIs. From near surface and up to the 500 hPa level, WAIs cause on average warming, the magnitude of which gradually becomes smaller. At the 250 hPa level a cooling by 3 K is detected for the WAI group.

The water vapor measurements from WALES are in accordance with the findings from the ERA-5 data. A mean water vapor mixing ratio of 888 ppm is measured along the flight tracks of research flights performed under WAI conditions, compared to 352 ppm for flights under AC conditions. On the vertical axis, the amount of water vapor steadily decreases from the surface to the upper troposphere. Research flights performed under WAI conditions had a higher average water vapor mixing ratio by around 2.5 times, compared to the AC flights on all four defined layers from 0 to 12 km altitude.

Table 4.3: Differences in available water vapor and ambient temperature during research flights of the HALO-(AC)^3 campaign under arctic (AC) and warm air intrusion (WAI) conditions. Overview from both ERA-5 reanalysis data and data from WALES measurements. Results presented in mean values over the defined areas with standard deviation.

		AC	WAI	WAI-AC	Difference %
ERA-5 means					
	Total column water vapor ($kg \cdot m^{-2}$)	3.4 ± 0.4	6.9 ± 1.9	3.5	103.3
	Temperature (K) at:				
	250 hPa	219 ± 5	216 ± 6	-3	-1.6
	500 hPa	237 ± 2	242 ± 4	5	2.2
	850 hPa	257 ± 1	266 ± 3	8	3.2
	1000 hPa	260 ± 1	270 ± 4	10	3.8
WALES means					
	Total water vapor mixing ratio (ppm)	352 ± 93	888 ± 280	536	152.4
	Water vapor mixing ratio (ppm) for:				
	9-12 km	8 ± 2	22 ± 10	14	171.0
	6-9 km	70± 32	177 ± 49	107	152.0
	3-6 km	382± 107	908 ± 183	526	137.4
	0-3 km	947 ± 149	2446 ± 528	1499	158.3

Geometrical and optical characteristics

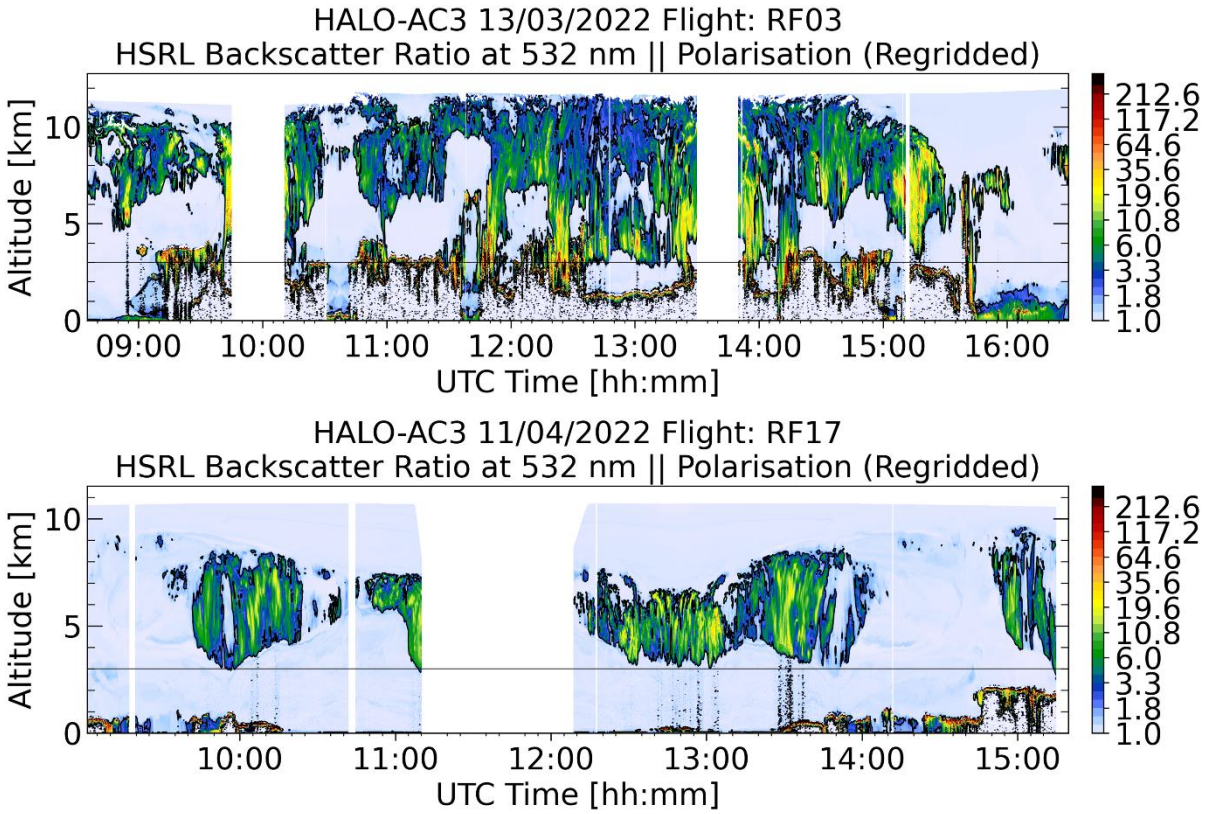

Figure 4.12: The BSR measured by WALES via the HSRL method at 532 nm for a) RF03 conducted on 13/03 during an active WAI event and b) RF17 conducted on 11/04 under undisturbed arctic conditions. Characteristic during the WAI are the lower level clouds found at altitudes up to 4 km, as well as the greater geometrical extent of WAI cirrus, which also reach up to higher altitudes. The black contours and line represent the parameters of the cirrus cloud mask.

Having established that during WAI events the ambient conditions in the arctic change significantly compared to AC conditions, I move onto the analysis of the cirrus clouds in the two groups. I start with the geometrical and optical characteristics of cirrus clouds measured under AC and WAI conditions. The results of this analysis are summarized in Table 4.4.

Starting with the average geometrical depth, AC cirrus are found to be thinner than WAI cirrus having mean cloud depths of 2037 m and 3141 m respectively. The average cloud base height of WAI cirrus is higher than that of AC cirrus by 652 m (4990 m and 4338 m respectively), but the average cloud top altitude of WAI cirrus is higher by an even bigger margin (1755 m) compared to AC cirrus, with 8131 m and 6376 m respectively. Thus, the greater average cloud depth for WAI cirrus stems mainly from them extending higher into the troposphere, than having formed lower.

Regarding the study of geometrical depths an implication must be kept in mind. For some clouds the actual cloud base might be filtered out by the applied cloud mask, or more importantly during some measurements, the lidar signal can become completely attenuated or the receiver completely saturated, which can lead to the actual cloud base not being measured. In those cases, the lowest available data point is considered as the cloud base by the algorithm. The HAMP (HALO Microwave Package) cloud radar (Ewald et al., 2019), which was performing simultaneous measurements with WALES, does not have this problem. For this reason, the cloud base heights that were defined from the lidar measurements were compared to the ones measured by HAMP. An average difference (WALES -HAMP) of 388 m for WAI cirrus and -118 m for AC cirrus was detected.

Following the methodology described in Sect. 3.5, the average optical depths for the AC and WAI cirrus were also calculated, based on the lidar measurements. As shown in Table 4.4, WAI cirrus are found to have on average an almost two times greater optical depth than AC cirrus. The exact values being 2.48 and 1.39 respectively.

Table 4.4: Differences in cloud geometric and optical characteristics during research flights of the HALO-(AC)^3 campaign under arctic (AC) and warm air intrusion (WAI) conditions, based on WALES measurements. Results presented as mean value of each parameter and group with standard deviation.

	AC	WAI	WAI-AC	Difference %
Cloud geometrical depth (m)	2037 ± 855	3141 ± 734	1104	54.2
Cloud top height (m)	6376 ± 1195	8131 ± 1229	1755	27.5
Cloud base height (m)	4338 ± 609	4990 ± 1284	652	15.0
Optical depth	1.39 ± 0.34	2.48 ± 0.98	1.09	78.4

Distribution of RHi

In this subsection the differences in RHi between AC cirrus and WAI cirrus are presented (see Sect. 3.8.2). More precisely the 2-D probability densities of RHi with respect to ambient temperature for the in-cloud, near-cloud and cloud-free areas of the AC and WAI cirrus groups respectively are calculated and presented in the six panels of Fig. 4.13. Plotted on each panel are also four lines representing the ice saturation threshold at RHi = 100 %, as well as three temperature dependent ice nucleation thresholds. Two thresholds for HET nucleation on mineral dust (MD) and coated soot (CS) as INPs and one for HOM nucleation.

The probability density of RHi for the AC cirrus in-cloud data is highest at ice saturation (RHi = 100 %) and a temperature of 242 K. The majority of the data are found around ice saturation and for temperatures between 252 K and 212 K. RHi values are mostly above 75 % throughout the whole temperature range. The MD activation threshold is very frequently reached for temperatures down to 220 K. Over the MD threshold the probability of detection decreases and is close to zero for RHi over the CS activation threshold and up to the HOM threshold.

The in-cloud data for WAI cirrus are detected on a wider temperature range than for the AC cirrus, both on the warmer and the colder end, extending between 200 K and 262 K. The highest probability density for RHi is once again at saturation (RHi = 99 %), but at a slightly warmer temperature of 246 K. The range of RHi values is also broader for WAI cirrus. On the lower end the distribution has a rather flat temperature-independent cut-off. The majority of the data is found over 70 % RHi. On the higher end, RHi values follow the CS activation threshold, thus also reaching up to higher supersaturations at colder temperatures. Data points up to and over the HOM nucleation threshold are rare but more frequent than for AC cirrus. WAI cirrus are found to be generally more frequently supersaturated. The MD threshold is exceeded throughout a larger temperature range and RHi up to the CS activation threshold are also more common throughout the temperature range down to 202 K. WAI cirrus in-cloud data are also more frequently detected with RHi over the CS activation threshold compared to AC cirrus and even over the HOM threshold, although here the probability remains very small.

The near-cloud areas around AC and WAI cirrus (Fig. 4.13b & e) have similar temperature ranges to their respective in-cloud data, i.e. warmer and colder temperatures for the WAI group, with the difference that both have higher probabilities at colder temperatures compared to their respective in-cloud. Both AC and WAI cirrus have the majority of their data below saturation, although high supersaturations are also frequent. More specifically the near-cloud area around AC cirrus is most frequently between 208 K and 246 K and subsaturated. Supersaturations up to the MD activation threshold remain frequent and also extend to colder temperatures than for the in-cloud area. The CS activation threshold is reached mostly for temperatures between 250 K and 220 K. RHi values over the CS threshold are very rare and even less frequent over the HOM threshold. The near-cloud area of the WAI cirrus, is also strongly dominated by RHi values below saturation with high probability densities even at RHi close to 0. Despite that, supersaturation is also present. The probability density for RHi over the MD threshold and up to the CS threshold is high throughout the whole temperature range. Near-cloud data of WAI cirrus are also frequently detected over the CS threshold and even over the HOM threshold. The probability of high supersaturation is noticeably higher for WAI cirrus near-cloud data compared to AC cirrus near-cloud and even compared to WAI in-cloud data.

The cloud-free areas around AC and WAI cirrus also share similar temperature ranges to the respective in-cloud and near-cloud areas, with WAI cirrus having a wider temperature range on both ends. For both AC and WAI cirrus most of the cloud-free data are subsaturated down to very low RHi values close to 0. The very few supersaturated data for the cloud-free area around AC cirrus reach mostly up to the MD activation threshold. For the WAI cirrus supersaturation seems to be even less frequent but there are some sporadic data reaching higher RHi even to the CS threshold. The HOM regime is practically not populated for any of the two cirrus types.

A more quantitative, temperature and INP independent scope of the characteristics of RHi is provided in Table 4.5. Once again, the in-cloud, near-cloud and cloud-free data for AC and WAI cirrus groups are analyzed and the probabilities of RHi are calculated in four regimes: subsaturated, low HET, high HET and HOM. Here the two HET regimes are defined based only on the RHi and are not connected to specific INP. The regimes are not indicative of a specific nucleation process, but contain RHi values at which HET and HOM nucleation could be possible. For details see also Sect. 3.5.

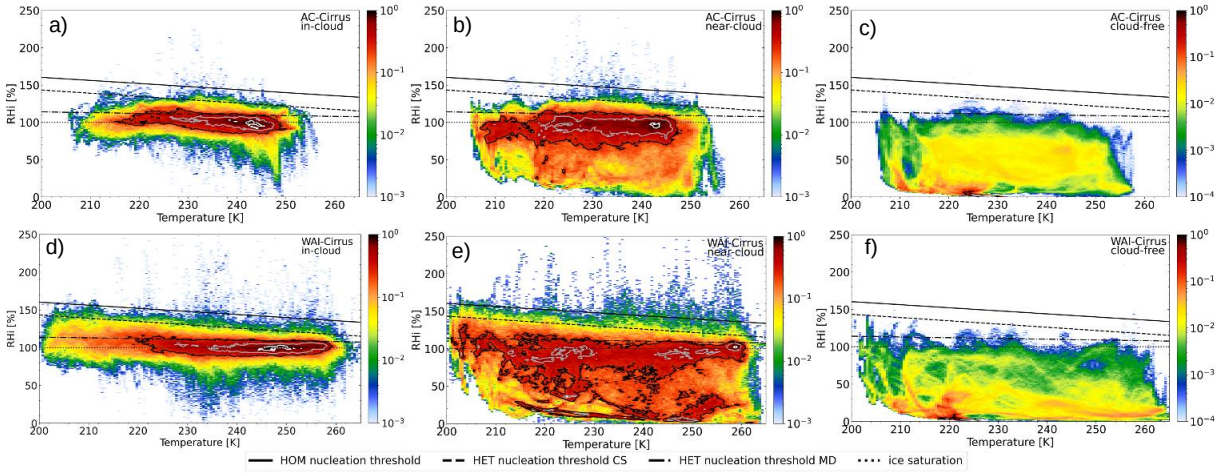

Figure 4.13: Probability densities of Relative Humidity over ice (RHi) with respect to temperature for: a) Cirrus clouds measured under arctic conditions (AC cirrus), in-cloud b) near-cloud area around AC cirrus c) cloud-free area around AC cirrus d) Cirrus clouds measured under WAI conditions (WAI cirrus), in-cloud e) near-cloud area around WAI cirrus f) cloud-free area around WAI cirrus. Panels c) and f) have a different range in the color scale than the other panels, but same to each other. The bin sizes are 0.5 K and 1 % RHi. The contour lines represent the 0.25, 0.5 and 0.85 probability contours in black, grey and white respectively. The dotted line represents the ice saturation threshold (RHi = 100 %). The dash-dotted line corresponds to the threshold for heterogeneous nucleation (HET) with mineral dust (MD) as the INP. The dashed line is the threshold for HET nucleation with coated soot (CS) as INP. The solid line denotes the threshold for homogeneous nucleation (HOM).

Table 4.5: Probabilities of RHi for the in-cloud, near-cloud and cloud-free regions of the AC and WAI cirrus groups.

	In-cloud		Near-cloud		Cloud-free	
	AC	WAI	AC	WAI	AC	WAI
# of data points	687,481	942,111	1,627,909	1,202,003	4,378,911	1,617,644
RHi probability [%]						
≥ 100%	53.91	57.39	22.83	24.18	0.69	0.64
RHi probability [%]						
HET (100 % - 147 %)	53.87	57.15	22.80	23.78	0.69	0.64
Low HET (100 % - 123 %)	51.88	52.12	22.02	19.72	0.68	0.60
High HET (123 % - 147 %)	1.99	5.03	0.78	4.06	0.01	0.04
HOM (≥ 147 %)	0.04	0.23	0.04	0.41	0.00	0.00

From Table 4.5 it is confirmed that the in-cloud area for both AC and WAI cirrus is most frequently supersaturated with a higher percentage for WAI cirrus, 57.39 % compared to AC cirrus, 53.91 %. For AC cirrus the majority of the data is found in the HET regime, 53.87 %, and more specifically the low HET regime, 51.88 %. The high HET regime, including RHi values from 123 % to 147 %, has a probability of 1.99 % and only 0.04 % of the data are in the HOM regime. Similar is the case for the WAI in-cloud data. The majority of the data are found in the HET regime, 57.15 %, and more specifically the low HET regime, 52.12 %, with probabilities reducing gradually for the high HET, 5.03 %, and HOM regimes, 0.23 %. When comparing the two cloud types it is apparent, that WAI cirrus have higher probabilities in all four regimes with differences being greater for the high supersaturations at the high HET and HOM regime.

The near-cloud data around both AC and WAI cirrus are mostly subsaturated as they have a supersaturation probability of 22.83 % and 24.18 % respectively. Similarly to the in-cloud data, both cirrus types have the majority of their near-cloud data points in the HET regime and specifically the low HET regime with probabilities significantly lower for the high HET and HOM regimes. Also similar to the in-cloud area, WAI cirrus near-cloud data have higher probabilities compared to AC cirrus in all supersaturation regimes bar one, the low HET. More precisely, near-cloud data for WAI cirrus are more frequently in the HET regime, with 23.78 % compared to 22.8 % for AC cirrus. This comes as a result of the bigger difference they have in the high HET regimes with probabilities of 4.06 % for WAI cirrus and 0.78 % for AC cirrus, as in fact AC cirrus have a slightly higher probability in the low HET regime, 22.02 %, compared to 19.72 % for WAI cirrus. In the HOM regime the probability is once again low for both cloud types but higher for near-cloud data of WAI cirrus with 0.41 %, compared to 0.04 % for AC cirrus.

Finally, the cloud-free data around both AC and WAI cirrus are strongly subsaturated. Only 0.69 % for the AC cirrus and 0.64 % for the WAI cirrus are supersaturated. All of the supersaturated data for both cirrus types are found in the HET regime, leaving the HOM regime unpopulated. In the low HET regime AC cirrus have a slightly higher probability of 0.68 % compared to 0.6 % for WAI cirrus. On the contrary, in the high HET regime, it is the WAI data with a higher probability, 0.04 % against 0.01 % for the AC cirrus.

A two-sample t-test was performed on the data presented in Table 4.5 in order to verify the statistical significance of the findings. Before performing the test, the variance, skewness and kurtosis of each data group were calculated to verify its applicability. For all comparisons between the two cirrus groups the test returned t-statistics above 0 and p-values less than 0.05 %.

Vertical structure of RHi inside AC and WAI cirrus

Figure 4.14 contains results regarding the distribution of RHi in AC and WAI cirrus on the vertical axis. On the left side, the analysis is performed by defining the cloud base and cloud top of each cirrus and then splitting the total extent of each cloud into slices, each containing 10 % of the total cloud depth. The same method has been applied and explained more extensively in Sect 3.5, 4.1.2 & 4.2.2. On the right side of Fig. 4.14 the probability density of RHi with respect to altitude is plotted for the in-cloud data of the two cirrus types.

Looking at the RHi distribution with respect to cloud depth (Fig. 4.14a & c), for both AC and WAI cirrus, they are reminiscent of the overall structure presented in Fig. 4.10 and the midlatitude cirrus described in Sect. 4.1. The cloud tops are mostly supersaturated with high RHi and the

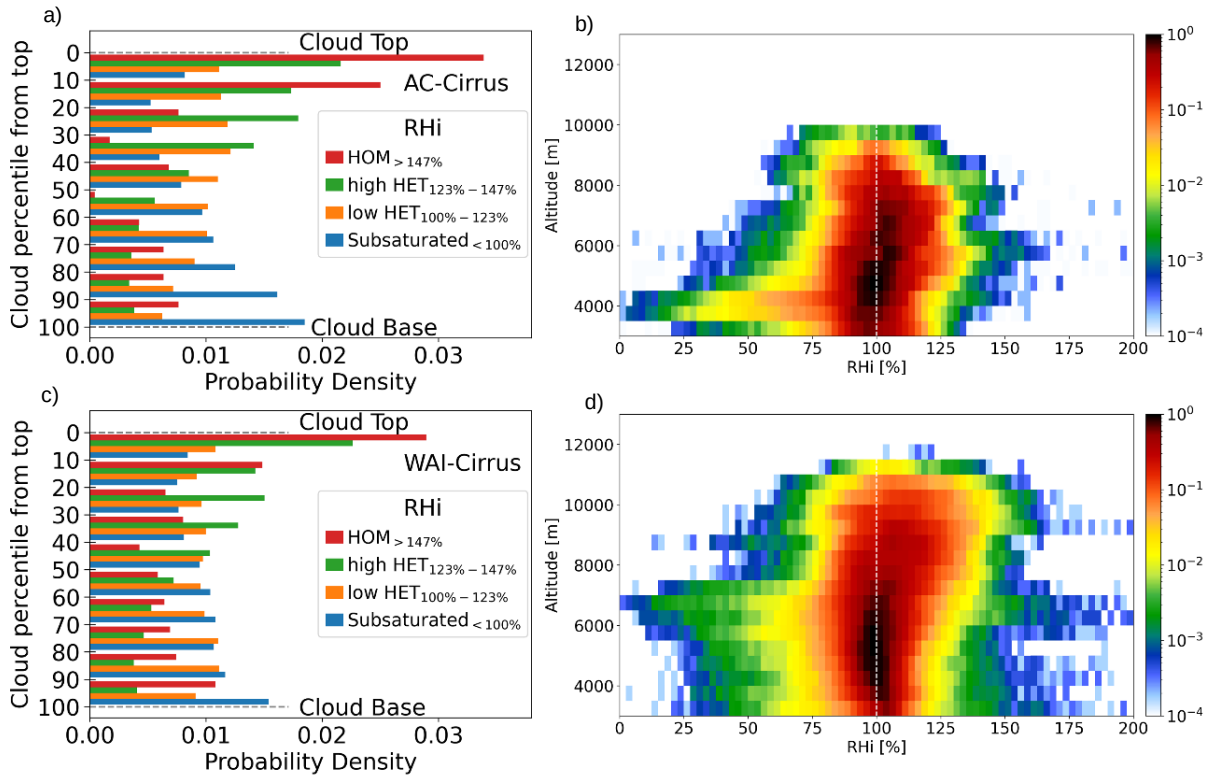

Figure 4.14: Left: Probability densities of in-cloud RHi in a relative location to the cloud top. Every cloud is split into ten percentiles from cloud top to cloud base and for each percentile the probability densities of each RHi bin (subsaturated, low HET, high HET and HOM (see Sect. 3.5)) are calculated. Right: Probability densities of in-cloud RHi with respect to altitude. Bin sizes are 2.5% RHi and 500 m altitude. Top row: Cirrus clouds measured under AC conditions. Bottom row: Cirrus clouds measured under WAI conditions.

cloud bases rather subsaturated. A more detailed inspection however does reveal differences between the two cirrus groups.

AC cirrus are clearly dominated by high supersaturations in the HOM regime down to a cloud depth of 20 %. Lower in the cloud the HOM regime becomes gradually less populated and the high HET regime is the most dominant until 40 % cloud depth. From there and down to 60 % of the total extent of the cloud, supersaturations in the low HET regime are the most frequent. Between 60 % and 70 % cloud depth most of the data are subsaturated while low supersaturations are still present. Moving down to the cloud base from there, subsaturation becomes increasingly more dominant, while high supersaturations in the HOM regime also increase again.

Similarly, WAI cirrus are also dominated by high supersaturations in the HOM regime at the first 20 % of their total extent, although already after the first 10 % cloud depth lower supersaturations in the high HET regime become significant. From 20 % cloud depth and down to cloud middle, the high HET regime is the most dominant with its probability gradually decreasing. Already just below cloud middle the subsaturated RHi are the most probable until cloud base. Interestingly,

the low HET regime also has a high contribution and even data in the HOM regime become once again more frequent at cloud base.

As for the probability densities of RHi with respect to altitude (Fig. 4.14b & d), first the higher vertical extent and thus also colder temperatures for WAI cirrus are confirmed. For AC cirrus it is shown that at lower altitudes mostly below 5km subsaturation is the most frequent. As the altitude increases, so do also the RHi values. Subsaturation becomes less probable while the distribution is skewed to higher RHi. For WAI cirrus the lower altitudes are mostly around ice saturation. From 3 km, which is the lower level introduced by the cloud mask (see Sect. 3.7), and up to around 7.5 km the structure remains stable around saturation. From an altitude of 8 km and up to 11 km there is a clear trend towards higher RHi with increasing altitudes.

Chapter 5

Discussion

Airborne lidar measurements have been shown to be an effective way to study cirrus clouds. Compared to ground-based measurements they present the advantage of mobility. A ground-based instrument can only detect cirrus that happen to pass over its location at a certain time, while airborne instruments can be transported to chosen regions, over sea and land, at selected times and probe cirrus with a specific purpose. Airborne lidar measurements are also advantageous compared to in-situ measurements. While in-situ instruments do frequently have high accuracies, they can only measure a one-dimensional line through a cloud. Airborne lidar instruments on the other hand, provide measurements in form of a two-dimensional curtain along the flight track. Thus, a single overpass is enough to probe a cirrus cloud, including information on its whole vertical extent. The limitations of airborne measurements are few. Namely, a close collaboration with air traffic authorities is always necessary and not all air spaces are open for all operations. Additionally, due to the high speed at which airborne measurements are conducted, following the airmass transformation of a system or evolution of a cloud with time is not as easy as for example by geostationary satellite measurements.

Advanced lidar measurement techniques such as the HSRL and DIAL can improve the accuracy and quality of the measurements by eliminating the necessity for additional atmospheric or instrument constants. They also provide simultaneous measurements of many different parameters, thus reducing the necessity for external data, such as reanalysis, which might have a lower resolution and greater errors. Despite the many advantages of HSRL and DIAL instruments, they are often complicated to build, maintain and operate.

The WALES lidar system is a combined HSRL and water vapor DIAL instrument capable of performing airborne measurements of aerosol extinction and backscatter, particle linear depolarization and water vapor concentration. It does so with great accuracy and resolution and has been used in many studies with focus on various topics, including also ice clouds e.g. Groß et al., 2012, 2014; Urbanek et al., 2017; Gutleben et al., 2019; Krüger et al., 2022; Dekoutsidis et al., 2023a. Despite its proven great properties and capabilities, WALES also suffers from a common problem found in the study of cirrus clouds via airborne lidar. As seen in the lidar equation, there is a dependency of the backscattered signal to the square of the distance. This may result in very strong signals being backscattered into the instrument if the measured cloud is too close to it. This in turn can lead to a saturation of the detectors of the instrument resulting in the cloud not being properly measured. To counteract this phenomenon a minimum distance between the lidar instrument and cloud top must be kept. For WALES this distance is around 2 km.

WALES has been developed and is operated by the German Aerospace Center (DLR). It is built in such a way, that it can be integrated in various research aircraft also operated by DLR. One of these is the German research aircraft HALO. HALO is a business jet that has been specifically modified to facilitate atmospheric measurements for example by creating openings in the fuselage for the laser beams of the lidar. Among its many characteristics that make it, not only suitable

but preferable for the study of cirrus clouds, is its high flight ceiling. This allows flights at a distance great enough from cirrus cloud top in order to minimize the abovementioned problem of saturation of the detectors. More advantages of HALO include its long range, allowing for measurements over long distances and times as well as its heavy payload allowing for the transportation of instruments and other equipment.

For the ML-CIRRUS and HALO-(AC)^3 campaigns WALES was aboard HALO and performed measurements over the mid- and high latitudes respectively. The collected data were used for this thesis. First, the water vapor measurements were combined with temperature data from ECMWF in order to calculate the RHi. A similar method using WALES data and ECMWF temperatures has also been applied in other studies e.g. Groß et al., 2014 and Urbanek et al., 2018. After, masks were applied on the measured and calculated data, in order to single out the cirrus clouds in the data sets of the two campaigns. Finally, statistical analyses were performed aiming to study the characteristics of cirrus clouds over the mid- and high latitudes based on their formation and nucleation process, their ambient conditions and temporal evolution.

5.1 Cirrus cloud characteristics over the midlatitudes

The midlatitudes are a region characterized by an abundance of different dynamical weather systems occurring. A clear fingerprint of the human effect can also be identified by the elevated aerosol emissions and most importantly by the dense air traffic. All these result in cirrus clouds forming with different mechanisms and under varying conditions and thus having a wide range of different characteristics. This results in difficulties when including them in weather forecasting models and trying to quantify their climate effects.

During the ML-CIRRUS campaign, cirrus clouds were measured via airborne lidar over the midlatitudes. Following the method described in Chapter 3, I studied the measured clouds. The results of this analysis are presented in Sect. 4.1 and will be discussed in the following.

5.1.1 Relative humidity in midlatitude cirrus clouds

Properties of RHi

From my research, I conclude that the most commonly detected RHi value in midlatitude cirrus clouds is 96 %, which is very close to ice saturation (Table 4.1). This value has a maximum possible uncertainty of 10 - 15 %, which stems from uncertainties in the model temperatures used to calculate the RHi. This result compares very well to other studies and is also confirmed via in-situ measurements. More specifically, Kaufmann et al. (2018), Kübbeler et al. (2011), Ovarlez et al. (2002), Petzold et al. (2017) and Ström et al. (2003) used in-situ measurements, Gensch et al. (2008) used in-situ measurements and a model, Comstock et al. (2004) used ground-based Raman lidar measurements and Krämer et al. (2009, 2020) used in-situ and satellite remote sensing (lidar and radar) measurements and also found an RHi mode close to ice saturation for midlatitude cirrus clouds. A more immediate comparison can be done to Groß et al. (2014). They used water vapor data collected by WALES over Germany during Fall of 2010, and found an RHi mode of 98 %.

Despite the mode value of the RHi distribution being close to saturation, the in-cloud data are not evenly distributed over and under saturation and only 34 % are supersaturated with respect to ice. Thus, the majority of in-cloud data are subsaturated, with RHi values remaining predominantly over 70 % (Fig. 4.1). This finding might be counterintuitive, since ice crystals would be expected to sublimate under these conditions. Despite that, it has been frequently observed also in other remote sensing and in-situ studies over the mid- and high latitudes e.g. (Ovarlez et al., 2002; Ström et al., 2003; Spichtinger et al., 2004; Kärcher, 2005; Kübbeler et al., 2011; Kaufmann et al., 2018; Li et al., 2023). This might be the case, because ice crystals need a long time to fully evaporate in a subsaturated environment, depending on their size, the ambient RHi and available water vapor (Kübbeler et al., 2011; Schumann, 2012; Li et al., 2023). Kübbeler et al. (2011), for example performed simulations and found that small ice crystals can survive in subsaturation for several minutes, while large ice crystals remain in subsaturation in the timescale of hours. Li et al. (2023), calculated a time of approximately 4 hours for ice particles to completely sublimate while in subsaturation. Hence, I can also confirm that midlatitude cirrus are frequently detected in slight subsaturation.

Regarding the percentage of ice supersaturation I find that it is in accordance with Groß et al. (2014) who analyzed water vapor measurements by WALES taken over Germany, and found 30 % of the in-cloud data in supersaturation. Other studies also found supersaturation frequencies around 30 % in midlatitude cirrus clouds, but with other data and methods to my study. Comstock et al. (2004) analyzed Raman lidar measurements taken over the Southern Great Plains and Ovarlez et al. (2002) in-situ measurements over Scotland, during the INCA (INter hemispheric difference in Cirrus properties from Anthropogenic emissions) campaign (Ström et al., 2003). Jensen et al. (2001) report 49 % of their measured data in supersaturation, which is higher than my findings. It should be noted, that they used in-situ measurements taken over an area close to the Southern Great Plains during the SUCCESS aircraft field campaign, which generally focused in measuring areas with high ice supersaturations.

The majority of the supersaturated data, 30.3 %, were found with RHi up to 120 %, 3.8 % of all in-cloud data points had RHi values higher than 120 % and 0.5 % even exceed 140 % RHi. Introducing nucleation processes into the discussion, this would mean that only a minimal amount of data is over the threshold for HOM nucleation and the bulk of the RHi values is under the activation threshold for HET nucleation on coated soot (Fig. 4.1).

Higher supersaturations were seen at colder temperatures, a trend also seen in other studies such as Comstock et al. (2004), Jensen et al. (2013) and Krämer et al. (2009, 2020). Groß et al. (2014) reported only 2 % of data points over RHi 120 %, which is slightly less compared to my finding. Potential sources for this difference may arise due to the different season during which the measurements were taken, and the fact that they performed measurements only in one atmospheric system, while I analyze a more variable and extended dataset (Kahn et al., 2008; Dzambo and Turner, 2016).

The cloud-free air in the vicinity of the measured cirrus clouds is predominantly subsaturated with the RHi mode being 68 %. Voigt et al. (2010) also find the majority of the cloud-free data around midlatitude cirrus below saturation and more specifically between RHi 70 % and 100 %. Only 6.8 % of the cloud-free data are supersaturated and only 1.2 % have RHi over 120 %. Similar to the in-cloud, higher RHi are measured at lower temperatures (Fig. 4.1). Comstock et al. (2004) found a supersaturation frequency of 9 % in their cloud-free data, which is higher compared to

my result. Aircraft-based studies as for example Gierens et al. (1999, 2000), Heymsfield et al. (1998), Jensen et al. (2001, 2005), also detected high RHi supersaturations in the upper troposphere of the midlatitudes. Considering the possible ice nucleation processes, most of the supersaturated data points in my analysis are in the HET regime and very few are also detected close to or in the HOM regime. This was also detected by Cziczo et al. (2013), Krämer et al. (2009, 2020) and Ovarlez et al. (2002).

Distribution of RHi through the cloud layers

The topmost layer of the measured midlatitude cirrus clouds, is a mixture of supersaturations from 100 % to over 140 %. The subsequent layers are progressively populated by lower RHi supersaturations and after cloud middle most data points are subsaturated (Fig. 4.2). Following Diao et al. (2013, 2015) who define the ice nucleation, growth and sublimation stages based on the measured ice super- and subsaturation, I conclude that ice crystals are more likely to form near the cloud top, grow around the cloud middle and sublimate at cloud base. This vertical distribution of RHi values has also been predicted via model simulations by Heymsfield and Miloshevich, (1995) and Spichtinger and Gierens (2009). Several field studies also come to the same conclusion. Comstock et al. (2004) and Di Girolamo et al. (2009) used ground-based Raman lidar over the Southern Great Plains and Italy (EAQUATE Experiment), respectively, and noted higher ice supersaturation near cloud-top and subsaturation near cloud base, as did Sakai et al. (2014) via instrumented balloon and ground-based lidar measurements of cirrus clouds, Dzambo and Turner (2016), via a combination of radiosonde and millimeter-wavelength cloud radar data and Korolev and Isaac (2006) via in-situ measurements.

It has been established, that the vertical RHi structure follows a pattern. A subsaturated cloud base with subsaturation gradually decreasing towards cloud top and progressively higher supersaturations becoming dominant instead. As seen in Fig. 4.2, there seems to be an irregularity at cloud top, since it is not clearly dominated by high supersaturations as would be expected. This ambiguity led to a more detailed study of the individual clouds of the statistic. I found, that in some cases the topmost layer of a cirrus had lower supersaturations than the layers below it, or was even subsaturated. These cases were then studied in depth and it was found that they also commonly had a lower RHi mode and a low or negative skewness in their RHi distribution. These findings are consistent with the hypothesis that they were older clouds which had slowed down or completely ceased the production of new ice crystals. The same behavior war also detected by Groß et al. (2014) in one of their analyzed cases, leading them to the same interpretation.

5.1.2 Differences between liquid origin and in-situ formed cirrus

Characteristics of RHi with respect to temperature

In Fig. 4.1 I presented the probability density of RHi for midlatitude cirrus with respect to ambient temperature and noted an apparent bimodality. One peak was found around 225 K and close to ice saturation, RHi = 100 % and a second one at a colder temperature, 218 K and subsaturated, RHi = 79 %. Further analysis revealed that these two peaks could be attributed to two different cloud types being measured. Following the classification of cirrus clouds according to their formation process, as proposed by Krämer et al., 2016, the two cloud types are identified as in-situ formed and liquid origin cirrus. After grouping the measured clouds into the two groups, I

conclude that in-situ formed cirrus correspond to the colder subsaturated peak and liquid origin cirrus to the warmer, saturated peak. Gasparini et al. (2018), use a global aerosol climate model, which they validate using a cirrus climatology derived from the CALIPSO (CloudAerosol Lidar and Infrared Pathfinder Satellite Observations) satellite and also come to the same conclusion.

A more detailed analysis of RHi for the two cirrus types is shown in Fig. 4.3. There it is verified that in-situ cirrus are detected at colder temperatures, mostly below 225 K and have a significant amount of data in subsaturation. Supersaturation is nonetheless present and high RHi values are reached, although only in a small temperature range. Liquid origin cirrus on the other hand are found at warmer temperatures, mostly over 215 K. A significant amount of the in-cloud data points is subsaturated also for this cloud type. RHi values steadily increase and supersaturation becomes more frequent at colder temperatures, over a wider temperature range. This leads to liquid origin clouds being more frequently supersaturated, 36 % compared to 30.8 % for in-situ formed cirrus. The difference is greater for low supersaturations and the probabilities for RHi over 120 % are similar between the two cloud groups.

The cloud-free air around the clouds of the two groups also presents similar characteristics. Colder temperatures for in-situ formed clouds and warmer for liquid origin. Subsaturation is dominant for both cloud types, with the cloud-free air around liquid origin cirrus being slightly more frequently supersaturated, 7.5 % compared to 5.7 %. In both groups the cloud-free data reach higher supersaturations at colder temperatures, but remain mostly under 120 % RHi, which would generally coincide with the activation threshold for coated soot.

Vertical structure of RHi

Regarding their vertical structure, the two cloud types generally present with the expected behavior discussed in the previous. High supersaturation dominated cloud top dropping down to a subsaturated cloud base. This structure is very clear for liquid origin cirrus, indicating distinct layers for ice formation, growth and sublimation. For in-situ formed cirrus, the transition to subsaturation happens at an earlier point. Additionally, supersaturations in the low HET regime (RHi 100 % - 120 %) are frequently present throughout the clouds and even at cloud base.

The role of the ambient updraft

Many factors might contribute to the differences detected between liquid origin and in-situ formed cirrus clouds. The ambient updraft or downdraft during the clouds formation and evolution can potentially play a significant role. The intensity and direction of the vertical velocity can affect the cooling rate of the clouds airmass, which might alter the supersaturation over ice, finally leading to a different nucleation process and macro- and microphysical characteristics. With that in mind and aiding to this discussion, I used vertical velocities from the ERA-5 reanalysis dataset and collocated them to the cirrus found along the flight paths of the missions of the ML-CIRRUS campaign. Fig. 5.1 contains the results of this analysis in form of probability densities of vertical velocities for the two cloud types.

Both in-situ formed as well as liquid origin clouds are detected with ambient vertical velocities close to zero. The modes of both distributions in Fig. 5.1 are ever so slightly negative indicating an updraft. The distribution of vertical velocities is wider for the liquid origin cirrus. These clouds are also slightly more frequently detected with stronger updrafts. This might contribute to their vertical structure discussed above. Most liquid origin clouds in the ML-CIRRUS data set are found

in the outflow regions of warm conveyor belts (WCB), which are known to be accompanied by higher updrafts especially over their main axis. Krämer et al. (2016) also expect liquid origin clouds in higher updrafts and consider clouds from WCB systems to be slow updraft liquid origin clouds, thus also supporting the findings presented here and the differences between the two cloud types.

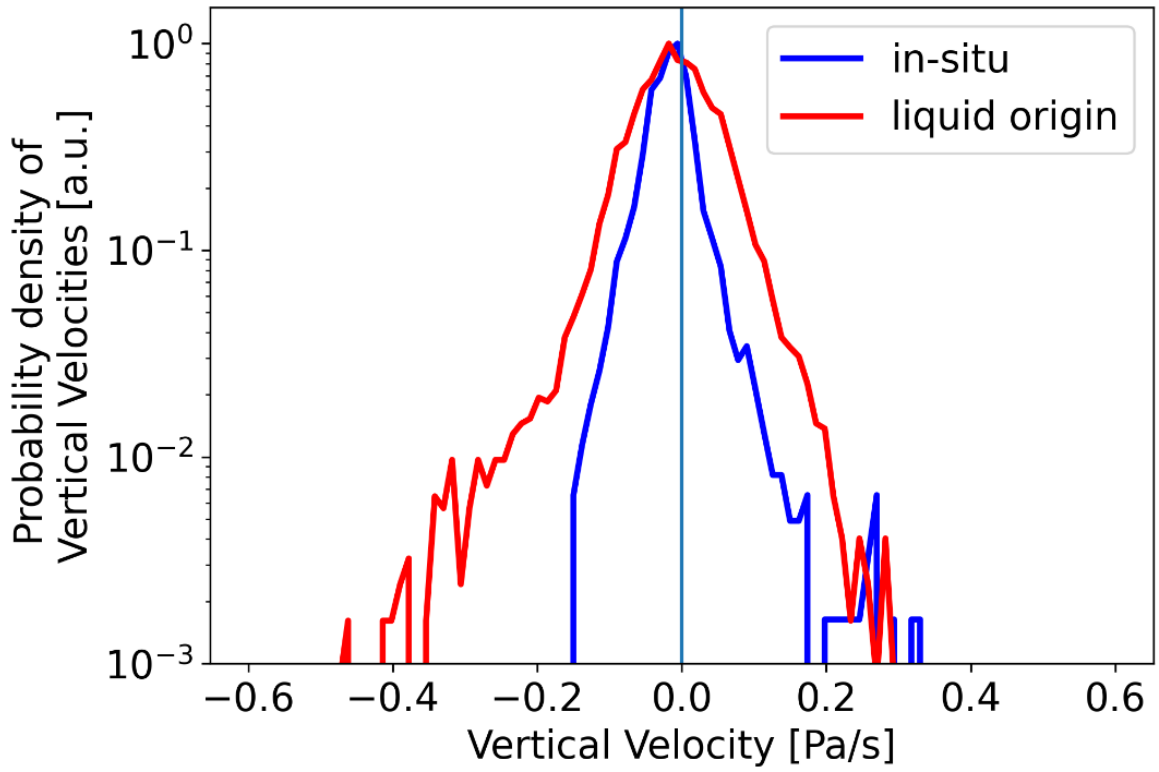

Figure 5.1: Probability densities of the vertical velocities for in-situ formed and liquid origin cirrus.

5.1.3 Temporal evolution of RHi distribution with cloud age

The distribution and structure of RHi in cirrus clouds changes for different evolutionary stages of the clouds as I showed in Sect. 4.1.4. From my analysis of two cases, I propose that the RHi present in a cirrus cloud and its vertical structure can be used as an indicator of the clouds evolutionary stage. It should be noted that the two studied cases included liquid origin cirrus. Further, I define three different cloud stages with unique characteristics of RHi each.

Young cirrus, that have just started forming and producing new ice crystals, have an RHi mode close to ice saturation. The distribution of RHi is skewed towards positive values resembling a Rayleigh distribution that reaches high supersaturations, which could facilitate HOM nucleation. Supersaturations tend to be higher at higher altitudes and skewness stronger. Despite that, ice nucleation is also possible at lower altitudes were lower supersaturations are more frequently detected.

Mature clouds also have an RHi mode around ice saturation and a slight positive skewness towards higher supersaturations. High supersaturations are reached over a big range of altitudes, but are mostly found higher whereas subsaturation appears more frequently at lower altitudes. This is indicative of a still ongoing active nucleation mostly near the cloud tops.

Older, stable clouds have RHi modes close to but under saturation. For this cloud stage the RHi distribution closely resembles a nearly Gaussian curve due to the fact that the skewness is close to zero. The vertical layers can each be described by a near Gaussian distribution with a progressively lower mode value starting from slight supersaturation at higher altitudes to subsaturation at lower ones. At this stage ice nucleation might still be ongoing but is less frequent and mostly present near the cloud tops, while sublimation is occurring near cloud base.

A case study focusing on the behavior of RHi during the evolution of a cirrus cloud is also presented by Comstock et al. (2004). They come to similar conclusions regarding the cloud evolutionary stages as presented herein. In-situ measurements studied by Diao et al. (2013 & 2015) also confirm similar cirrus evolutionary stages. Ovarlez et al. (2002) follow a different methodology. They split their observed cirrus into a warm and a cold regime with a threshold set at -40 °C and conclude that a Rayleigh distribution can be fitted over the ones in the cold regime, due to a positive skewness, and a Gaussian over the ones in the warm regime. Similar to my findings, they conclude that their observation can be explained by the different timescales necessary for a cloud to reach a stable state, where depositional growth and sublimation of ice crystals are in equilibrium (Khvorostyanov and Sassen, 1998; Hoyle et al., 2005). Also in accordance with my study, they interpret the positive skewness and thus the Rayleigh form, as an indication of an active cloud that has not yet reached maturity. Spichtinger et al. (2004) use cirrus cloud data measured during MOZAIC (Measurement of Ozone by Airbus In-service aircraft project) and also find positive skewness in the RHi distributions in the higher/colder parts of the clouds. They also attribute their findings to the relaxation times and the effects of vertical motion on them (Gierens, 2003). Groß et al. (2014) inversely, take the shape of the RHi distribution to draw conclusions about the evolutionary stage and activity of the cloud in the case study they present.

One thing that should be kept in mind, as already mentioned in Sect. 3.1.3 & 4.2.3, is that for very active optically thick cirrus the lower parts of a cloud might not be sufficiently measured due to complete attenuation of the lidar light, thus leading to higher average supersaturations when the statistical calculations are performed.

5.2 Cirrus cloud characteristics over the arctic

The arctic is a remote region of the Earth, not immediately related with daily human activities and has thus for many years received lesser academic interest. As a result, it still holds many open questions also regarding high latitude cirrus clouds, their prediction and representation in weather and climate models. In a changing climate, the arctic doesn't remain unfazed, on the contrary, an amplified warming has been detected over the high latitudes. Cirrus clouds in the arctic, acting as thermal blankets are expected to play a role. Warm air intrusions into the arctic from the midlatitudes are becoming more frequent and long-lasting also potentially contributing to this arctic amplification. They significantly alter the ambient conditions in which cirrus clouds also

form, introducing even more uncertainties regarding their properties and formation processes, which are necessary to accurately study them.

In this subsection the results of the analysis of the cirrus clouds measured during the HALO-(AC)^3 campaign in the arctic are discussed and compared to the findings from the midlatitude cirrus. The methodology of the analysis is presented in Chapter 3 and the results are presented in Sect. 4.2.

5.2.1 RHi of cirrus clouds in the arctic

RHi distribution with respect to temperature

Cirrus clouds in the arctic are detected with temperatures down to 200 K and up to almost 265 K. The wide temperature range is a sign of the variability of conditions under which cirrus form. The warm temperatures found in high latitude cirrus can indicate either that in some cases large amount of water vapor are advected to high altitudes and/or that easily activated INP are frequently available for HET ice nucleation. Warm air intrusions can result in both an increase of available moisture and aerosols, and are also capable of lifting these to ice-forming altitudes.

Almost 56 % of the in-cloud data of high latitude cirrus are supersaturated. RHi values become higher at lower temperatures, as is expected. The distribution of RHi follows the activation threshold for coated soot, which is considered a not-easily activated INP. RHi values that would allow HOM nucleation to take place are also frequently detected throughout the whole temperature range. Kärcher (2005), performed a modeling case study of a polar cloud and also found very high RHi values inside the cloud. He identified continuous weak cooling of an airmass, such as during a WAI, to cause an increase in RHi to high values and also sustain this supersaturation.

The near-cloud region surrounding the clouds is where new ice crystals mostly form. This is pictured in the near-cloud RHi distribution. Higher RHi values are reached, frequently also over the threshold for HOM nucleation. Thus, both nucleation processes play an important role in the formation of cirrus in the arctic.

The findings both on the in-cloud and near-cloud regions are also dependent on the evolutionary stage of the clouds as well as the ambient conditions. Young clouds, or clouds with a continuous supply of moisture to higher altitudes, are expected to appear more active with higher RHi inside and around them.

In-cloud RHi layers

The layering of RHi values within arctic cirrus clouds is similar to the one reported for midlatitude cirrus. High supersaturations are found near the cloud top, with lower supersaturations becoming dominant until around cloud middle where the clouds become predominantly subsaturated down to the cloud base. Interestingly, high supersaturations, capable of supporting HOM nucleation, are found throughout the cloud and are also an important part of the cloud base. From the above it can be concluded that new ice formation takes place at cloud top with HOM nucleation playing a significant role. It is also evident that the formed ice crystals can survive in a subsaturated environment. Kärcher (2005) comes to a similar result after performing a modeling case study of a polar cirrus cloud. He concludes that the cloud top region has high supersaturations and is

populated by a high number of small ice crystals. This is indicative of HOM nucleation taking place. He also detects subsaturation around cloud base, concluding that larger ice crystals can survive in this environment as they need longer times to fully evaporate under cold temperatures.

5.2.2 Warm air intrusions into the arctic

In this thesis I defined two different atmospheric states in the arctic, one with undisturbed arctic conditions (AC) and one with prevailing Warm Air Intrusions (WAI). Analyzing the temperature data from the ERA-5 reanalysis dataset from the earth's surface up to the 500 hPa pressure level, revealed that the arctic troposphere is on average 8 K warmer during a prevailing WAI. The difference is greater at surface level, which is 10 K warmer during an active WAI. Fig. 5.2 contains the probability densities of temperature with respect to altitude for the two cloud groups. The two plots confirm that the WAI cirrus group has a higher average temperature at ground level, but also a sharper cooling rate with altitude, leading to smaller temperature differences at higher altitudes.

Similarly, Stramler et al. (2011), also define two atmospheric states in the arctic during winter. One is characterized as cloudy and warm, and the other as being mostly clear-sky and colder. These states could coincide with the WAI and AC conditions defined herein. More importantly, they find a temperature difference of 13 K between their two states at surface level, closely matching my findings. Johansson et al. (2017) use satellite measurements and report an increase of surface temperature by 5.3 K in winter during airmass intrusion events.

The temperature difference between AC and WAI conditions steadily decreases at higher altitudes and, as shown in Sect. 4.2.3 and Table 4.3, at the 250 hPa pressure level WAI even becomes slightly colder than AC. A probable explanation for this observation could be that due to the colder temperatures noted for the AC conditions the troposphere is more compressed and the 250 hPa level is located already in the stratosphere where temperatures tend to increase again. This is also indicated in Fig. 5.2, where the thermal tropopause, i.e. the altitude at which the ambient temperature stops decreasing with a stable rate, is visibly higher for the WAI cirrus group (right panel).

In order to study the change in water vapor concentration in the arctic during a WAI event, both the total column water vapor data from ERA-5 and the vertically resolved data collected by the WALES lidar system during the HALO-$(AC)^3$ campaign were used. The ERA-5 data indicated a doubling of the water vapor concentration during prevailing WAI. The WALES measurements revealed an average increase of 2.5 times in the water vapor concentration during WAI events compared to AC conditions, from 352 ppm for AC conditions to 888 ppm for WAI. Despite the water vapor mixing ratio steadily decreasing at higher altitudes, the 2.5 times difference between the two states of the arctic troposphere remains. Gierens et al. (2020) used radiosondes to study the ice supersaturated regions of the arctic and reported water vapor mixing ratios of up to 500 ppm. Doyle et al. (2011) studied one WAI case by means of ground-based measurements and report an even stronger change in the water vapor mixing ratio, by four times between their WAI case and background measurements.

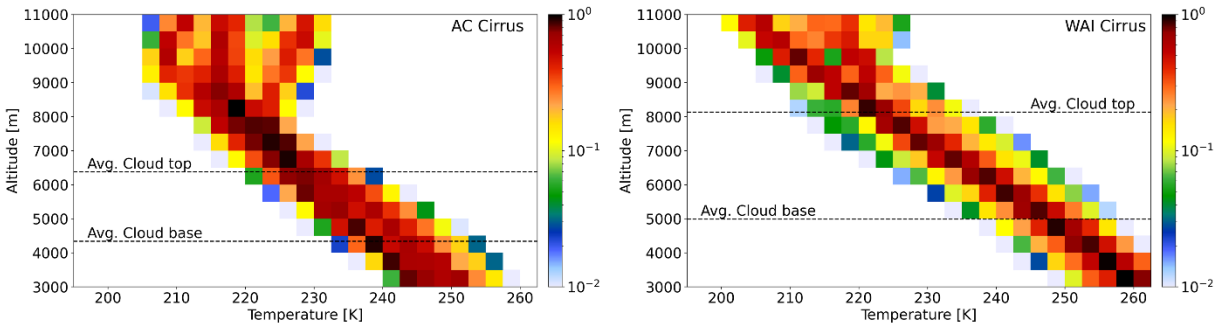

Figure 5.2: Probability density function of ambient temperature with respect to altitude for AC Cirrus group (Left) and WAI Cirrus group (Right). For each cloud group the respective average cloud base and cloud top heights are also plotted. Temperature data from ECMWF IFS.

5.2.3 Cirrus clouds under AC and WAI conditions

Geometrical and optical properties

Cirrus clouds that form in the arctic during a prevailing WAI (WAI cirrus) have different geometrical and optical properties to the ones that form during undisturbed arctic conditions (AC cirrus). Starting off with the geometrical properties I found that WAI cirrus are on average thicker than AC cirrus with a mean cloud depth around 3141 m and 2037 m respectively. Looking at the average cloud base heights, the WAI cirrus actually tend to form at higher altitudes (4990 m compared to 4338m), but end up having a bigger overall cloud depth due to their cloud tops reaching much higher altitudes. WAI cirrus cloud tops are on average 1755 m higher than AC cirrus with average cloud top heights of 8131 m and 6376 m respectively (Fig. 5.2). The warmer air advected into the arctic might be the deciding factor for this difference. On the one hand, regarding the cloud base, higher altitudes are necessary for the ambient temperature to drop low enough so that ice supersaturation is achieved and cirrus formation can initiate. On the other hand, looking at the cloud tops, the warmer temperatures can cause the whole arctic troposphere to extend to higher altitudes (Fig. 5.2). That, in combination with the stronger updrafts commonly accompanying a WAI, can result in the higher cloud top height.

Devasthale et al. (2011) used satellite data to study the geometrical properties of cirrus clouds in the arctic over a time period of four years and found an average geometrical depth of 0.4 km to 1 km with an average cloud base height around 6 km to 8 km and an average cloud top height of 7 km to 9 km. Compared to my findings they report much thinner clouds with higher cloud bases. It should be kept in mind, that they only studied clouds with an optical depth < 3, which could explain the difference in thickness. Nakoudi et al. (2021) used an earthbound Raman lidar stationed at Ny-Ålesund, Svalbard as well as radiosondes and measured cirrus cloud properties between 2011 and 2020. For the winter months they report average cirrus cloud depths of 2.1 km, with a cloud base around 7.1 km and a cloud top around 9.3 km. A similar finding to them is also presented by Schäfer et al. (2022). They used ground based and space-born lidar and measured cirrus clouds over the Norwegian arctic for a period of seven years. They report an annual average

cloud depth of 2.2 km with an average cloud base height of 6.9 km and an average cloud top height of 9.1 km.

Moving on to the optical properties, I used the measured two-way optical transmission due to particle extinction and calculated the optical depths of the AC and WAI cirrus. I conclude that WAI cirrus are on average optically thicker than AC cirrus, having mean optical depths of 2.5 and 1.4 respectively. While it might be expected for a cloud group that is on average geometrically thicker to also be optically thicker, this is also a strong indication that the microphysical properties of the two cloud types differ.

Differences in RHi distribution

WAI cirrus are detected in a wider temperature range extending to colder and warmer temperatures compared to AC cirrus. Inside both cloud types, supersaturation is frequent. Higher supersaturations are reached within WAI cirrus, partly also because of the colder temperatures in which they are detected. The temperature dependent RHi distribution (Fig. 4.13) reveals that AC cirrus are less frequently supersaturated and are mainly detected with RHi up to the activation threshold for CS, while WAI cirrus frequently reach over this threshold throughout almost the whole temperature range. WAI cirrus are also more frequently found at higher supersaturations over the HOM nucleation threshold with the probability nevertheless remaining very low. Kärcher (2005) performs a modeling case study of a polar cirrus cloud and also concludes that continuous weak cooling of an airmass, such as during a WAI, can result in high in-cloud RHi values.

The near-cloud regions around the two cloud groups, introduced in Sect. 3.7, also present interesting characteristics. Apart from sharing the same temperature ranges to their respective in-cloud regions, they have some notable difference to them and to each other. For both AC and WAI cirrus the majority of the data are subsaturated, but higher supersaturations, throughout the whole temperature range, are also detected, compared to their respective in-cloud areas. The RHi distribution in the near-cloud area around AC cirrus now reaches up to thee CS activation threshold over a wider temperature range. For the WAI cirrus group the RHi distribution exceeds the HOM nucleation threshold more frequently compared to the respective WAI in-cloud data as well as the AC near-cloud data.

The RHi values measured in the cloud-free air under AC and WAI conditions, are predominantly subsaturated. While the probability for supersaturation remains very low for both conditions, the AC group is slightly more frequently supersaturated but at lower RHi values, whereas the WAI group reaches higher supersaturations slightly more frequently.

A scarcity of studies on the topic of ice supersaturation in arctic cirrus clouds, makes it difficult to perform an immediate comparison of my findings to works of other researchers. Although many other studies have also previously reported high supersaturations in and around cirrus clouds, they focus mostly on the midlatitudes (e.g. Jensen et al., 2001; Ovarlez et al., 2002; Comstock et al., 2004; Gensch et al., 2008; Krämer et al., 2009; Cziczo et al., 2013; Dekoutsidis et al., 2023a). De La Torre Castro et al. (2023) use in-situ measurements taken during the Cirrus-HL campaign and also report high supersaturations with a median RHi of 125 % for cirrus clouds that formed and were detected at high latitudes. This value is higher compared to the mode value of 99 % found in my analysis, but it should be kept in mind that they select 60°N as their threshold for a cloud to be considered arctic. Additionally, during the Cirrus-HL campaign, it was the cloud top regions that were mostly probed, where higher supersaturations are generally detected. Gierens et

al. (2020) analyzed RHi measurements performed via radiosondes and reported RHi values reaching and sometimes exceeding 150 % - 160% in ice supersaturated regions. This would be in accordance with the supersaturations I detect in the HOM regime.

In-cloud vertical RHi layers

Looking into the vertical structure of RHi within AC and WAI cirrus, the general characteristics are similar. Cloud tops dominated by high supersaturations in the HOM regime gradually moving to a predominantly subsaturated cloud base. That being said, there are also differences. Focusing first on the cloud top regions, AC cirrus are clearly dominated by RHi in the HOM regime (RHi $>$ 147 %) down to 20 % cloud depth, whereas for WAI cirrus only the first 10 % of the total cloud depth have a clear HOM domination with lower supersaturation becoming almost equally probable at the next layer. Just below cloud middle, the AC cirrus group transitions to being predominantly subsaturated with a steadily increasing probability in lower layers towards the cloud base. There, the probability density for the HOM regime increases again. For the WAI cirrus, this transition is not so clear. WAI cirrus transition from high HET dominated directly to subsaturated at cloud middle. Following the common structure, subsaturation does become more probable from cloud middle to cloud base but the HOM and low HET regimes also have a significant contribution. Notable is the high probability for the HOM regime at cloud base.

Summing up, AC cirrus have clearer layers, transitioning from very high supersaturations at the cloud top to subsaturation at cloud base, whereas WAI cirrus seem to have RHi in different regimes at close probabilities throughout most of the cloud. Kärcher, (2005) studies a polar cirrus cloud, which is described similar to an AC cirrus as defined herein, and also reports a thin cloud top layer dominated by high supersaturations with a gradual decrease of RHi at lower levels in the cloud. Gierens et al. (2020) detect ice supersaturation most frequently directly under the tropopause. This area coincides with the cloud tops of many cirrus included in this work, which are also found to be supersaturated.

Nucleation processes and microphysics

Analyzing the RHi within and in the vicinity of AC and WAI cirrus, showed that only a very small percentage of the data had high enough RHi that would allow for HOM nucleation to take place. Comparing the two cloud types to each other though, it becomes clear that WAI cirrus are more frequently detected with higher supersaturations, also in the HOM regime. The possible explanations to this observation are contradictory to each other. On the one hand this could mean that AC cirrus form predominantly via HET nucleation since the high RHi values for HOM are not detected. On the other hand, it could be considered that older, mature clouds were measured in the AC cirrus group, which already used up their higher RHi to form new ice crystals via HET and HOM nucleation, thus depleting the available water vapor and causing the observed reduction in RHi. This would imply, that the measured WAI cirrus are younger and still produce new ice crystals via HET and also HOM nucleation, since the needed high RHi values are detected.

The RHi is strongly connected to the nucleation process of cirrus clouds, which in turn affects their micro- and macrophysical properties. In order to explain the ambiguous result discussed in the previous paragraph cloud age and microphysical properties must be studied. For this, I used the optimal estimate retrieval VarCloud (Delanoë and Hogan, 2008; Cazenave et al., 2019; Aubry et al., 2024). It allows the retrieval of cirrus microphysical properties by combining measurements

of the WALES lidar with the HAMP radar (Ewald et al., 2019), which was also aboard HALO for the HALO-(AC)^3 campaign. Additionally, in order to gain insights on the cloud age and evolution, I used calculated backwards trajectories from two different models. The Lagrangian analysis tool LAGRANTO (Sprenger and Wernli, 2015) and the CLaMS-Ice model, which combines a Chemical Lagrangian Model with two-moment ice microphysics (McKenna et al., 2002). The findings are presented in Table 5.1.

Regarding the average cloud age of AC and WAI cirrus, both CLaMS-Ice and LAGRANTO are used. The measured AC and WAI cirrus are used as the starting point for the calculation of backwards trajectories. Two different ways are used to define the point at which the clouds formed along these trajectories. The first one is based on the ice water content (IWC). The point along the backwards trajectory where the IWC drops below 0.1 mg/kg for the first time is considered the time of formation. The second one is based on the RHi. The point along the trajectory where the RHi reaches its maximum value is considered the moment of ice nucleation and thus cirrus formation. Despite the exact value being different between the two models and methods, AC cirrus appear to be slightly older in all of them, but by a small margin. This is an indication, that the detected differences in RHi between AC and WAI cirrus might not be a result solely of their different age and evolutionary stage.

Table 5.1: Analysis of AC and WAI cirrus properties aiding in the discussion of the findings presented herein. Blue: calculations from CLaMS-Ice, Red: calculations from LAGRANTO, Green: retrieval from VarCloud.

		AC cirrus	WAI cirrus
Cloud Age	Hours since IWC < 0.1 mg/kg	21.9 ± 22.1	20 ± 16.9
	Hours since maximum RHi	37.7 ± 35.1	32.5 ± 34.1
	Hours since maximum RHi	9.2 ± 8.2	8.3 ± 8.1
Microphysics	Cloud Ice Mixing Ratio (**IWC**) [ppm]		
	Heterogeneous freezing class	0.45 ± 1.92	0.82 ± 3.26
	Homogeneous freezing class	6.04 ± 14.76	8.08 ± 14.16
	Cloud Ice Effective Radius ($\mathbf{R_{eff}}$) [µm]	48.7 ± 15.7	45.6 ± 19.9
	Ice Crystal Number Concentration (**ICN**) [1/kg]		
	Heterogeneous freezing class	$0.56 \cdot 10^3 \pm 2.37 \cdot 10^3$	$1.16 \cdot 10^3 \pm 4.54 \cdot 10^3$
	Homogeneous freezing class	$3.10 \cdot 10^5 \pm 2.70 \cdot 10^6$	$6.30 \cdot 10^5 \pm 3.10 \cdot 10^6$

The nucleation process, HET or HOM, which took place during the cloud formation is the other factor which might explain the detected RHi characteristics for the two cloud types. Two different methods to draw conclusions about the nucleation process are used. On the one hand, this information is directly provided by the CLaMS-Ice calculations and on the other hand the ice crystal number concentration (ICN) combined with the ice effective radius (R_{eff}) can be used as an indication.

The IWC and ICN calculated by CLaMS-Ice come in two classes, HET and HOM. For both AC and WAI cirrus it is evident that both nucleation processes took place during the cloud formation, but HOM contributes significantly more compared to HET. As already mentioned in Chapter 1, the nucleation process can affect the micro- and macrophysical properties of the cloud. More precisely, HOM nucleation tends to produce clouds with higher ICN and smaller R_{eff}, whereas HET nucleated clouds tend to have higher ICN and smaller R_{eff} (DeMott et al., 1997; Jensen and Toon, 1997; Sassen and Benson, 2000; Lin et al., 2002). Using the R_{eff} retrieved by VarCloud and the ICN calculated by CLaMS-Ice, it is evident that WAI cirrus have on average a slightly smaller R_{eff} and a substantially higher ICN. This could indicate that more HOM nucleation took place during formation of WAI cirrus compared to AC cirrus. This is also in accordance with the much higher probability of detection for very high supersaturations in WAI cirrus. It should although be kept in mind that WAI and AC cirrus were measured in different temperature ranges. The temperature also has an effect on the observed properties and might alter the magnitude of the difference and potentially also the conclusion.

Kärcher, (2005) detects a layer of high supersaturation, high ICN and small R_{eff} at the cloud top of a polar cirrus cloud, similar to the characteristics of WAI cirrus in this study, and also concludes that HOM nucleation played a significant role in the clouds formation. De La Torre Castro et al. (2023) on the other hand, conclude that the high latitude clouds in their study formed mainly by HET nucleation in an environment with few INP and a high RHi, as they detected low ICN and large R_{eff}. Rolf et al. (2022), used in-situ measurements from the same campaign as them and although they also report high supersaturations inside and outside cirrus clouds they find HOM nucleation as the leading ice-forming process.

What cannot be directly accounted for when comparing studies that performed statistical analyses is the evolutionary stage of the measured cirrus clouds. As proven by the two case studies in Sect. 4.1.4, the age of a cloud can affect the distribution of RHi within it and potentially also its microphysical properties such as ICN and R_{eff}, thus creating a distorted conclusion regarding the nucleation process.

5.3 Differences between the mid- and high latitudes

The mid- and high latitudes, are two regions with different characteristics. The midlatitudes are characterized by the big variety of dynamical meteorological systems, the increased aerosol load and the dense air traffic. On the other hand, the high latitudes are generally colder and drier with fewer aerosol emissions and a smaller aerosol load. All these factors, i.e. the temperature, available moisture and INPs, updraft speeds connected to synoptic systems and convection, meridional transports and uplifting and others, have an effect on the properties of the cirrus clouds that form

over the two regions under various conditions, by affecting their nucleation process and evolution. This in turn leads to the cirrus also having different effects on the atmosphere and climate.

In this thesis the properties of cirrus clouds over the midlatitudes that formed in-situ or had a liquid origin and cirrus that formed during undisturbed arctic conditions or in advected midlatitude airmasses over the high latitudes were studied, providing a comprehensive overview of the majority of different cirrus types found in the northern hemisphere. In the following I present a direct comparison of the macrophysical properties of cirrus clouds that formed over the mid- and high latitudes with various processes and in different ambient conditions.

5.3.1 Overview

RHi distribution with respect to temperature

Cirrus clouds in the arctic are detected with temperatures down to 200 K, which, as probably expected, is lower than for midlatitude cirrus. This also contributes to the fact that cirrus in the arctic are found with higher supersaturations, since higher RHi are possible at lower temperatures. Another difference between cirrus over the high and midlatitudes is the probability density of supersaturation. Cirrus clouds measured over the arctic tend to be more frequently supersaturated compared to midlatitude cirrus with the probabilities being 56 % and 34 % respectively. Interestingly, this difference stems mostly from RHi values in the lower HET regime.

A difference in available INP can provide an explanation to this observation. The generally less polluted arctic can be expected to also contain less INP and especially less easily activated INP. This in turn might result in higher RHi being necessary more frequently in order for HET ice nucleation to take place or it might even be an indication that HOM nucleation is more common during the formation of arctic cirrus.

In-cloud RHi layers

The layering of RHi values within arctic and midlatitude cirrus clouds is similar on the big picture but differences do arise at a closer observation. Both cloud types are dominated by high supersaturations near cloud top, with lower supersaturations becoming dominant until around cloud middle where the clouds become predominantly subsaturated down to the cloud base. Differences for cirrus clouds over the two latitude ranges are detected at cloud top and cloud base. As presented in Sect. 4.1.2 the cloud top of midlatitude cirrus is a mixture of supersaturated RHi values, while arctic cirrus have a cloud top clearly dominated by the highest RHi values allowing for HOM nucleation to take place. This behavior is switched at the cloud base. Midlatitude cirrus have a clearly subsaturated cloud base, with increasingly smaller probabilities for higher supersaturations. On the other hand, the cloud base of arctic cirrus, although still predominantly subsaturated, contains a significant amount of data with very high supersaturations even in the HOM nucleation regime. A lower INP abundance in the arctic could explain why HOM nucleation plays a significant role even near the cirrus cloud base.

As was presented in Sect. 4.1.4, the structure of RHi within a cirrus cloud is dependent on its evolutionary stage. Spichtinger et al. (2004) find that colder clouds, such as over the arctic, need longer times to transition from formation to maturity. Thus, it is more likely for them to be measured with higher supersaturations representative of a young, ice-forming cloud. The presented observation can also be explained by considering the nucleation processes. HET nucleation

commonly results in fewer but bigger ice crystals. These ice crystals can survive over longer periods even in subsaturated environments before completely melting. During their fall, these ice crystals might extend the cirrus cloud base into the subsaturated region below it, resulting in the abovementioned vertical structure. This assumption, that HET nucleation is more common over the midlatitudes, is contradictory to De La Torre Castro et al. (2023). They compare the microphysical properties of cirrus clouds over the mid- and high latitudes and conclude that in fact high latitude cirrus have lower ice crystal concentrations with bigger effective diameters, which is generally indicative of HET nucleation.

5.3.2 Cirrus types with different location, formation and airmass

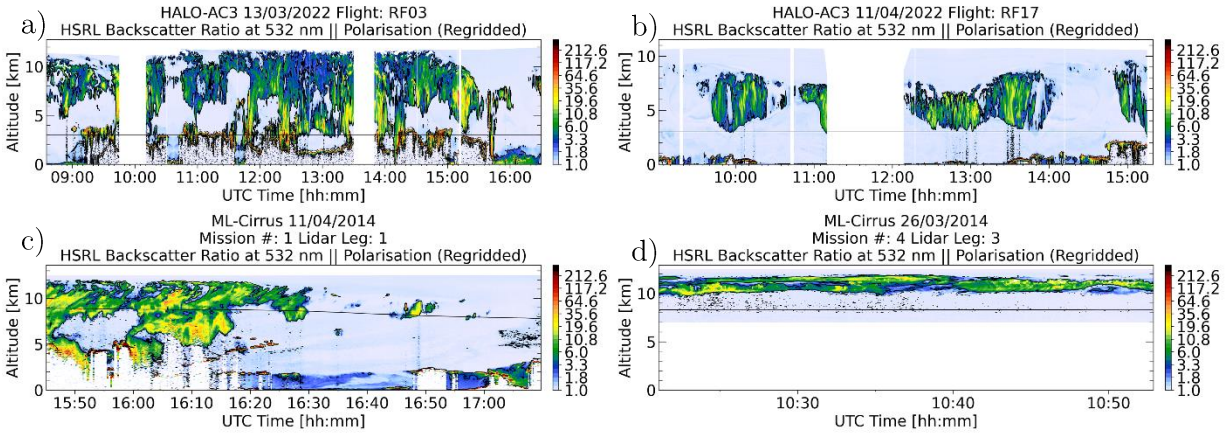

Figure 5.3: Examples of the measured BSR of four types of cirrus clouds, two in the high latitudes and two in the midlatitudes. a) RF03 of the HALO-(AC)^3 campaign. Cirrus measured in the high latitudes in an airmass transported from the midlatitudes during a WAI event. b) RF17 of the HALO-(AC)^3 campaign. Example of a cirrus measured under undisturbed arctic conditions in the high latitudes. c) Mission 14 of the ML-CIRRUS campaign including a midlatitude cirrus that had a liquid origin predecessor and formed in the outflow of a WCB. d) Mission 4, Leg 3 of the ML-CIRRUS campaign. Example of a cirrus cloud that formed in-situ over the midlatitudes.

An overview of the differences in RHi between cirrus clouds over the mid- and high latitudes has been presented above. In this study I further split cirrus clouds into more categories depending on their formation process and ambient conditions. Thus, I can present a comprehensive comparison of four different cirrus types, ranging from the mid- to the high latitudes and from warmer to colder temperatures. An example of each type is shown in Fig. 5.3.

The first type are the liquid origin cirrus over the midlatitudes (Fig. 5.3c). These cirrus have a liquid cloud as a predecessor. Lifting of this cloud to cold enough temperatures can result in its glaciation and thus the formation of a cirrus. They are commonly formed over the midlatitudes in frontal systems and warm conveyor belts (WCB) and are commonly accompanied by updrafts transporting moisture and aerosols to the upper troposphere. The case presented in Fig. 5.3c is

also from the outflow region of a WCB. Visible in the figure are its vertical extent, the liquid cloud accompanying it and also low-level clouds.

The second type are cirrus clouds that form in-situ over the midlatitudes (Fig. 5.3d). These clouds form directly as ice clouds at high altitudes and cold temperatures. Atmospheric fluctuations such as orographic Lee waves or human influence such as air traffic can trigger the formation of these cirrus. The case presented in Fig 5.3d was measured in the vicinity of a jet stream and also interacted with contrails. As is shown it is geometrically thinner compared to the liquid origin cirrus, appears to be more stratiform and is also found at a slightly higher altitude and colder temperature.

The third type are cirrus clouds that form in the arctic but in airmasses transported there from the midlatitudes during a warm air intrusion (WAI cirrus) (Fig. 5.3a). Despite being in the high latitudes, these clouds form in an uncharacteristic environment for the region with warm, aerosol- and moisture-rich airmasses also accompanied by updrafts. The cirrus case shown in Fig. 5.3a was measured during such a WAI event. WAI cirrus have a big geometric extent reaching from low in the arctic troposphere up to the tropopause. As seen in the figure they are accompanied also by low level liquid and mixed-phase clouds.

From the provided descriptions and by comparing Fig. 5.3 a) and c) it is shown that WAI cirrus in the arctic and liquid origin cirrus over the midlatitudes have several similarities. WAI cirrus form lower in the troposphere as the temperatures in the arctic are colder at lower altitudes. Both clouds are affected by an increased aerosol load and in airmasses being lifted to the upper troposphere.

The fourth and final type are cirrus that form in the arctic in undisturbed arctic conditions (AC cirrus) (Fig.5.3b). These clouds form in cold airmasses with a lower aerosol load and low updraft speeds. As seen in the AC cirrus case in Fig. 5.3b, they have a vertical extent smaller than WAI cirrus and midlatitude liquid origin cirrus. Given the cold temperatures in which they form, their cloud base remains relatively low. Since they do not form as a part of a larger system they are accompanied by fewer or no low-level clouds.

From the descriptions given above, AC cirrus seem to have some things in common with the in-situ formed midlatitude cirrus. Both form without being affected by a larger scale dynamical weather system, in colder temperatures and low or no updrafts. They do differ in their geometrical extent with AC cirrus being thicker and the aerosol loads in which they form. In-situ formed midlatitude cirrus are affected by the increased aerosol load of the midlatitudes as well as the much denser air traffic there.

Distribution and vertical structure of RHi from mid- to high latitudes

Following the definition and characterization of the four cirrus types above, in the following I compare the characteristics of RHi between them, starting with the temperature dependent probability densities shown in Fig 5.4.

The clouds over the mid- and high latitudes, where measured in different temperature ranges. This comes as a result of the natural temperature difference but also the different cirrus cloud masks applied on the clouds measured during the two campaign over the mid- and high latitudes. The commonly occurring liquid clouds in the midlatitude cirrus dataset required a stricter cirrus cloud mask in order to be removed. This in some cases had as a result that the cloud base of some

midlatitude cirrus was also cut off, and thus not the whole cloud was represented in the analyzed data. This was more commonly the case for midlatitude liquid origin cirrus as is also visible in Fig. 5.4c from the sudden end of the distribution. Despite that in the few cases where this occurred only a small part of the cloud base was removed and the bulk of data has been analyzed.

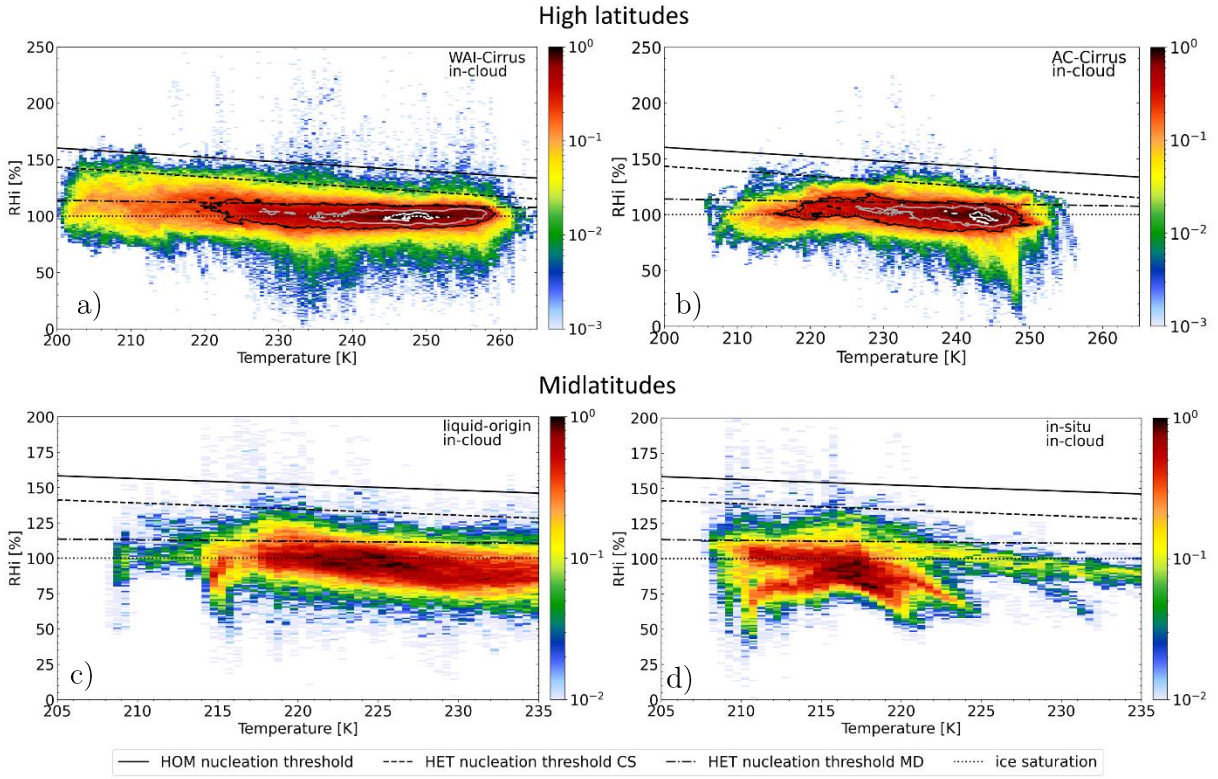

Figure 5.4: Probability densities of Relative Humidity over ice (RHi) with respect to temperature for: a) Cirrus clouds measured over the high latitudes under WAI conditions (WAI cirrus) b) Cirrus clouds measured over the high latitudes under arctic conditions (AC cirrus) c) cirrus clouds measured over the midlatitudes that had a liquid origin d) cirrus clouds measured over the midlatitudes that formed in-situ. The bin sizes are 0.5 K and 1 % RHi. The contour lines in a) and b) represent the 0.25, 0.5 and 0.85 probability contours in black, grey and white respectively. The dotted line represents the ice saturation threshold (RHi = 100 %). The dash-dotted line corresponds to the threshold for heterogeneous nucleation (HET) with mineral dust (MD) as the INP. The dashed line is the threshold for HET nucleation with coated soot (CS) as INP. The solid line denotes the threshold for homogeneous nucleation (HOM). Due to the differences in the measured clouds, the temperature and RHi range as well as the range of the color scale differ between clouds measured over the mid- and high latitudes.

As noted before, based on Fig. 5.3, midlatitude liquid origin cirrus have some similarities to WAI cirrus measured in the arctic. A similar conclusion can also be drawn based on the RHi distributions presented in Fig. 5.4. Midlatitude liquid origin clouds occupy a wider temperature range than their latitudinal counterpart, as is the case in the arctic between WAI and AC cirrus. A possible explanation for this is the greater geometrical extent of midlatitude liquid-origin and WAI cirrus compared to midlatitude in-situ formed and AC cirrus.

The shape of the distribution between midlatitude liquid origin and WAI cirrus in the arctic is also similar following the form of the CS activation threshold. Both cirrus types are also more frequently supersaturated compared to their latitudinal counterparts, although WAI cirrus more frequently reach higher supersaturations compared to midlatitude liquid origin clouds. Over the midlatitudes, although liquid origin clouds are more frequently supersaturated, the difference is in the lower range of supersaturations. Due to their colder temperatures midlatitude in-situ formed clouds are slightly more frequently found with higher supersaturations in the higher HET and HOM regimes. In the arctic, WAI cirrus are both more frequently supersaturated and also reach higher supersaturations compared to AC cirrus.

The smaller aerosol load over the high latitudes can also be translated in a smaller abundance of INPs in general and especially easily activated ones. This in turn might explain why WAI cirrus are more frequently detected with high supersaturations in the HOM regime. Warm, water-vapor-rich airmasses being lifted in the cold arctic troposphere without enough INP available lead to HOM nucleation playing a more important role.

On the other hand, midlatitude in-situ formed cirrus and AC cirrus in the arctic also present similarities to one another. Both have a narrower temperature range where mostly the warmer part is missing, compared to their latitudinal counterparts. This is an indication that they did not form because of ascending air from the lower troposphere but formed at higher altitudes.

A difference between the two cirrus types is noted regarding their supersaturations. While AC cirrus are more frequently supersaturated up to the CS activation threshold, they are rarely found with high supersaturations in the HOM regime. Contrary, midlatitude in-situ formed clouds are more frequently found with supersaturations in the higher HET and HOM regimes.

In Fig. 5.5, the vertical structure of RHi within the four cirrus types is presented. The comparison between them paints a different picture compared to the discussion above. The cloud tops of all cirrus types, except for the midlatitude liquid origin, are strongly dominated by high supersaturation in the HOM regime. The midlatitude liquid origin cirrus also have a supersaturated cloud top but the first 10 % of the total cloud depth have a mixture of supersaturations, although in the next 20 % cloud depth they are dominated by the HOM regime, similar to the other types.

The strong contribution from the HOM regime it the high latitude cirrus types, is characteristic and has been discussed in the previous and is also present in both high latitude cirrus types, playing a slightly more significant role in WAI cirrus. From cloud middle to cloud base, contrary to the discussion above, similarities are rather detected between midlatitude in-situ formed cirrus and WAI cirrus in the arctic as well as between midlatitude liquid origin cirrus and AC cirrus. The second pair, has a turning point at cloud middle, below which the clouds become progressively more dominated by subsaturated data points. Over the cloud middle on the other hand, both

cirrus types become progressively dominated but higher supersaturations, until the peculiarity at the cloud top of midlatitude liquid origin cirrus mentioned above.

The midlatitude in-situ formed cirrus are similar to the WAI cirrus in the arctic, in that they are never strongly dominated by subsaturated data and always have a significant amount of supersaturation throughout their depth, and especially their cloud base.

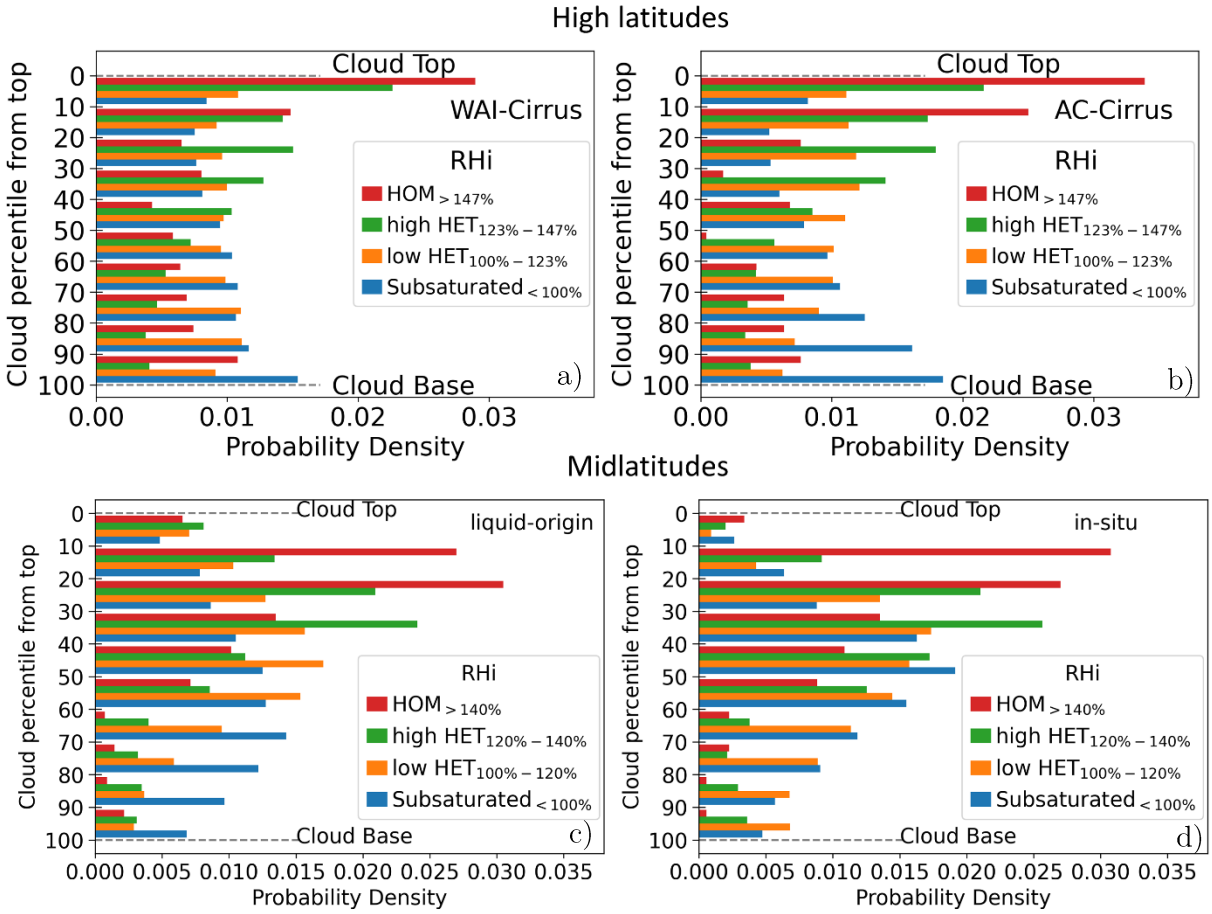

Figure 5.5: Probability densities of RHi in relative location to cloud top for: a) Cirrus clouds measured over the high latitudes under WAI conditions (WAI cirrus) b) Cirrus clouds measured over the high latitudes under arctic conditions (AC cirrus) c) cirrus clouds measured over the midlatitudes that had a liquid origin d) cirrus clouds measured over the midlatitudes that formed in-situ. Due to the different temperature ranges over the mid- and high latitudes, the nucleation regimes also have slightly different thresholds in order to be representative of their location. A more detailed description of the methodology for this plot is given in Sect. 3.5 and Fig. 4.2 and supporting text.

5.4 Assessment of the uncertainties of RHi

The main parameter used throughout this thesis is the relative humidity over ice (RHi). RHi is not directly measured but calculated by other parameters. More specifically the equation is:

$$RH_i = \frac{r_{wv}\rho k_B T}{e_{s_i}(T)} \tag{5.1}$$

where r_{wv} is the water vapor mixing ratio, ρ is the volume number density of air, k_B the Boltzmann constant, $e_{si}(T)$ the saturation vapor pressure for water over ice and T the temperature. The process of RHi calculation is described in more detail in Sect. 2.2 & 3.5.

Since most conclusions drawn in this thesis are based on the RHi values, their validity strongly depends on the systematic error of RHi. In Eq. 5.1 two sources of uncertainties in the calculation of RHi can be detected. On one hand the water vapor mixing ratio, which in this thesis is provided by WALES and the temperature, which is taken from the ECMWF-IFS.

The water vapor mixing ratio is measured by WALES with an accuracy of 5 %, which comprises uncertainties in the definition of the water vapor absorption cross-sections for the various used wavelengths, the air density profile used, and the calibration and maintenance of the DIAL wavelengths to the selected values (Kiemle et al., 2008; Urbanek, 2019). The signal backscattered from inside cirrus clouds is spatially inhomogeneous. As a result, there might be a difference in the volume illuminated by the online and offline wavelengths, which in turn might induce errors in the retrieval of the water vapor mixing ratio. Groß et al. (2014) conclude that the high repetition rate of WALES counteracts this problem to some extent. The few cases where strong gradients result in an error over 5 %, because of these inhomogeneities, are filtered out based on a variability estimate deduced from the raw signals. The Rayleigh–Doppler effect, i.e. the change from elastic scattering by ice crystals to broadened Rayleigh scattering by air molecules at the cloud edges is also corrected in the retrieval, with the residual error being below 2 % (Groß et al., 2014).

Since WALES was the instrument used for the retrieval of the water vapor mixing ratio used in all the analyses presented in this thesis, it can be neglected in all comparisons between clouds, such as mid- and high latitudes, liquid origin and in-situ formed and WAI and AC cirrus. It might lead to a reduced validity of the conclusions regarding the nucleation processes where RHi thresholds are used. In that regard, Groß et al. (2014) performed a direct comparison of water vapor DIAL measurements from WALES, performed during a flight of the HALO TECHNO mission, with simultaneous in-situ measurements taken from an aircraft flying below (their Fig. 4). The two aircraft where flying at different speeds, but for the time periods when their horizontal separation was small, they found a deviation of < 1 % between WALES and the in-situ measurements at the same altitudes. This gives additional confidence in the validity of the results presented herein.

The second potential source of uncertainties in the RHi are the temperature fields from ECMWF. For the ML-CIRRUS campaign, unfortunately there were no independent temperature measurements available, for example from dropsondes, in order to investigate the accuracy of the used temperature fields. Groß et al. (2014) used ambient temperatures measured by in-situ instruments onboard HALO during descents into and ascents from airports and compared them to the ECMWF temperatures. For the typical height and temperature ranges of cirrus clouds over

the midlatitude they found a difference of 0.8 K (T_{HALO} - T_{ECMWF}). According to their calculations this would induce a maximum error of about 10 % to 15 % in the calculated RHi for cirrus clouds. The measurements they used were performed over the midlatitudes similar to the ML-CIRRUS campaign. Assuming that the in-situ measurements had an absolute accuracy and the change in season has a minimal effect, the same error can be adopted also for the results presented here.

Similar to the error induced from the uncertainty in the water vapor measurements, only the conclusions where RHi is used as a threshold to describe for example nucleation processes would be affected. When comparing different clouds, the error is significantly lessened as ECMWF would have to systematically overestimate the temperature in one group and underestimate the other in order for this maximum error to be valid.

Further, this maximum error is only representative of single RHi values. Assuming that the uncertainty in the temperature is random the means of the distributions studied herein would have an even smaller uncertainty. For the ML-CIRRUS campaign a total of 16 flights are analyzed leading to an error of 3.75 % for the mean value of the distribution. For the comparison between in-situ formed and liquid origin cirrus, 12 and 13 lidar legs were used respectively, leading to an uncertainty of 4.3 % and 4.2 % when comparing the means of the distributions for the two cloud types.

During the HALO-$(AC)^3$ campaign, a large number of dropsondes were launched for each research flight adding up to 339 in total. This allowed for a more accurate comparison of the ECMWF-IFS model temperatures with measured data throughout the whole measurement area covered and under the same conditions for each flight (Wirth and Groß, 2023). The comparison resulted in an average temperature bias of around 0.2 K, with a precision of 0.4 K, which translates into an RHi error of 2 % bias and 4 % precision, induced by the use of ECMWF temperatures.

Similar to above, this error is representative for the single values while the mean values of the distributions have a smaller error. More precisely, 19 research flights are analyzed from the HALO-$(AC)^3$ campaign leading to an error of 0.9 % in the mean value of the distribution of cirrus clouds in the arctic. For the comparison between AC and WAI cirrus 8 and 9 flights were used respectively leading to an error of 1.4 % and 1.3 % for the average values of the distributions.

Based on all the above, due to the high accuracy of the water vapor mixing ratio retrieved by WALES, the small discrepancies of the ECMWF-IFS model temperatures when compared with in-situ measurements and dropsondes and importantly the good agreement with in-situ measurements reported by Groß et al. (2014) as well as Urbanek (2019), there is strong confidence in the accuracy of the analyses presented in this thesis.

Chapter 6

Conclusion and outlook

6.1 Summary

The importance of cirrus clouds to the earth's atmosphere and climate and their contribution to various processes and interactions in an ever-evolving system is undeniable. The technological improvements over the years, have led to the introduction of better, more accurate and versatile instruments for atmospheric measurements, such as the lidar. This in turn created new opportunities to study cirrus clouds and improve the understanding of their properties and effects. Despite that, many questions are still unanswered and a changing climate results in even more open questions being introduced.

The objective of this work, is to study and characterize the properties of relative humidity over ice (RHi) in cirrus clouds, depending on their location, formation process, evolutionary stage and ambient meteorological conditions. The aim is to improve the overall understanding of cirrus clouds, the processes that take place during their formation and evolution, and how these change depending on their age and the general state of the atmosphere. The RHi, is a parameter that holds a lot of value and information. It is the decisive parameter regarding the ice nucleation and thus cirrus formation process and microphysics, but is also affected by the ambient conditions and cloud age, thus also reflecting these.

In order to achieve the goals of this work, I used airborne cirrus cloud measurements conducted by the WALES lidar system during the ML-CIRRUS and HALO-(AC)^3 campaigns. The two campaigns took place at a similar time of year over the midlatitudes and arctic respectively, allowing for a direct comparison of the characteristics of cirrus clouds at the two different locations. The cirrus clouds measured during the two campaigns were also split into groups based on their formation process, ambient conditions and age and analyzed with respect to these characteristics.

Having completed my analysis, I can answer the scientific questions I set in Sect. 1.5:

S.Q. 1: What are the characteristics of ice supersaturation in cirrus clouds at mid- and high latitudes depending on the meteorological conditions, their formation process and their evolutionary stage?

Meteorological conditions

Cirrus clouds that form under different conditions at the same location are different to each other. Clouds that form in the arctic during a WAI event are geometrically as well as optically thicker. This is an indication that not only the macro- but also the microphysical properties are affected. Regarding the characteristics of RHi, I find that cirrus that form under undisturbed arctic conditions are less frequently supersaturated at low as well as high supersaturations, making HOM nucleation less probable. They

also have a clearer distinction between their in-cloud RHi layers, whereas WAI cirrus have high supersaturations throughout their whole depth and even at cloud base.

A brief analysis of their microphysical properties also reveals differences. Cirrus that form during WAI events have on average a slightly smaller R_{eff} and a substantially higher ICN. This finding indicates that these clouds might have formed with a greater contribution by HOM nucleation, thus confirming the findings in the macrophysical realm. From the above, I can conclude that a difference in ambient conditions can result in different nucleation and evolution processes taking place, manifesting in the microphysical properties of the clouds and being detected in the macrophysical.

Formation process

The origin of a cirrus cloud is also represented in the characteristics of RHi. In-situ formed cirrus are generally colder and more frequently subsaturated compared to liquid origin cirrus which are warmer and more frequently supersaturated. The vertical structure of RHi in liquid origin cirrus, is clear with high supersaturations at cloud top and subsaturation at cloud base. For in-situ formed cirrus low supersaturations are frequently detected over all layers and even at cloud base.

A probable explanation for these observations might be that liquid origin cirrus tend to form in systems, such as warm conveyor belts, with higher updrafts and more moisture. On the one hand this can mean that moisture is constantly transported to the cirrus cloud formation level, thus keeping RHi values high. On the other hand, INP might be used already for the formation of cloud droplets and become unavailable for ice nucleation, or the larger amounts of moisture might be too much for the amount of easily activate INP available, thus leading to higher probability for higher supersaturation in liquid origin cirrus.

Evolutionary stage

Analyzing the two cases where the temporal evolution of cirrus could be studied, reveals that the distribution and structure of RHi can be used as an indication of the clouds age. Young, newly formed clouds start with an RHi mode value at slight supersaturation with a strong positive skewness towards higher supersaturations, closely resembling a Rayleigh distribution. Cloud layers at higher altitudes have an even higher RHi mode and stronger skewness. As the cloud ages, the distribution of RHi has a continuously smaller skewness and starts resembling rather a Gaussian distribution. The RHi mode also drops to saturation and then subsaturation and the differences from layers at lower and higher altitudes become less pronounced.

S.Q. 2: What are the differences of cirrus clouds between the mid- and high latitudes?

The analysis of cirrus RHi over both the mid- and high latitudes, reveals that cirrus clouds are frequently detected in subsaturation. This is a potential indication that ice crystals can survive over longer time periods in a subsaturated environment until they completely dissipate. Higher overall supersaturations are detected in arctic cirrus, an observation most probably resulting from the lower temperatures at which they are measured. Cirrus clouds over the arctic are also more frequently supersaturated, the difference to midlatitude cirrus being predominantly for low supersaturations where only HET nucleation would be possible. This leads to the conclusion that HOM nucleation is more probable in arctic cirrus, which also implies that the clouds that form there might have different microphysical properties. Another reason for the detected difference in supersaturation might be the lower abundance of easily activated INP in the arctic in comparison to the midlatitudes.

The vertical structure of RHi within mid- and high latitude cirrus is generally similar, going from a cloud top with very high supersaturations to a subsaturated cloud base. Midlatitude cirrus present with an ambiguity at their cloud top, where a mix of high and low supersaturations is detected rather than only high ones. This could be an indication that both HET and HOM nucleation is taking place simultaneously or a reflection of the generally larger variability in the midlatitudes. Arctic cirrus on the other hand, have a less stratified layering, as high supersaturations are present throughout the cloud and even at cloud base.

The datasets I use in this thesis have a certain amount of inaccuracies. The method applied also introduces some errors. These have been presented and discussed in the previous chapters. The quality of the datasets and the applicability of the methods are both verified also by other studies on similar topics and are deemed to be sufficient to support my findings. The majority of the results I present in this work are novel. In the instance that other scientists have studied similar topics using for example other data, method, area, classification or other, I have tried to cite them and compare to them. I find that my results compare well with findings presented already in academic literature.

With my work I have managed to find answers to the scientific questions I set to investigate. Despite that many questions regarding cirrus clouds, their characteristics and effects are still open. An added value of the findings presented herein lies also in the fact that they can be used as a stepping stone to further extend the knowledge about the properties of cirrus clouds, such as microphysical and radiative, and their effects for example on climate change and arctic amplification.

6.2 Open questions

In this thesis the characteristics of relative humidity over ice for cirrus clouds depending on location, formation process, ambient conditions and evolutionary stage were studied. Although all scientific questions asked where answered, many open questions still remain regarding this topic.

How do various aerosols interact with cirrus clouds under different conditions, what effects do they have on their formation, evolution, microphysical and radiative properties, is one of these questions. A lack of direct measurements of aerosols and especially INP at low temperatures in the upper troposphere poses an obstacle in answering this question, and highlights the necessity of measurement campaigns focusing on this topic. Based on the properties of the measured aerosols and INP, laboratory work, for example with cloud chambers, could then be used to provide more details into how those INP activate and how they affect the microphysical properties of cirrus.

Another important missing piece in the cirrus puzzle, is a so-called radiative closure. As mentioned in Chapters 1 and 2, it is accepted that cirrus clouds cause a net annual warming globally. It has also been established, that cirrus characteristics and effects can differ depending on their location, formation, age and ambient conditions. Thus, it is important to more extensively measure the microphysical properties of cirrus clouds, study how they differ depending on these parameters and define more precisely how they affect their radiative properties and climate effects.

The anthropogenic effect on cirrus clouds is also a topic with many unanswered questions and great significance. Through the dense and ever-increasing air traffic, humans can induce the formation of ice clouds, contrails and contrail cirrus, in regions where they would not occur naturally and with unique characteristics and effects. Cirrus cloud cover might also be affected by the changing ambient conditions due to climate change. An increase in cirrus cloud cover be it due to natural or anthropogenic reasons, might result in a stronger cirrus radiative effect globally or locally. How does the cirrus cover change under different ambient conditions and over different locations with and without human influence, is another open question to be answered.

All the abovementioned unknowns regarding the properties of cirrus clouds, their formation and evolution under different conditions introduce uncertainties when trying to model them. Thus, another open question is, what are the necessary parametrizations for better prediction and representation of cirrus clouds in weather forecasting and climate models?

In order to answer the open questions, measurements of the macro- and microphysical properties of cirrus clouds are necessary. The ML-CIRRUS and HALO-(AC)^3 campaigns, which are used herein, provided measurements of cirrus clouds over vast regions and under many different conditions. Cirrus clouds though, do appear over the whole globe and throughout all seasons, thus leaving a lot more to be discovered. Future campaigns could focus on measuring cirrus clouds over regions where data are scarce, such as the Antarctic in order to provide a comparison to their effects noticed in the arctic. Cirrus cloud measurements during different seasons with distinct characteristics as for example polar day and night could also shed light into their formation, properties and effects by removing one of the affecting parameters, solar radiation. Additionally, satellite observations could prove helpful in tracking the location and evolution of cirrus with time, thus also aiding to their more accurate prediction.

Abbreviations and Symbols

List of Abbreviations

Abbreviation	Definition / Explanation
AC	Arctic Conditions
APD	Avalanche Photo Diodes
BELUGA	Balloon-bornE moduLar Utility for profilinG the lower Atmosphere
BSR	Backscatter Ratio
CLaMS	Chemical Lagrangian Model of the Stratosphere
CS	Coated Soot
DAC	Data Acquisition Computer
DFB	Distributed Feedback diode lasers
DIAL	Differential Absorption Lidar
DLR	German Aerospace Center
ECMWF	European Centre for Medium-Range Weather Forecasts
ERA-5	ECMWF reanalysis
FAAM	Facility for Airborne Atmospheric Measurements
HALO	High Altitude and LOng-range research aircraft
HALO-(AC)^3	HALO measurements campaign over the arctic
HAMP	HALO Microwave Package
HET	Heterogeneous Nucleation
HOM	Homogeneous Nucleation
HSRL	High Spectral Resolution Lidar
ICN	Ice Crystal Number Concentration
IFS	Integrated Forecasting System
INP	Ice Nucleating Particle
IVT	Integrated Water Vapor Transport
IWC	Ice Water Content
KTP	Potassium Titanyl Phosphate
LAGRANTO	Lagrangian Analysis Tool
M#	Missions of the ML-CIRRUS campaign
MCS	Mesoscale Convective System
MCS	Mesoscale Convective System
MD	Mineral Dust

Abbreviation	Definition / Explanation
ML-CIRRUS	Midlatitude Cirrus experiment
Nd:YAG	Neodymium-doped Yttrium Aluminum Garnet
OPO	Optical Parametric Oscillator
PBS	Polarizing Beam Splitter
PDF	Probability Density Function
PLDR	Particle Linear Depolarization Ratio
PM	Photo-Multiplier
RF	Research Flight during the HALO-$(AC)^3$ campaign
RHi	Relative Humidity with respect to ice
SAFIRE	Service des Avions Français Instrumentés pour la Recherche en Environnement
SHG	Second-Harmonic Generator
STP	Standard Temperature and Pressure
WAI	Warm Air Intrusion
WALES	Water Vapor Lidar Experiment in Space
WCB	Warm Conveyor Belt
WVMR	Water Vapor Mixing Ratio

List of Symbols

Symbol	Meaning	Unit
RHi_{HET}^{CS}	RHi threshold for the initiation of heterogeneous nucleation on coated soot	%
RHi_{HET}^{MD}	RHi threshold for the initiation of heterogeneous nucleation on mineral dust	%
BSR	backscatter ratio (total -molecular and particle- to molecular)	-
C_{mol}	HSRL lidar instrument constant for the molecular backscatter channel	m^3sr
CRE	cloud radiative effect	W/m^2
C_{tot}	HSRL lidar instrument constant for the total backscatter channel	m^3sr
$e_{s,i}$	water vapor saturation pressure over ice	Pa
H	altitude	m
ICN	ice crystal number concentration	kg^{-1}
IWC	ice water content	mg/kg or ppm
L_{mol}	molecular lidar ratio (extinction-to-backscatter)	sr
L_{par}	particle lidar ratio (extinction-to-backscatter)	sr
N	molecular number density	m^{-3}
P	power of light signal	W
$P_{0[off]}$	emitted power on the offline wavelength	W
$P_{0[on]}$	emitted power on the on-line wavelength	W
$PLDR$	particle linear depolarization ratio	%
P_{mol}	power received from molecular backscatter	W
P_{off}	power received from the backscattering of the offline signal	W
P_{on}	power received from backscattering of the on-line signal	W
P_{tot}	total power received from molecular and particle backscatter	W
R_{eff}	ice crystal effective radius	µm
RHi	relative humidity over ice	%
RHi_{HOM}	rhi threshold for initiation of homogeneous nucleation	%
T	temperature	K
$wvmr$	water vapor volume mixing ratio	ppm
α	extinction coefficient	m^{-1}

Symbol	Meaning	Unit
α_{mol}	molecular extinction coefficient	m^{-1}
$\alpha_{mol,abs}$	molecular extinction coefficient due to absorption	m^{-1}
$\alpha_{mol,sca}$	molecular extinction coefficient due to scattering	m^{-1}
α_{off}	extinction coefficient of the offline wavelength	m^{-1}
α_{on}	extinction coefficient of the on-line wavelength	m^{-1}
α_{par}	particle extinction coefficient	m^{-1}
$\alpha_{par,abs}$	particle extinction coefficient due to absorption	m^{-1}
$\alpha_{par,sca}$	particle extinction coefficient due to scattering	m^{-1}
β	backscatter coefficient	$m^{-1}sr^{-1}$
β_{mol}	molecular backscatter coefficient	$m^{-1}sr^{-1}$
$\beta_{mol,s}$	molecular backscatter coefficient at STP conditions	$m^{-1}sr^{-1}$
β_{off}	backscatter coefficient of the offline wavelength	$m^{-1}sr^{-1}$
β_{on}	backscatter coefficient of the on-line wavelength	$m^{-1}sr^{-1}$
β_{par}	particle backscatter coefficient	$m^{-1}sr^{-1}$
$\Delta\alpha$	difference in extinction coefficient between on- and offline	m^{-1}
$\Delta\sigma$	difference in molecular absorption cross section between on-and offline	m^2
θ	temperature	^oC
λ_{off}	offline wavelength for the DIAL method	m
λ_{on}	on-line wavelength for the DIAL method	m
σ_{abs}	molecular absorption cross-section	m^2
τ	cloud optical depth	-

List of Figures

1.1 Photograph of cirrus clouds in nature 1
1.2 Global Ice cloud cover (Schumann et al., 2015) 3
1.3 Maps of ice cloud CRE (Gasparini and Lohmann, 2016) 4
1.4 Schematic of ice cloud interaction with radiation 5
1.5 Diagram and pictures of ice crystal habits (Bailey and Hallett, 2009; SnowCrystals.com, 2024) 7
1.6 Time series of annually averaged near-surface air temperature anomalies (Wendisch et al., 2023) 10
2.1 Diagram of the basic setup of an atmospheric lidar system 16
2.2 High Spectral Resolution Lidar (HSRL) basic principle 21
2.3 Differential Absorption Lidar (DIAL) basic principle 22
2.4 Depolarization measurements with lidar basic principle 25
2.5 Graphic representation of the possible ice nucleation pathways 27
3.1 Graphic representation of the WALES lidar system (Wirth et al., 2009) 30
3.2 Schematic of the WALES transmitter working principle 31
3.3 Schematic of the WALES receiver layout 33
3.4 Photograph of WALES inside HALO 34
3.5 Example of WALES measurement products 36
3.6 Photograph of the research aircraft HALO in Kiruna 37
3.7 Window in the fuselage of HALO for lidar measurements 37
3.8 Map of the ML-CIRRUS flight tracks 39
3.9 Map of the HALO-(AC)^3 flight tracks 42
3.10 Definition of RHi regimes based on nucleation thresholds 47
3.11 Application of the cirrus cloud mask on an ML-CIRRUS mission 51
3.12 Application of the cirrus cloud mask on a HALO-(AC)^3 research flight 52
3.13 Graphic explaining in-situ and liquid origin cirrus (Luebke et al., 2016) 53
3.14 Ambient conditions during an AC and a WAI flight 54
3.15 Maps containing the backwards trajectories of AC and WAI cirrus 56
4.1 Distribution of RHi in and around midlatitude cirrus 58

4.2 Vertical structure of RHi in midlatitude cirrus 61
4.3 Distribution of RHi in and around in-situ and liquid origin cirrus 62
4.4 Vertical structure of RHi in in-situ and liquid origin cirrus 65
4.5 BSR curtain of the MCS case 66
4.6 RHi PDF for the three evolutionary stages of the MCS case 67
4.7 BSR curtain of the WCB outflow case 68
4.8 RHi PDF for the three evolutionary stages of the WCB outflow case 68
4.9 Distribution of RHi in and around high latitude cirrus 70
4.10 Vertical structure of RHi in high latitude cirrus 72
4.11 Maps containing the total column water vapor concentrations along the flight tracks of AC and WAI flights 73
4.12 BSR curtains for a WAI and an AC cirrus 75
4.13 Distribution of RHi in and around cirrus measured under WAI and AC conditions 78
4.14 Vertical structure of RHi and RHi distribution with altitude for AC and WAI cirrus 80
5.1 Probability densities of the vertical velocities for in-situ formed and liquid origin cirrus 88
5.2 Probability density of ambient temperature with respect to altitude for AC Cirrus and WAI Cirrus. 92
5.3 BSR curtains representative of in-situ and liquid origin cirrus over the midlatitudes and WAI and AC cirrus over the arctic. 98
5.4 Comparison of in-cloud RHi PDF for in-situ and liquid-origin cirrus over the midlatitudes and WAI and AC cirrus over the arctic. 100
5.5 Comparison of the vertical structure of RHi for in-situ and liquid-origin cirrus over the midlatitudes and WAI and AC cirrus over the arctic. 102

List of Tables

3.1 WALES transmitter performance parameters 35

3.2 Characteristics of WALES DIAL and HSRL measurements 35

3.3 Characteristics of the research aircraft HALO 38

3.4 Overview off the ML-CIRRUS missions 41

3.5 Overview of the research flights performed during the HALO-(AC)^3 campaign 44

3.6 The cirrus cloud mask applied on the ML-CIRRUS data 49

3.7 The cirrus cloud mask applied on the HALO-(AC)^3 data 50

4.1 Compilation of the findings from the analysis of RHi from the ML-CIRRUS campaign 60

4.2 Compilation of the findings from the analysis of RHi from the HALO-(AC)^3 campaign 71

4.3 Findings regarding the water vapor concentration and temperature under AC and WAI conditions 74

4.4 Geometrical and optical properties of cirrus measured in the arctic under AC and WAI conditions 76

4.5 Findings from the analysis of the RHi within and around cirrus measured under AC and WAI conditions 78

5.1 Comparison of age and microphysical properties between AC and WAI cirrus 95

References

Ansmann, A., Mamouri, R.-E., Bühl, J., Seifert, P., Engelmann, R., Hofer, J., Nisantzi, A., Atkinson, J. D., Kanji, Z. A., Sierau, B., Vrekoussis, M., and Sciare, J.: Ice-nucleating particle versus ice crystal number concentrationin altocumulus and cirrus layers embedded in Saharan dust:a closure study, Atmospheric Chemistry and Physics, 19, 15087–15115, https://doi.org/10.5194/acp-19-15087-2019, 2019.

Aratus of Soli: Φαινόμενα και Διοδημεία, 3rd century BC.

Aristotle: Μετεωρολογικά τοῦ Ἀριστοτέλους, Book I, Chapter 9, 340BC.

Aubry, C., Delanoë, J., Groß, S., Ewald, F., Tridon, F., Jourdan, O., and Mioche, G.: Lidar-radar synergistic method to retrieve ice, supercooled and mixed-phase clouds properties, Atmospheric Measurement Techniques Discussions, 1–28, https://doi.org/10.5194/amt-2023-252, 2024.

Bailey, M. and Hallett, J.: Growth Rates and Habits of Ice Crystals between −20° and −70°C, Journal of the Atmospheric Sciences, 61, 514–544, https://doi.org/10.1175/1520-0469(2004)061<0514:GRAHOI>2.0.CO;2, 2004.

Bailey, M. P. and Hallett, J.: A Comprehensive Habit Diagram for Atmospheric Ice Crystals: Confirmation from the Laboratory, AIRS II, and Other Field Studies, Journal of the Atmospheric Sciences, 66, 2888–2899, https://doi.org/10.1175/2009JAS2883.1, 2009.

Bauer, P., Thorpe, A., and Brunet, G.: The quiet revolution of numerical weather prediction, Nature, 525, 47–55, https://doi.org/10.1038/nature14956, 2015.

Beer, C. G., Hendricks, J., and Righi, M.: A global climatology of ice-nucleating particles under cirrus conditions derived from model simulations with MADE3 in EMAC, Atmospheric Chemistry and Physics, 22, 15887–15907, https://doi.org/10.5194/acp-22-15887-2022, 2022.

Behrendt, A. and Nakamura, T.: Calculation of the calibration constant of polarization lidar and its dependency on atmospheric temperature, Opt. Express, OE, 10, 805–817, https://doi.org/10.1364/OE.10.000805, 2002.

Biele, J., Beyerle, G., and Baumgarten, G.: Polarization lidar: Corrections of instrumental effects, Opt. Express, OE, 7, 427–435, https://doi.org/10.1364/OE.7.000427, 2000.

Binder, H., Boettcher, M., Grams, C. M., Joos, H., Pfahl, S., and Wernli, H.: Exceptional Air Mass Transport and Dynamical Drivers of an Extreme Wintertime Arctic Warm Event, Geophysical Research Letters, 44, 12,028-12,036, https://doi.org/10.1002/2017GL075841, 2017.

Bohren, C. F. and Huffman, D. R.: Absorption and Scattering of Light by Small Particles, John Wiley & Sons, 547 pp., 2008.

Bösenberg, J.: Ground-based differential absorption lidar for water-vapor and temperature profiling: methodology, Appl. Opt., AO, 37, 3845–3860, https://doi.org/10.1364/AO.37.003845, 1998.

Boucher, O., Randall, D., Artaxo, P., Bretherton, C., Feingold, G., Forster, P., Kerminen, V.-M., Kondo, Y., Liao, H., Lohmann, U., Rasch, P., Satheesh, S. K., Sherwood, S., Stevens, B., and Zhan, X. Y.: Clouds and Aerosols, in: Climate Change 2013: The Physical Science Basis. Contribution of Working Group I to the Fifth Assessment Report of the Intergovernmental Panel on Climate Change [Stocker, T.F., D. Qin, G.-K. Plattner, M. Tignor, S.K. Allen, J. Boschung, A. Nauels, Y. Xia, V. Bex and P.M. Midgley (eds.)], Cambridge University Press, Cambridge, United Kingdom and New York, NY, USA., 2013.

Browell, E. V., Wilkerson, T. D., and Mcilrath, T. J.: Water vapor differential absorption lidar development and evaluation, Appl. Opt., AO, 18, 3474–3483, https://doi.org/10.1364/AO.18.003474, 1979.

Bucholtz, A.: Rayleigh-scattering calculations for the terrestrial atmosphere, Appl. Opt., AO, 34, 2765–2773, https://doi.org/10.1364/AO.34.002765, 1995.

Bureau, R.: Measures en Météorologie, Météorologie, 3, 292, 1946.

Burkhardt, U.: Extending a PDF cloud scheme in order to accommodate cirrus physics, ECMWF Workshop on Parametrization of Clouds and Precipitation, 2012.

Campbell, J. R., Dolinar, E. K., Lolli, S., Fochesatto, G. J., Gu, Y., Lewis, J. R., Marquis, J. W., McHardy, T. M., Ryglicki, D. R., and Welton, E. J.: Cirrus Cloud Top-of-the-Atmosphere Net Daytime Forcing in the Alaskan Subarctic from Ground-Based MPLNET Monitoring, Journal of Applied Meteorology and Climatology, 60, 51–63, https://doi.org/10.1175/JAMC-D-20-0077.1, 2021.

Cazenave, Q., Ceccaldi, M., Delanoë, J., Pelon, J., Groß, S., and Heymsfield, A.: Evolution of DARDAR-CLOUD ice cloud retrievals: new parameters and impacts on the retrieved microphysical properties, Atmospheric Measurement Techniques, 12, 2819–2835, https://doi.org/10.5194/amt-12-2819-2019, 2019.

Chen, T., Rossow, W. B., and Zhang, Y.: Radiative Effects of Cloud-Type Variations, Journal of Climate, 13, 264–286, https://doi.org/10.1175/1520-0442(2000)013<0264:REOCTV>2.0.CO;2, 2000.

Chen, W.-N., Chiang, C.-W., and Nee, J.-B.: Lidar ratio and depolarization ratio for cirrus clouds, Appl. Opt., AO, 41, 6470–6476, https://doi.org/10.1364/AO.41.006470, 2002.

Clemesha, B. R., Kent, G. S., and Wright, R. W.: A study of the feasibility of measuring atmospheric densities by using a laser - searchlight technique, University Of The West Indies Kingston (Jamaica) Dept Of Physics, AF-AFOSR, 616-64, 1965.

Collis, R. T. H.: Lidar: A new atmospheric probe, Quarterly Journal of the Royal Meteorological Society, 92, 220–230, https://doi.org/10.1002/qj.49709239205, 1966.

Collis, R. T. H. and Russell, P. B.: Lidar measurement of particles and gases by elastic backscattering and differential absorption, in: Laser Monitoring of the Atmosphere, edited by: Hinkley, E. D., Springer, Berlin, Heidelberg, 71–151, https://doi.org/10.1007/3-540-07743-X_18, 1976.

Comstock, J. M., Ackerman, T. P., and Mace, G. G.: Ground-based lidar and radar remote sensing of tropical cirrus clouds at Nauru Island: Cloud statistics and radiative impacts, Journal of Geophysical Research: Atmospheres, 107, AAC 16-1-AAC 16-14, https://doi.org/10.1029/2002JD002203, 2002.

Comstock, J. M., Ackerman, T. P., and Turner, D. D.: Evidence of high ice supersaturation in cirrus clouds using ARM Raman lidar measurements, Geophysical Research Letters, 31, L11106, https://doi.org/10.1029/2004GL019705, 2004.

Comstock, J. M., Lin, R.-F., Starr, D. O., and Yang, P.: Understanding ice supersaturation, particle growth, and number concentration in cirrus clouds, Journal of Geophysical Research: Atmospheres, 113, D23211, https://doi.org/10.1029/2008JD010332, 2008.

Cox, S. K.: Cirrus Clouds and the Climate, Journal of the Atmospheric Sciences, 28, 1513–1515, https://doi.org/10.1175/1520-0469(1971)028<1513:CCATC>2.0.CO;2, 1971.

Curcio, J. A. and Knestrick, G. L.: Correlation of Atmospheric Transmission with Backscattering, J. Opt. Soc. Am., JOSA, 48, 686–689, https://doi.org/10.1364/JOSA.48.000686, 1958.

Cziczo, D. J., Froyd, K. D., Hoose, C., Jensen, E. J., Diao, M., Zondlo, M. A., Smith, J. B., Twohy, C. H., and Murphy, D. M.: Clarifying the Dominant Sources and Mechanisms of Cirrus Cloud Formation, Science, 340, 1320–1324, https://doi.org/10.1126/science.1234145, 2013.

Dada, L., Angot, H., Beck, I., Baccarini, A., Quéléver, L. L. J., Boyer, M., Laurila, T., Brasseur, Z., Jozef, G., de Boer, G., Shupe, M. D., Henning, S., Bucci, S., Dütsch, M., Stohl, A., Petäjä, T., Daellenbach, K. R., Jokinen, T., and Schmale, J.: A central arctic extreme aerosol event triggered by a warm air-mass intrusion, Nat Commun, 13, 5290, https://doi.org/10.1038/s41467-022-32872-2, 2022.

Dahlke, S. and Maturilli, M.: Contribution of Atmospheric Advection to the Amplified Winter Warming in the Arctic North Atlantic Region, Advances in Meteorology, 2017, e4928620, https://doi.org/10.1155/2017/4928620, 2017.

De La Torre Castro, E., Jurkat-Witschas, T., Afchine, A., Grewe, V., Hahn, V., Kirschler, S., Krämer, M., Lucke, J., Spelten, N., Wernli, H., Zöger, M., and Voigt, C.: Differences in microphysical properties of cirrus at high and mid-latitudes, Atmospheric Chemistry and Physics, 23, 13167–13189, https://doi.org/10.5194/acp-23-13167-2023, 2023.

Dekoutsidis, G., Groß, S., Wirth, M., Krämer, M., and Rolf, C.: Characteristics of supersaturation in midlatitude cirrus clouds and their adjacent cloud-free air, Atmos. Chem. Phys., 23, 3103–3117, https://doi.org/10.5194/acp-23-3103-2023, 2023a.

Dekoutsidis, G., Feidas, H., and Bugliaro, L.: Contrail detection on SEVIRI images and 1-year study of their physical properties and the atmospheric conditions favoring their formation over Europe, Theor Appl Climatol, 151, 1931–1948, https://doi.org/10.1007/s00704-023-04357-9, 2023b.

Dekoutsidis, G., Wirth, M., and Groß, S.: The effects of warm-air intrusions in the high Arctic on cirrus clouds, Atmospheric Chemistry and Physics, 24, 5971–5987, https://doi.org/10.5194/acp-24-5971-2024, 2024.

Delanoë, J. and Hogan, R. J.: A variational scheme for retrieving ice cloud properties from combined radar, lidar, and infrared radiometer, Journal of Geophysical Research: Atmospheres, 113, https://doi.org/10.1029/2007JD009000, 2008.

DeMott, P. J., Rogers, D. C., and Kreidenweis, S. M.: The susceptibility of ice formation in upper tropospheric clouds to insoluble aerosol components, Journal of Geophysical Research: Atmospheres, 102, 19575–19584, https://doi.org/10.1029/97JD01138, 1997.

HALO database: https://halo-db.pa.op.dlr.de/, last access: 28 November 2023.

Devasthale, A., Tjernström, M., Karlsson, K.-G., Thomas, M. A., Jones, C., Sedlar, J., and Omar, A. H.: The vertical distribution of thin features over the Arctic analysed from CALIPSO observations: Part I: Optically thin clouds, Tellus B: Chemical and Physical Meteorology, 63, 77–85, https://doi.org/10.1111/j.1600-0889.2010.00516.x, 2011.

Di Girolamo, P., Summa, D., Lin, R.-F., Maestri, T., Rizzi, R., and Masiello, G.: UV Raman lidar measurements of relative humidity for the characterization of cirrus cloud microphysical properties, Atmospheric Chemistry and Physics, 9, 8799–8811, https://doi.org/10.5194/acp-9-8799-2009, 2009.

Diao, M., Zondlo, M. A., Heymsfield, A. J., Beaton, S. P., and Rogers, D. C.: Evolution of ice crystal regions on the microscale based on in situ observations, Geophysical Research Letters, 40, 3473–3478, https://doi.org/10.1002/grl.50665, 2013.

Diao, M., Jensen, J. B., Pan, L. L., Homeyer, C. R., Honomichl, S., Bresch, J. F., and Bansemer, A.: Distributions of ice supersaturation and ice crystals from airborne observations in relation to upper tropospheric dynamical boundaries, Journal of Geophysical Research: Atmospheres, 120, 5101–5121, https://doi.org/10.1002/2015JD023139, 2015.

Doyle, J. G., Lesins, G., Thackray, C. P., Perro, C., Nott, G. J., Duck, T. J., Damoah, R., and Drummond, J. R.: Water vapor intrusions into the High Arctic during winter, Geophysical Research Letters, 38, L12806, https://doi.org/10.1029/2011GL047493, 2011.

Dzambo, A. M. and Turner, D. D.: Characterizing relative humidity with respect to ice in midlatitude cirrus clouds as a function of atmospheric state, Journal of Geophysical Research: Atmospheres, 121, 12,253-12,269, https://doi.org/10.1002/2015JD024643, 2016.

Egerer, U., Gottschalk, M., Siebert, H., Ehrlich, A., and Wendisch, M.: The new BELUGA setup for collocated turbulence and radiation measurements using a tethered balloon: first applications in the cloudy Arctic boundary layer, Atmospheric Measurement Techniques, 12, 4019–4038, https://doi.org/10.5194/amt-12-4019-2019, 2019.

Ehret, G., Kiemle, C., Renger, W., and Simmet, G.: Airborne remote sensing of tropospheric water vapor with a near–infrared differential absorption lidar system, Appl. Opt., AO, 32, 4534–4551, https://doi.org/10.1364/AO.32.004534, 1993.

Ehrlich, A., Wendisch, M., Klingebiel, M., Mech, M., Crewell, S., Herber, A., and Lüpkes, C.: HALO-(AC)3: Airborne Observations of Arctic Clouds in Airmass Transformations, Copernicus Meetings, https://doi.org/10.5194/egusphere-egu23-7246, 2023.

Elterman, L.: The measurement of stratospheric density distribution with the searchlight technique, Journal of Geophysical Research (1896-1977), 56, 509–520, https://doi.org/10.1029/JZ056i004p00509, 1951.

Esselborn, M., Wirth, M., Fix, A., Tesche, M., and Ehret, G.: Airborne high spectral resolution lidar for measuring aerosol extinction and backscatter coefficients, Appl. Opt., AO, 47, 346–358, https://doi.org/10.1364/AO.47.000346, 2008.

Evans, W. E.: Remote probing of high cloud cover via satellite-borne lidar Final report, NASA-CR-96893, 1968.

Ewald, F., Groß, S., Hagen, M., Hirsch, L., Delanoë, J., and Bauer-Pfundstein, M.: Calibration of a 35 GHz airborne cloud radar: lessons learned and intercomparisons with 94 GHz cloud radars,

Atmospheric Measurement Techniques, 12, 1815–1839, https://doi.org/10.5194/amt-12-1815-2019, 2019.

Ewald, F., Groß, S., Wirth, M., Delanoë, J., Fox, S., and Mayer, B.: Why we need radar, lidar, and solar radiance observations to constrain ice cloud microphysics, Atmospheric Measurement Techniques, 14, 5029–5047, https://doi.org/10.5194/amt-14-5029-2021, 2021.

Fiocco, G. and Dewolf, J. B.: Frequency Spectrum of Laser Echoes from Atmospheric Constituents and Determination of the Aerosol Content of Air., Journal of the Atmospheric Sciences, 25, 488–496, https://doi.org/10.1175/1520-0469(1968)025<0488:FSOLEF>2.0.CO;2, 1968.

Fix, A., Steinebach, F., Wirth, M., Schäfler, A., and Ehret, G.: Development and application of an airborne differential absorption lidar for the simultaneous measurement of ozone and water vapor profiles in the tropopause region, Appl. Opt., AO, 58, 5892–5900, https://doi.org/10.1364/AO.58.005892, 2019.

Freudenthaler, V., Esselborn, M., Wiegner, M., Heese, B., Tesche, M., Ansmann, A., Müller, D., Althausen, D., Wirth, M., Fix, A., Ehret, G., Knippertz, P., Toledano, C., Gasteiger, J., Garhammer, M., and Seefeldner, M.: Depolarization ratio profiling at several wavelengths in pure Saharan dust during SAMUM 2006, Tellus B, 61, 165–179, https://doi.org/10.1111/j.1600-0889.2008.00396.x, 2009.

Friedland, S. S., Katzenstein, J., and Zatzick, M. R.: Pulsed searchlighting the atmosphere, Journal of Geophysical Research (1896-1977), 61, 415–434, https://doi.org/10.1029/JZ061i003p00415, 1956.

Fusina, F., Spichtinger, P., and Lohmann, U.: Impact of ice supersaturated regions and thin cirrus on radiation in the midlatitudes, Journal of Geophysical Research: Atmospheres, 112, https://doi.org/10.1029/2007JD008449, 2007.

Gasparini, B. and Lohmann, U.: Why cirrus cloud seeding cannot substantially cool the planet, Journal of Geophysical Research: Atmospheres, 121, 4877–4893, https://doi.org/10.1002/2015JD024666, 2016.

Gasparini, B., Meyer, A., Neubauer, D., Münch, S., and Lohmann, U.: Cirrus Cloud Properties as Seen by the CALIPSO Satellite and ECHAM-HAM Global Climate Model, Journal of Climate, 31, 1983–2003, https://doi.org/10.1175/JCLI-D-16-0608.1, 2018.

Gasparini, B., McGraw, Z., Storelvmo, T., and Lohmann, U.: To what extent can cirrus cloud seeding counteract global warming?, Environ. Res. Lett., 15, 054002, https://doi.org/10.1088/1748-9326/ab71a3, 2020.

Gensch, I. V., Bunz, H., Baumgardner, D. G., Christensen, L. E., Fahey, D. W., Herman, R. L., Popp, P. J., Smith, J. B., Troy, R. F., Webster, C. R., Weinstock, E. M., Wilson, J. C., Peter, T., and Krämer, M.: Supersaturations, microphysics and nitric acid partitioning in a cold cirrus cloud observed during CR-AVE 2006: an observation–modelling intercomparison study, Environ. Res. Lett., 3, 035003, https://doi.org/10.1088/1748-9326/3/3/035003, 2008.

Gierens, K.: On the transition between heterogeneous and homogeneous freezing, Atmospheric Chemistry and Physics, 3, 437–446, https://doi.org/10.5194/acp-3-437-2003, 2003.

Gierens, K., Schumann, U., Helten, M., Smit, H., and Marenco, A.: A distribution law for relative humidity in the upper troposphere and lower stratosphere derived from three years of MOZAIC measurements, Annales Geophysicae, 17, 1218–1226, https://doi.org/10.1007/s00585-999-1218-7, 1999.

Gierens, K., Schumann, U., Helten, M., Smit, H., and Wang, P.-H.: Ice-supersaturated regions and subvisible cirrus in the northern midlatitude upper troposphere, Journal of Geophysical Research: Atmospheres, 105, 22743–22753, https://doi.org/10.1029/2000JD900341, 2000.

Gierens, K., Wilhelm, L., Sommer, M., and Weaver, D.: On ice supersaturation over the Arctic, metz, 29, 165–176, https://doi.org/10.1127/metz/2020/1012, 2020.

Gimmestad, G. G. and Roberts, D. W.: Lidar Engineering: Introduction to Basic Principles, Cambridge University Press, 368 pp., 2023.

Gobbi, G. P.: Polarization lidar returns from aerosols and thin clouds: a framework for the analysis, Appl. Opt., AO, 37, 5505–5508, https://doi.org/10.1364/AO.37.005505, 1998.

Goyer, G. G. and Watson, R.: The Laser and its Application to Meteorology, Bulletin of the American Meteorological Society, 44, 564–570, 1963.

Graham, R. M., Cohen, L., Petty, A. A., Boisvert, L. N., Rinke, A., Hudson, S. R., Nicolaus, M., and Granskog, M. A.: Increasing frequency and duration of Arctic winter warming events, Geophysical Research Letters, 44, 6974–6983, https://doi.org/10.1002/2017GL073395, 2017.

Graversen, R. G. and Wang, M.: Polar amplification in a coupled climate model with locked albedo, Clim Dyn, 33, 629–643, https://doi.org/10.1007/s00382-009-0535-6, 2009.

Groß, S., Wiegner, M., Freudenthaler, V., and Toledano, C.: Lidar ratio of Saharan dust over Cape Verde Islands: Assessment and error calculation, Journal of Geophysical Research: Atmospheres, 116, https://doi.org/10.1029/2010JD015435, 2011.

Groß, S., Wirth, M., and Esselborn, M.: Aerosol Classification by Advanced Backscatter Lidar Techniques, in: Atmospheric Physics: Background – Methods – Trends, edited by: Schumann, U., Springer, Berlin, Heidelberg, 477–486, https://doi.org/10.1007/978-3-642-30183-4_29, 2012.

Groß, S., Wirth, M., Schäfler, A., Fix, A., Kaufmann, S., and Voigt, C.: Potential of airborne lidar measurements for cirrus cloud studies, Atmospheric Measurement Techniques, 7, 2745–2755, https://doi.org/10.5194/amt-7-2745-2014, 2014.

Gutleben, M., Groß, S., Wirth, M., Emde, C., and Mayer, B.: Impacts of Water Vapor on Saharan Air Layer Radiative Heating, Geophysical Research Letters, 46, 14854–14862, https://doi.org/10.1029/2019GL085344, 2019.

Haag, W. and Kärcher, B.: The impact of aerosols and gravity waves on cirrus clouds at midlatitudes, Journal of Geophysical Research: Atmospheres, 109, https://doi.org/10.1029/2004JD004579, 2004.

Haag, W., Kärcher, B., Ström, J., Minikin, A., Lohmann, U., Ovarlez, J., and Stohl, A.: Freezing thresholds and cirrus cloud formation mechanisms inferred from in situ measurements of relative humidity, Atmospheric Chemistry and Physics, 3, 1791–1806, https://doi.org/10.5194/acp-3-1791-2003, 2003.

Haladay, T. and Stephens, G.: Characteristics of tropical thin cirrus clouds deduced from joint CloudSat and CALIPSO observations, Journal of Geophysical Research: Atmospheres, 114, https://doi.org/10.1029/2008JD010675, 2009.

Hansen, J., Ruedy, R., Sato, M., and Lo, K.: Global Surface Temperature Change, Reviews of Geophysics, 48, RG4004, https://doi.org/10.1029/2010RG000345, 2010.

Hartmann, D. L., Ockert-Bell, M. E., and Michelsen, M. L.: The Effect of Cloud Type on Earth's Energy Balance: Global Analysis, Journal of Climate, 5, 1281–1304, https://doi.org/10.1175/1520-0442(1992)005<1281:TEOCTO>2.0.CO;2, 1992.

Hartmann, M., Blunier, T., Brügger, S. o., Schmale, J., Schwikowski, M., Vogel, A., Wex, H., and Stratmann, F.: Variation of Ice Nucleating Particles in the European Arctic Over the Last Centuries, Geophysical Research Letters, 46, 4007–4016, https://doi.org/10.1029/2019GL082311, 2019.

Hartmann, M., Gong, X., Kecorius, S., van Pinxteren, M., Vogl, T., Welti, A., Wex, H., Zeppenfeld, S., Herrmann, H., Wiedensohler, A., and Stratmann, F.: Terrestrial or marine – indications towards the origin of ice-nucleating particles during melt season in the European Arctic up to 83.7° N, Atmospheric Chemistry and Physics, 21, 11613–11636, https://doi.org/10.5194/acp-21-11613-2021, 2021.

Henderson, D. S., L'Ecuyer, T., Stephens, G., Partain, P., and Sekiguchi, M.: A Multisensor Perspective on the Radiative Impacts of Clouds and Aerosols, Journal of Applied Meteorology and Climatology, 52, 853–871, https://doi.org/10.1175/JAMC-D-12-025.1, 2013.

Henderson, G. R., Barrett, B. S., Wachowicz, L. J., Mattingly, K. S., Preece, J. R., and Mote, T. L.: Local and Remote Atmospheric Circulation Drivers of Arctic Change: A Review, Frontiers in Earth Science, 9, 709896, https://doi.org/10.3389/feart.2021.709896, 2021.

Herber, A., Dethloff, K., Haas, C., Steinhage, D., Strapp, J. W., McElroy, T., and Yamanouchi, T.: POLAR 5 – a new research aircraft for improved access to the Arctic, in: Drastic Change under the Global Warming, ISAR-1, 54–57, 2008.

Hersbach, H., Bell, B., Berrisford, P., and P., Biavati, G., Horányi, A., Muñoz Sabater, J., Nicolas, J., Peubey, C., Radu, R., Rozum, I., Schepers, D., Simmons, A., Soci, C., Dee, D., Thépaut, J-N: ERA5 hourly data on single levels from 1940 to present, Copernicus Climate Change Service (C3S) Data Store (CDS), 2018.

Heymsfield, A., Baumgardner, D., DeMott, P., Forster, P., Gierens, K., and Kärcher, B.: Contrail Microphysics, Bulletin of the American Meteorological Society, 91, 465–472, https://doi.org/10.1175/2009BAMS2839.1, 2010.

Heymsfield, A. J.: Precipitation Development in Stratiform Ice Clouds: A Microphysical and Dynamical Study, Journal of the Atmospheric Sciences, 34, 367–381, https://doi.org/10.1175/1520-0469(1977)034<0367:PDISIC>2.0.CO;2, 1977.

Heymsfield, A. J. and Miloshevich, L. M.: Relative Humidity and Temperature Influences on Cirrus Formation and Evolution: Observations from Wave Clouds and FIRE II, Journal of the Atmospheric Sciences, 52, 4302–4326, https://doi.org/10.1175/1520-0469(1995)052<4302:RHATIO>2.0.CO;2, 1995.

Heymsfield, A. J., Miloshevich, L. M., Twohy, C., Sachse, G., and Oltmans, S.: Upper-tropospheric relative humidity observations and implications for cirrus ice nucleation, Geophysical Research Letters, 25, 1343–1346, https://doi.org/10.1029/98GL01089, 1998.

Hong, Y. and Liu, G.: The Characteristics of Ice Cloud Properties Derived from CloudSat and CALIPSO Measurements, Journal of Climate, 28, 3880–3901, https://doi.org/10.1175/JCLI-D-14-00666.1, 2015.

Hong, Y., Liu, G., and Li, J.-L. F.: Assessing the Radiative Effects of Global Ice Clouds Based on CloudSat and CALIPSO Measurements, Journal of Climate, 29, 7651–7674, https://doi.org/10.1175/JCLI-D-15-0799.1, 2016.

Hoose, C. and Möhler, O.: Heterogeneous ice nucleation on atmospheric aerosols: a review of results from laboratory experiments, Atmos. Chem. Phys., 12, 9817–9854, https://doi.org/10.5194/acp-12-9817-2012, 2012.

Horman, M. H.: Measurement of Atmospheric Transmissivity using Backscattered Light from a Pulsed Light Beam*, J. Opt. Soc. Am., JOSA, 51, 681–691, https://doi.org/10.1364/JOSA.51.000681, 1961.

Hoyle, C. R., Luo, B. P., and Peter, T.: The Origin of High Ice Crystal Number Densities in Cirrus Clouds, Journal of the Atmospheric Sciences, 62, 2568–2579, https://doi.org/10.1175/JAS3487.1, 2005.

Huang, J.: A Simple Accurate Formula for Calculating Saturation Vapor Pressure of Water and Ice, Journal of Applied Meteorology and Climatology, 57, 1265–1272, https://doi.org/10.1175/JAMC-D-17-0334.1, 2018.

Hulburt, E. O.: Observations of a Searchlight Beam to an Altitude of 28 Kilometers, J. Opt. Soc. Am., 27, 377, https://doi.org/10.1364/JOSA.27.000377, 1937.

IPCC: Climate Change 2021: The Physical Science Basis. Contribution of Working Group I to the Sixth Assessment Report of the Intergovernmental Panel on Climate Change, , In Press, https://doi.org/10.1017/9781009157896, 2021.

Jensen, E. J. and Toon, Owen. B.: The potential impact of soot particles from aircraft exhaust on cirrus clouds, Geophysical Research Letters, 24, 249–252, https://doi.org/10.1029/96GL03235, 1997.

Jensen, E. J., Toon, O. B., Vay, S. A., Ovarlez, J., May, R., Bui, T. P., Twohy, Cynthia. H., Gandrud, B. W., Pueschel, R. F., and Schumann, U.: Prevalence of ice-supersaturated regions in the upper troposphere: Implications for optically thin ice cloud formation, Journal of Geophysical Research: Atmospheres, 106, 17253–17266, https://doi.org/10.1029/2000JD900526, 2001.

Jensen, E. J., Smith, J. B., Pfister, L., Pittman, J. V., Weinstock, E. M., Sayres, D. S., Herman, R. L., Troy, R. F., Rosenlof, K., Thompson, T. L., Fridlind, A. M., Hudson, P. K., Cziczo, D. J., Heymsfield, A. J., Schmitt, C., and Wilson, J. C.: Ice supersaturations exceeding 100% at the cold tropical tropopause: implications for cirrus formation and dehydration, Atmospheric Chemistry and Physics, 5, 851–862, https://doi.org/10.5194/acp-5-851-2005, 2005.

Jensen, E. J., Diskin, G., Lawson, R. P., Lance, S., Bui, T. P., Hlavka, D., McGill, M., Pfister, L., Toon, O. B., and Gao, R.: Ice nucleation and dehydration in the Tropical Tropopause Layer, Proceedings of the National Academy of Sciences, 110, 2041–2046, https://doi.org/10.1073/pnas.1217104110, 2013.

Johansson, E., Devasthale, A., Tjernström, M., Ekman, A. M. L., and L'Ecuyer, T.: Response of the lower troposphere to moisture intrusions into the Arctic, Geophysical Research Letters, 44, 2527–2536, https://doi.org/10.1002/2017GL072687, 2017.

Johnson, E. A., Meyer, R. C., Hopkins, R. E., and Mock, W. H.: The Measurement of Light Scattered by the Upper Atmosphere from a Search-Light Beam, J. Opt. Soc. Am., JOSA, 29, 512–517, https://doi.org/10.1364/JOSA.29.000512, 1939.

Kahn, B. H., Liang, C. K., Eldering, A., Gettelman, A., Yue, Q., and Liou, K. N.: Tropical thin cirrus and relative humidity observed by the Atmospheric Infrared Sounder, Atmospheric Chemistry and Physics, 8, 1501–1518, https://doi.org/10.5194/acp-8-1501-2008, 2008.

Kärcher, B.: Supersaturation, dehydration, and denitrification in Arctic cirrus, Atmospheric Chemistry and Physics, 5, 1757–1772, https://doi.org/10.5194/acp-5-1757-2005, 2005.

Kärcher, B.: Atmospheric Ice Formation Processes, in: Atmospheric Physics: Background – Methods – Trends, edited by: Schumann, U., Springer, Berlin, Heidelberg, 151–167, https://doi.org/10.1007/978-3-642-30183-4_10, 2012.

Kärcher, B.: Cirrus Clouds and Their Response to Anthropogenic Activities, Curr Clim Change Rep, 3, 45–57, https://doi.org/10.1007/s40641-017-0060-3, 2017.

Kärcher, B. and Lohmann, U.: A parameterization of cirrus cloud formation: Homogeneous freezing of supercooled aerosols, Journal of Geophysical Research: Atmospheres, 107, AAC 4-1-AAC 4-10, https://doi.org/10.1029/2001JD000470, 2002.

Kärcher, B. and Lohmann, U.: A parameterization of cirrus cloud formation: Heterogeneous freezing, Journal of Geophysical Research: Atmospheres, 108, 4402, https://doi.org/10.1029/2002JD003220, 2003.

Kärcher, B. and Seifert, A.: On homogeneous ice formation in liquid clouds, Quarterly Journal of the Royal Meteorological Society, 142, 1320–1334, https://doi.org/10.1002/qj.2735, 2016.

Kärcher, B., Hendricks, J., and Lohmann, U.: Physically based parameterization of cirrus cloud formation for use in global atmospheric models, Journal of Geophysical Research: Atmospheres, 111, https://doi.org/10.1029/2005JD006219, 2006.

Kaufmann, S., Voigt, C., Heller, R., Jurkat-Witschas, T., Krämer, M., Rolf, C., Zöger, M., Giez, A., Buchholz, B., Ebert, V., Thornberry, T., and Schumann, U.: Intercomparison of midlatitude tropospheric and lower-stratospheric water vapor measurements and comparison to ECMWF humidity data, Atmospheric Chemistry and Physics, 18, 16729–16745, https://doi.org/10.5194/acp-18-16729-2018, 2018.

Khvorostyanov, V. I. and Curry, J. A.: Critical humidities of homogeneous and heterogeneous ice nucleation: Inferences from extended classical nucleation theory, Journal of Geophysical Research: Atmospheres, 114, https://doi.org/10.1029/2008JD011197, 2009.

Khvorostyanov, V. I. and Sassen, K.: Cirrus Cloud Simulation Using Explicit Microphysics and Radiation. Part II: Microphysics, Vapor and Ice Mass Budgets, and Optical and Radiative Properties, Journal of the Atmospheric Sciences, 55, 1822–1845, https://doi.org/10.1175/1520-0469(1998)055<1822:CCSUEM>2.0.CO;2, 1998.

Kiemle, C., Wirth, M., Fix, A., Ehret, G., Schumann, U., Gardiner, T., Schiller, C., Sitnikov, N., and Stiller, G.: First airborne water vapor lidar measurements in the tropical upper troposphere and mid-latitudes lower stratosphere: accuracy evaluation and intercomparisons with other instruments, Atmospheric Chemistry and Physics, 8, 5245–5261, https://doi.org/10.5194/acp-8-5245-2008, 2008.

Klett, J. D.: Stable analytical inversion solution for processing lidar returns, Appl Opt, 20, 211–220, https://doi.org/10.1364/AO.20.000211, 1981.

Koop, T., Luo, B., Tsias, A., and Peter, T.: Water activity as the determinant for homogeneous ice nucleation in aqueous solutions, Nature, 406, 611–614, https://doi.org/10.1038/35020537, 2000.

Korolev, A. and Isaac, G. A.: Relative Humidity in Liquid, Mixed-Phase, and Ice Clouds, Journal of the Atmospheric Sciences, 63, 2865–2880, https://doi.org/10.1175/JAS3784.1, 2006.

Krämer, M., Schiller, C., Afchine, A., Bauer, R., Gensch, I., Mangold, A., Schlicht, S., Spelten, N., Sitnikov, N., Borrmann, S., de Reus, M., and Spichtinger, P.: Ice supersaturations and cirrus cloud crystal numbers, Atmospheric Chemistry and Physics, 9, 3505–3522, https://doi.org/10.5194/acp-9-3505-2009, 2009.

Krämer, M., Rolf, C., Luebke, A., Afchine, A., Spelten, N., Costa, A., Meyer, J., Zöger, M., Smith, J., Herman, R. L., Buchholz, B., Ebert, V., Baumgardner, D., Borrmann, S., Klingebiel, M., and Avallone, L.: A microphysics guide to cirrus clouds – Part 1: Cirrus types, Atmospheric Chemistry and Physics, 16, 3463–3483, https://doi.org/10.5194/acp-16-3463-2016, 2016.

Krämer, M., Rolf, C., Spelten, N., Afchine, A., Fahey, D., Jensen, E., Khaykin, S., Kuhn, T., Lawson, P., Lykov, A., Pan, L. L., Riese, M., Rollins, A., Stroh, F., Thornberry, T., Wolf, V., Woods, S., Spichtinger, P., Quaas, J., and Sourdeval, O.: A microphysics guide to cirrus – Part 2: Climatologies of clouds and humidity from observations, Atmospheric Chemistry and Physics, 20, 12569–12608, https://doi.org/10.5194/acp-20-12569-2020, 2020.

Krautstrunk, M. and Giez, A.: The Transition From FALCON to HALO Era Airborne Atmospheric Research, in: Atmospheric Physics, edited by: Schumann, U., Springer Berlin Heidelberg, Berlin, Heidelberg, 609–624, https://doi.org/10.1007/978-3-642-30183-4_37, 2012.

Krüger, K., Schäfler, A., Wirth, M., Weissmann, M., and Craig, G. C.: Vertical structure of the lower-stratospheric moist bias in the ERA5 reanalysis and its connection to mixing processes,

Atmospheric Chemistry and Physics, 22, 15559–15577, https://doi.org/10.5194/acp-22-15559-2022, 2022.

Kübbeler, M., Hildebrandt, M., Meyer, J., Schiller, C., Hamburger, Th., Jurkat, T., Minikin, A., Petzold, A., Rautenhaus, M., Schlager, H., Schumann, U., Voigt, C., Spichtinger, P., Gayet, J.-F., Gourbeyre, C., and Krämer, M.: Thin and subvisible cirrus and contrails in a subsaturated environment, Atmos. Chem. Phys., 11, 5853–5865, https://doi.org/10.5194/acp-11-5853-2011, 2011.

Li, Y., Mahnke, C., Rohs, S., Bundke, U., Spelten, N., Dekoutsidis, G., Groß, S., Voigt, C., Schumann, U., Petzold, A., and Krämer, M.: Upper-tropospheric slightly ice-subsaturated regions: frequency of occurrence and statistical evidence for the appearance of contrail cirrus, Atmospheric Chemistry and Physics, 23, 2251–2271, https://doi.org/10.5194/acp-23-2251-2023, 2023.

SnowCrystals.com: http://www.snowcrystals.com/, last access: 29 May 2024.

Lin, R.-F., Starr, D. O., DeMott, P. J., Cotton, R., Sassen, K., Jensen, E., Kärcher, B., and Liu, X.: Cirrus Parcel Model Comparison Project. Phase 1: The Critical Components to Simulate Cirrus Initiation Explicitly, Journal of the Atmospheric Sciences, 59, 2305–2329, https://doi.org/10.1175/1520-0469(2002)059<2305:CPMCPP>2.0.CO;2, 2002.

Liou, K.-N.: Influence of Cirrus Clouds on Weather and Climate Processes: A Global Perspective, Monthly Weather Review, 114, 1167–1199, https://doi.org/10.1175/1520-0493(1986)114<1167:IOCCOW>2.0.CO;2, 1986.

Liu, X. and Penner, J. E.: Ice nucleation parameterization for global models, Meteorologische Zeitschrift, 499–514, https://doi.org/10.1127/0941-2948/2005/0059, 2005.

Liu, X., Penner, J. E., Ghan, S. J., and Wang, M.: Inclusion of Ice Microphysics in the NCAR Community Atmospheric Model Version 3 (CAM3), Journal of Climate, 20, 4526–4547, https://doi.org/10.1175/JCLI4264.1, 2007.

Liu, Y., Key, J. R., Vavrus, S., and Woods, C.: Time Evolution of the Cloud Response to Moisture Intrusions into the Arctic during Winter, Journal of Climate, 31, 9389–9405, https://doi.org/10.1175/JCLI-D-17-0896.1, 2018.

Lohmann, U., Kärcher, B., and Hendricks, J.: Sensitivity studies of cirrus clouds formed by heterogeneous freezing in the ECHAM GCM, Journal of Geophysical Research: Atmospheres, 109, D16204, https://doi.org/10.1029/2003JD004443, 2004.

Luebke, A. E., Afchine, A., Costa, A., Grooß, J.-U., Meyer, J., Rolf, C., Spelten, N., Avallone, L. M., Baumgardner, D., and Krämer, M.: The origin of midlatitude ice clouds and the resulting influence on their microphysical properties, Atmospheric Chemistry and Physics, 16, 5793–5809, https://doi.org/10.5194/acp-16-5793-2016, 2016.

Lynch, D. K., Sassen, K., Starr, D. O., and Stephens, G.: Cirrus, Oxford University Press, 499 pp., 2002.

Maiman, T. H.: Stimulated Optical Radiation in Ruby, Nature, 187, 493–494, https://doi.org/10.1038/187493a0, 1960.

Manabe, S. and Strickler, R. F.: Thermal Equilibrium of the Atmosphere with a Convective Adjustment, Journal of the Atmospheric Sciences, 21, 361–385, https://doi.org/10.1175/1520-0469(1964)021<0361:TEOTAW>2.0.CO;2, 1964.

Marsing, A., Meerkötter, R., Heller, R., Kaufmann, S., Jurkat-Witschas, T., Krämer, M., Rolf, C., and Voigt, C.: Investigating the radiative effect of Arctic cirrus measured in situ during the winter 2015–2016, Atmospheric Chemistry and Physics, 23, 587–609, https://doi.org/10.5194/acp-23-587-2023, 2023.

Martins, E., Noel, V., and Chepfer, H.: Properties of cirrus and subvisible cirrus from nighttime Cloud-Aerosol Lidar with Orthogonal Polarization (CALIOP), related to atmospheric dynamics and water vapor, Journal of Geophysical Research: Atmospheres, 116, https://doi.org/10.1029/2010JD014519, 2011.

McCartney, E. J.: Optics of the atmosphere: Scattering by molecules and particles, 1976.

McClung, F. J. and Hellwarth, R. W.: Giant Optical Pulsations from Ruby, Journal of Applied Physics, 33, 828–829, https://doi.org/10.1063/1.1777174, 1962.

McFarquhar, G. M., Heymsfield, A. J., Spinhirne, J., and Hart, B.: Thin and Subvisual Tropopause Tropical Cirrus: Observations and Radiative Impacts, Journal of the Atmospheric Sciences, 57, 1841–1853, https://doi.org/10.1175/1520-0469(2000)057<1841:TASTTC>2.0.CO;2, 2000.

McKenna, D. S., Konopka, P., Grooß, J.-U., Günther, G., Müller, R., Spang, R., Offermann, D., and Orsolini, Y.: A new Chemical Lagrangian Model of the Stratosphere (CLaMS) 1. Formulation of advection and mixing, Journal of Geophysical Research: Atmospheres, 107, ACH 15-1-ACH 15-15, https://doi.org/10.1029/2000JD000114, 2002.

Middleton, W. E. K. and Spilhaus, A. F.: Meteorological Instruments, 3rd ed. revised., University of Toronto Press, Toronto, 1953.

Nakoudi, K., Ritter, C., and Stachlewska, I. S.: Properties of Cirrus Clouds over the European Arctic (Ny-Ålesund, Svalbard), Remote Sensing, 13, 4555, https://doi.org/10.3390/rs13224555, 2021.

Ovarlez, J., Gayet, J.-F., Gierens, K., Ström, J., Ovarlez, H., Auriol, F., Busen, R., and Schumann, U.: Water vapour measurements inside cirrus clouds in Northern and Southern hemispheres during INCA, Geophysical Research Letters, 29, 60-1-60–4, https://doi.org/10.1029/2001GL014440, 2002.

Oxford English Dictionary: "cirrus (n. 1 and 4)," https://doi.org/10.1093/OED/3257191364, 2023.

Park, D.-S. R., Lee, S., and Feldstein, S. B.: Attribution of the Recent Winter Sea Ice Decline over the Atlantic Sector of the Arctic Ocean, Journal of Climate, 28, 4027–4033, https://doi.org/10.1175/JCLI-D-15-0042.1, 2015.

Petzold, A., Krämer, M., Neis, P., Rolf, C., Rohs, S., Berkes, F., Smit, H., Gallagher, M., Beswick, K., Lloyd, G., Baumgardner, D., Spichtinger, P., Nédélec, P., Ebert, V., Buchholz, B., Riese, M., and Wahner, A.: Upper tropospheric water vapour and its interaction with cirrus clouds as seen from IAGOS long-term routine: In situ observations, Faraday Discussions, 200, https://doi.org/10.1039/C7FD00006E, 2017.

Phillips, V. T. J., DeMott, P. J., and Andronache, C.: An Empirical Parameterization of Heterogeneous Ice Nucleation for Multiple Chemical Species of Aerosol, Journal of the Atmospheric Sciences, 65, 2757–2783, https://doi.org/10.1175/2007JAS2546.1, 2008.

Pithan, F., Svensson, G., Caballero, R., Chechin, D., Cronin, T. W., Ekman, A. M. L., Neggers, R., Shupe, M. D., Solomon, A., Tjernström, M., and Wendisch, M.: Role of air-mass transformations in exchange between the Arctic and mid-latitudes, Nature Geosci, 11, 805–812, https://doi.org/10.1038/s41561-018-0234-1, 2018.

Pruppacher, H. R. and Klett, J. D.: Microphysics of Clouds and Precipitation, Springer Netherlands, Dordrecht, https://doi.org/10.1007/978-0-306-48100-0, 2010.

Ramanathan, V., Pitcher, E. J., Malone, R. C., and Blackmon, M. L.: The Response of a Spectral General Circulation Model to Refinements in Radiative Processes, Journal of the Atmospheric Sciences, 40, 605–630, https://doi.org/10.1175/1520-0469(1983)040<0605:TROASG>2.0.CO;2, 1983.

Rolf, C., Krämer, M., Spelten, N., Afchine, A., and Zöger, M.: Mid-latitude and Arctic supersaturations observed during Cirrus-HL, Copernicus Meetings, https://doi.org/10.5194/egusphere-egu22-11087, 2022.

Sakai, T., Orikasa, N., Nagai, T., Murakami, M., Tajiri, T., Saito, A., Yamashita, K., and Hashimoto, A.: Balloon-borne and Raman lidar observations of Asian dust and cirrus cloud properties over Tsukuba, Japan, Journal of Geophysical Research: Atmospheres, 119, 3295–3308, https://doi.org/10.1002/2013JD020987, 2014.

Sassen, K. and Benson, S.: Ice nucleation in cirrus clouds: A model study of the homogeneous and heterogeneous modes, Geophysical Research Letters, 27, 521–524, https://doi.org/10.1029/1999GL010883, 2000.

Sassen, K., Wang, Z., and Liu, D.: Global distribution of cirrus clouds from CloudSat/Cloud-Aerosol Lidar and Infrared Pathfinder Satellite Observations (CALIPSO) measurements, Journal of Geophysical Research: Atmospheres, 113, https://doi.org/10.1029/2008JD009972, 2008.

Schäfer, B., Carlsen, T., Hanssen, I., Gausa, M., and Storelvmo, T.: Observations of cold-cloud properties in the Norwegian Arctic using ground-based and spaceborne lidar, Atmospheric Chemistry and Physics, 22, 9537–9551, https://doi.org/10.5194/acp-22-9537-2022, 2022.

Schäfler, A., Harvey, B., Methven, J., Doyle, J. D., Rahm, S., Reitebuch, O., Weiler, F., and Witschas, B.: Observation of Jet Stream Winds during NAWDEX and Characterization of Systematic Meteorological Analysis Errors, Monthly Weather Review, 148, 2889–2907, https://doi.org/10.1175/MWR-D-19-0229.1, 2020.

Schotland, R. M.: The Determination of the Vertical Profile of Atmospheric Gases by Means of a Ground Based Optical Radar, in: Proceedings of the Third Symposium on Remote Sensing of Environment, October 1964, U. Michigan, Ann Arbor, 1965.

Schotland, R. M.: Some observations of the vertical profile of water vapor by a laser optical radar, in: Proc. Fourth Symp. Remote Sens. Environ., Ann Arbor, Michigan, ERIM, 273, 1966.

Schumann, U.: A contrail cirrus prediction model, Geoscientific Model Development, 5, 543–580, https://doi.org/10.5194/gmd-5-543-2012, 2012.

Schumann, U., Penner, J. E., Chen, Y., Zhou, C., and Graf, K.: Dehydration effects from contrails in a coupled contrail–climate model, Atmos. Chem. Phys., 15, 11179–11199, https://doi.org/10.5194/acp-15-11179-2015, 2015.

Seifert, M., Ström, J., Krejci, R., Minikin, A., Petzold, A., Gayet, J.-F., Schlager, H., Ziereis, H., Schumann, U., and Ovarlez, J.: Aerosol-cirrus interactions: a number based phenomenon at all?, Atmospheric Chemistry and Physics, 4, 293–305, https://doi.org/10.5194/acp-4-293-2004, 2004.

Seinfeld, J. H. and Pandis, S. N.: Atmospheric Chemistry and Physics: From Air Pollution to Climate Change, John Wiley & Sons, 1146 pp., 2016.

Serreze, M. C. and Francis, J. A.: The Arctic Amplification Debate, Climatic Change, 76, 241–264, https://doi.org/10.1007/s10584-005-9017-y, 2006.

Shi, X., Liu, Y., and Liu, J.: A Numerical Modeling Study on the Earth's Surface Brightening Effect of Cirrus Thinning, Atmosphere, 15, 189, https://doi.org/10.3390/atmos15020189, 2024.

Spichtinger, P. and Gierens, K. M.: Modelling of cirrus clouds – Part 1b: Structuring cirrus clouds by dynamics, Atmos. Chem. Phys., 9, 707–719, https://doi.org/10.5194/acp-9-707-2009, 2009.

Spichtinger, P., Gierens, K., Smit, H. G. J., and Ovarlez, J.: On the distribution of relative humidity in cirrus clouds, Atmos. Chem. Phys., 2004.

Sprenger, M. and Wernli, H.: The LAGRANTO Lagrangian analysis tool – version 2.0, Geosci. Model Dev., 8, 2569–2586, https://doi.org/10.5194/gmd-8-2569-2015, 2015.

Stephens, G. L., Tsay, S.-C., Stackhouse, P. W., and Flatau, P. J.: The Relevance of the Microphysical and Radiative Properties of Cirrus Clouds to Climate and Climatic Feedback, Journal of the Atmospheric Sciences, 47, 1742–1754, https://doi.org/10.1175/1520-0469(1990)047<1742:TROTMA>2.0.CO;2, 1990.

Stevens, B. and Bony, S.: What Are Climate Models Missing?, Science, 340, 1053–1054, https://doi.org/10.1126/science.1237554, 2013.

Stevens, B., Giorgetta, M., Esch, M., Mauritsen, T., Crueger, T., Rast, S., Salzmann, M., Schmidt, H., Bader, J., Block, K., Brokopf, R., Fast, I., Kinne, S., Kornblueh, L., Lohmann, U., Pincus, R., Reichler, T., and Roeckner, E.: Atmospheric component of the MPI-M Earth System Model: ECHAM6, Journal of Advances in Modeling Earth Systems, 5, 146–172, https://doi.org/10.1002/jame.20015, 2013.

Stramler, K., Genio, A. D. D., and Rossow, W. B.: Synoptically Driven Arctic Winter States, Journal of Climate, 24, 1747–1762, https://doi.org/10.1175/2010JCLI3817.1, 2011.

Ström, J., Seifert, M., Kärcher, B., Ovarlez, J., Minikin, A., Gayet, J.-F., Krejci, R., Petzold, A., Auriol, F., Haag, W., Busen, R., Schumann, U., and Hansson, H. C.: Cirrus cloud occurrence as function of ambient relative humidity: a comparison of observations obtained during the INCA experiment, Atmospheric Chemistry and Physics, 3, 1807–1816, https://doi.org/10.5194/acp-3-1807-2003, 2003.

Stubenrauch, C. J., Rossow, W. B., Kinne, S., Ackerman, S., Cesana, G., Chepfer, H., Girolamo, L. D., Getzewich, B., Guignard, A., Heidinger, A., Maddux, B. C., Menzel, W. P., Minnis, P., Pearl, C., Platnick, S., Poulsen, C., Riedi, J., Sun-Mack, S., Walther, A., Winker, D., Zeng, S., and Zhao, G.: Assessment of Global Cloud Datasets from Satellites: Project and Database Initiated by the GEWEX Radiation Panel, Bulletin of the American Meteorological Society, 94, 1031–1049, https://doi.org/10.1175/BAMS-D-12-00117.1, 2013.

Stuecker, M. F., Bitz, C. M., Armour, K. C., Proistosescu, C., Kang, S. M., Xie, S.-P., Kim, D., McGregor, S., Zhang, W., Zhao, S., Cai, W., Dong, Y., and Jin, F.-F.: Polar amplification dominated by local forcing and feedbacks, Nature Clim Change, 8, 1076–1081, https://doi.org/10.1038/s41558-018-0339-y, 2018.

Synge, E. H.: XCI. A method of investigating the higher atmosphere, The London, Edinburgh, and Dublin Philosophical Magazine and Journal of Science, 9, 1014–1020, https://doi.org/10.1080/14786443008565070, 1930.

Theophrastus of Eresus: Περί σημείων υδάτων και πνευμάτων και χειμώνων και ευδιών, 3rd century BC.

Tuve, M. A., Johnson, E. A., and Wulf, O. R.: A new experimental method for study of the upper atmosphere, Terrestrial Magnetism and Atmospheric Electricity, 40, 452–454, https://doi.org/10.1029/TE040i004p00452, 1935.

Urbanek, B.: Characterization of midlatitude cirrus clouds with airborne lidar - investigating an indirect aviation effect, Text.PhDThesis, Ludwig-Maximilians-Universität München, 2019.

Urbanek, B., Groß, S., Schäfler, A., and Wirth, M.: Determining stages of cirrus evolution: a cloud classification scheme, Atmos. Meas. Tech., 10, 1653–1664, https://doi.org/10.5194/amt-10-1653-2017, 2017.

Urbanek, B., Groß, S., Wirth, M., Rolf, C., Krämer, M., and Voigt, C.: High Depolarization Ratios of Naturally Occurring Cirrus Clouds Near Air Traffic Regions Over Europe, Geophysical Research Letters, 45, 13,166-13,172, https://doi.org/10.1029/2018GL079345, 2018.

Voigt, C., Schumann, U., Jurkat, T., Schäuble, D., Schlager, H., Petzold, A., Gayet, J.-F., Krämer, M., Schneider, J., Borrmann, S., Schmale, J., Jessberger, P., Hamburger, T., Lichtenstern, M., Scheibe, M., Gourbeyre, C., Meyer, J., Kübbeler, M., Frey, W., Kalesse, H., Butler, T., Lawrence, M. G., Holzäpfel, F., Arnold, F., Wendisch, M., Döpelheuer, A., Gottschaldt, K., Baumann, R., Zöger, M., Sölch, I., Rautenhaus, M., and Dörnbrack, A.: In-situ observations of young contrails – overview and selected results from the CONCERT campaign, Atmos. Chem. Phys., 10, 9039–9056, https://doi.org/10.5194/acp-10-9039-2010, 2010.

Voigt, C., Schumann, U., Minikin, A., Abdelmonem, A., Afchine, A., Borrmann, S., Boettcher, M., Buchholz, B., Bugliaro, L., Costa, A., Curtius, J., Dollner, M., Dörnbrack, A., Dreiling, V., Ebert, V., Ehrlich, A., Fix, A., Forster, L., Frank, F., Fütterer, D., Giez, A., Graf, K., Grooß, J.-U., Groß, S., Heimerl, K., Heinold, B., Hüneke, T., Järvinen, E., Jurkat, T., Kaufmann, S., Kenntner, M., Klingebiel, M., Klimach, T., Kohl, R., Krämer, M., Krisna, T. C., Luebke, A., Mayer, B., Mertes, S., Molleker, S., Petzold, A., Pfeilsticker, K., Port, M., Rapp, M., Reutter, P., Rolf, C., Rose, D., Sauer, D., Schäfler, A., Schlage, R., Schnaiter, M., Schneider, J., Spelten, N., Spichtinger, P., Stock, P., Walser, A., Weigel, R., Weinzierl, B., Wendisch, M., Werner, F., Wernli, H., Wirth, M., Zahn, A., Ziereis, H., and Zöger, M.: ML-CIRRUS: The Airborne Experiment on Natural Cirrus and Contrail Cirrus with the High-Altitude Long-Range Research Aircraft HALO, Bulletin of the American Meteorological Society, 98, 271–288, https://doi.org/10.1175/BAMS-D-15-00213.1, 2017.

Wang, M. and Penner, J. E.: Cirrus clouds in a global climate model with a statistical cirrus cloud scheme, Atmos. Chem. Phys., 10, 5449–5474, https://doi.org/10.5194/acp-10-5449-2010, 2010.

Weitkamp, C. (Ed.): Lidar, Springer-Verlag, New York, https://doi.org/10.1007/b106786, 2005.

Wendisch, M., Macke, A., Ehrlich, A., Lüpkes, C., Mech, M., Chechin, D., Dethloff, K., Velasco, C. B., Bozem, H., Brückner, M., Clemen, H.-C., Crewell, S., Donth, T., Dupuy, R., Ebell, K., Egerer, U., Engelmann, R., Engler, C., Eppers, O., Gehrmann, M., Gong, X., Gottschalk, M., Gourbeyre, C., Griesche, H., Hartmann, J., Hartmann, M., Heinold, B., Herber, A., Herrmann, H., Heygster, G., Hoor, P., Jafariserajehlou, S., Jäkel, E., Järvinen, E., Jourdan, O., Kästner, U., Kecorius, S., Knudsen, E. M., Köllner, F., Kretzschmar, J., Lelli, L., Leroy, D., Maturilli, M., Mei, L., Mertes, S., Mioche, G., Neuber, R., Nicolaus, M., Nomokonova, T., Notholt, J., Palm, M., Pinxteren, M. van, Quaas, J., Richter, P., Ruiz-Donoso, E., Schäfer, M., Schmieder, K., Schnaiter, M., Schneider, J., Schwarzenböck, A., Seifert, P., Shupe, M. D., Siebert, H., Spreen, G., Stapf, J., Stratmann, F., Vogl, T., Welti, A., Wex, H., Wiedensohler, A., Zanatta, M., and Zeppenfeld, S.: The Arctic Cloud Puzzle: Using ACLOUD/PASCAL Multiplatform Observations to Unravel the Role of Clouds and Aerosol Particles in Arctic Amplification, Bulletin of the American Meteorological Society, 100, 841–871, https://doi.org/10.1175/BAMS-D-18-0072.1, 2019.

Wendisch, M., Brückner, M., Crewell, S., Ehrlich, A., Notholt, J., Lüpkes, C., Macke, A., Burrows, J. P., Rinke, A., Quaas, J., Maturilli, M., Schemann, V., Shupe, M. D., Akansu, E. F., Barrientos-Velasco, C., Bärfuss, K., Blechschmidt, A.-M., Block, K., Bougoudis, I., Bozem, H., Böckmann, C., Bracher, A., Bresson, H., Bretschneider, L., Buschmann, M., Chechin, D. G., Chylik, J., Dahlke, S., Deneke, H., Dethloff, K., Donth, T., Dorn, W., Dupuy, R., Ebell, K., Egerer, U., Engelmann, R., Eppers, O., Gerdes, R., Gierens, R., Gorodetskaya, I. V., Gottschalk, M., Griesche, H., Gryanik, V. M., Handorf, D., Harm-Altstädter, B., Hartmann, J., Hartmann, M., Heinold, B., Herber, A., Herrmann, H., Heygster, G., Höschel, I., Hofmann, Z., Hölemann, J., Hünerbein, A., Jafariserajehlou, S., Jäkel, E., Jacobi, C., Janout, M., Jansen, F., Jourdan, O., Jurányi, Z., Kalesse-Los, H., Kanzow, T., Käthner, R., Kliesch, L. L., Klingebiel, M., Knudsen, E. M., Kovács, T., Körtke, W., Krampe, D., Kretzschmar, J., Kreyling, D., Kulla, B., Kunkel, D., Lampert, A., Lauer, M., Lelli, L., Lerber, A. von, Linke, O., Löhnert, U., Lonardi, M., Losa, S. N., Losch, M., Maahn, M., Mech, M., Mei, L., Mertes, S., Metzner, E., Mewes, D., Michaelis, J., Mioche, G., Moser, M., Nakoudi, K., Neggers, R., Neuber, R., Nomokonova, T., Oelker, J., Papakonstantinou-Presvelou, I., et al.: Atmospheric and Surface Processes, and Feedback Mechanisms Determining Arctic Amplification: A Review of First Results and Prospects of the (AC)3 Project, Bulletin of the American Meteorological Society, 104, E208–E242, https://doi.org/10.1175/BAMS-D-21-0218.1, 2023.

Wendisch, M., Crewell, S., Ehrlich, A., Herber, A., Kirbus, B., Lüpkes, C., Mech, M., Abel, S. J., Akansu, E. F., Ament, F., Aubry, C., Becker, S., Borrmann, S., Bozem, H., Brückner, M., Clemen, H.-C., Dahlke, S., Dekoutsidis, G., Delanoë, J., De La Torre Castro, E., Dorff, H., Dupuy, R., Eppers, O., Ewald, F., George, G., Gorodetskaya, I. V., Grawe, S., Groß, S., Hartmann, J.,

Henning, S., Hirsch, L., Jäkel, E., Joppe, P., Jourdan, O., Jurányi, Z., Karalis, M., Kellermann, M., Klingebiel, M., Lonardi, M., Lucke, J., Luebke, A., Maahn, M., Maherndl, N., Maturilli, M., Mayer, B., Mayer, J., Mertes, S., Michaelis, J., Michalkov, M., Mioche, G., Moser, M., Müller, H., Neggers, R., Ori, D., Paul, D., Paulus, F., Pilz, C., Pithan, F., Pöhlker, M., Pörtge, V., Ringel, M., Risse, N., Roberts, G. C., Rosenburg, S., Röttenbacher, J., Rückert, J., Schäfer, M., Schäfer, J., Schemannn, V., Schirmacher, I., Schmidt, J., Schmidt, S., Schneider, J., Schnitt, S., Schwarz, A., Siebert, H., Sodemann, H., Sperzel, T., Spreen, G., Stevens, B., Stratmann, F., Svensson, G., Tatzelt, C., Tuch, T., Vihma, T., Voigt, C., Volkmer, L., Walbröl, A., Weber, A., Wehner, B., Wetzel, B., Wirth, M., and Zinner, T.: Overview: Quasi-Lagrangian observations of Arctic air mass transformations – Introduction and initial results of the HALO–(AC)^3 aircraft campaign, EGUsphere, 1–46, https://doi.org/10.5194/egusphere-2024-783, 2024.

HALO AC3: https://halo-ac3.de/, last access: 24 March 2023.

Winton, M.: Amplified Arctic climate change: What does surface albedo feedback have to do with it?, Geophysical Research Letters, 33, L03701, https://doi.org/10.1029/2005GL025244, 2006.

Wirth, M. and Groß, S.: Characterisation of Arctic Cirrus by Airborne Water Vapor and High Spectral Resolution Lidar, Copernicus Meetings, https://doi.org/10.5194/egusphere-egu23-2024, 2023.

Wirth, M., Fix, A., Mahnke, P., Schwarzer, H., Schrandt, F., and Ehret, G.: The airborne multi-wavelength water vapor differential absorption lidar WALES: system design and performance, Appl. Phys. B, 96, 201–213, https://doi.org/10.1007/s00340-009-3365-7, 2009.

WMO International Cloud Atlas, 2017 Edition: https://cloudatlas.wmo.int/home.html, last access: 29 May 2024.

Woods, C. and Caballero, R.: The Role of Moist Intrusions in Winter Arctic Warming and Sea Ice Decline, Journal of Climate, 29, 4473–4485, https://doi.org/10.1175/JCLI-D-15-0773.1, 2016.

Wylie, D. P. and Menzel, W. P.: Eight Years of High Cloud Statistics Using HIRS, Journal of Climate, 12, 170–184, https://doi.org/10.1175/1520-0442(1999)012<0170:EYOHCS>2.0.CO;2, 1999.

Yau, M. K. and Rogers, R. R.: A Short Course in Cloud Physics, 3rd ed., Elsevier, 308 pp., 1996.

Young, A. T.: Rayleigh scattering, Physics Today, 35, 42–48, 1982.

Zhang, K., O'Donnell, D., Kazil, J., Stier, P., Kinne, S., Lohmann, U., Ferrachat, S., Croft, B., Quaas, J., Wan, H., Rast, S., and Feichter, J.: The global aerosol-climate model ECHAM-HAM, version 2: sensitivity to improvements in process representations, Atmospheric Chemistry and Physics, 12, 8911–8949, https://doi.org/10.5194/acp-12-8911-2012, 2012.

Zhao, M. and Shi, X.: A Study on the Wide Range of Relative Humidity in Cirrus Clouds Using Large-Ensemble Parcel Model Simulations, Atmosphere, 14, 583, https://doi.org/10.3390/atmos14030583, 2023.

Acknowledgements

This work is the result of the research I conducted at the Institute of Atmospheric Physics (IPA) of the German Aerospace Center (DLR) in Oberpfaffenhofen, with the help and support of many people whom I would like to thank in the following.

First of all, I want to wholeheartedly thank Dr. Silke Groß for giving me the opportunity to embark on this journey, for her support and guidance throughout it, for the knowledge I gained from our discussions and for her patience all these years. Further, I would like to thank Dr. Martin Wirth for sharing his brilliant knowledge on the WALES lidar system and teaching me how to operate it, as well as for his feedback and scientific advice. I would also like to thank my supervisor Prof. Dr. Markus Rapp, for the continuous support and always helpful feedback.

I thank also Dr. Martina Krämer and Dr. Christian Rolf for the wonderful collaboration we had, for providing the backwards trajectories for both campaigns and for the fruitful discussions, which helped me better understand and explain my findings.

Special thanks to my colleagues and mates from office 320, starting with the Cloudonauts Christian Heske, Clemantyne Aubry and Konstantin Krüger and also Eleni Tetoni, Adithya Pankan, Matteo Faccioni, Manuel Gutleben and Robert Reichert for creating a wonderful office environment, for our interdisciplinary discussions and for all the great memories we created over the years. Also, thanks to all my colleagues in the lidar department for the open and welcoming environment, their friendliness and their readiness to provide help and advice, as also for the helpful comments in writing this thesis.

I want to thank also the German Academic Exchange Service (DAAD) for granting me a PhD-scholarship at DLR and for the associated financial support.

Last but not least I would like to thank my family, my parents and my sister for the continuous help and support in any way possible despite the distance. This work would not have been possible without the care and support of my partner Pinelopi.

Thank you!